Preparation of Novel Composite PolyHIPE Polymers and their Applications in Intensified Removal of Tars from Syngas

A Thesis Submitted to Newcastle University for the Degree of Doctor of Philosophy

by

HASNI HASAN

School of Chemical Engineering & Advanced Materials

Newcastle University

June 2013

Disclaimer

This thesis is submitted in fulfilment of the requirements for the degree of Doctor of Philosophy at Newcastle University, Newcastle upon Tyne, United Kingdom. All the studies described within are solely my work otherwise expressly stated, and were undertaken at the School of Chemical Engineering and Advanced Materials under the guidance and supervision of Professor Galip Akay between November 2006 and August 2010.

I certify that none of the material offered in this thesis has been previously submitted for a degree or any other qualification at the above or any other university or institute.

Neither the author nor the Newcastle University at Newcastle upon Tyne accepts any liability for the contents of this document.

Abstract

In this study, several techniques were applied in order to produce PolyHIPE Polymer (PHP) with improved morphology and properties. Several types of PolyHIPE Polymers (PHPs), silica, vinyl trimethoxy silane (VTMS), and VTMS-silica PHPs, were successfully produced and compared to basic PHPs. The VTMS-silica PHP produced has the highest surface area, followed by silica-PHP and then by VTMS-PHP when compared to typical (basic) PHP. For VTMS PHP, only PHPs with 30, 35 and 40% VTMS exhibit higher surface area than basic PHP. There was no improvement of surface area for PHP with VTMS percentage lower than 30%. All VTMS-silica PHPs have higher pore volume of all types of modified PHPs. The highest pore volume was observed for S30B30, the PHP with 30% VTMS in the oil phase and 30% silica in the aqueous phase. VTMS PHPs with VTMS percentage of 20% and above and silica PHP with 30 % silica have significantly higher pore volume than basic PHP. None of the PHPs showed the existence of micropore volume.

Silica and VTMS were successfully reinforced into the HIPE producing novel PHP. This was confirmed by the results produced through FTIR spectroscopy and EDX (Energy Dispersive X-Ray) analysis. Novelty was observed in the morphology of VTMS and VTMS-silica PHP whereas silica-PHP retained the typical morphology of PolyHIPE polymer. The novel morphology of banana-like strands with coral-like pore was produced due to functionalising of VTMS to the HIPE through VTMS incorporation in the oil phase. VTMS-silica PHP is best described as having morphology of knobbly structure produced through incorporation of silica CC30 solution through aqueous phase with VTMS through oil phase.

Sulphonated silica-PHP was successfully produced through microwave irradiation and thermal treatment whereas sulphonated-VTMS PHP was successfully produced through thermal treatment only. The sulphonation process decreased the surface area of silica and VTMS PHPs significantly. There was no significant difference between the pore volumes of silica PHPs and those of sulphonated silica PHPs whereas pore volumes of VTMS PHPs decreased significantly due to sulphonation. The sulphonation process retained the morphology of silica and VTMS PHPs except for minor cracks.

The project also involved a study on tar removal/conversion using the modified PHP developed in the laboratory, high voltage and non-thermal plasma technique, specifically dielectric barrier discharge. The PHPs combined with dielectric barrier discharge was applied in the fine cleaning system. Due to complexity of the crude oil used as the tar model, no valid conclusion could be made about the tar removal or conversion. However, important positive effects from the treatment were observed in the removal of model tar from the model syngas under electric field or non-thermal plasma.

Dedication

This thesis is dedicated to my husband Mohd Sohaimi Ramli and my children Anis, Anas, Afif and Alif whose laughter and smile always bright up my days.

This thesis is dedicated to my sister Husna Hasan for being the best sister I could ever have since the death of our mother.

The thesis is especially dedicated to my late parents for opening my eyes to the wonders of the world and for inculcating in me the true importance of seeking knowledge.

Thank you all and may Allah bless you all. I could not have done this without you.

Acknowledgement

All praise is due to the Most Merciful, the Most Gracious. I am truly and thoroughly grateful for Thee for giving me the ability and knowledge to complete this work and for giving me the patience, strength and perseverance throughout my study.

I would also like to acknowledge my sponsor, Public Services Department of Malaysia, for giving me the opportunity to further my studies for the past 4 years. Thanks also to the Malaysian Nuclear Agency for supporting me through and through.

I would like to express my gratitude and appreciation for my supervisor; Professor Galip Akay who is a sea of knowledge and also for sharing with me his treasure of knowledge and wisdom. I am very thankful for his invaluable support and guidance in answering all my questions no matter how trivial they might have seemed.

I would like to thank my family for their undivided love and support throughout my study. To my husband and my children, very special thanks for their love, patience, support and understanding. My gratitude also goes to my sisters, brother and my mother-in-law for all their support and encouragement. To my late parents and my Aunt Bibisoom, thanks for raising me to be who I am today.

Finally, to all my friends and colleagues, especially at the Chemical Engineering & Advanced Materials School and at Malaysian Nuclear Agency, I really appreciate your help, support and concern for me.

Publications

Process Intensification in Tar and Moisture Removal from Syngas, International Workshop on Process Intensification 2008 (IWPI 2008), October 15-18, 2008, Tokyo Institute of Technology O-okayama Campus, Tokyo, Japan.

Preparation of nanostructured microporous composite foams, International Application Published under the Patent Cooperation Treaty, International Application Number: PCT/GB2009/002403. WO 2010/041014 (A2) published on 15 April 2010.

Preparation of nanostructured microporous composite foams, European Patent Application, EP 2342272 A2 published on 13 July 2011.

Preparation of nanostructured microporous composite foams, United States Patent Application, US 2012/0064243 A1 published on 15 March 2012.

Table of Contents

List of Tables

List of Figures

Nomenclature

H_2	Hydrogen
CO	Carbon Monoxide
CO_2	Carbon Dioxide
CH_4	Methane
H_2O	Water
N_2	Nitrogen
H_2S	Hydrogen Sulphide
HCl	Hydrochloric acid
NH_3	Ammonia
HCN	Hydrocyanic acid / Hydrogen cyanide
$CaMg(CO_3)_2$	Calcium Magnesium Ore
MgO	Magnesium oxide
CaO	Calcium oxide
SiC	Silicon carbide
MPa	Mega Pascal
$CaCO_3$	Calcium Carbonate
OH	Hydroxide
Al_2O_3	Aluminium oxide / Alumina
Ni	Nickel
ZrO_2	Zirconium dioxide / zirconia
SiO_2	Silicon Dioxide
Ca	Calsium
Mg	Magnesium

Abbreviation

PHP	PolyHIPE polymer
HLB	Hydrophile-Lipophile Balance
SEM	Scanning Electron Microscopy
GC	Gas Chromatography
FTIR	Fourier Transfer Infra Red
DVB	Divinyl benzene
BTEX	Benzene, toluene, ethyl benzene & xylene
DC	Direct Current
AC	Alternating current
VOC	Volatile organic compound
HIPE	High internal phase emulsion
SPAN 80	Sorbiton monooleate
PEGDMA	Polyethylene glycol dimethacrylate
VTMS	Vinyl trimethoxy silane
O\W	Oil-in-water
T	Toluene
CB	chlorobenzene
CEB	2-chloroethylbenzene
BET	Brunauer-Emmet-Teller
CEN	ComiteEuropeen de Normalisation
T_4EG	Tetraethylene glycol
EG	Ethylene Glycol
DEG	Diehtylene glycol
TEG	Triehtylene glycol
EG	Ethylene Glycol
DC/AC	Direct current / alternative current
AIBN	Azobisisobutyronitrile

1 Introduction

1.1 *PolyHIPE polymer (PHP)*

PolyHIPE polymer is a highly porous material that can be easily prepared by polymerisation of the monomeric continuous phase of a high internal phase emulsion (HIPE). These polymeric foams were coined the generic name PolyHIPE by researchers at Unilever Research Port Sunlight Laboratory, UK (Barby and Haq, 1982).

The process of preparing polyHIPE polymer is quite simple. Droplets of aqueous phase are added to the mixture of oil phase, consisting of monomer, crosslinker and surfactant while mixing. Mixing is needed to break up large droplets. Mixing is further continued after addition of the internal phase to get a smaller pore volume. The emulsion is then cured in the oven; the resulting porous material was then washed in the soxhlet, and dried.

In this study, several novel PolyHIPE polymer preparation techniques whereby, functional 'filler' (chemical/material which can be particulate) was incorporated into the aqueous phase and oil phase were tried. Subsequently, the chemical/material can be activated after polymerisation in order to functionalize the resulting PolyHIPE polymer. In the case of 'fillers' added in the oil phase, the concentration of such 'fillers' in the oil phase is restricted due to the low volume of the oil phase.

One of the effects of having 'fillers' in the continuous or dispersed phase of the emulsion is the formation of nano-pores within the pore walls of the larger micron sized pores. These nano pores are useful in many applications.

1.2 *Tar in biomass gasification*

In the pursuit to meet more stringent environmental policy and legislation, coupled with the worry of fossil fuels depletion, biomass gasification technology has gained increasing interest in the field of power generation due to its high efficiency and environmentally friendly technology. Social, political and economic benefits are

positive factors that favour the biomass thermochemical conversion in the production of fuels, chemicals and combined heat and power. Some advantages of this biorefinery concept are revitalising rural economies by generating several products and revenues, improving national security by reducing dependence on foreign oil imports, and improving the environment globally towards achieving sustainable development by reducing fossil fuel emissions, greenhouse gases, oxides of nitrogen and sulphur. Gasification technologies open up venues in converting renewable biomass feedstock into clean fuel gases or synthesis gases. Gasification has an advantage over direct combustion since its gaseous fuels burn more cleanly with higher efficiency than solid fuels and are applicable in advanced power cycle at smaller scale, such as engine or turbine power plant.

Biomass gasification product gas, rich in H_2 and CO can be applied in methanol or Fisher-Tropsch liquid synthesis upon conditioning and upgrading. Further additional conditioning can produce high purity hydrogen product gas that is applicable in transportation, chemical production, or electricity generation in fuel cells. This leads to a more challenging need in gas clean-up for each specific application, including tar removal.

The product gas produced from biomass gasification contains major elements of CO, H_2, CO_2, CH_4, H_2O and N_2. In addition to these elements, it also contains organic impurities, tar and inorganic impurities, H_2S, HCl, NH_3 and alkali metals, and particulates. The organic impurities exist in the range of low molecular weight hydrocarbons to high molecular weight polynuclear aromatic hydrocarbons. Even though lower molecular weight hydrocarbons can be utilised as fuel in gas turbine and engine applications, they are unwanted species in fuel cell applications and methanol synthesis. The higher molecular weight hydrocarbons are collectively known as ‘tar’ (Dayton, 2002). Thus, depending on the end use application of gaseous product, gas clean-up plays a very important role in biomass gasification. A crucial technical and economic obstacle to commercialisation of biomass gasification is the removal, destruction or conversion of tars.

Tars are undesirable component in integrated biomass gasification systems due to several reasons. Tars can lead to blockages of pipes and clogging of filters since tars condense in exit piping and on particulate filters. Tars also interfere in downstream processes, for example, in internal combustion engine; there are possibilities for tar to clog fuel lines and injectors. In pressurised combined-cycle

systems which involve burning of product gases in a gas turbine, luminous combustion and erosion from soot formation are bound to occur. Since the product gas from an atmospheric pressure gasification process need to be compressed before burning it in a gas turbine, tars can condense in the compressor and in the transfer lines as the product cools down in the process. For fuel cell applications, the tars have an impact since different purities of product gas are tolerable by different kinds of fuel cells. Molten carbonate and solid oxide fuel cells with integrated internal reforming do not have a problem as polymer electrolyte membrane fuel cell that tolerates only pure hydrogen. For catalytic synthesis of methanol and other liquid fuels, tars are undesirable since substantial conditioning of product gas is required in achieving the gas composition of H_2: CO ratio of 2:1.

In addition to the factors discussed in the previous paragraph, tar formation results in reduction of gasification efficiency as less biomass is converted to synthesis gas. Tars would degrade the performance of the systems using the product gas since tar can deactivate the reforming catalyst and some fuel cells tolerances of tars are low. For the operation at temperatures above 400 ºC, subsequent dehydration reactions of tars are possible resulting in formation of char and coke that further plugs the systems.

1.3 *Objectives*

In the efforts to meet the demand in producing sustainable energy, the research was undertaken as part of the Process Intensification and Miniaturisation (PIM) group activities in the Intensified Integrated Bio-refinery project to generate power. The objective of the research is to find an effective method of tar removal or conversion in gas cleaning technologies which cover the following:

1. To develop catalyst\monolith of PolyHIPE polymer based with improved morphology and properties.
2. To study tar adsorption capability of PolyHIPE polymers produced in the lab on the simulated syngas.
3. To find the optimum method of several techniques tried in removing or converting tar in simulated syngas. The techniques are high voltage, non-thermal plasma, PolyHIPE polymers, and combination of both non-thermal plasma and PolyHIPE polymers.

1.4 *Thesis Structure*

Chapter 1 introduces the structure of the thesis and the objectives of the studies. Introduction of the subjects studied are also discussed.

Chapter 2 covers the literature review on the subjects involved in the study which are PolyHIPE polymer and the techniques of tar removal or conversion in gas cleaning technologies.

Chapter 3 discusses the methodology used in performing the laboratory works, analysing the samples produced in the research and analysing the effectiveness of gas cleaning technologies.

Chapter 4 gives results of polyHIPE polymer (PHP) produced and discusses several properties of polyHIPE polymers produced which are basic, alumina, bindzil (silica), vinyl trimethoxy silane (VTMS) and bindzil-VTMS PHPs. The discussion covers the morphology, surface area, pore size distribution and compounds or functional groups identification.

Chapter 5 covers the results and discussion on tar removal experiments which include PHPs as the adsorbent materials, high voltage technique, non-thermal plasma technique, and combination of PHPs and non-thermal plasma technique.

Chapter 6 concludes the finding of the studies.

Chapter 7 proposes future work needed based on the findings.

2 Literature Review.

2.1 *Overview of High Internal Phase Emulsions (HIPE) and PolyHIPE Polymer (PHP)*

As defined by Lissant (1974), high internal-phase ratio emulsions are those with more than 74% internal phase volume, Φ. The Φ value of 74% represents the maximum volume that can be occupied by uniform non-deformable spheres when packed in the most efficient manner. These days, also known as high internal phase emulsion (HIPE), the value of Φ can be as high as 99%. At this high value of Φ, closely packed monodispersed spheres is no longer physically possible in internal or dispersed phase. Thus, at this high internal phase volume, the shape is deformed into non-spherical polyhedral droplets which appeared to be monodispersed in size, as quoted by Cameron and Sherrington (1996) on the work done by Lissant. The droplets have relatively large contact area, are surrounded by continuous phase and stabilized by thin surfactant films. The continuous phase, which generally constitutes less than 26% of the final volume of HIPE, normally contains monomer, cross-linking agent, surfactant and oil-phase initiator. Due to HIPE unique characteristics, HIPE have been used for many years in many applications such as food preparation, cosmetics, oil recovery and many others. One of the most important applications of HIPE is the ability to be used as template systems for the synthesis of a range of polymeric materials.

The HIPE processing can be divided into two stages as discussed by Akay et al. (2005). During the first stage of the processing, the dispersed (aqueous) phase is continuously dosed into a mixing vessel containing the continuous phase (oil phase). Care is taken in minimizing the jet mixing of the two phases since addition of aqueous phase alone creates mixing. There is a reduction in the droplet size of the aqueous phase due to the rotation of the impeller during dosing. In the second stage of processing, further mixing is carried out upon completion of dosing in order to reduce aqueous phase droplet size (i.e. size of pores after polymerization) and to obtain HIPE

of narrow droplet size distribution. No additional mixing (homogenization) stage is needed for the case of a very low dosing rate.

The relative dosing rate having a dimension of deformation rate is used to characterize the aqueous phase dosing rate

$$R_D = \frac{V_A}{t_D V_O} \qquad \text{Eq 2.1}$$

where V_A = volume of aqueous phase added over a period of time, t_D, and

V_O = volume of the oil phase placed in the batch mixer.

The total mixing time t is defined as

$$t = t_D + t_H \qquad \text{Eq 2.2}$$

where t_H = homogenization time.

The mixing rate is defined as

$$R_M = \frac{D_I}{D_O}\Omega \qquad \text{Eq 2.3}$$

where D_O = diameter of the batch mixer

D_I = diameter of the impellers:and

Ω = rotational speed of the impellers.

In the case of very large relative dosing rate and small mixing rate, instead of HIPE formation, dilute (low) internal oil-in-water (O\W) emulsion is formed. When HIPE is stable, polymerization without phase separation will take place.

The monomer-based HIPE can be polymerised to obtain micro-porous polyHIPE polymers (PHP). Barby and Haq (1982) discovered that open-cell HIPE-based polymer can be polymerised by using relatively simple low HLB (Hydrophile-Lipophile Balance) surfactant and HIPEs composing of styrene-divinylbenzene (DVB) as shown schematically in Figure 2.1.

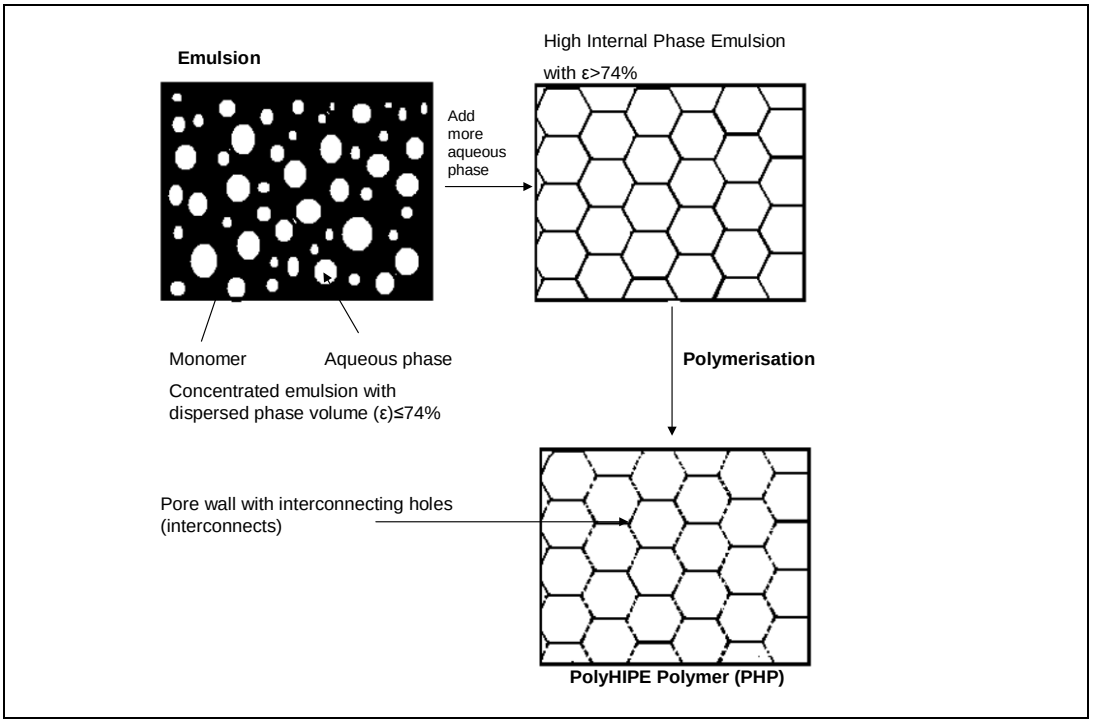

Figure 2.1: Schematic representation of PHP formation (Byron, 2000).

The internal (aqueous) phase used in preparing the HIPE can be easily and rapidly removed from the PHP to produce a highly porous material with very low density. Another important characteristic of PHP is that it can be specifically tailor-made according to its application. For example, PHP can be produced with specific interconnect size, d, e.g. as d of $0<d/D<0.5$, D is pore size. Moreover, a highly porous interconnected monolithic material of PHP with a well-defined and uniform microstructure of very low dry density can also be produced. The structure of PHP is shown in Figure 2.2 (adapted from (Akay et al., 2005b)). The materials can be produced over a wide range of pore size, D, ($0.5\ \mu m<D<5000\ \mu m$), based on the conditions of the starting emulsions. PHP having pore size greater than 200 μm can be produced through a coalescence polymerisation technique (Akay et al., 2005a; Akay et al., 2002). Furthermore, the porosity of PHP surface can be controlled by varying the surface chemistry of materials against which the HIPEs are polymerised. This allows the production of asymmetric materials.

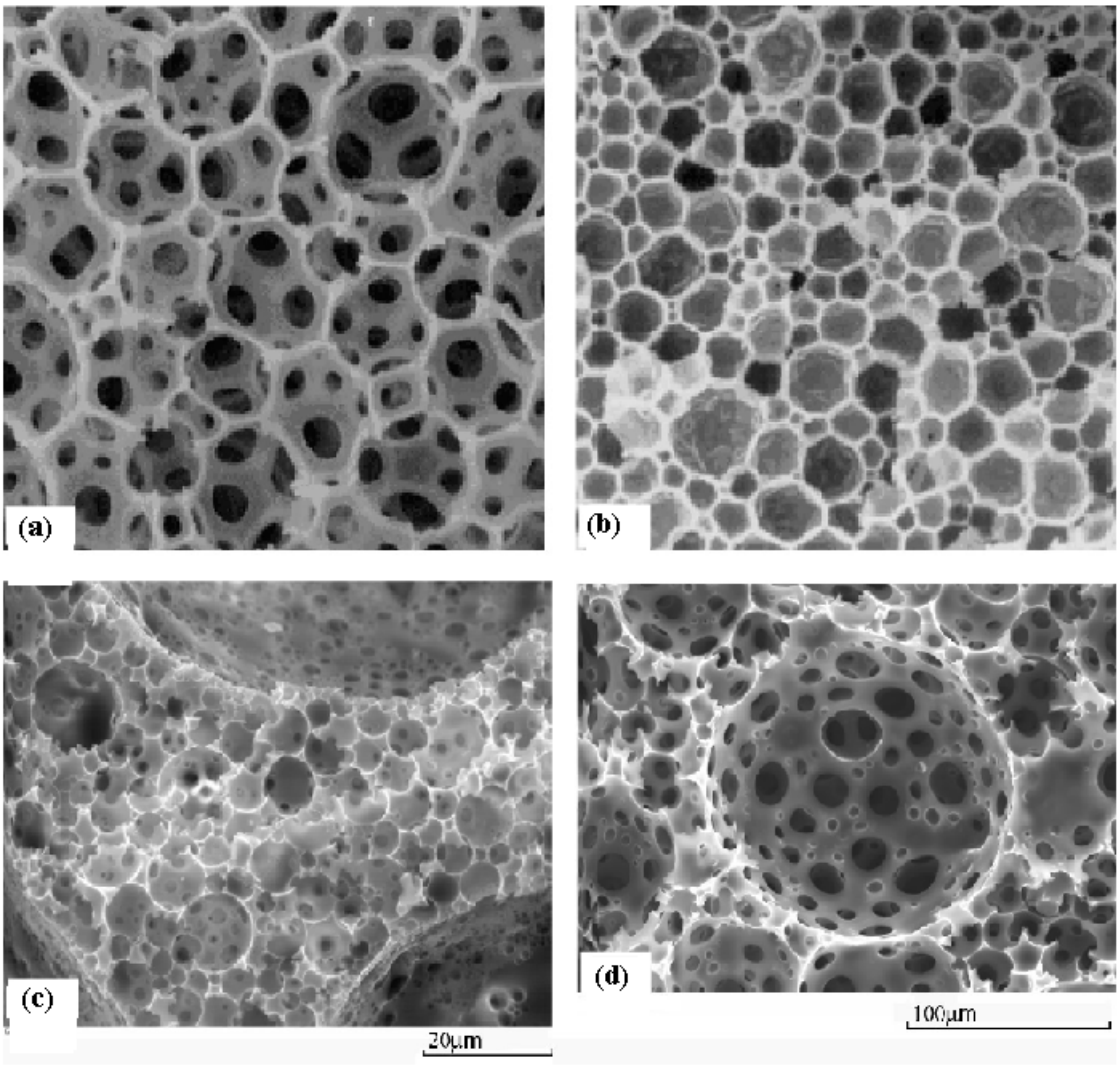

Figure 2.2: Basic PolyHIPE Polymer Structures. (a) Primary pores with large interconnecting holes, (b) Primary pores with nano-sized interconnecting holes, (c) Large coalescence pores (3 such pores are partially shown) dispersed into the primary pores in the process of coalescence; (d) Detail of the coalescence pores. (Adapted from (Akay et al., 2005b)

Due to PHPs unique structures and properties, PHPs have made ways in diverse fields of intensified processes, especially in biology, where their applications include the discovery of a number of of size-dependent phenomena in bioprocesses (Akay, 2006a; Akay et al., 2004; Akay et al., 2002), tissue engineering (Akay, 2005; Akay et al., 2004; Bokhari, 2003; Bokhari et al., 2003; Umez-Eronini, 2003; Byron, 2000) and other intensified bioprocesses (Akay, 2006b; Akay, 2005).

Both hydrophilic and hydrophobic PHPs have been utilised in several other applications such as intensification demulsification processes (Akay et al., 2005d; Noor et al., 2005; Vickers, 2001), gas liquid separation (Akay et al., 2005b; Calkan et al., 2005; Dogru and Akay, 2004), and metal ion removal in water treatment (Katsoyiannis, 2002; Wakeman et al., 1998). PHPs have also been applied in other intensified processes , for instance, foams and filtration fabrications (Tai et al., 2001; Walsh, 1996; Bhumgara, 1995a; Bhumgara, 1995b), metal plating (Akay et al., 2005b; Calkan et al., 2005; Brown et al., 1999; Sotiropoulos et al., 1998), and organic chemistry processes (Moine et al., 2003).

As listed by (Noor, 2006) and discussed by (Akay et al., 2005b), for PHP to be utilized in the applications mentioned above, the preparation and modification of PHP materials has to meet the following criteria:

i) able to produce PHP with a required internal architecture or morphology, for instance, specific pore/interconnect sizes and the presence of arterial channels;
ii) able to form monolithic structures;
iii) able to chemically/biologically functionalise or optimise the PHP for a specific application;
iv) and ensure the sustainable production and modification of PHP.

2.1.1 PolyHIPE Polymer Morphology

PHPs are being widely utilised in various applications based on each specific required property of the materials, for instance, morphology, physical, mechanical, or thermal properties. Therefore, control over PHP properties is essential to ensure viability of application. Having several advantages of accessibility of the pores, controllability of internal architecture, such as the pore and interconnect structures, versatility of fabrication and chemical modification of the walls, PHP is a high potential material. Another advantage of PHP is that it can also be fabricated from a very thin membrane to a very large well-organised monolithic article.

The typical structure of PHP is an open cellular structure of spherical cavities. These cavities are known as voids or pores having windows for interconnecting the

pores. This phenomenon is possible due to the trapped internal (aqueous) phase inside the continuous phase during the polymerisation process. Generally, the stability level of the prepared HIPE has a direct relation to the pore size of PHP. In a system with high emulsion stability, a smaller droplet size will be produced due to the lower interfacial tension which allows larger interfacial area. In a less stable emulsion system, emulsion droplets tend to coalesce and lead to a larger cell once the polymer is formed. There are several factors that govern the stability of HIPEs. Similar to other emulsions, HIPE stability is highly dependent on the preparation parameters, which are shear stress (mixing speed) and mixing time. In order to produce a more stable emulsion, high mixing speed is needed to uniformly break the emulsions into small droplets. Similar effect was also observed by (Walsh, 1996) when a mixing time was increased. The study showed that there was a reduction in the size of water cavity and an increase in the number of windows leading to production of more micro-size open structure material with the increase of mixing time.

There are some other less apparent parameters that can have influence on PHP pore size. Williams et al.(1990) discovered that the ratio of styrene/DVB (divinyl benzene) used in preparation of HIPE play an important role in the formation of PHP. It was observed that the emulsion with DVB alone can easily and more uniformly get blended compared to the emulsion with styrene alone. Thus, increasing the ratio of styrene/DVB in a HIPE led to the increase in emulsion stability, leading to the decrease in pore size diameter from 15 to 5μm. In addition, it was also observed that even a small increase in the amount of surfactant used would result in reducing the pore size even though 50 % and more of surfactant concentration (w/w relative to the monomer content) led to crumbled or weak PHP. Furthermore, the influence of electrolyte concentration in the aqueous phase was also studied. The study showed that in the test with 5% DVB in the oil phase and azobisisobutyronitrile (AIBN) as an initiator, a 10-fold reduction in cell size was observed when the salt concentration in the aqueous phase was increased from 0 to 10g/100ml.

A study by Akay et al. (2005b) has shown that the temperature also plays a role in the pore size of PHP. The study showed that the pore size can be controlled by elevating the emulsification temperature. This information is useful whenever a large pore size is needed. Findings from the research are as shown Figure 2.3 and Figure 2.4.

A closed–cellular cell structure can also be produced. The factors that determine the cellular condition of the material was first studied by Williams and Wrobleski (1988). The result showed that the surfactant is more important in determining the cellular structure of PHP although internal phase volume has some effects. It was discovered that low concentration of surfactant, (i.e. <5% in term of w/w) relative to the monomer phase resulted in closed-structure materials whereas high concentration (i.e. >7%) of the same surfactant resulted in opened-cellular materials. This phenomenon occurred due to the decrease in the thickness of monomer film separating the adjacent droplets when the surfactant concentration was increased. During polymerisation process, windows between adjacent droplets appeared at a specific critical film thickness. On the other hand, when the monomer was less dense than the polymer (with low concentration of surfactant), these windows shrank to produce a closed-cellular structure.

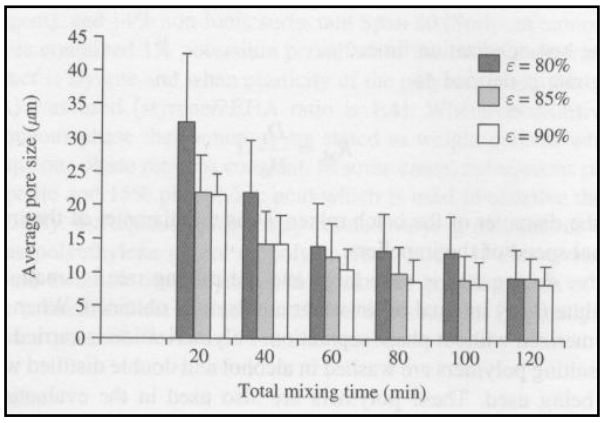

Figure 2.3: Variation of average pore size (D) with total mixing time (t) as a function of dispersed phase volume fraction (ε). Dosing time = 10 min, impeller speed Ω = 300 rpm, emulsification temperature T = 25 ºC. Pore size is evaluated from scanning electron micrographs of the polymers (Akay et al., 2005b).

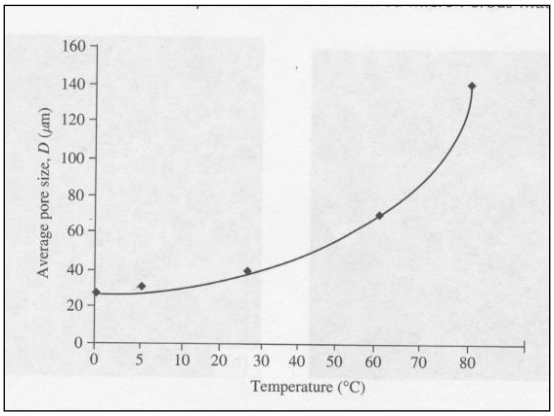

Figure 2.4: Variation of average pore size with emulsification temperature when dosing time = 40 s, total mixing time = 100 s, impeller speed = 300rpm, phase volume = 90 % (Akay et al., 2005b).

2.1.2 PolyHIPE Polymer Properties

PHP has highly permeable pores and interconnected walls; however, the surface area is still low, with a typical range of 3-10 m^2/g. This is explainable due to the relatively large pore size of 10s of microns. This low surface is a drawback for application of PHP in chromatographic support (Krajnc et al., 2005) which requires high surface area of hundreds m^2/g . This leads to further study by Hainey et al. (1991) to significantly enhance the surface area of PHP. They discovered that the surface area can dramatically be increased by substituting one of the monomers with organic porogenic (porogen – pore-forming component) solvent and by adding big amount of cross linker (DVB) in the continuous phase. This results in producing PHP with large surface area of 350 m^2/g. However, despite having a high surface area, the mechanical properties of the materials were seriously affected. The monolith structure easily collapsed when the material was subjected to low to moderate stress and to a flow through liquid.

Barbetta and Cameron (2004a; 2004b) then carried out a further study in finding a better porogenic solvent without sacrificing the mechanical properties of the material. They discovered that by substituting the solvent from toluene (T) to chlorobenzene (CB) and to 2-chloroethylbenzene (CEB), BET (Brunauer-Emmet-Teller) surface area was increased from 350 to 550 m^2/g. For PHP with CEB, not only

is the surface area increased significantly, the morphology also changed resulting in the formation of larger size of windows. Unfortunately, the mechanical properties of the produced PHP were not improved.

Cameron (2005) carried out a study using a 1:1 volume ratio of CEB:CB. The material produced retained the original morphology of original PHP with the same value of surface area, 550 m^2/g. However, this type of PHP is not as robust as the PHP produced using styrene/DVB. Recently there have been studies done by Haibach et al.(2006) and Menner et al (2006) on synthesis low-density polymer foams with superior mechanical properties. The continuous phase of the emulsions was increased up to 40%. Haibach et al. discovered that the Young's modulus of silica reinforced foams increased by 280% and the crush strength by 218% when compared to non-reinforced foams. However, the surface area was not significantly improved. Menner et al. used polyethylene glycol dimethacrylate (PEGDMA) as a main crosslinker. The produced foams did not exhibit any brittleness or chalkiness. They discovered that Young's Modulus and crush strength of silica reinforced foams increased by up to 360% and by up to 300%, respectively, when compared to non-reinforced foams. There was no report on surface area of the materials.

2.2 *Biomass Gasification and Tar Decomposition Chemistry Overview.*

Biomass gasification involves a complex thermochemical process involving several elementary chemical reactions. The process begins with the partial oxidation of a lignocellulosic fuel with a gasifying agent, air, oxygen or steam. The released volatile matter (biomass fuel) is then heated and partially oxidised producing combustion products of H_2O and CO_2; heat produced is used in the endothermic gasification process. Further heating causes vaporisation of water and results in continuing process of biomass pyrolysis. At higher temperature, thermal decomposition and partial oxidation of the pyrolysis vapours take place, producing a composition of product gas of CO, CO_2, H_2O, H_2, CH_4, other gaseous hydrocarbons,

tars, char, inorganic components, and ash. A general reaction representing biomass gasification is as follows (Dayton, 2002):

$$\begin{aligned} biomass + O_2 (or\ H_2O) &\rightarrow CO, CO_2, H_2O, H_2, CH_4 + other\ hydrocarbons \\ &\rightarrow tar + char + ash \\ &\rightarrow HCN + NH_3 + HCl + H_2S + other\ sulfur\ gases \end{aligned} \quad \text{Eq 2.4}$$

The actual amount of CO, CO_2, H_2O, H_2, tars, and hydrocarbons depends on the partial oxidation of the volatile products, as shown in equation 2.5, quoted by Dayton (2002):

$$C_nH_m + (n/2 + m/4)O_2 \rightarrow nCO + (m/2)H_2O \quad \text{Eq 2.5}$$

Reactions of tar decomposition are as shown below (Devi et al., 2005):

$$Cracking \qquad pC_nH_x \rightarrow qC_mH_y + rH_2 \quad \text{Eq 2.6}$$

$$Steam\ reforming \quad C_nH_x + nH_2O \rightarrow (n + x/2)H_2 + nCO \quad \text{Eq 2.7}$$

$$Dry\ reforming \quad C_nH_x + nCO_2 \rightarrow (x/2)H_2 + 2nCO \quad \text{Eq 2.8}$$

$$Carbon\ formation \quad C_nH_x \rightarrow nC + x/2H_2 \quad \text{Eq 2.9}$$

C_nH_x represents tar while C_mH_y represents hydrocarbon with smaller carbon number than C_nH_x. As discussed by Dayton (2002), catalytic steam reforming is an attractive hot gas conditioning method due to several advantages:

- catalyst reactor temperatures can be thermally integrated with the gasifier exit temperature;
- the composition of the product gas can be catalytically adjusted;
- and steam can be added to the catalyst reactor to ensure complete reforming of tars.

2.3 *Tar Removal Technology.*

The definition of tar is still an issue. An excellent report on operational definition of tars was given by Milne et al. (1998). The difference in the operational definitions of tars results from the variable product gas compositions produced depending on a particular end-use application and the method in which tars are collected and analysed. Even though the methods are not widely established yet, Simell et. al. (2000) and Neeft et. al. (1999b) have developed tar sampling protocols in the effort to standardise the methods tars are collected. The protocols for standardised methods in tar collection and measurement for both small- and large-scale gasification systems have been developed and published by Maniatis and Beenakers (2000), Abatzouglou et. al. (2000), Knoeff and Koele (2000), Simel et. al (2000) and Knoef (2000). Thus, the expectation is the consistency and comparability of data produced by different sites could be realised and produced much-needed data for the gasification research community. Recently, there was a standard written by CEN (ComiteEuropeen de Normalisation) Task Force for sampling and analysis of tar which is available online (Good et al., 2005; CEN Task Force, 2004; Neeft).

As discussed by Devi et al. (2005), tars are divided into 5 classes:

- Class 1-GC undetectable tars, they are heavy tars, cannot be detected by GC.
- Class 2-Heterocyclic compounds, tars containing heteroatoms, highly water soluble compounds.
- Class 3-Aromatic compounds, light hydrocarbons with single ring, do not pose a problem regarding condensability and solubility.
- Class 4-Light polyaromatic compounds, two and three ring compounds, condense at low temperature even at very low concentration.
- Class 5-Heavy polyaromatic compounds, larger than three rings, these components condense at high temperatures at low concentration.

Devi et al. (2005) reported that naphthalene (class 4 tar) is the most stable tar and the most difficult tar to be decomposed, according to Coll et al (2001) and Jess (1996).

Tar removal is critical in systems where:

- product gas is cooled prior to use resulting in condensation in pipes and other parts of the system; operational problems will occur.

- product gas must be compressed prior to use in some mechanical systems such as piston engine; tars condense in the compressor and transfer lines as gas cools down.

Apart from tackling the technology of tar removal, a better approach is to minimize tar production in the raw product gas exiting from the gasifier especially for application in the systems where tolerance to tars is low. This can be partly realised by selecting a gasifier with optimum design that produces the lowest tar concentration; the summary of tar level for different types of gasifier designs is as shown in the following Table 2.1:

Table 2.1: Comparison of measured particulate and tar levels from different biomass gasifier designs. (Graham, 1993) and (Neeft et al., 1999a).

Gasifier Type	Particulate Loading (g/Nm^3)			Tar Loading (g/Nm^3)		
	Low	High	Representative Range	Min	Max	Representative Range
Fixed Bed						
Downdraft	0.01	10	0.1 – 0.2	0.04	6.0	0.1 – 1.2
Updraft	0.1	3	0.1 – 1.0	1	150	20 - 100
Moving Bed						
Fluidized Bed	1	100	2 - 20	<0.1	23	1 - 15
Circulating fluidized Bed	8	100	10 - 35	<1	30	1 - 15

Note: The representative range is presented as a qualitative comparison of emissions from different gasifier types. Measurements are from selected facilities and may not be representative of all gasifiers in a particular class. Actual emissions from any specific gasifier depend on many factors and must be measured under steady-state operating conditions.

The first crucial step is selecting suitable gasifier performance to match with the requirement of end use application. In dealing with tar accumulation problems, each part in the systems should be designed to address the tar issue since tar production is unavoidable in any gasifier.

2.3.1 Technologies in tar removal.

Normally, tars in the product gas are present as vaporised form, aerosols of condensed tars, or combinations of both. Several approaches have been reported in the literature in the development of the most economical and optimised method of tar removal. The important factor to be considered is the method used should not affect the formation or the quality of the gaseous product. Generally, tar removal technologies can be divided into two approaches:

- Primary methods – treatments are done inside the gasifier itself.
- Secondary methods – physical tar removal, and hot gas cleaning and conditioning after the gasifier.

The concepts of the two approaches are as shown in Figure 2.5 and Figure 2.6 (Devi et al., 2003).

Primary methods consider the measures need to be taken in order prevent tar formation and tar conversion in the gasifier itself. Considerations should be given on the proper selection of the operating conditions, the use of proper bed additives or catalysts in the gasifier itself, and a proper gasifier design. A comprehensive literature review on this method is discussed by Devi et al. (2003). Figure 2.5 represents the ideal primary method concept which eliminates the need for secondary treatments.

Technologies involved in secondary methods of tar removal from the product gas are physical tar removal, and catalytic and thermal destruction. These two approaches are discussed in this review.

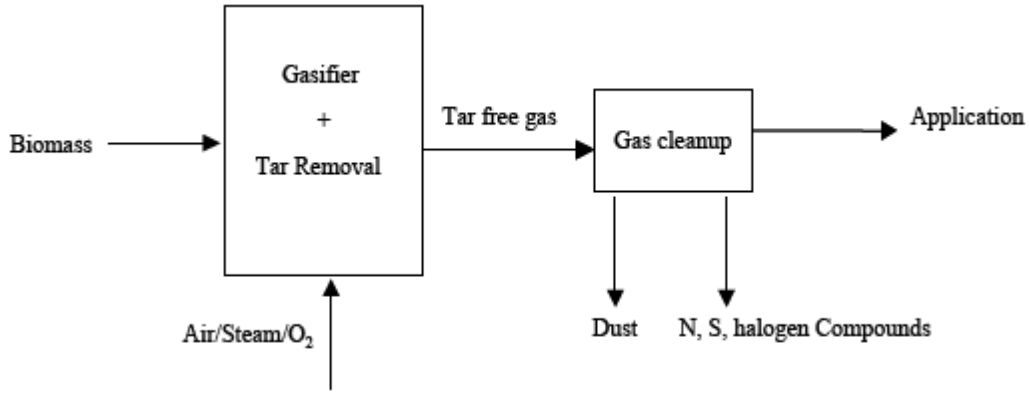

Figure 2.5: Tar reduction concept by primary method (Devi et al., 2003).

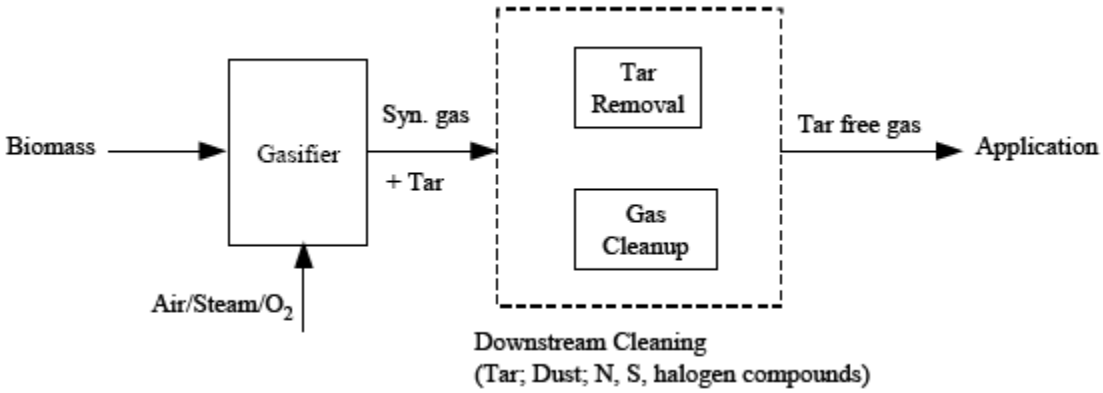

Figure 2.6: Tar reduction concept by secondary method (Devi et al., 2003).

Since the primary methods are not yet fully understood and are yet to be applied commercially as quoted by Devi et al. (2003), this paper will discuss more on the secondary methods. Nevertheless, some points regarding the appropriate application of the primary methods are also made when discussing the catalysts.

2.3.2 Physical Tar Removal

Physical tar removal is possible when requirement of product gas end use is a low temperature (of near to ambient temperature). It is an effective gas conditioning

process; the technology is available and can be optimised. In this technique, tars are removed by cooling the product gas and allowing the tar to condense into aerosol droplets; the droplets are then removed using the similar method used in particulate removal. The technique normally utilises wet scrubbers, electrostatic precipitators, barrier filters or cyclone filters as discussed by Stevens (2001). Even though particulates and tars can be removed simultaneously, tars are removed separately in order to avoid the condensation of sticky tars on particulate surfaces that can lead to further plugging and fouling of gas conditioning equipment.

2.3.2.1 Wet Scrubbers

The tars are collected through the impingement of the material on water droplets. The tar and liquid flow to a demister or decanter, in which bulk tars are separated from the aqueous phase. Since the scrubbers use water, the gas temperature at the exit must be in the range of 35 – 60 ºC.

There are various designs of scrubbers that have been used such as spray towers, impingement scrubbers, baffle scrubbers, and venturi scrubbers. Table 2.2 shows the variation of relationship between complexity and efficiency of the scrubbers.

Table 2.2: Relative efficiencies of tar removal for wet scrubbers (adapted from Baker et al. (1986)).

	Pressure drop, cm water	Particle size (μm) for 80% collection
Spray Tower	1.5 – 4.0	10
Impingement	5 - 125	1 - 5
Packed Bed	5 - 125	1 -10
Venturi	10 - 250	0.2 – 0.8

Applications of wet scrubbers on various gasification systems are widely used but there are no unanimous results of the actual performance. The summary of performance of various types of scrubbers used in biomass gasification is presented in Table 2.3.

Table 2.3: Reported tar removal efficiencies of wet scrubbers in biomass gasification systems (adapted from Neeft et al. (1999a)).

Technology	Tar removal efficiency
Spray tower	11-25% heavy Tars
	40-60% PAH
	0-60% phenolics
Spray tower	29% heavy Tars
Venturi Scrubber	50-90% not given
Venturi and Spray Scrubber	83-99% condensable material
Venturi + cyclonic demister	93-99% condensable organics
Vortex scrubber	66-78% evaporation residues

2.3.2.2 Wet Electrostatic Precipitators

The principle applied in this technique is the same principle used in particulate removal. Tar droplets are ionised and the ionised droplets migrated to a charged collecting point. Instead of using the place collectors as used in particulate removal, wire and tube designs are employed to collect the tars. Tars are removed by continuously washing the collector surfaces. This technique is available at operating temperature of up to 150 ºC but lower temperature is favoured in order to avoid tar vaporisation.

2.3.2.3 Barrier filter

Various types of this technology have been applied for tar removal in biomass gasification system. The principle applied is trapping tars through the impingement of condensed aerosols on the filter surface. However, the presence of tars in liquid form makes them more difficult to be removed from the filter surface. The problem is worse in the presence of particulates. Stevens (2001) quoted that packed bed filters with packing materials made of sawdust, wood chips, cork and sand tested on small-scale biomass gasification systems provided sufficient tar filtration, but operational problems of filter cleaning and waste disposal were encountered.

2.3.2.4 Cyclone Filters

Operating on centrifugal force principle, the solids and aerosols are separated from the gases. Separators used are cyclones, u-tubes or vortex. This technique is suitable only for removing particles with diameters of 5 μm and above.

2.3.3 Catalytic and Thermal Tar Destruction

This method of removal is applicable if the product gas end use requires high temperature or temperature slightly below the exit temperature of the gasifier. This hot gas conditioning does not physically remove tars but rather converts them into desired product components. The advantage is their chemical energy content is retained in the product gas.

In this technique, tars are thermally decomposed resulting in the formation of additional product gas and occasional chars. Tars can be destroyed by thermal energy alone at temperatures of above 1200 ºC or with the incorporation of catalyst at moderate temperatures of 750-900 ºC.

2.3.3.1 Catalytic Tar Destruction

The study on this technique has been on going for more than twenty years. There are several works published by Mudge et al., (1981), Ekstrom et al., (1982), Bridgwater, (1994), Beenakers, (1994), Aznar et al, (1997), Abatzoglou, et al., (1997), Milne et al.,(1998), Neeft, (1999a), Corella et al., (1999a) and Caballero et al., (1999). The function of the catalysts in the process is assisting the cracking and destruction of tars; hence it is operational at moderate temperature. The catalysts have been applied either in the gasifier itself (primary method) or in downstream equipment of the gasifier (secondary method). Applications of similar catalysts that have been used in catalytic steam reforming of hydrocarbons are used for biomass gasifier tar reforming.

Dayton (2002) divided the catalysts into three groups, which are alkali metals, non-metallic oxides, and supported metallic oxides. Alkali metals are used as the primary catalysts; direct mixing of alkali salts into the biomass feed is done as the feed is supplied into the gasifier. Several fundamental studies on cellulose and

biomass pyrolyis has shown that char formation reaction is enhanced in the presence of alkali metal during the thermochemical conversion, reported by Richards and Zheng (1991), Antal and Várgheyi (1995) and Raveendran et al. (1996; 1995). Commercially, alkali metals are unfavourable due to the difficulty in alkali metals recovery, poorer carbon conversion and increase in ash content. The non-metallic and supported metallic oxide catalysts are usually used as secondary catalysts. The catalysts are applied at the downstream of the gasifier in a separate fixed bed. An example of non-metallic catalysts that have been studied extensively for conversion of tar in biomass gasification are dolomites-calcium magnesium carbonates (calcined dolomites). Metallic oxide catalysts that have been a subject of interest in tar reforming are Ni-based catalysts. These two types of catalysts will be discussed further in the next section.

2.3.3.1.1 Non-metallic Oxides

Naturally occurring catalysts, dolomites, have been extensively studied for tar destruction in biomass gasification. Dolomite is a calcium magnesium ore with the general chemical formula $CaMg(CO_3)_2$ that contains ~20% MgO, ~30% CaO, 45%CO_2 on a weight basis, with other minor mineral impurities (Dayton, 2002). The dolomites need to be calcinated at high temperature of 800 – 900 ºC to make high catalyst activity.

Simell and co-workers tested on the effectiveness of dolomites and other carbonate rocks in reforming using model compounds of tar surrogates. The activities of Finnish and Swedish dolomites, dolomitic limestone, and SiC for toluene decomposition at 900-1000 ºC and 2MPa were investigated by Simell, Leppalahti, and Kurkela (1995). Toluene conversion efficiencies of more than 97% was achieved by using calcined dolomites (calcination at 900 ºC), but calcined dolomites nearly lost their catalytic activities when the CO_2 partial pressure was higher than the equilibrium decomposition pressure of $CaCO_3$. A mechanistic model describing the catalytic decomposition of benzene using Finnish dolomite at similar condition was reported by Simell et al. (1997b). Application of dolomites, limestones and iron ores at operating temperature of 900 ºC (to condition a slipstream) on product gas stream from a peat-fired air-blown gasifier was studied earlier by Simell and Bredenberg (1990) and Simell, Leppalahti, and Bredenberg (1992). Efficiency of tar destruction achieved was

in the range of 86% to 99%. As the Ca:Mg ratio increased, the catalytic activity of the dolomites also increased, the addition of iron further enhanced the catalytic activity.

There was a reported work on the pilot plant gasification studies using calcined dolomite by Corella and co-workers. Olivares et al. (1997) studied the use of 20g calcined dolomite per kilogram of biomass in the gasifier bed of the pilot plant. The results was a 4-6 fold decrease in tar content, the double increase of hydrogen content and a twofold reduction of CO content of the product gas. There were also work done by Delgado et al (1997; 1996) on calcined dolomite, magnesite and calcite in a downstream reactor operated at 800-880 ºC. Initial tar conversion was 99% and decreased as the catalysts became deactivated during the process. Comprehensive results on Malaga dolomite tested were reported by Perez et al (1997).

There were several other works by other groups, Taralas et al. (1996; 1991) studied tar reforming of cyclohexane and n-heptane using the catalysts calcined dolomite, quicklime, and dolomitic magnesium oxide. Calcined dolomite was applied by Vassilatos et al. (1992) in catalytic conditioning of biomass pyrolysis vapors at 700-900 ºC.

A summary from the numerous published literatures regarding calcined dolomite studies on catalyst composition, calcining and operating temperatures, feedstock and gasifier conditions, and reported conversion efficiencies is discussed elsewhere (Dayton, 2002).

Alternative to calcined dolomite, application of non-metallic oxides has been using olivine, a magnesium aluminosilicate. Rapagna et al. (2000) found that tar reforming activity of olivine is comparable to calcined dolomite. Devi et al. (2005) discovered that pretreatment of olivine by heating at 900 °C in the presence of air improves the catalytic activity of olivine. Steam reforming reaction of naphthalene as model biomass tar compound was used to study the catalytic activity of olivine. The result achieved is the increase in conversion with the increase in pretreatment time; 80% conversion of naphthalene was observed with formation of 50 % gaseous products from both steam and dry reforming at 10 hours of olivine pretreatment time.

2.3.3.1.2 Commercial Nickel Reforming Catalyst

There is wide variety of nickel-based steam reforming catalysts available commercially as there are wide variations of its applications in petrochemical industry, for example, the production of syngas from naphtha and methane reforming.

Garcia et al.(2000) simplified the process of catalytic tar reforming as follows. Methane or other hydrocarbons are first dissociatively adsorbed onto a metal site where metal –catalysed dehydrogenation takes place. The ceramic support provides provision for water to dissociatively adsorb onto it, resulting in hydroxylating the surface. It is then followed by migration OH radicals to the metal sites at the appropriate temperature. This leads to the oxidation of the intermediate hydrocarbon fragments and surface carbon to $CO + H_2$.

Dayton (2002) reviewed lengthily the work done on nickel-based reforming catalyst for tar conversion in product gas. The literature of numerous studies on the use of commercial Ni-based catalysts for tar reforming is described too. The differences in catalyst formulations are due to the loading of Ni used, the composition of the support material and the trace amounts of various promoters that are incorporated into the matrix.

Baker et al. (1987) did a test on nickel catalysts as primary bed catalysts; the problems encountered are speedy lost of conversion activity due to coke formation and catalyst attrition. As a result, nickel-based catalysts are typically applied in secondary fixed bed reactors. There are systems where calcined dolomite are used as catalyst in a guard bed in conjunction with nickel catalyst in secondary fixed bed reactor in order to minimise the level of tars from the gasifier and prolong the lifetime of Nickel catalysts.

There are a number of papers published by Corella and co-workers (1999b; 1998; 1996), Narvaez et al. (1997) and Caballero et al. (2000) on commercial steam reforming catalysts for tar conversion in biomass gasification system. In the studies, calcined dolomite guard bed was used and the Nickel catalysts temperature was maintained between 750 – 850 °C; the observed tar initial conversion efficiencies were more than 99%. In many cases, the catalysts became deactivated after a few hours time-on-stream. However, there were cases where some catalysts performed for more than 100 hours without showing any sign of deactivation.

There are also several works done by Simell et al. (1997) by using the toluene as a model tar compound to investigate the effectiveness of Ni/Al_2O_3 catalysts at elevated pressures. Application of catalysts with various Ni content, operated at 900 °C and 0.5-20 MPa in various gas atmospheres was studied. Hepola and Simell (1997a; 1997b) also reported the effects of sulphur poisoning on catalysts activities and ammonia decomposition. The ammonia conversion activity was more susceptible to sulphur poisoning than tar conversion activity.

There was reported work of Simell and co-workers (Simell and Kurkela, 1997a; Simell et al., 1997; Simell et al., 1996a; Simell et al., 1996b) on the use of commercially available (BASF AG) Ni monolith catalyst on tar conversion in biomass gasification system. The tests were done in a pressurised gasification system using various feed stocks such as wood waste, bark wood chips, and peat. For catalyst operation at temperature of 900 °C and pressure of 5 MPa, a complete conversion of tar and 80% ammonia conversion were achieved. Ni monolith catalysts can last for more than 500 hours of operation.

Kinoshita, Wang et al. (1995) reported the use of commercial nickel catalyst (UC G-90B) in parametric studies on catalytic reforming of tars produced from bench-scale gasification system at various temperatures of 650-800 °C. An optimum conversion of 97% was achieved. There was also a reported work by Gebhard et al. (1994) on reforming of synthetic tar mixture by commercial Ni reforming catalyst.

There are also studies done on various model compounds, benzene, toluene, naphthalene, anthracene and pyrene using commercial nickel catalysts by a number of researchers as reported by Dayton (2002). The slowest steam reforming rate was naphthalene and the most reactive was benzene as reported by Coll et al (2001). Coke formation was also increased with the increase of the molecular weight of the model compound.

2.3.3.1.3 Other Catalysts

In addition to commercial nickel catalysts, there were attempts to utilise the olivine activity and the success of Ni steam reforming catalysts by developing olivine supported nickel catalyst. There was a work done by Courson et al. (2000); 2.8 wt % Ni impregnated in natural olivine was prepared by calcination of catalyst in air at 900

°C, 1100 °C, and 1400 °C. The catalyst calcined at 1100 °C had the highest activity in methane conversion.

Juutilainen et al. (2006) studied the selective oxidation of tar and ammonia in biomass gasification using catalyst containing zirconia and alumina. Toluene as tar model compound was investigated. Zirconia and alumina-doped zirconia demonstrated high conversion of toluene and ammonia even at temperature below 600 °C in the presence of oxygen; they are the most active catalysts for toluene oxidation below 700 °C and the most active catalysts for ammonia oxidation below 650 °C. At higher temperature, the impregnated ZrO_2/Al_2O_3 has a better performance. It was reported that the oxidation activity was enhanced by zirconia while oxidation selectivity was enhanced by alumina. Alumina-doped zirconia exhibited a good resistant to H_2S poisoning.

2.3.3.2 Thermal Tar Destruction

Tar destruction can also be done thermally without the presence of any catalyst. However, operation at higher temperature of 1200 ºC and above is required. For efficient destruction, the minimum required temperature is not clearly described but it is dependent on type of tars formed. For example, oxygenated tars from updraft gasifier are treated at 900 ºC while the refractory tars from high temperature reactors need to be treated at temperatures of 1200 ºC and above. Thermal cracking for large-scale gasifier is less attractive due to the difficulties in achieving complete thermal cracking, operational problems and high cost.

The technique has also been tested on tar destruction in pyrolysis or gasification of organic wastes. The application in systems designed for waste reduction is more economical compared to the one that uses clean biomass since energy by-products are produced along with the elimination of waste. Neeft et al. (1999a) reviewed several processes applied in disposal of organic waste systems.

In tar thermal decomposition using electric arc plasmas, plasmas are created by heating gases in the discharge arc between two electrodes. Due to electric discharge and the temperature increase in the arc, parts of the gases are ionized and followed by reactions. A review on tests of several plasma arc reactors was discussed by Neeft et al. (1999a). It is not likely feasible for applications in big-scale biomass gasification systems due to high cost of electricity and a large gas volumes to be treated.

Further discussion on plasma technology is done in Section 2.4.

2.4 *Plasma Technology.*

Plasmas are found everywhere in the universe – 99% of the matter in the observable cosmos is in the plasma state (Graham, 2001). Plasma can be defined as the fourth state of matter after solid, liquid and gas as introduced by Langmuir in 1928.

2.4.1 What is Plasma?

As quoted by Whitehead (2007), plasma is a partially or completely ionised gas containing electrons, ions, excited and ground state atoms and/ or molecules, reactive free radicals and photons. Plasmas can be categorized based on the operating pressure; low pressure or atmospheric pressure. Plasmas can also be described by their degree of equilibrium. High pressure or thermal plasmas have all species (electrons, ions, atoms and molecules) at a thermal equilibrium; they can be described by a single temperature. Atmospheric pressure or non-thermal plasmas are those with high temperature electrons compared to the temperature of ions, atoms and molecules. A high degree of nonsequilibrium exists in non-thermal plasmas; the electrons have a very high energy (temperature of tens of thousands of degrees Kelvin), the ions are less energetic, and the residual gas atoms and molecules are close to room temperature. Lately, most of the studies have been centred on the application of non-thermal, atmospheric pressure plasmas.

Plasmas can be created by applying an electrical field created by a high voltage alternating current, a direct current discharge (continuous or pulsed), and a microwave or radiofrequency field to a gas. In the field, electrons are stripped from some or all of the gas atoms or molecules; the electrons then gain energy. These energetic electrons then collide with the atoms and molecules in the gas, producing more ions and excited states. Electrons can also cause the molecules to split apart producing reactive fragments or free radicals. However, not all the molecules are dissociated.

Even though the study on gas discharges began as early as 1808 by Sir Humpry Davy, Sir William Crookes was the first one to produce and recognise plasmas in 1839. He heated a solid to very high temperatures, melted it, vaporised it to a gas and then broke the gas into electrons and ions.

Plasmas have two main characteristics, temperatures and energy densities which are very important for practical applications. The temperatures and energy densities produced by plasma are greater than those produced by ordinary chemical mechanisms. In other words, plasma performances are not possible by any other methods. In fact, plasmas can provide an efficient increase in processing methods and in comparison to more conventional processes may often reduce impact on the environment (Fridman, 2004). The focus of this research is the application of non-thermal plasma discharges and particularly the dielectric-barrier discharge or (DBD).

2.4.2 Plasma in Pollution Abatement

Low-temperature, nonequilibrium plasmas are among the emerging technologies used in treating low volatile organic compound (VOC) emissions and other industrial exhausts. Amongst the wide range of emission products effectively treated using the plasma processes are aliphatic hydrocarbons, chlorofluorocarbons, methyl cyanide, phosgene, formaldehyde, sulphur and organophosphorus compounds, and sulphur and nitrogen oxides.

In a non-thermal plasma , molecules will be dissociated by high energy electrons of 6 ~ 10 eV (Van Veldhuizen, 2000), resulting in the creation of a favourable reactive environment, regardless of the gas temperature. Therefore, conversion of tars is possible for a system with low temperature gas. This is another added advantage when compared to catalytic cracking which is possible at 800 °C and thermal cracking at a temperature of >1000 °C. Even though non-thermal plasma produces a host of species and reactive radicals, it does not have selectivity towards the desired process. Consequently, in many cases, the radicals are not efficiently utilized, leading to high energy consumption as discussed previously. In order to overcome this problem, the studies on a combination of plasma and catalyst have been actively pursued to find an alternative in reducing the energy consumption (Pemen et al., 2007; Nozaki et al., 2004b; Nozaki et al., 2004a; Wang et al., 2004).

Nair et al. (2005; 2004; 2003) discussed in details the corona plasma system for tar removal in biomass gasification. The studies were done using pulsed corona plasma system and, streamer corona generation by an alternative DC/AC power source. Results demonstrated that the chemical efficiencies of both pulsed corona system and DC/AC system were about the same.

Pemen et al. (2007) studied the application and synergistic effect of both plasma and catalyst on removal of tars from gas produced by biomass gasification. Tar removal process was enhanced by a combination of streamer corona plasma and a monolith, made of cordierite, having 400 cpsi (cells per square inch). A cordierite monolith was chosen as a catalyst due to its low pressure drop and its easiness to be incorporated into a non-thermal plasma reactor. The result demonstrated the decrease in energy requirement at the temperature of 300 °C. Thus, the system has a potential for lowering the operating temperature of the process, and for enhancing tar removal processes.

Pacheco et al. (2008) studied the removal of nitric oxides and sulphur dioxide from a mixture of air and water vapour. Results from the developed chemical model demonstrated a very good agreement with experimental data collected, which was 95% removal efficiency.

3 Methodology.

3.1 *Preparation of polyHIPE*

Polyhipe polymer (PHP) is a highly porous polymeric material made through a high internal phase emulsion (HIPE) polymerisation route. The materials used in preparation of polyHIPE were styrene, divinyl benzene as the monomer, sorbitan monooleate (SPAN 80) or sorbitan trioleate (SPAN 85) as the surfactant, and lauroyl peroxide or potassium persulfate as the initiator. For silica PHP and alumina PHP, Bindzil CC30 and Bindzil CC40 (colloidal silica under the trade name of Bindzil), and aluminium chloride hexahydrate were used in the aqueous phase, respectively. For silane (VTMS) PHP, vinyl trimethoxy silane (VTMS) was used in the oil phase. All the materials used were reagent grade chemicals without any further purification. The ratio of the reactants used was varied according to the desired characteristics of the polyHIPE.

PolyHIPE polymers were prepared using the HIPE polymerisation route as described in the literature (Akay, 2005; Akay et al., 2005c; Akay, 2004; Akay et al., 2004; Akay and Vickers, 2003; Akay et al., 2002; Akay, 1995; Akay et al., 1995). The techniques used in this study ensure the preparation of microporous polymers with well controlled internal architecture, pore and interconnect sizes and their distributions (Akay, 2005). The schematic diagram of the experimental set up used in preparing the polymers is given in Figure 3.1. The pictures of the set-up, the impeller and the mixing vessel are presented in Figure 3.2.

In the case of silica or bindzil PHP, the high internal phase emulsion (HIPE) was prepared by first mixing the oil phase comprised of 12 wt % surfactant (Span 80), 67 wt % monomer (styrene), 20 wt % cross-linking agent (divinyl benzene), and 1 wt % oil phase initiator (lauroyl peroxide). The produced continuous phase of HIPE would then eventually undergo polymerization and cross-linking. 50 ml of this reactive mixture is placed in the mixing vessel having internal diameter of 12 cm. 200 cm^3 of the aqueous phase, comprised of bindzil solution was then dosed into the continuous phase while mixing them simultaneously. The B10 (10 wt. %) and B20 (20 wt. %) solutions of the aqueous phase were diluted using the bindzil CC40 solution (in the

first phase) and double distilled water. The B10 aqueous phase solution was produced by diluting Bindzil CC 30 (in the second phase) in double distilled water. As specified by the supplier (EKA Chemiclas), Bindzil CC (Clear Coat) products are transparent liquid, aqueous colloidal solution and produced by formulations of water-based organo modified colloidal silica. Bindzil CC30 is a colloidal solution with 30% SO_2 by weight and having average particle size of 7 nm whereas Bindzil CC40 is a colloidal solution with 40% SO_2 by weight and having average particle size of 12 nm.

Preparation of alumina PHP was also performed during the same apparatus and technique as discussed in the previous paragraph and the same composition of HIPE was used. The alumina PHP was prepared using 80% internal (aqueous) phase and 20% continuous (oil) phase. The aqueous phase was prepared using 300 g of aluminium chloride hexahydrate and 700 ml of double distilled water.

The silane or VTMS PHP was also prepared using the same composition, which is 80% internal (aqueous) phase and 20% continuous (oil) phase. The VTMS percentage was varied from 5% up to 40% of the oil phase composition. Both aqueous and oil phase initiators were used to prepare the silane PHP at 5 % VTMS. The rest of VTMS PHPs with different percentages of VTMS were prepared using aqueous phase initiator. Both aqueous phase initiator and oil phase initiator were used to produce S10m, VTMS PHP with both types of initiators.

VTMS-Bindzil PHP was prepared by incorporating VTMS in the oil phase and Bindzil/silica in the aqueous phase. The same composition of 80% aqueous phase and 20 % oil phase was used in the experiment. The percentage of VTMS and Bindzil was varied as presented and discussed in Chapter 4.

Basic PHP was prepared using the HIPE consists of 68 wt. % monomer styrene, 20 wt % cross-linking agent (DVB) and 12 wt. % surfactant (Span 80). The aqueous phase was prepared using 10 g of potassium persulphate in 1000 ml double distilled water (1 wt. % initiator). The HIPE composition, the oil phase percentage, the aqueous phase percentage, the dosing time and the mixing time were varied as presented and discussed in Chapter 4.

In summary, the oil phase and aqueous phase prepared and used in the experiments were listed in Table 3.1. The standard dosing time and mixing time used in this study are 10 minutes and 50 minutes, respectively. In some cases, the dosing and mixing times were varied.

Table 3.1: Composition of oil phase and aqueous phase of PHPs.

Type of polymer	Oil phase	Aqueous phase
Basic PHP	Styrene, 68 wt. %	Distilled water
	Divinyl benzene, 20 wt. %	Potassium persulphate, 1 wt. %
	Sorbitan monooleate (SPAN 80), 12 wt. %	
Silica/Bindzil PHP	Styrene, 67 wt. %	Distilled water
	Divinyl benzene, 20 wt %	Bindzil CC30 or Bindzil CC40
	Sorbitan monooleate (SPAN 80), 12 wt. %	
	Lauroyl peroxide, 1 wt. %	
Silane/VTMS PHP	Styrene, 68 – X wt.%	Distilled water
	Divinyl benzene, 20 wt. %	Potassium persulphate, 1 wt. %
	Sorbitan monooleate (SPAN 80), 12 wt. %	
	Vinyl trimethoxy silane, X wt. %	
VTMS-Bindzil PHP	Styrene, 68 – X wt. %	Distilled water
	Divinyl benzene, 20 wt. %	Potassium persulphate, 1 wt %
	Sorbitan monooleate (SPAN 80), 12 wt. %	
	Vinyl trimethoxy silane, X wt. %	Bindzil CC30
Alumina	Styrene, 67 wt. %	Distilled water
	Divinyl benzene, 20 wt. %	Aluminium chloride hexahydrate
	Sorbitan monooleate (SPAN 80), 12 wt. %	
	Lauroyl peroxide, 1wt. %	

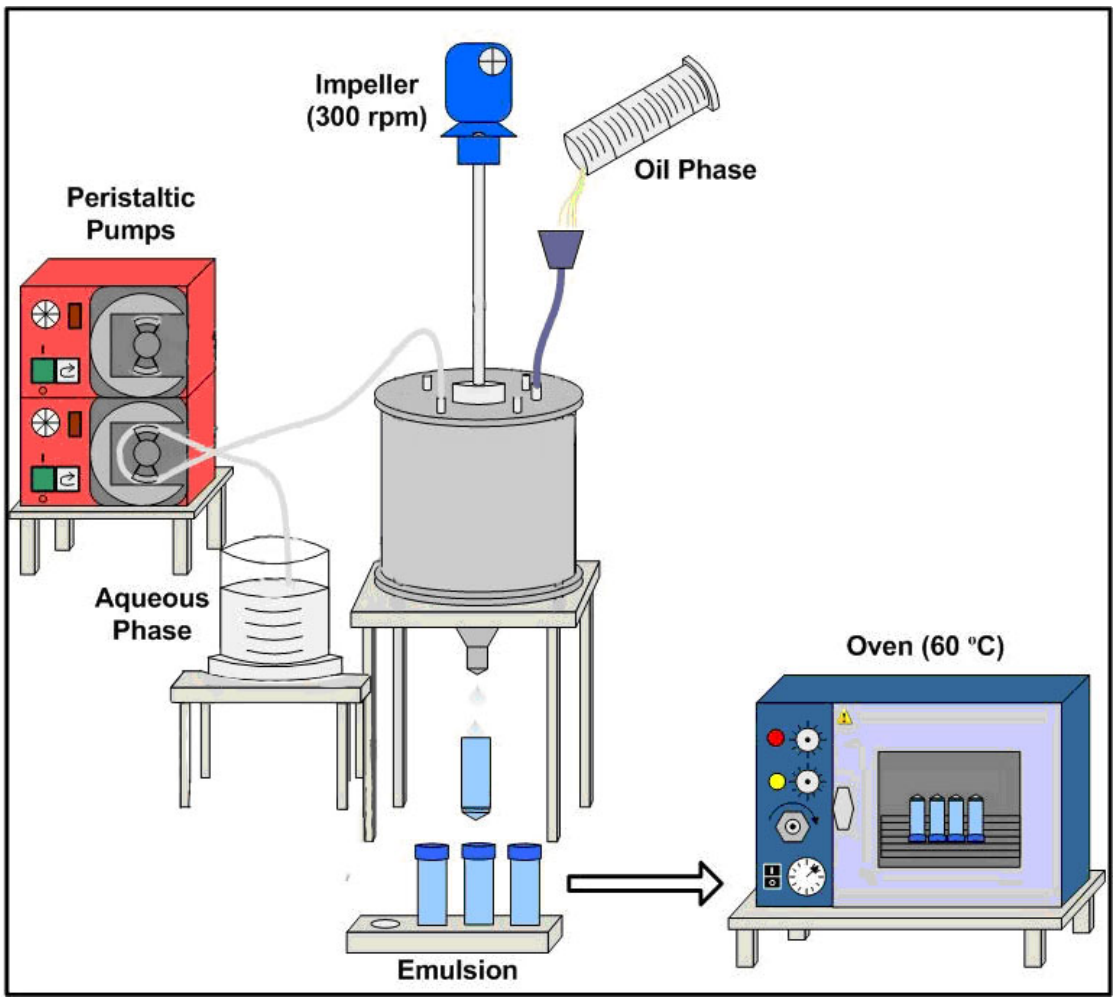

Figure 3.1: Schematic diagram of the apparatus used in preparing the emulsion.

Mixing was carried out by using two sets of impellers with each set having two flat paddles of 9 cm diameter. The two sets are stacked at right-angle to each other and the impeller bottom is placed at the closest possible distance to the bottom of the mixing vessel. The impeller was operated at constant rotational speed of 300 rpm. The pore and interconnect sizes of the micro-porous polymer are controlled through the temperature of the emulsification, mixing speed and total mixing time. Details of these parameters in obtaining specific pore size and structure are available in the literature (Akay, 2005; Akay et al., 2002).

(a) Set-up

(b) impeller

Figure 3.2: Pictures of apparatus used in PolyHIPE making.

The impeller was simultaneously started as the aqueous phase was dosed into the vessel. Upon completion of dosing all the aqueous phase into the vessel, the mixture may be further stirred for some period of times. The produced emulsion was then transferred into 50 mL polypropylene containers having internal diameter of 2.6 cm. The polypropylene containers filled with emulsion were then placed in a pre-heated, 60 °C oven where polymerization took place for about 8 hours. After polymerization, the solidified PHP blocks were removed out of the polypropylene containers and cut into 0.4 cm discs. The discs were then dried by leaving them on the paper towel overnight in a fume cupboard, and can be stored for subsequent modifications and applications.

3.1.1 Washing of PolyHIPE polymers

All the PolyHIPE discs, except the first phase of silica PHP, were washed in a soxhlet set up as shown in Figure 3.3 to remove the surfactants. The washing was first

done using iso-propanol for 3 hours, and then followed by 3 hours washing in double distilled water to get rid of any remaining residues in the pores and interconnects.

The silica PolyHIPE discs (first phase) were washed four times in a beaker of distilled water at 80 °C, stirred by magnetic stirrer. Each wash was done for 30 minutes.

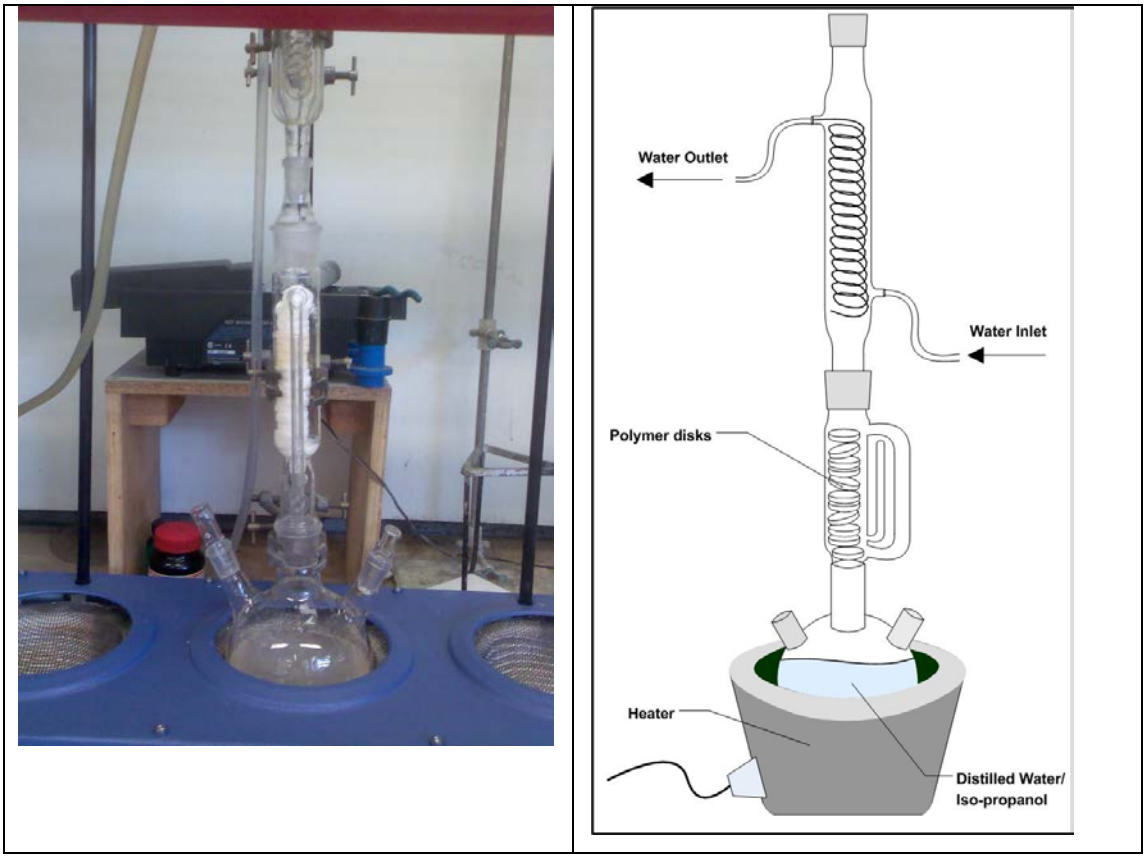

Figure 3.3: Picture and schematic diagram of the soxhlet used for polymer washing.

3.1.2 Sulphonation of PHP.

Sulphonation was tried using two methods, which are thermal (conventional) and microwave irradiation methods. Prior to thermal treatment or microwave irradiation, the PHP discs were soaked in concentrated sulphuric acid. Details of the soaking time and concentration of the acid used are presented in section 4.9. Microwave irradiation of PHP was done for a total time of 40 seconds; comprising 4

times of 10 second irradiation period while flipping over the PHP disc after every 10 seconds. In thermal method, PHP was heat treated in a conventional oven at 95 °C. The method is graphically shown in Figure 3.4.

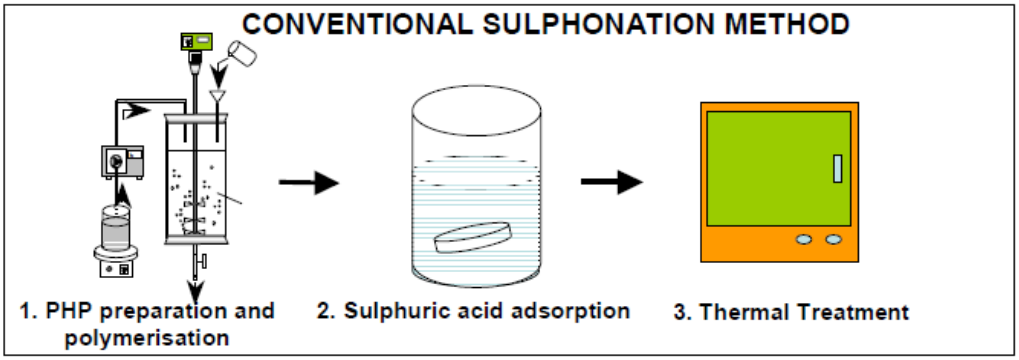

Figure 3.4: The Conventional PolyHIPE Sulphonation method. Adapted from (Burke et al., 2006).

3.2 *Analytical methods*

The analytical methods used in the study are Scanning Electron Microscopy (SEM), surface area and pore size analysis, Fourier Transform Infrared spectroscopy (FTIR) and gas chromatography (GC).

3.2.1 Scanning Electron Microscopy (SEM)

The Scanning Electron Microscope (SEM) provides information relating to topographical features, morphology, phase distribution, compositional differences, crystal structure, crystal orientation, and the presence and location of electrical defects. The SEM is a microscope that uses electrons rather than light to form an image. There are many advantages to using the SEM instead of a light microscope. The SEM has a large depth of field, which allows a large amount of the sample to be in focus at one time. The SEM also produces images of high resolution, which means that closely spaced features can be examined at a high magnification. Preparation of the samples is relatively easy since most SEMs only require the sample to be

conductive. The combination of higher magnification, larger depth of focus, greater resolution, and ease of sample observation makes the SEM one of the most heavily used instruments in research areas today.

The SEM equipment used in this work was an environmental SEM model Hitachi S2400 Scanning Electron Microscope fitted with an Oxford Instrument Isis 200 Ultra-Thin Window X-ray detector. The picture of the machine is presented in Figure 3.5. Since the SEM operation uses vacuum conditions and electrons to form an image, special preparation of the sample is compulsory. All water, solvents or other materials that may vaporise while in a vacuum must be removed prior to analysing the sample. Therefore, the sample was dried in a vacuum oven at 60°C for 4 hours before cutting and mounting it on a stub.

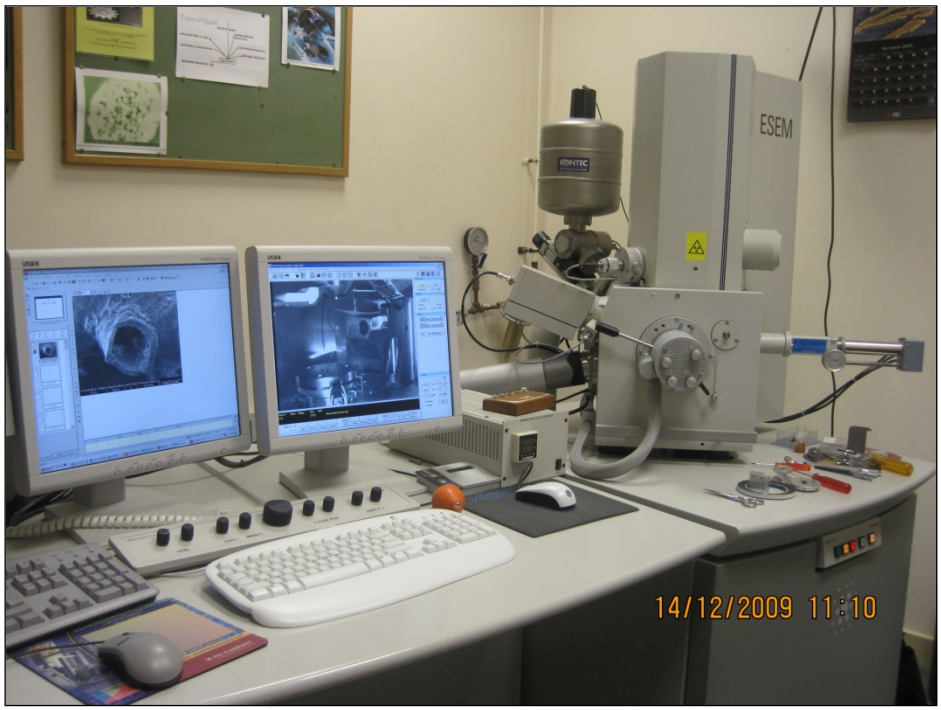

Figure 3.5: Picture of Scanning Electron Microscope (SEM).

For the sample to withstand the vacuum inside the column, care must be taken in preparing the sample. In order to protect the inner structure of the sample, sample was carefully broken/ cut into a small piece prior to mounting it to the sample holder, an aluminium stub. The sample was glued onto an aluminium stub with carbon cement or copper tape. Carbon cement was only used for the samples that are not adhesive enough on the copper tape. For the samples glued with carbon cement; they were left

overnight for the carbon to dry off, so that it can withstand the vacuum. The extra caution in mounting procedure is very important to ensure a good quality result. Since the samples were analysed in an environmental SEM, non-conductive samples could be examined without being coated with conductive material. However, for achieving better clarity, samples were coated with a very thin layer of gold using a gold sputter coater. Figure 3.6 shows how the sample was mounted on the aluminium stub.

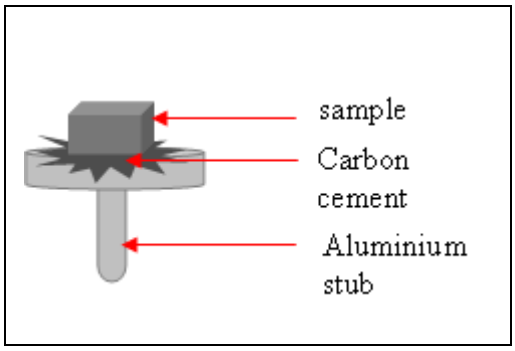

Figure 3.6: Sample glued on aluminium stub by carbon cement/copper tape.

3.2.2 Surface Area and Pore Size Analysis

In this study, the instrument used to measure the surface area and pore size distribution of PHPs is Coulter SA 3100 analyser, manufactured by the Beckman-Coulter company. The picture of the machine is shown in Figure 3.7. This instrument uses Gas Sorption technique to obtain total surface area and pore size distributions of 0.4 to 200 nm diameter. Nitrogen was used as the adsorbates. The technique can be described as the physical characterisation of material structures whereby gas molecules of known size are condensed (adsorbed) on surfaces of the sample at a constant temperature. The quantity of the gas adsorbed and the resultant sample pressure are recorded and used in constructing isotherm. The data from the isotherm are then used in subsequent calculation models. In this study, BET (Brunauer, Emmet and Teller) calculation model is used for specific surface area and BJH (Barret, Joyner and Halenda) calculation model is used for pore size distribution.

During the adsorption process, when the adsorbate molecules are attached to the surface of the materials, the molecules are then retained by physisorption or chemisorption process. The machine assumes that all adsorption detected is due to physically adsorbed gas. Hence, all calculation models are based on physisorption process and not on chemisorption process.

Figure 3.7: Surface area analyser, SA3100

3.2.2.1 Adsorption and desorption isotherm

The SA 3100 measures both, adsorption and desorption isotherm branches. The surface area is determined based on the adsorption branch whereas the pore size distribution is determined based on either adsorption or desorption branch and on both branches. The adsorption isotherm is a set of incremental data based on quantity of adsorbate gas condensed on the surface of the materials at a given pressure and at a constant temperature. The gas volume is measured at STP (Standard Temperature and Pressure) conditions and reported in cc/g. Desorption branch represents the reverse adsorption process and reported as a set of decremental data. Adsorptive pressures vary with temperature; hence, isotherm data is unique at a given analysis temperature.

The isotherm is represented as volume adsorbed (cc/g) against the relative pressure. The relative pressure is calculated as the sample pressure divided by the saturation vapour pressure. The sample pressure is the residual pressure in the sample chamber that formed from the leftover molecules that are not adsorbed during the gas adsorption on to the material surface. In other words, not all adsorbate gas molecules get adsorbed. The range of measurable values of relative pressure with SA3100 is 0 to 0.995. The boiling pressure of the liquid gas may be taken as the saturation vapour pressure. However, due to the contamination of the liquid nitrogen by the condensation of atmospheric gases, it is important that the saturation vapour pressure is measured throughout the duration of sample analysis.

The adsorption process is measured volumetrically using the static fully equilibrated method. Adapting this method, discreet data points are taken and each point is equilibrated to pre-defined limits. High resolution results are obtainable using a large number of data points. Volume of the sample tube unoccupied by the sample is measured by using Helium gas and is termed freespace. The pressure of each data point is measured and subsequently used to calculate the volume of adsorbate gas retained by the sample. The volume of each dose of gas is constant and has been pre-calibrated at the factory. The isotherm data for adsorbed gas (y-axis) is determined by subtracting the freespace of the sample tube from the total volume of gas dosed to the sample. The isotherm data for relative pressure (x-axis) is obtained by dividing sample pressure by saturation vapour pressure.

3.2.2.2 Freespace

The freespace and volume of dosed gas are determined using the ideal gas law. The moles of gas dosed into the manifold, n is calculated using Equation 3.1. P_M, V_M, and T_M are pressure, volume and temperature of the dose manifold respectively, and R is the gas constant.

$$P_M V_M = nRT_M \qquad \text{Equation 3.1}$$

The volume of freespace is determined from the resultant pressure drop. The dose of helium gas is described by the Equation 3.2.

$$\frac{P_{M1}V_M}{T_M} = \frac{P_{M2}V_M}{T_M} + \frac{P_{M2}V_S}{T_S} \qquad \text{Equation 3.2}$$

where V_S = volume of the sample,

T_S = temperature of the sample,

V_M = volume of the manifold,

T_M = temperature of the manifold,

P_{M1} = pressure of the manifold before the dose of the gas and

P_{M2} = pressure of the manifold after the dose of the gas.

Volume of dosed gas is calculated using the following equation

$$Vd_n = \frac{(P_{M1} - P_{M2}) * V_M}{T_M} * \frac{273.15}{760} + Vd_{n-1} \qquad \text{Equation 3.3}$$

where Vd_n = volume dosed

P_{M1} = initial manifold pressure

P_{M2} = final manifold pressure

V_M = manifold volume

T_M = manifold temperature

Vd_{n-1} = volume dosed from previous data point and

273.15/760 = standard temperature and pressure conversion.

Three helium data points are measured at incremental pressures. The freespace correction for helium is determined from the linear plot of volume dosed vs. sample pressure. The slope of the line represents volume of the sample tube per unit of sample tube pressure. The determined freespace is then used in the calculation of volume adsorbed in Equation 3.4. The equation represents the subtraction of freespace volume from the dosed volume of the adsorbate. The calculation is done at each measured data point.

$$Vads_n = Vd_n - (P_{Sn} * slope + intercept) \qquad \text{Equation 3.4}$$

where $Vads_n$ = volume adsorbed

Vd_n = volume dosed

P_{Sn} = sample pressure

slope = freespace measurement slope, and

intercept = freespace measurement intercept.

A complete analysis for adsorption and desorption isotherm are performed to get BET surface area and BJH adsorption and desorption pore size distribution.

3.2.2.3 Surface area analysis

The most commonly used method; BET (Brunauer, Emmet and Teller) equation is used to calculate the surface area of PHPs.

$$\frac{P_S}{V_A(P_O - P_S)} = \frac{1}{V_M C} + \left[\frac{C-1}{V_M C}\right] * \frac{P_S}{P_O} \qquad \text{Equation 3.5}$$

where

$V_M = volume\ of\ monolayer$

$V_A = volume\ adsorbed$

$C = constant\ related\ to\ the\ enthalpy\ of\ adsorption$

$P_S = sample\ pressure$

$P_O = saturation\ pressure$

$\left[\frac{C-1}{V_M C}\right] = slope$

$\frac{1}{V_M C} = intercept$

The plot of Equation 3.5 against relative pressure Ps/Po should produce a linear form, a straight line having a slope of $\left[\frac{C-1}{V_M C}\right]$ and an intercept of $\frac{1}{V_M C}$.

The BET surface area is given by Equation 3.6 and the unit is m^2/g.

$$S_{BET} = \frac{V_M * N_A * A_M}{M_V} \qquad \text{Equation 3.6}$$

where N_A = Avogadro's number

A_M = the cross sectional area occupied by each adsorbate molecule, and

M_V = the gram molecular volume, 22414 mL.

Since nitrogen is used as the adsorbate, the cross-sectional area is assumed as 0.162 nm^2.

The BET parameters chosen without the t-Plot calculation was 'ten' which corresponds to 10 data points for the normal setting of relative pressure range, i.e. 0.05 to 0.2.

The t-Plot method is used to estimate the micropore volume and micropore area. The machine gives the value of meso and macropore surface area, and the micropore volume. Combine with the BET surface area, the micropore surface area is then calculated. The film thickness, t is calculated using either the Hasley calculation or Harkins and Jura calculation. In this study, the Harkins and Jura calculation is used, as shown in Equation 3.7.

$$t = 3.54 * \left[\frac{5}{2.303 * \log \frac{P_O}{P_S}} \right]^{1/3} \qquad \text{Equation 3.7}$$

The values of calculated volume thicknesses are then plotted against the volume of gas adsorbed. The Y-intercept value is used to calculate the micropore volume. The meso/macropore area is then calculated using the slope of the linear section of the t-Plot. The following equations are used to calculate the micropore volume and the mesopore surface area.

$$VOLUME_{MICROPORE} = (0.001547) * (t - Plot\ intercept) \qquad \text{Equation 3.8}$$

$$SURFACE\ AREA_{MESOPORE} = 1547 * (t - Plot\ intercept) \qquad \text{Equation 3.9}$$

The micropore surface area may then be calculated from Equation 3.10 (SURF = Surface).

$$SURF.AREA_{MICROPORE} = SURF.AREA_{BET} - SURF.AREA_{MESOPORE} \qquad \text{Equation 3.10}$$

The resolution chosen for t-Plot data points was normal which corresponds to approximately 20 data points. The t-Plot ranged chosen was the highest thickness range available with the machine and software installed, i.e. 0.50 to 0.70nm. This range was chosen due to a wide range of pore size distribution from the BJH calculation. Low BET range setting of 0.005 to 0.05 was chosen for t-Plot calculation.

3.2.2.4 Pore size analysis

Analysis of pore size distribution can be done using either the adsorption or desorption isotherm branch. In the calculation, a cylindrical pore model with open end, and pore network absence are assumed. The calculation is based on the BJH (Barret, Joyner, and Halenda) method. The Kelvin equation, Equation 3.11 is used to calculate the core radius of the liquid in the capillary,

$$R \ln\left[\frac{P_S}{P_O}\right] = -2\gamma \frac{V_M}{R_K} \qquad \text{Equation 3.11}$$

where

$R_K = Kelvin\ Radius$

$\gamma = adsorbate\ surface\ tension\ at\ T, in\ mN/m$

$R = the\ gas\ constant$

$P_S = sample\ pressure$

$P_O = saturation\ pressure$

$T = boiling\ point\ of\ nitrogen$

$V_M = the\ molar\ volume\ of\ nitrogen$.

Rearranging the terms in Equation 3.11 and substituting the value of the constants yields the following equation for Kelvin radius.

$$R_\kappa(angstroms) = 4.14 * \log\frac{P_O}{P_S} \qquad \text{Equation 3.12}$$

The thickness of the nitrogen film adsorbed on the pore walls at each relative pressure is calculated using the Harkins and Jura equation, Equation 3.7. The film thickness, t is added to the Kelvin radius, R_κ in order to get the actual radius of the pore, R_P. The values of the constants used by the machine in the analysis of pore size distribution are listed below:

Surface tension of nitrogen	=	8.855 mN/m
Molar volume, V_M	=	34.6 cm^3 mole
Normal boiling point of N_2, T	=	77.3 K
Ideal gas constant, R	=	8.314 J/moleK

	=	$8.31*10^7$ erg/moleK
	=	conversion factor for gas
STP to liquid volume	=	0.00156.

In choosing BJH parameters, the resolution selected was medium, which corresponds to 45 data points. The plot range chosen was auto scaling and the equation chosen was Harkins-Jura as mentioned in the previous paragraph.

3.2.2.5 Isotherm analysis

According to International Union of Pure and Applied Chemistry (IUPAC) pore size classification is divided as follows (Sing et al., 1985)

(i.) Pores with widths exceeding about 50 nm (0.05 μm) are called macropores;

(ii.) Pores of width between 2 nm and 50 nm are called mesopores;

(iii.) Pores with widths not exceeding about 2 nm are called micropores.

There are huge numbers of adsorption isotherms of various solids recorded in the literature based on the van der Waals adsorption of gases. Brunaeur et al. (1940) grouped majority of them into five different types of isotherms. The isotherms, shown in Figure 3.8, were based on the adsorption experiments of

1. oxygen on charcoal at -183 °C for Type I (Langmuir adsorption),
2. nitrogen on iron catalysts at -195 °C for Type II (S-shaped/sigmoid),
3. bromine on silica gel at 79 °C for Type III,
4. benzene on ferric oxide gel at 50 °C for Type IV,
5. and water vapour on charcoal at 100 °C for Type V.

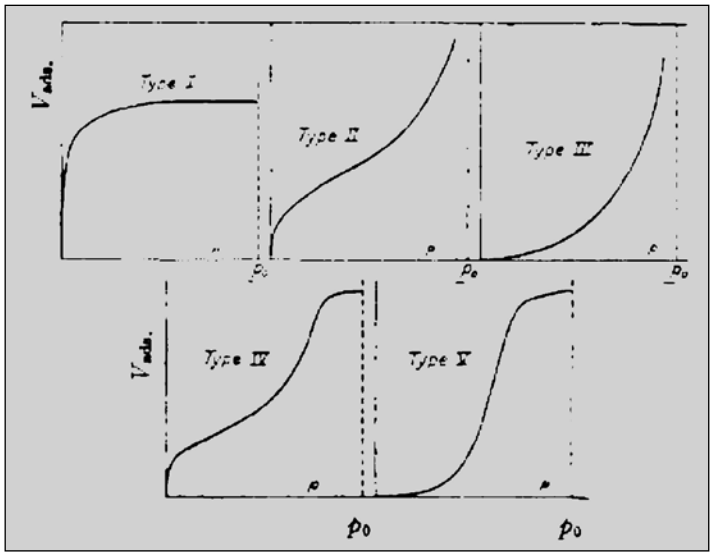

Figure 3.8: The five types of van der Waals adsorption isotherms. Adapted from (Brunauer et al., 1940).

Classification of physisorption isotherm and hysteresis are presented in Figure 3.9 and Figure 3.10 respectively. The isotherms are categorised into six different types, which are Type I, II, III, IV, V and VI and listed below, adapted from (Sing et al., 1985).

1. The reversible *Type I* isotherm is concave to the p/p^o axis and n^a (amount adsorbed) approaches a limiting value as $p/p^o \rightarrow 1$. Type I isotherms are given by microporous solids having relatively small external surfaces (e.g. activated carbons, molecular sieve zeolites and certain porous oxides), the limiting uptake being governed by the accessible micropore volume rather than by the internal surface area.
2. The reversible *Type II* isotherm is the normal form of isotherm obtained with a non-porous or macroporous adsorbent. The type II isotherm represents unrestricted monolayer-multilayer adsorption. Point B, the beginning of the almost linear middle section of the isotherm, is often taken to indicate the stage at which monolayer coverage is complete and multilayer adsorption about to begin.
3. The reversible *Type III* isotherm is convex to the p/p^o axis over its entire range and therefore does not exhibit a Point B. Isotherms of this type are not common, but there are a number of systems (e.g. nitrogen on polyethylene) which give isotherms with gradual curvature and an indistinct Point B. In such cases, the adsorbate-adsorbate interactions play an important role.

4. Characteristic features of the Type IV isotherm are its hysteresis loop, which is associated with capillary condensation taking place in mesopores, and the limiting uptake over a range of high p/p^o. The initial part of the type IV isotherm is attributed to monolayer-multilayer adsorption since it follows the same path as the corresponding part of a Type II isotherm obtained with the given adsorptive on the same surface area of the adsorbent in a non-porous form. Type IV isotherms are given by many mesoporous industrial adsorbents.
5. Type V isotherm is uncommon; it is related to the Type III isotherm in that the adsorbent-adsorbate interaction is weak, but is obtained with certain porous adsorbents.
6. Type VI isotherm, in which the sharpness of the steps depends on the system and the temperature, represents stepwise multilayer adsorption on a uniform non-porous surface. The step-height now represents the monolayer capacity for each adsorbed layer and, in the simplest case, remains nearly constant for two or three adsorbed layers. Amongst the best examples of Type VI isotherms are those obtained with argon or krypton on graphitised carbon blacks at liquid nitrogen temperature.

Nevertheless, there are considerable numbers of isotherms that do not match any of the classifications listed above (Gregg and Sing, 1982).

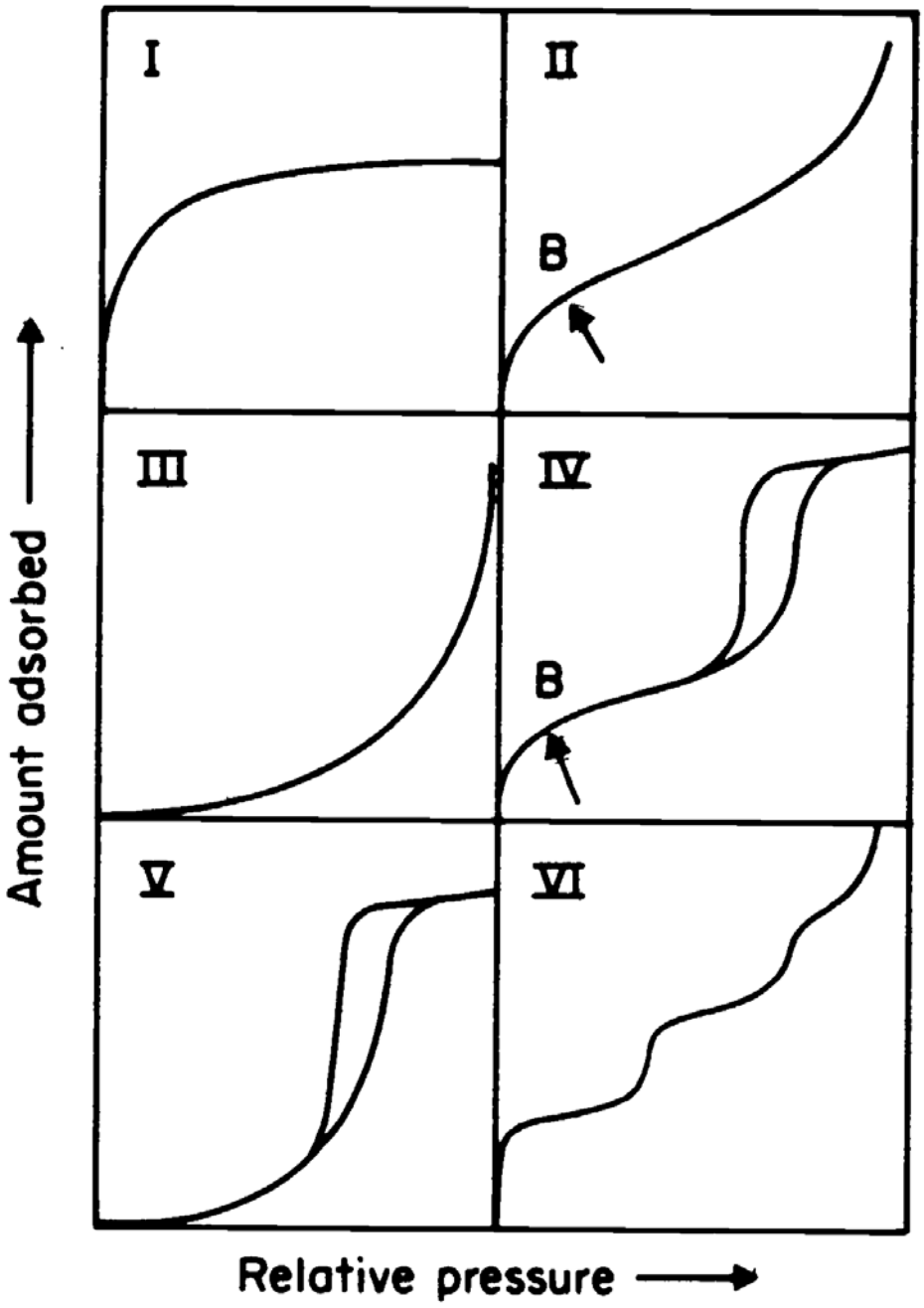

Figure 3.9: Types of physisorption isotherms. Adapted from (Sing et al., 1985).

As there is variety of isotherms, there is also variety of hysteresis shapes exist. Nevertheless, Sing et al. (1985) divided them into four different types which are H1, H2, H3 and H4. Hysteresis in multilayer physisorption process is always associated with capillary condensation in mesoporous materials. H1 and H4 are considered as extreme types whereas H2 and H3 are considered as intermediates of the two extremes. Even though the factors that contribute to the shape of hysteresis is not fully

understood yet, the shapes have always been associated with specific pore structures and is summarised in Table 3.2.

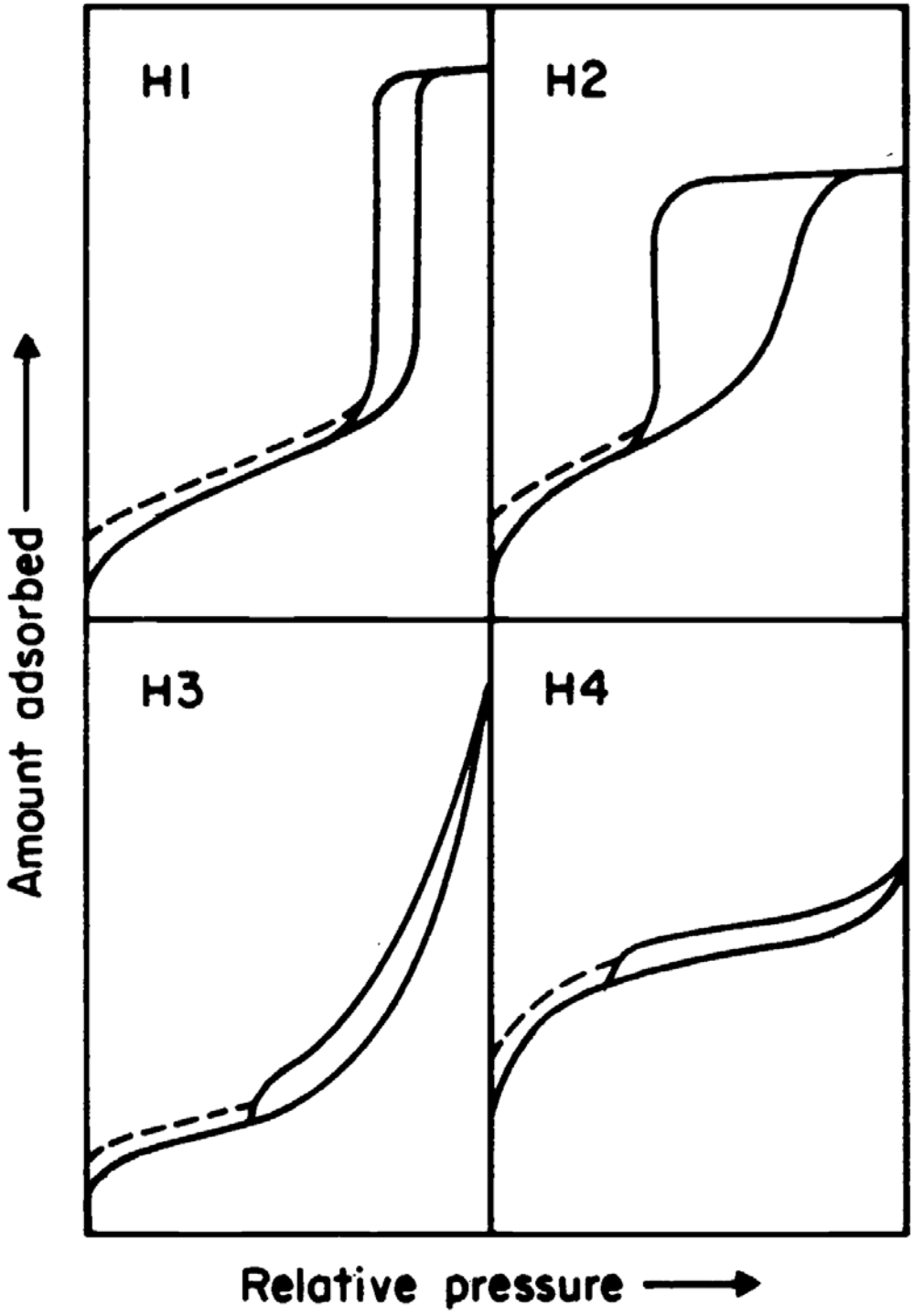

Figure 3.10: Types of hysteresis. Adapted from (Sing et al., 1985).

Table 3.2: Type of hysteresis and associated pore types (summarised from Sing et al.(1985)).

Hysteresis	Type of pore structure
Type H1	Porous materials consist of agglomerates or compacts of approximately uniform spheres in fairly regular array. Hence, pore size distribution of analysed materials is narrow.
Type H2	Associates with inorganic oxide gels and porous glasses which distribution of pore size and shape are not well defined. In the past, this shape was attributed to pores with narrow necks and wide bodies, referred as ink bottle pores- found to be oversimplified.
Type H3	Associates with aggregates of plate-like particles forming into slit-shaped pores.
Type H4	Associates with narrow slit-like pores.

3.2.2.6 Preparation of sample

All samples were crushed/cut to the smallest size possible. The sample was then transferred into the sample tube. Vacuum jacketed tube was used since the full cycle analysis was done. The weight of the samples used was chosen according to the optimal sample quantity needed as given in the manual and presented here in Table 3.3. Prior to analysis, all the samples were outgassed for 5 hours at 50 °C.

Table 3.3: Optimal sample quantity

Estimated specific surface area, m^2/g	Mass of sample for analysis, g
>30	0.1-0.2
10-30	0.3
3.0-9.9	1.0
2.0-2.9	1.5
1.5-1.9	2.0
1.0-1.4	3.0

3.2.3 Fourier Transform Infrared Spectroscopy (FTIR)

FTIR can be used to identify unknown materials, determine the quality or consistency of a sample, and determine the amount of components in a mixture. In this technique, infrared (IR) radiation is passed through a sample, some amount of the radiation is absorbed by the sample and some is passed through or transmitted. The result is translated into a spectrum of molecular absorption and transmission, creating a molecular fingerprint of the sample. Each fingerprint belongs to a unique molecular structure.

A Varian 800 FT-IR spectrometer system was used to analyse the solid samples. The machine produces spectra between 4000 cm^{-1} and 400 cm^{-1} from solid, liquid and oil samples using a Pike Technologies diamond crystal plate ATR (attenuated total reflection) immersion probe.

3.2.4 Gas Chromatography (GC)

The GC used in this study was a Varian 450-GC which is a robust and powerful gas chromatograph. The machine offers single, dual or triple channel configuration flexibility and automation for maximum productivity. It has full digital pneumatic control of all pneumatic parameters and all inlets can be operated up to 150 psi/10 bar.

The GC is equipped with two ovens, five columns and two detectors (TCD (Thermal Conductivity) and FID (Flame Ionization)). The first oven houses three columns to detect permanent gases. The second oven houses two columns, one for hydrocarbons and one for alcohols.

3.3 *Tar removal set-up*

The tar removal/conversion techniques involved several methods, which are PolyHIPE Polymer as an adsorbent, high voltage, plasma, and combination of plasma and PHP. The simulated syngas was produced by passing CO_2 gas through heated crude oil. The model used for tar in the experiment was crude oil. The crude oil was taken from a production field in North Sea and supplied by BP-Amoco. The colour was dark brown/black and the specific gravity was 0.80. Viscosity of crude oil was 153 mPa.s, measured by HAAKE VT 550 viscometer at shear rate of 1000 s^{-1} and temperature of 25^{o}C (Noor, 2006).

3.3.1 PolyHIPE Polymer

The CO_2 gas at a flow rate of 1.0 l/min was passed through the crude oil reactor, having a temperature of 80°C, for 3 hours. The syngas was then passed through a glass reactor filled with crushed PHPs. The reactor and pipes were covered with insulation material to minimise the temperature drop. The treated gas stream was then passed through a set of three glass u-tubes, packed with glass beads, silica gel and glass wool, respectively. The u-tubes were soaked in an ice bath. Gas sample was drawn from two sampling points, before and after glass reactor, using 5 ml plastic syringe and injected into Gas Chromatograph (GC). Since there was only one GC machine available, the sampling was done 30 minutes apart to avoid gas leakage. The schematic of the set up used is presented in Figure 3.11. The pictures of the crude oil reactor and the PHP filled glass reactor and the u-tubes are presented in Figure 3.12.

The polymer efficiency was determined gravimetrically, using the equation:

$$Polymer\ Efficiency = (\ Wt.\ PHP_{final} - Wt.\ PHP_{initial}\ ) / Wt.\ PHP_{initial} \qquad \text{Equation 3.13}$$

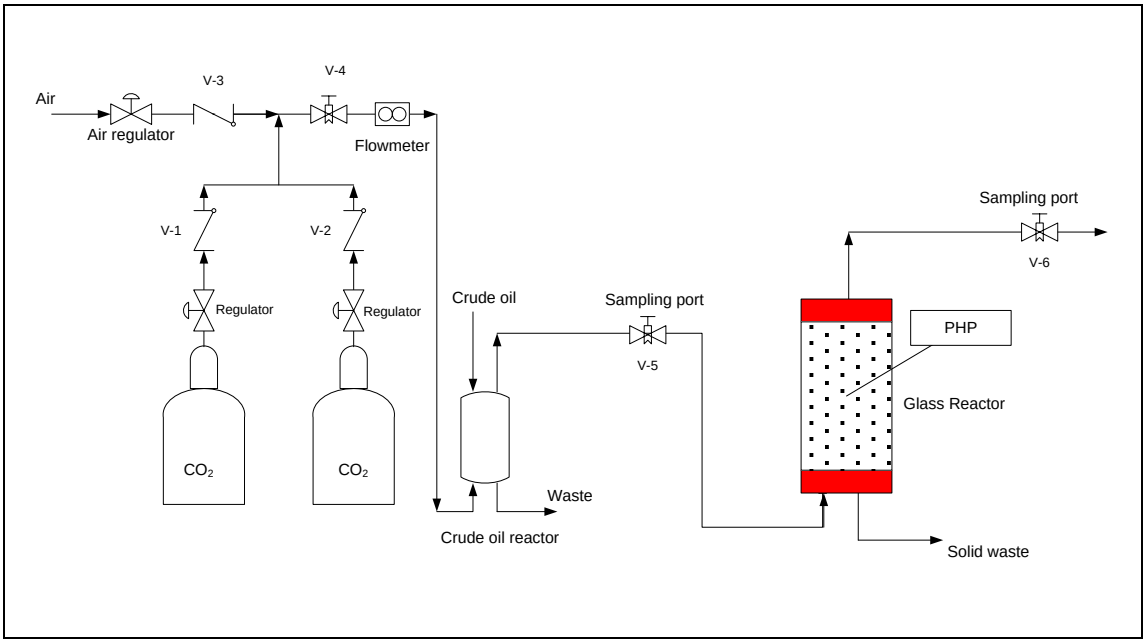

Figure 3.11: Schematic of tar removal set-up using PolyHIPE Polymer.

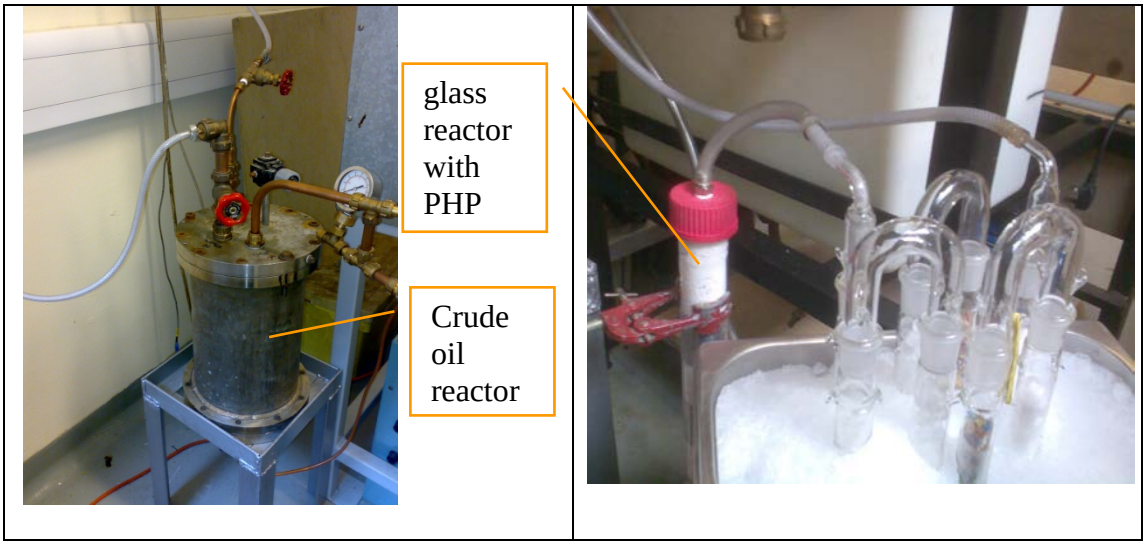

Figure 3.12: Pictures of apparatus used.

3.3.2 High Voltage

The same set-up used in section 3.3.1 was used in the high voltage experiment to produce syngas. The CO_2 gas at a flow rate of 1.0 l/min was passed through the crude oil reactor, having a temperature of 80°C, for 3 hours. The gas was then passed through the reactor having high voltage applied to it. The voltages applied were 10, 15 and 20 kV. The reactor was fitted with wire mesh and electrode inside it. Recemat was fixed in between the two wire meshes. Recemat is a metal foam plate and the one used here is nickel. (Specification of nickel used, number of pores: 47 - 53 /inch, average pore size: 0.4 mm, thickness: 1.6 mm). The gas sampling for GC analysis was done before and after the reactor using the same technique in section 3.3.1. After treatment, the treated gas stream was then passed through a set of glass u-tubes, packed with glass beads, silica gel and glass wool, respectively.

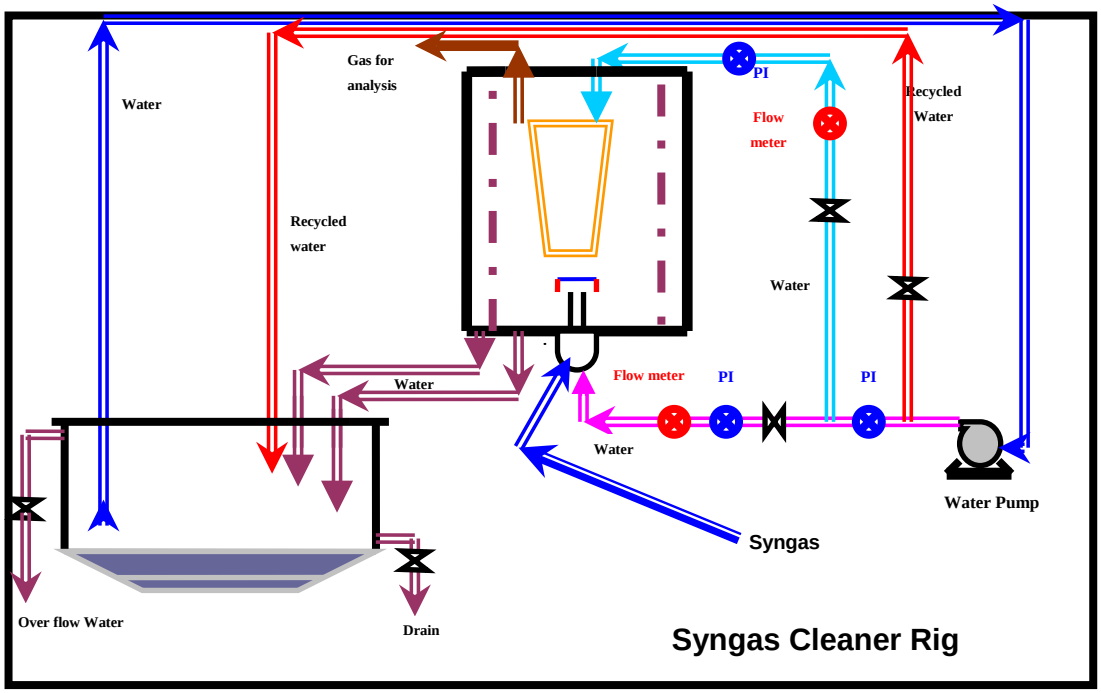

Figure 3.13: The schematic for tar removal using high voltage.

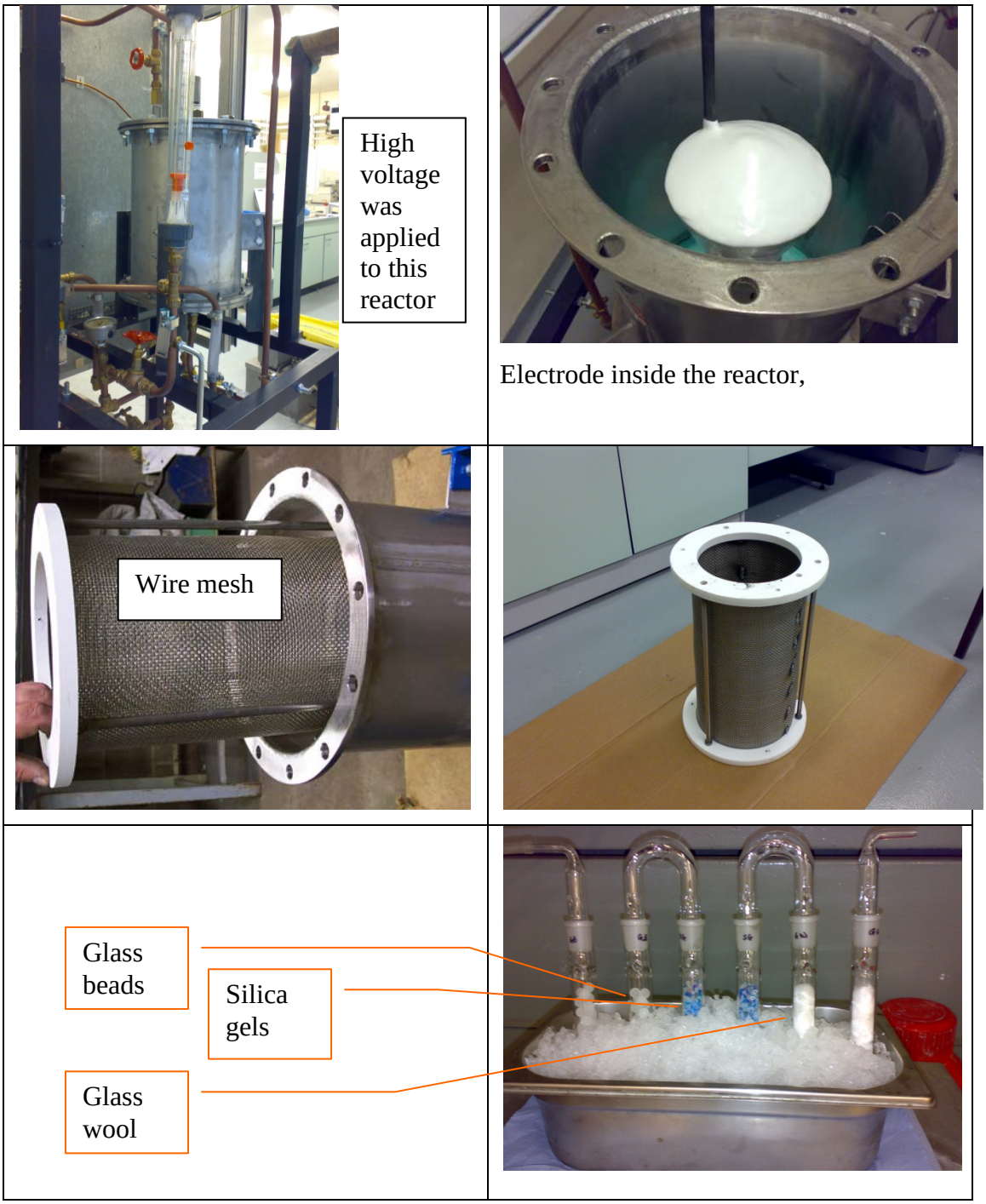

Figure 3.14: Pictures of apparatus used in the experiment.

3.3.3 Plasma (non-thermal)

Schematic of the set-up used in tar removal/conversion through non-thermal plasma (dielectric barrier discharge) technique is presented in Figure 3.15. The glass

reactor was filled with glass beads for experiments using plasma, and was filled with glass beads and PolyHIPE polymer for experiments using combination of dielectric barrier discharge and PHP. The pictures of the glass reactors are presented in Figure 3.16. The CO_2 gas at a flow rate of 1.0 liter/min passed through a crude oil reactor, at a temperature of 80°C, was used as a model for syngas. The gas sample was withdrawn before and after treatment using 5 ml syringe and then injected into GC machine. The treated gas stream was then passed through a set of three glass u-tubes, packed with glass beads, silica gel and glass wool.

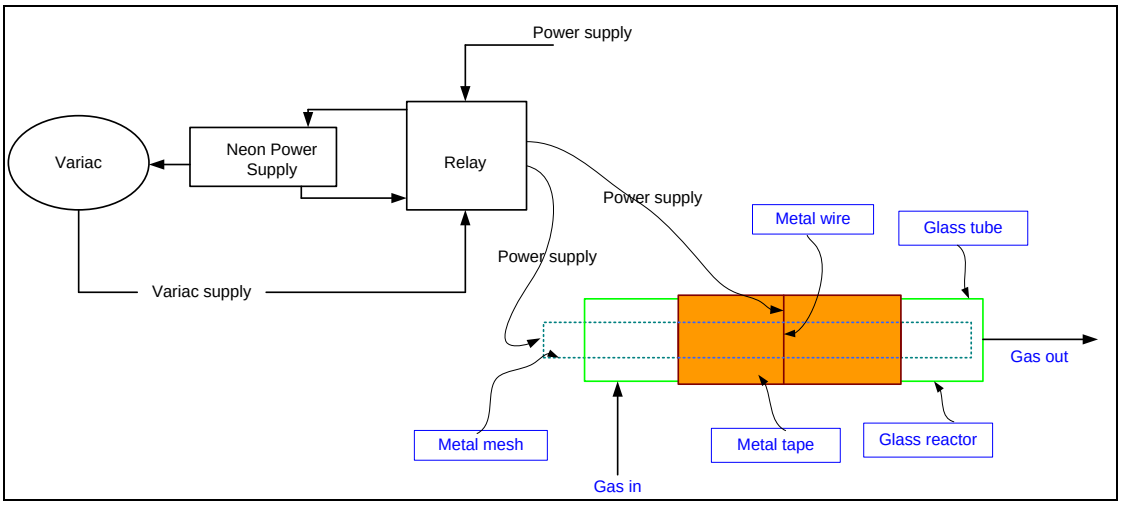

Figure 3.15: Schematic set-up for tar removal/conversion using Plasma

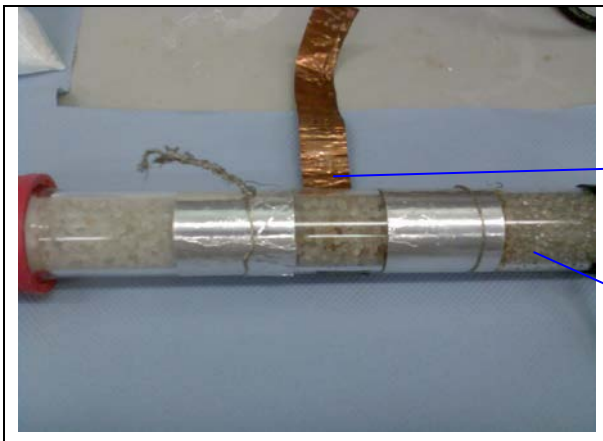

(a) Glass reactor filled with glass beads.

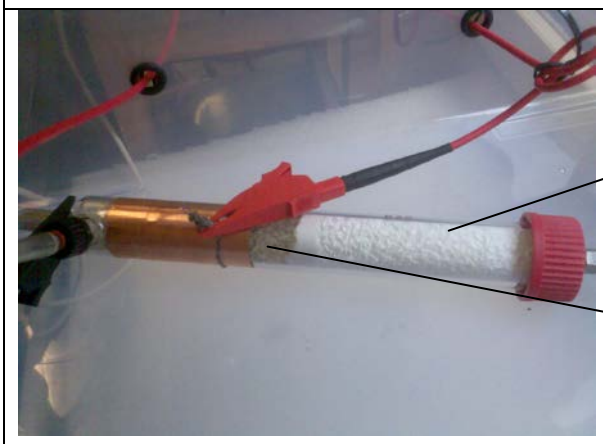

(b) Glass reactor filled with glass beads and PolyHIPE Polymer.

Figure 3.16: Image of glass reactor.

4 PolyHIPE Polymer: Results & Discussions.

This chapter discusses the morphology, surface area and pore size distribution as well as sulphonation of several PolyHIPE polymers produced from the methodology described in Chapter 3. Water adsorption, effects of type of initiator, the success of functionalization, comparison between the PHPs and the relationship between the isotherms and the morphology, surface area and pore size distribution are also discussed.

4.1 *Silica/Bindzil PHP – first phase.*

The Scanning Electron Microscope (SEM) images of the three different silica PHPs, B10, B30 and B40 are shown in Figure 4.1. From this general view of the three images, coalescence pores and primary pores are apparent.

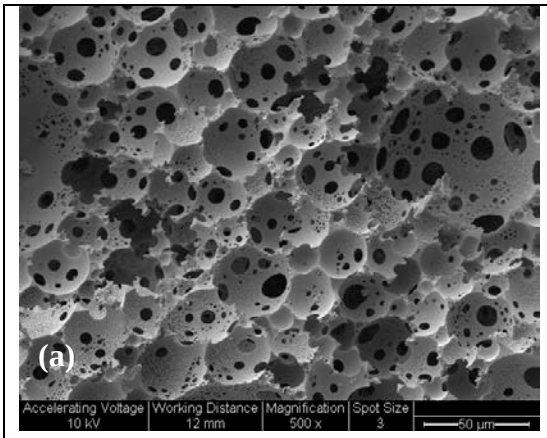

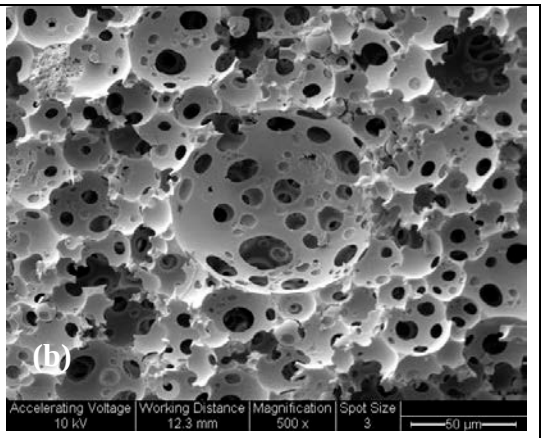

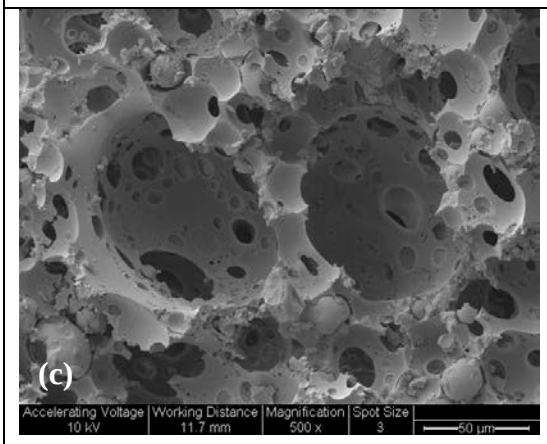

(a) B10-silica PHP, 500X.

(b) B30-silica PHP, 500X

(c) B40-silica PHP, 500X

Figure 4.1: SEM images of 3 different silica PHPs, general view.

Further SEM analysis of the silica PHP structure and surface is as presented in Figure 4.2 and Figure 4.3. The images show islands of non-covered polymer; and both smooth surface and porous surface next to one another. Some closed pores and interconnects are observed in Figure 4.4. From Figure 4.4 and Figure 4.5, the images of the inner structure could be observed. Further magnification of image as shown in Figure 4.5, revealed the exposed inner structure with other structures nearby, which are fractured wall, surface and hole. These structures further clarified the high value of surface area for silica PHP.

Another important difference that was spotted from SEM analysis was the presence of particles in the structure of silica PHP. This was not observed in the image of typical PHP. The SEM images are shown in Figure 4.6, Figure 4.7 and Figure 4.8. Figure 4.7 shows a structure of a small ball on a big ball, spotted in a coalescence pore. In order to verify the elements of this ball structure, EDX (Energy Dispersive Analysis with X-Rays) was done. The results for three different points are shown in Figure 4.10, Figure 4.11and Figure 4.12. The summary is presented in Table

4.1. All the three points show the presence of Silicon, with about the same percentage of Si.

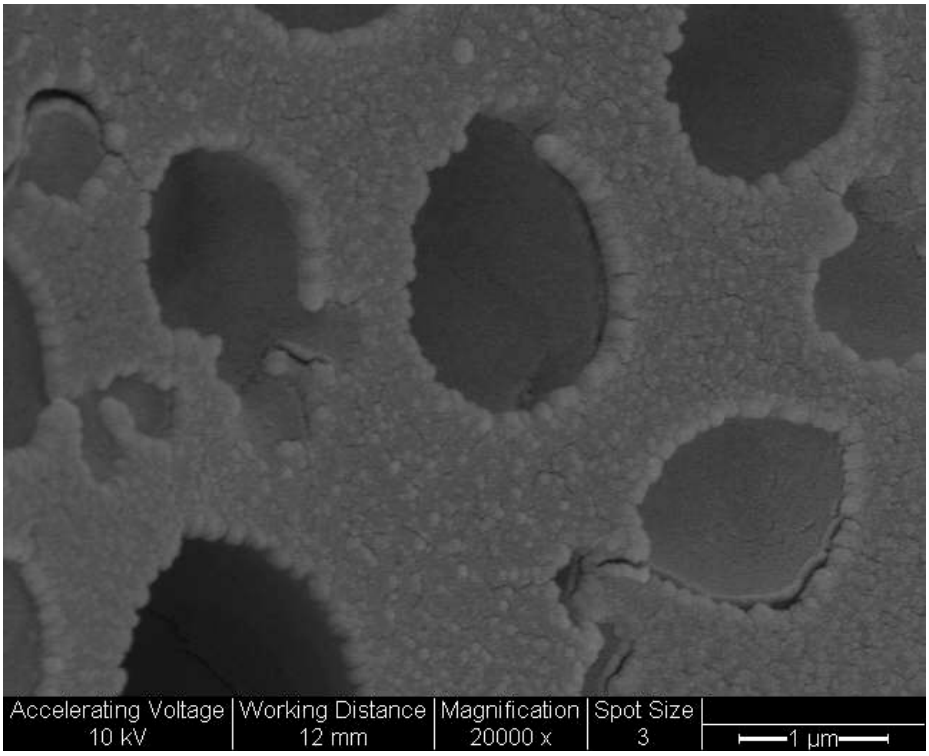

Figure 4.2: B10-silica, 20000X, surface structure of the pores showing islands of non-covered polymer.

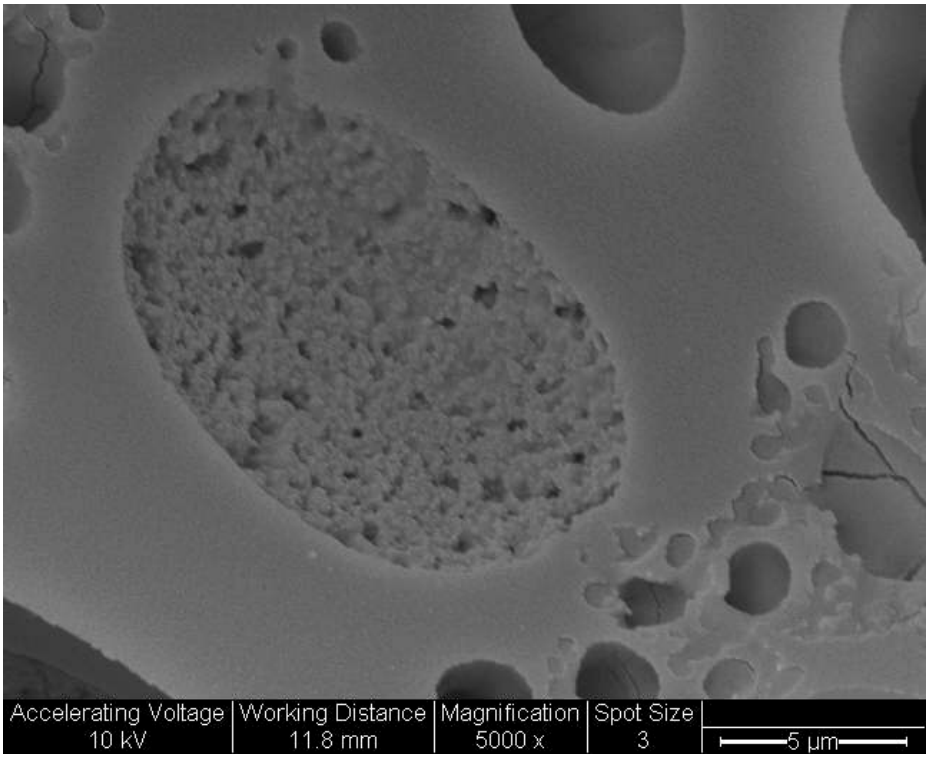

Figure 4.3: B40-silica, 5000X, image showing porous structure next to a smooth structure.

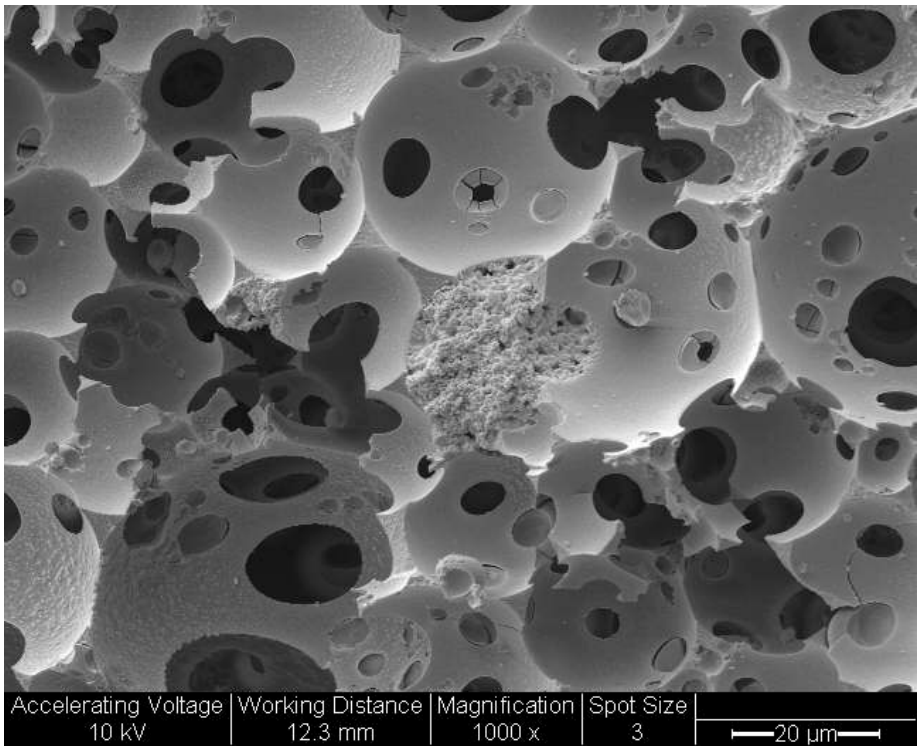

Figure 4.4: B30-silica PHP, 1000X, image showing spot of missing skin with exposed inner structure.

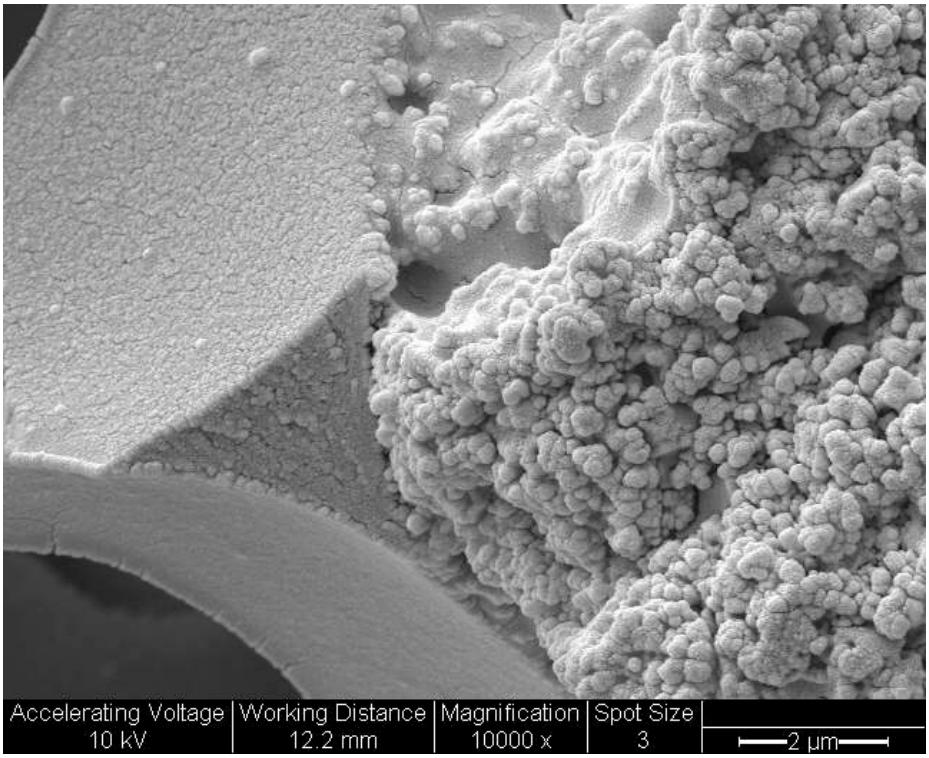

Figure 4.5: B30-silica PHP, 10000X, higher magnification of a spot of missing skin.

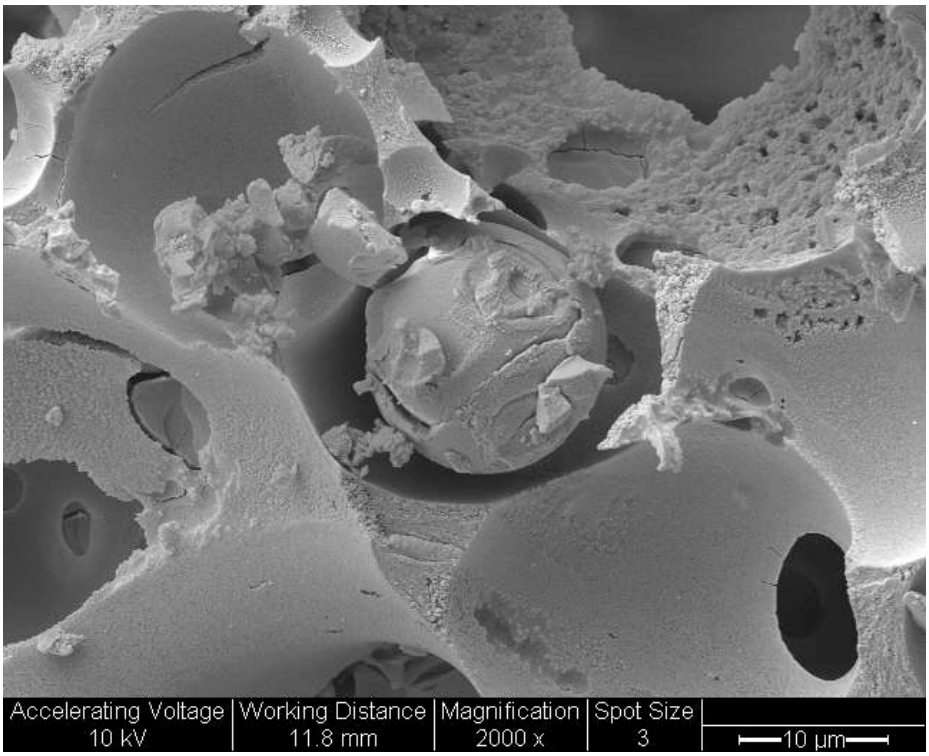

Figure 4.6: B40-silica PHP, 2000X, image showing presence of particles.

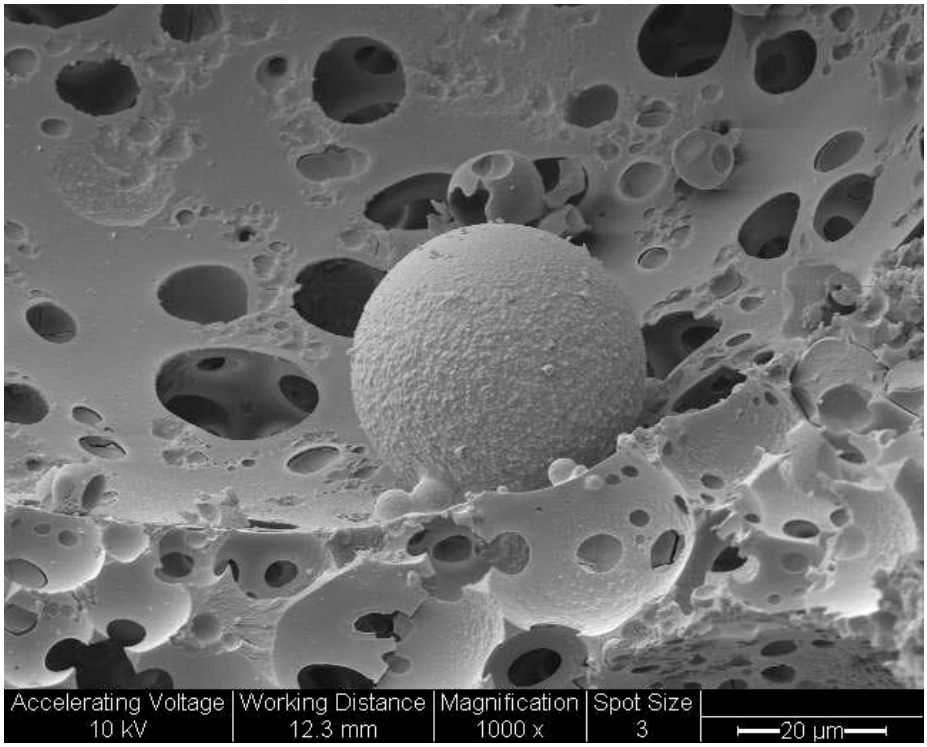

Figure 4.7: B30-silica, 1000X, ball structure in a coalescence pore.

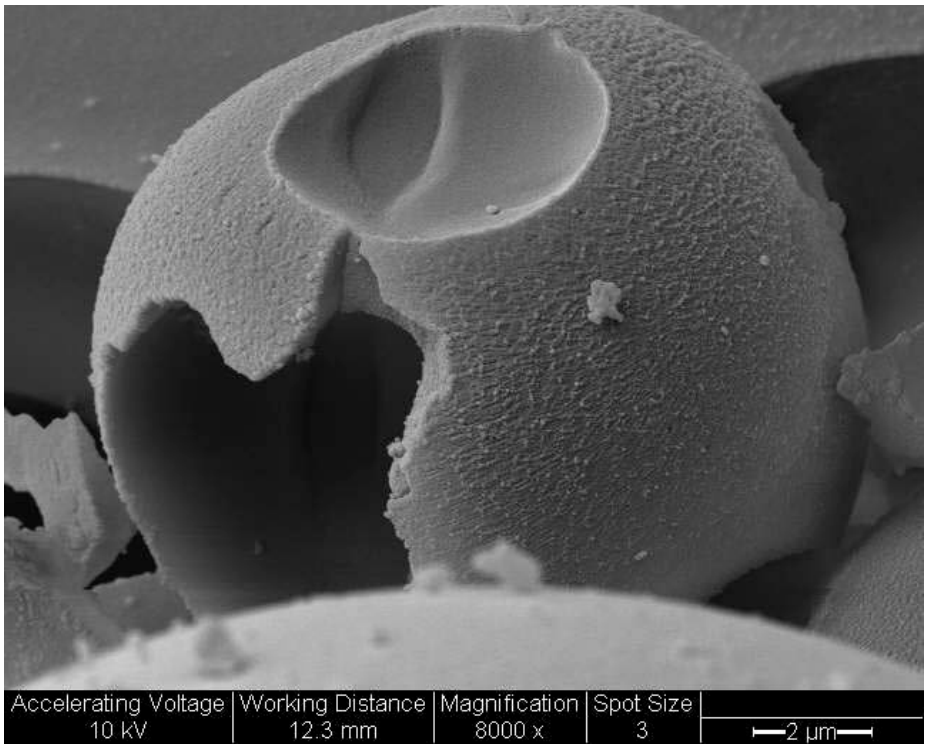

Figure 4.8: B30-silica PHP, 8000X, a small ball sitting on a big ball.

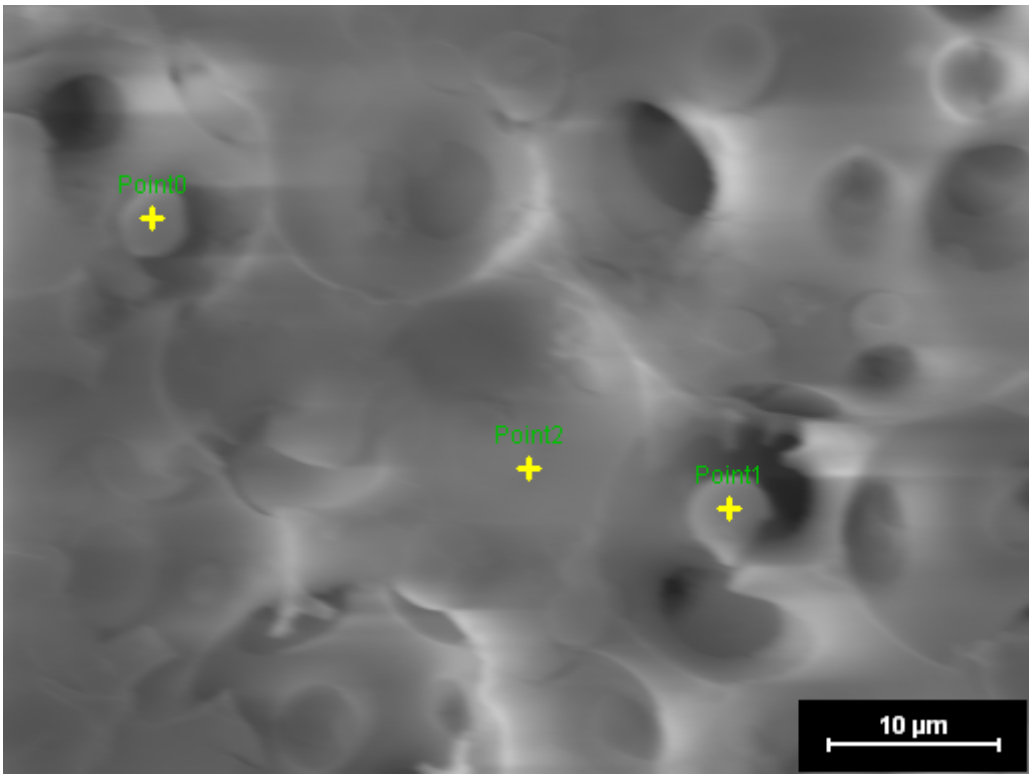

Figure 4.9: Three points for EDX analysis.

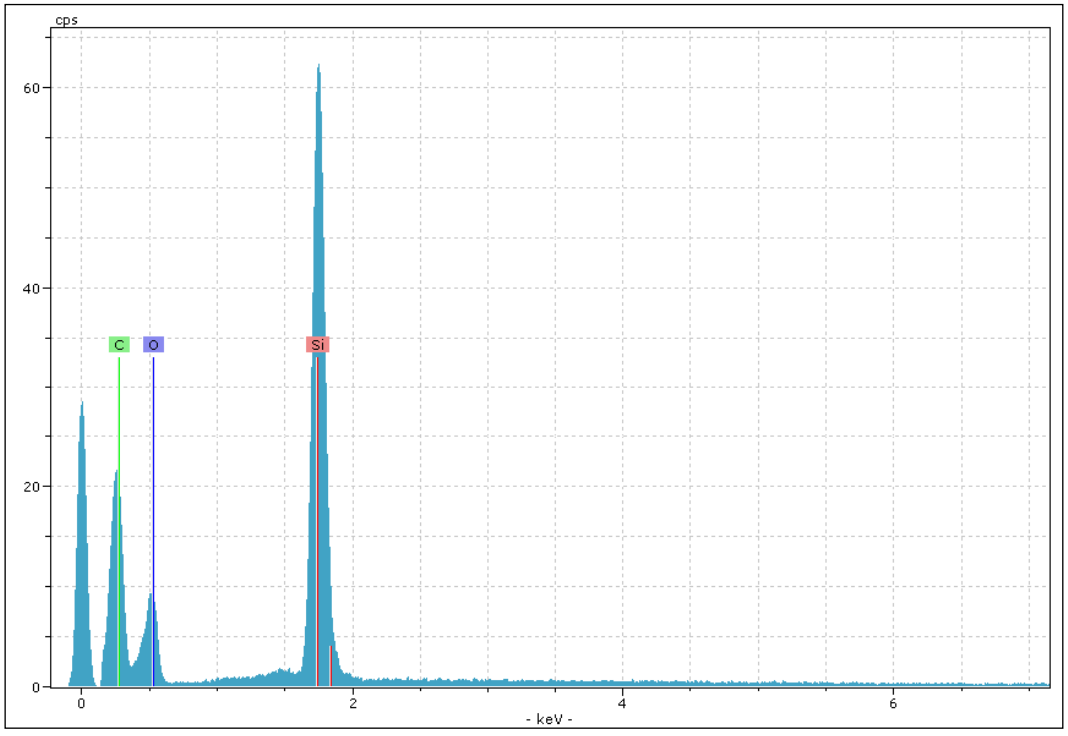

Figure 4.10: B30 point 0

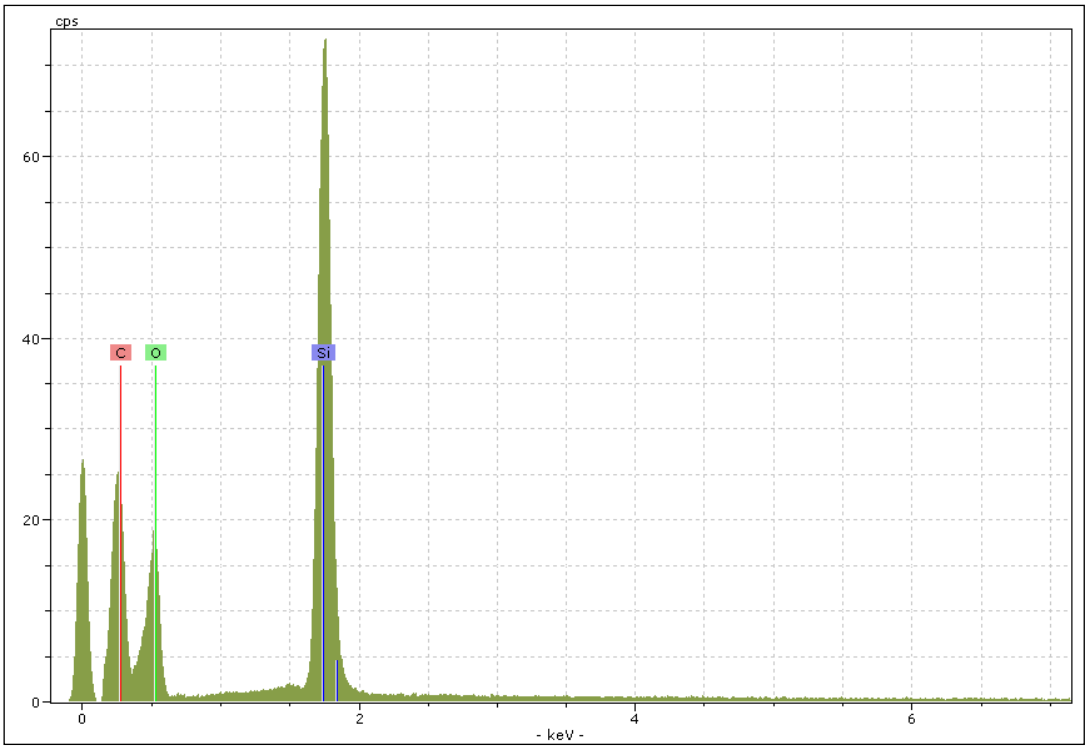

Figure 4.11: B30 point 1

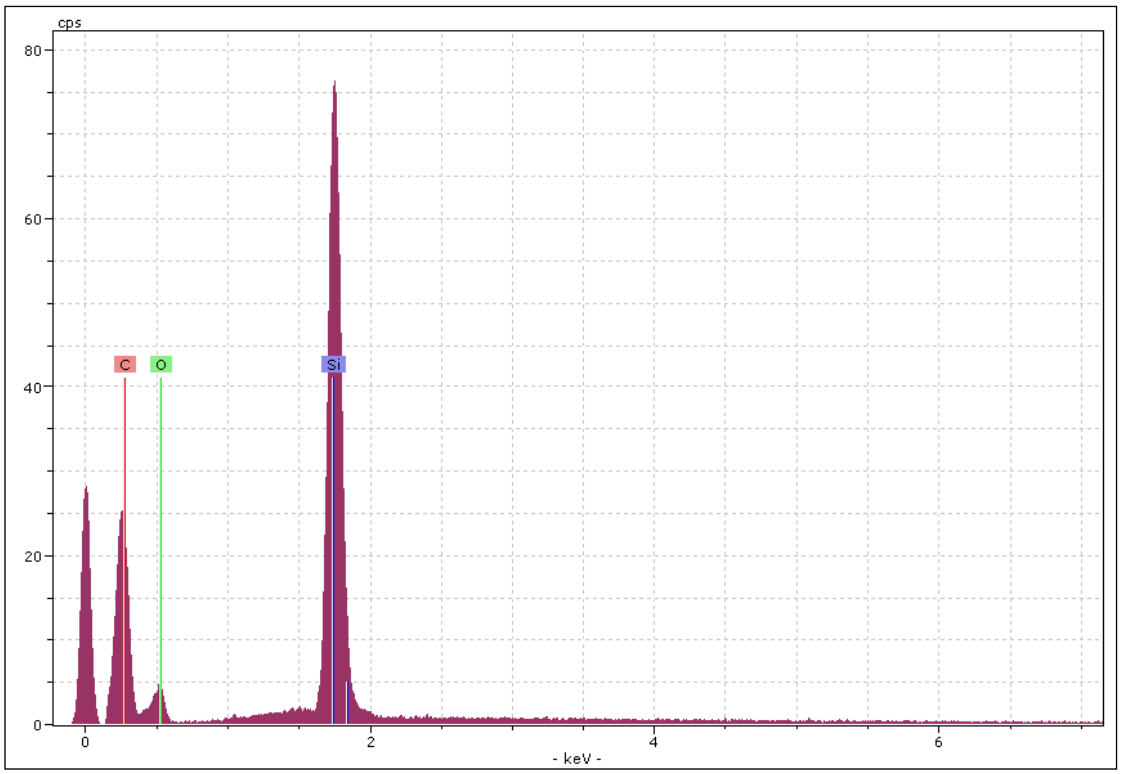

Figure 4.12: B30 point 2

Table 4.1: Summary of the EDX results for 3 points, 0, 1 and 2.

	Point 0		Point 1		Point 2	
Element	weight %	atomic %	weight %	atomic %	weight %	atomic %
Silicon	20.86	11.45	19.98	11.14	23.51	12.63
Carbon	38.27	49.15	32.51	42.37	48.50	60.96
Oxygen	40.87	39.40	47.51	46.49	27.99	26.41

The result of surface area for various silica polyHIPE polymers is presented in Table 4.2. The B30 sample has the highest surface area but the result was not consistent. Three different discs give three different values of surface areas. The lowest surface area is for B10 sample.

Table 4.2: Surface area of silica polyHIPE polymers (washed).

Sample ID	Surface Area, sq.m/g
B10 unshaken	15.83
B20 unshaken	49.34
B30 shaken 1st run	102.38
B30 shaken 2nd run	66.86
B30 shaken 3rd run	93.26
B40 shaken 1st run	58.36
B40 shaken 2nd run	57.94

In order to study the sedimentation effect during polymerisation, three different discs, which are from the top, medium and bottom of a single tube, were taken for surface area analysis. The result shows that there is no sedimentation effect since the bottom disc has the lowest surface area whilst the medium disc has the highest surface area (Table 4.3).

Table 4.3: Surface area for different position discs of silica PHP (washed) from a single container.

Sample ID	Surface Area sq.m/g
Washed B30	
Bottom disc	33.66
Medium disc	92.56
Top disc	53.86

Since there is no sedimentation effect, surface area analysis was then done using the unwashed silica PHP, B30 to check for leaching effect during washing process. The result for top and bottom disc from a single container is presented in Table 4.4. The bottom disc has a higher surface area of 1.69 sq.m/g more compared to the top disc. It shows that the variation in the surface areas of the different discs is due to the leaching during the washing process and not the sedimentation effect during polymerisation. Therefore, for further experiment of silica, the washing was done using the soxhlet apparatus rather than washing in a beaker stirred by magnetic stirrer.

Table 4.4: Surface area for different position discs of unwashed silica PHP from the same container.

Sample ID	Surface Area, sq.m/g
Unwashed B30	
Top disc	121.60
Bottom disc	123.29

4.2 *Alumina PHP*

The SEM images of the alumina polyHIPE are shown in Figure 4.13. Comparing the 3 images, the washed, unwashed and soaked alumina PHPs, no difference could be observed. The non-soaked, unwashed alumina PHP was further

heat treated at 800 °C. The sample crumbled after heat treatment; therefore, further study is needed on the composition of incorporated filler in the aqueous phase.

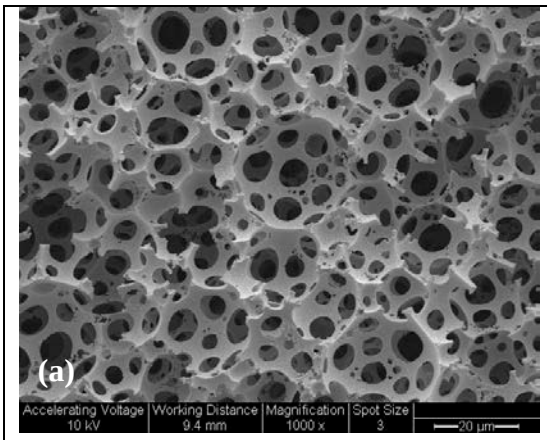

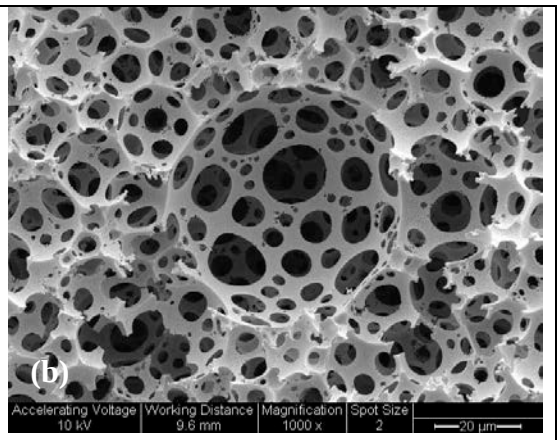

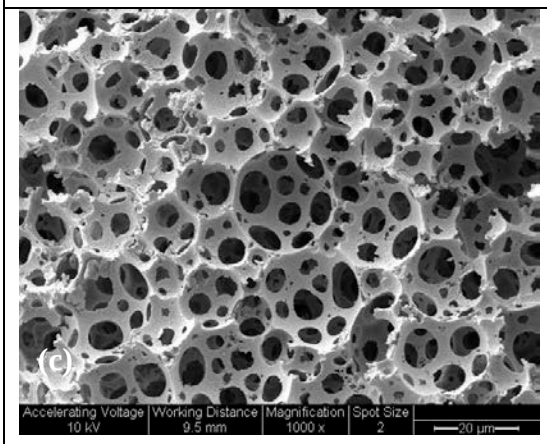

(a) Non-soaked, unwashed alumina polyHIPE, 1000X.
(b) Non-soaked, washed alumina polyHIPE, 1000X.
(c) Soaked (in 1M ammonium carbonate solution) alumina polyHIPE, 1000X.

Figure 4.13: Comparison of alumina PHP.

The surface area of the alumina PHP is presented in Table 4.5. The surface area obtained for both samples are in the range of typical surface area of PHP, 3-10 m^2/g. Thus, there is no significant increase or improvement in the surface area of the produced alumina PHP.

Table 4.5: Surface areas of alumina PHP.

Sample	Surface area, m^2/g
Unwashed alumina PHP	7.08
Washed Alumina PHP	6.72

4.3 *Comparison of Silica to Alumina PHP*

Comparison of SEM images of silica and alumina PHP is presented in Figure 4.14. The image of silica PHP shows some spots of particles whereas no particle could be observed in alumina PHP. The alumina PHP appears more porous and has more interconnects compared to Bindzil PHP.

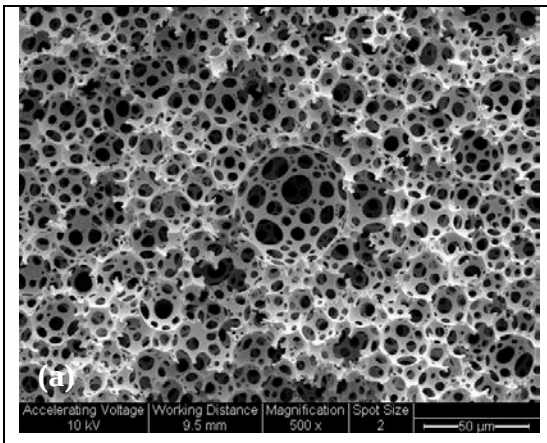

(a) Alumina PHP, 500X.

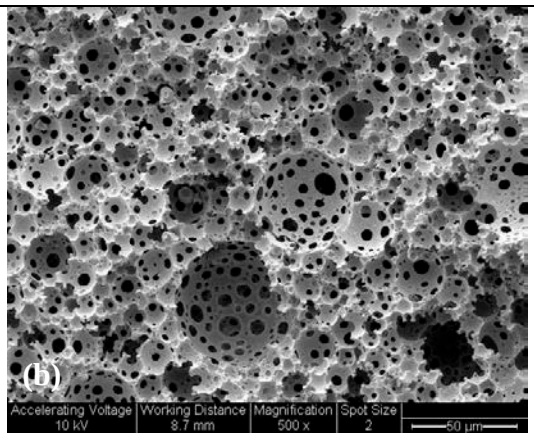

(b) Silica PHP, 500X.

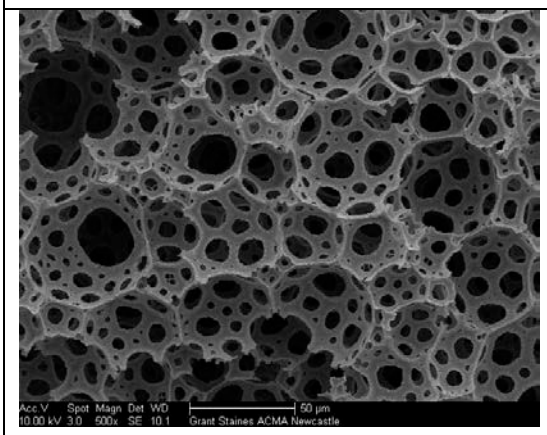

(c) basic PHP, 500X.

(a) Alumina PHP.

(b) Silica PHP.

(c) Typical morphology of basic PHP.

Figure 4.14: Comparison, general view of alumina and silica PHPs.

4.4 *Silane/VTMS (vinyl trimethoxy silane) PHP*

VTMS PHP was produced using the aqueous phase initiator and oil phase initiator by introducing VTMS in the oil phase solution. It was discovered that the

VTMS PHP with aqueous phase initiator produces a novel structure whereas the one with oil phase initiator retain the typical structure of polyHIPE pore. Pictures of the produced VTMS PHP are presented in Figure 4.15.

(a) VTMS PHP, in a cylindrical bottle

(b) Cut & washed VTMS PHP.

Figure 4.15: Picture of VTMS PHP, S10, 10 % VTMS.

4.4.1 Effect of initiator – aqueous phase initiator.

The SEM images of the S5 PHP, produced with 5% vinyl trimethoxy silane (VTMS) in the oil phase through aqueous phase initiator are presented in Figure 4.16. The images are best described as having pores of coral-like shape with internal banana-like strands. The interconnect pores are completely lost in this structure.

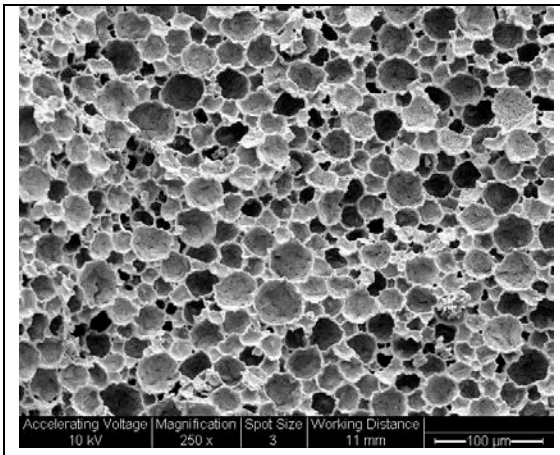

(a) 250X, general view.

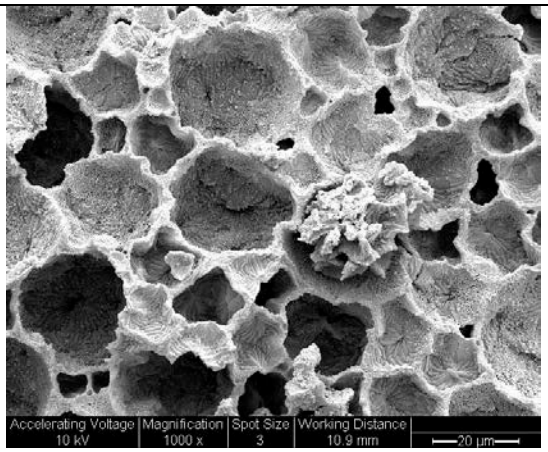

(b) 1000X, coral-like pores.

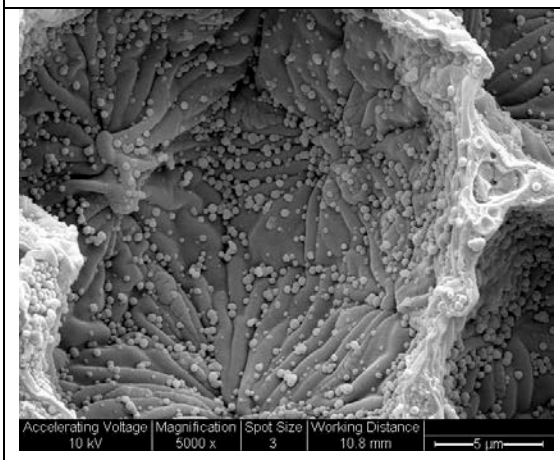

(c) 5000X, magnification of the pore.

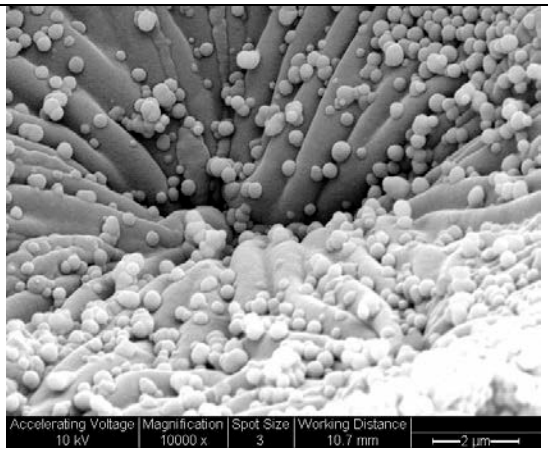

(d) 10000X, strand inside the pore.

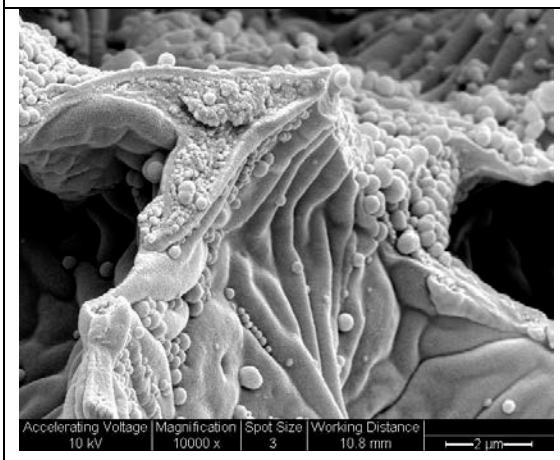

(e) 10000X, wall structure.

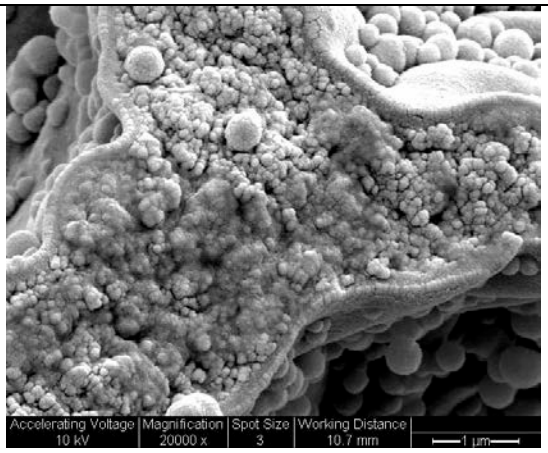

(f) 20000X, another wall.

Figure 4.16: Vinyl trimethoxy silane PolyHIPE polymer. The samples are unwashed. Oil phase: 63% styrene, 20% DVB (Divinylbenzene), 12% Span 80 (Sorbiton monooleate), 5% Vinyltrimethoxysilane. Aqueous phase: 1% Potassium persulphate in distilled water. Phase volume = 80%, Dosing time = 10 minutes, Mixing time = 50 minutes. Polymerisation temperature: 60 °C for 24 hours.

In order to study the presence of spherical particles, the polymers were washed in isopropanol followed by water for the duration of three hours in each solvent. The images for the washed samples are shown in Figure 4.17. It has been observed that the spherical particles still exist in the structure of the washed samples. Thus, washing did not eliminate the presence of spherical particles. Figure 4.16 and Figure 4.17 show that the surface contains agglomerated particles.

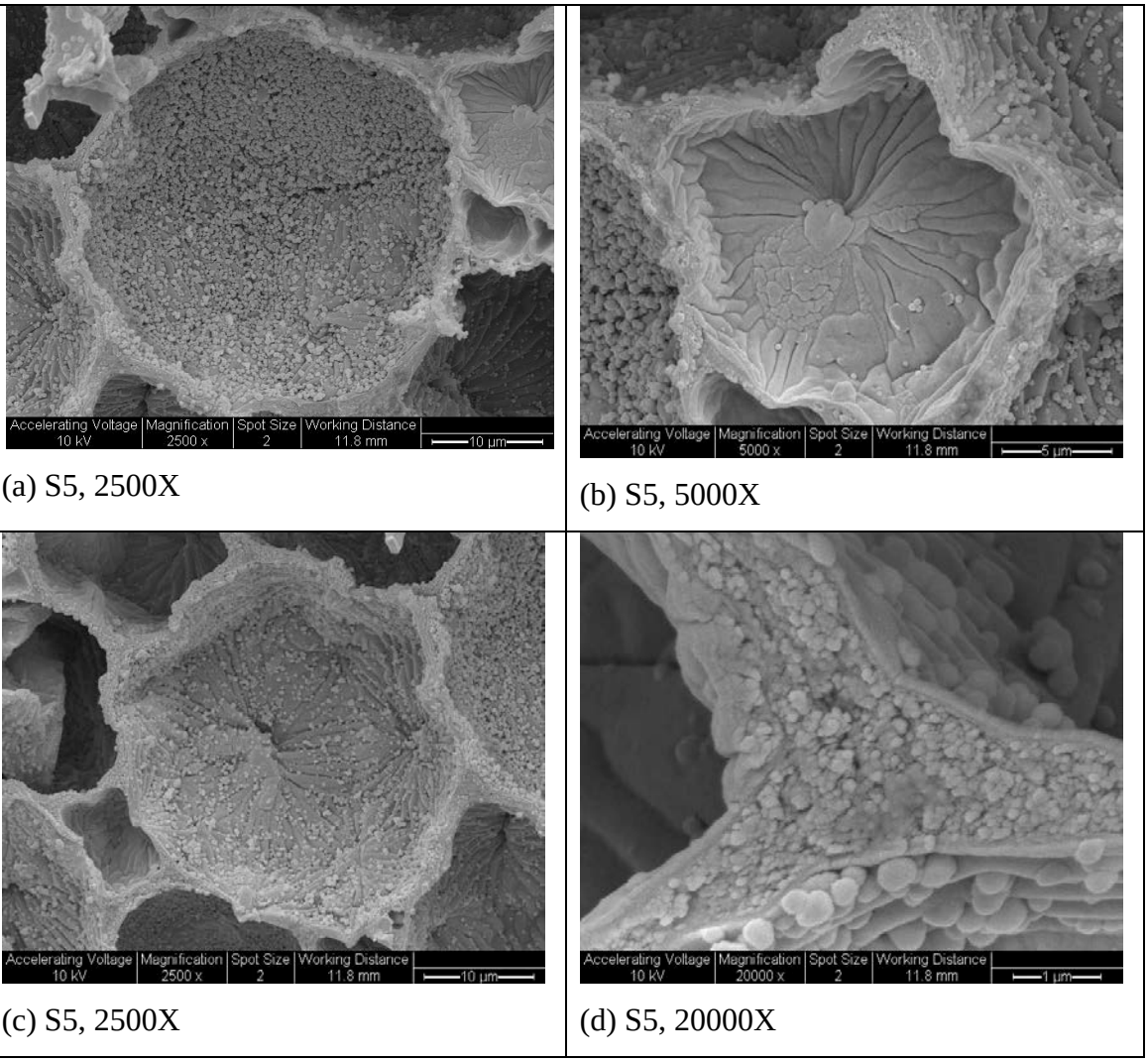

(a) S5, 2500X

(b) S5, 5000X

(c) S5, 2500X

(d) S5, 20000X

Figure 4.17: Vinyl trimethoxy silane PolyHIPE polymer, S5. The samples are washed. Oil phase: 63% styrene, 20% DVB (Divinylbenzene), 12% Span 80 (Sorbiton monooleate), 5% Vinyltrimethoxysilane. Aqueous phase: 1% Potassium persulphate in distilled water. Phase volume = 80%, Dosing time = 10 minutes, Mixing time = 50 minutes. Polymerisation temperature: 60 °C for 24 hours.

(a) Pore with lots of spherical particles. (b) Pore with no/few spherical particles.

(c) Pore with intermediate amount of spherical particles. (d) Wall strand in between pores.

In order to further study the effect of VTMS addition to the structure of polyHIPE, percentage VTMS was further varied. The results are shown in Figure 4.18. Comparing the results, only PHP with 5%, 10% and 30% VTMS have monodispersed pores. The rest have many coalescent pores. It is very difficult to produce VTMS PHP with high emulsion stability. This might be due to lack of stronger interfacial film around the droplet of the emulsions resulting in Oswald ripening (coalescence). The results presented here are chosen from the most stable emulsions produced for each percentage of VTMS after several attempts, as many as six trials. Attempts were also made to use both, aqueous and oil phase initiators, but the maximum could be incorporated was 10 % VTMS. The image is shown in Figure 4.19 (c), the pores look monodisperse.

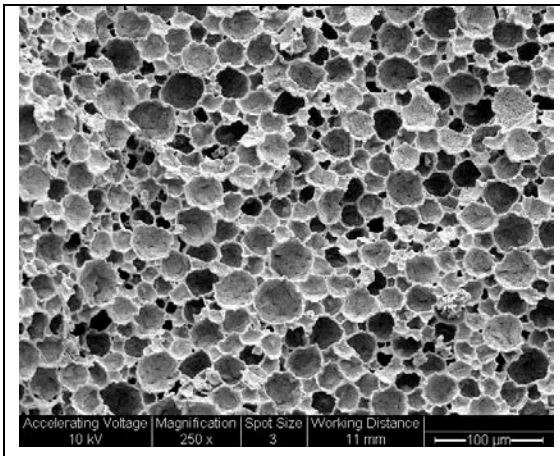

(a) S5, 250X

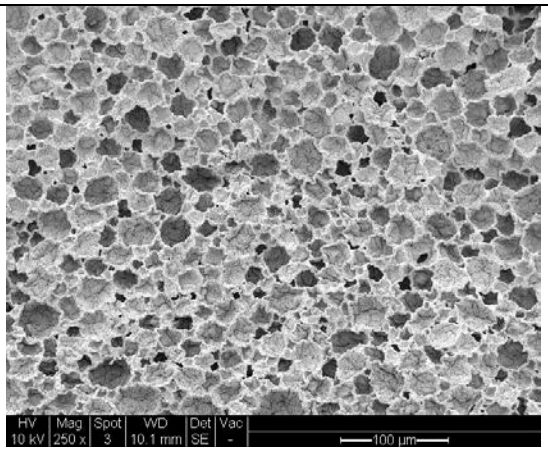

(b) S10, 250X

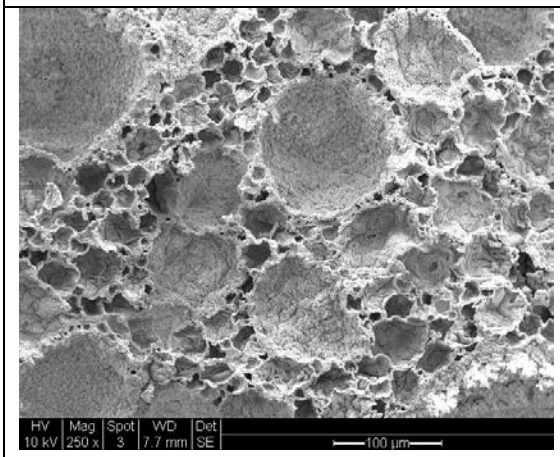

(c) S15, 250X

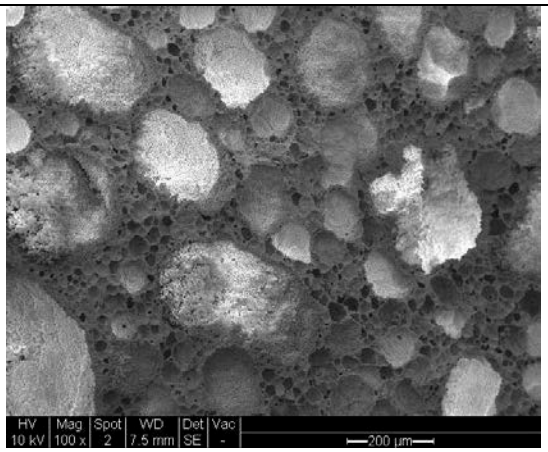

(d) S20, 100X

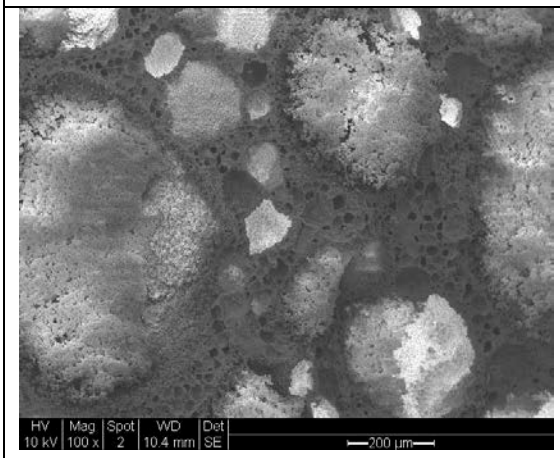

(e) S25, 100X

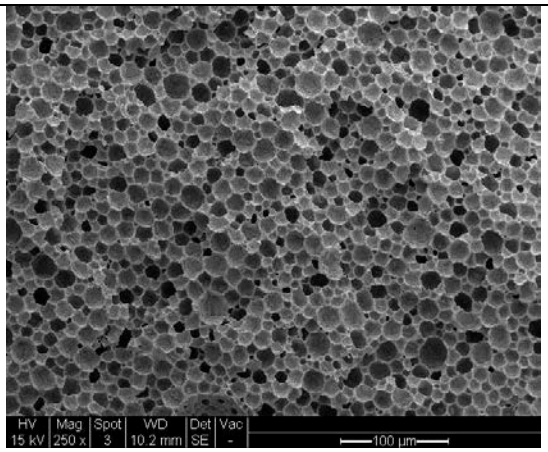

(f) S30, 250X

Figure 4.18: Vinyl trimethoxysilane PolyHIPE polymer. (a) 5% VTMS (b) 10% VTMS (c) 15% VTMS (d) 20% VTMS (e) 25% VTMS (f) 30% VTMS

Oil phase: X% Vinyltrimethoxysilane, (63-X)% styrene, 20% DVB (Divinylbenzene), 12% Span 80 (Sorbiton monooleate),.(e.g, for 10% silane, styrene was reduced to 58%). Aqueous phase: 1% Potassium persulphate in distilled water. Phase volume = 80%, Dosing time = 10 minutes, Mixing time = 50 minutes. Polymerisation temperature: 60 °C for 24 hours.

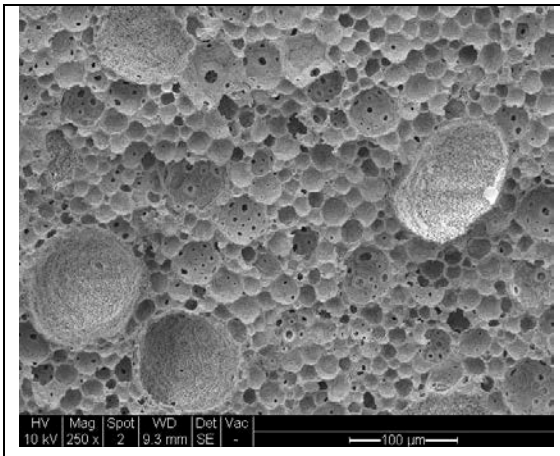

(a) S35, 250X

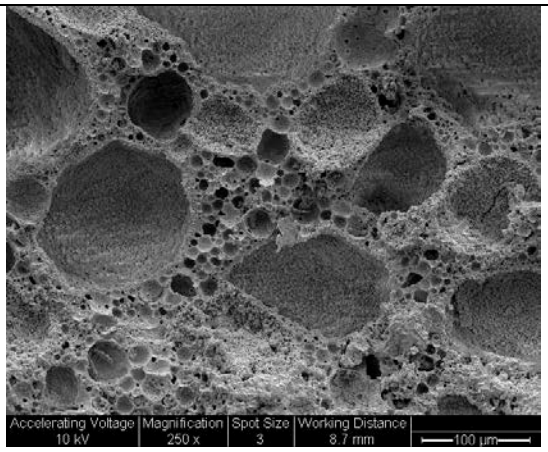

(b) S40, 250X

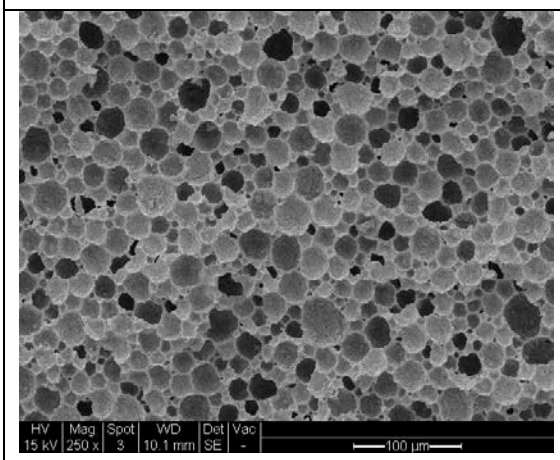

(c) S10m, 250X

(a)S35, many coalescent pores, pores with interconnects and coral-like structure and coral-like pores.
(b)S40, many coalescent pores.
(c)S10m – both oil and aqueous phase initiator are used.

Figure 4.19: (a) 35% VTMS (b) 40% VTMS (c) 10% VTMS with a mixed aqueous phase and oil phase initiator.

At higher magnification of 2500X in Figure 4.20 and Figure 4.21, spherical particles are apparent for S5, S10 and S10M PHP. Interconnects are apparent for pores of S35 and S40.

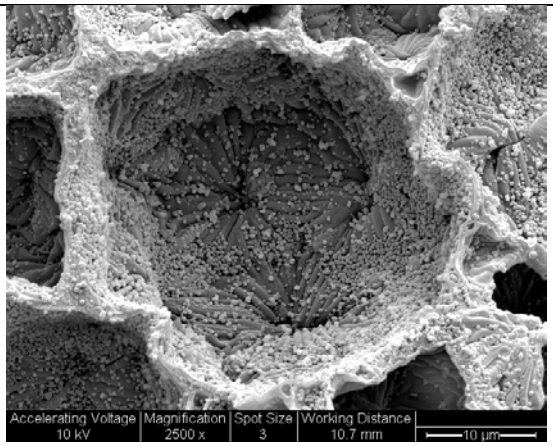

(a) S5, 2500X

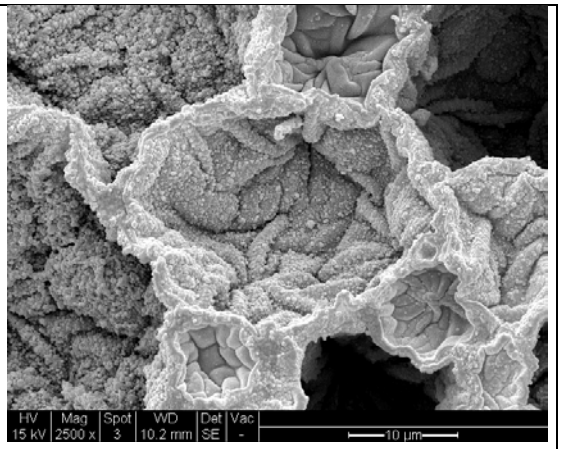

(b) S10, 2500X

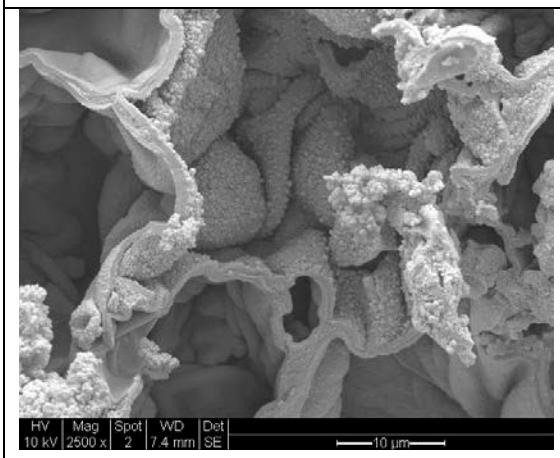

(c) S15, 2500X

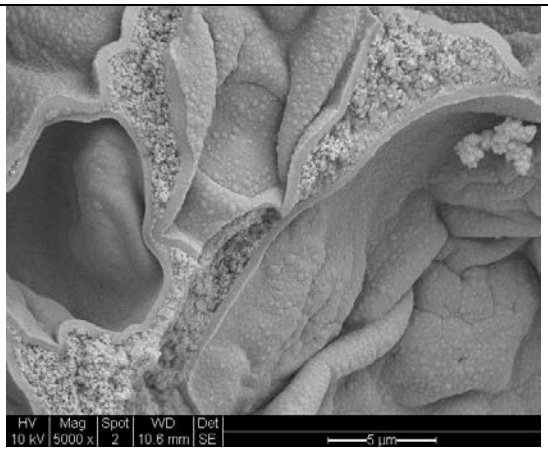

(d) S25, 5000X

Figure 4.20: Images of VTMS PHP at high magnification.

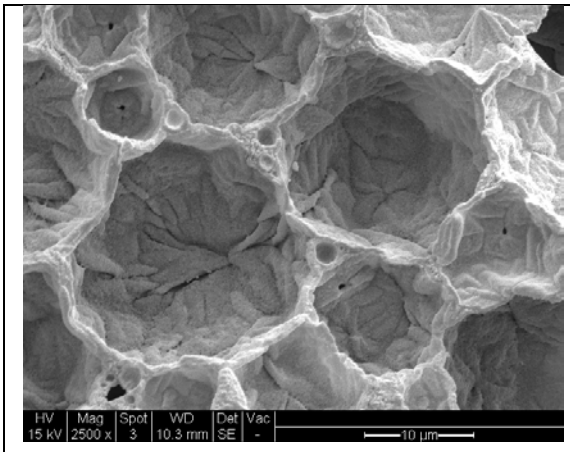

(a) S30, 2500X

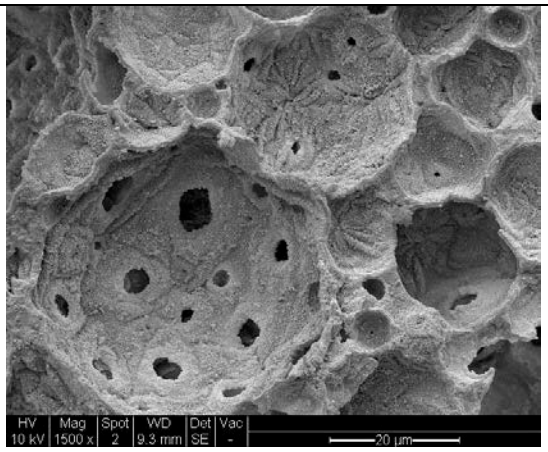

(b) S35, 1500X

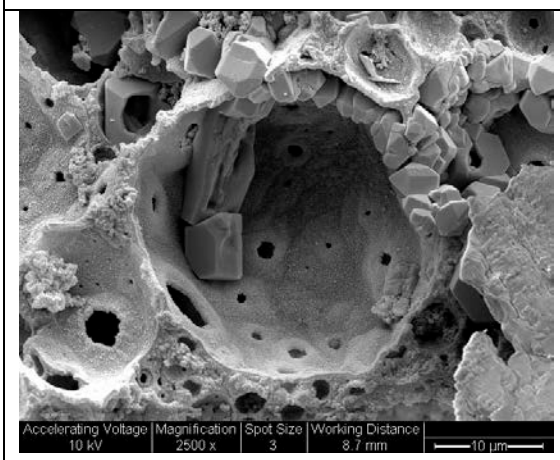

(c) S40, 2500X

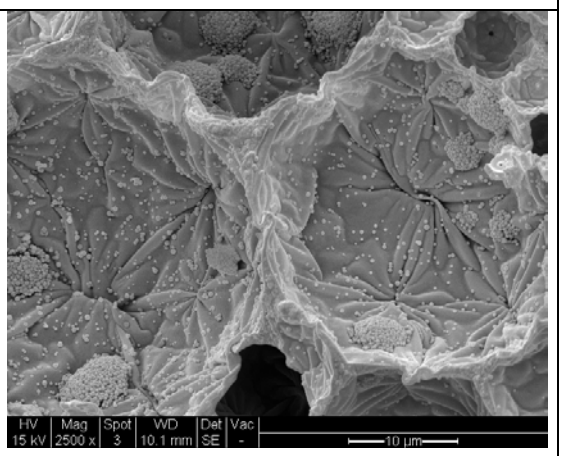

(d) S10M, 2500X

Figure 4.21: More images of VTMS PHP at high magnification.

Further magnification of the image at as high as 50000 magnifications, as shown in Figure 4.22 and Figure 4.23, shows that the surface contains agglomerated particles. Strand form or banana-like structure could be observed for all the seven images of VTMS PHP. It looks like the strands are formed from the fusion of spherical particles. Comparing all the VTMS PHPs to the basic PHP (Figure 4.23(c)) at this high magnification shows that the banana-strand is less apparent for basic polymer, S01 (0% silane). Thus, the novel morphology of banana-like strands with coral-like pore was produced due to functionalising of VTMS to the HIPE through VTMS incorporation in the oil phase and by using aqueous phase initiator.

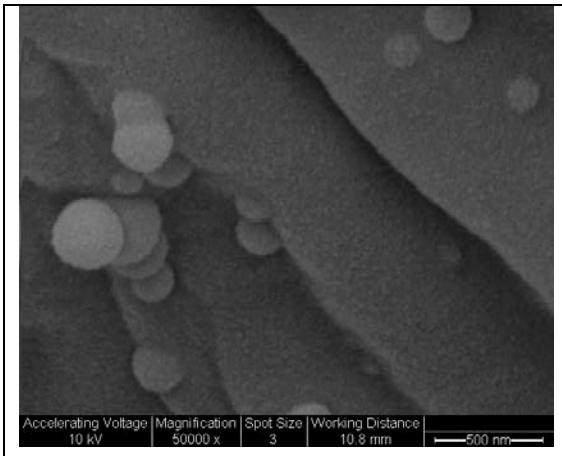

(a) S5, 50000X

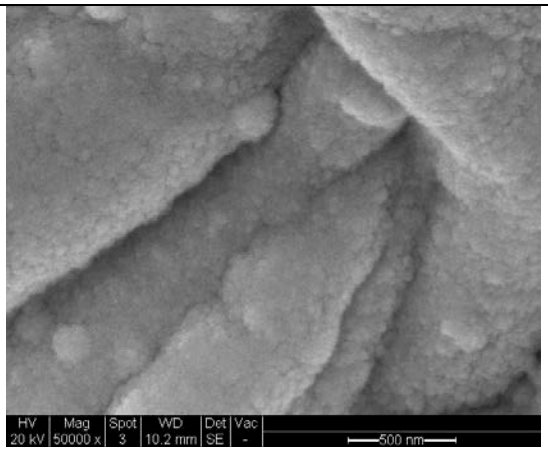

(b) S10, 50000X

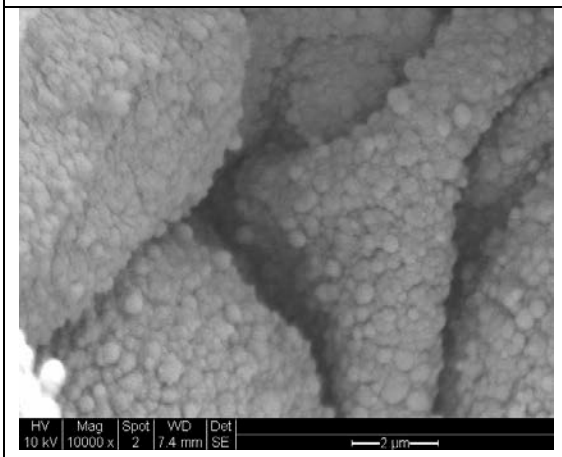

(c) S15, 10000X

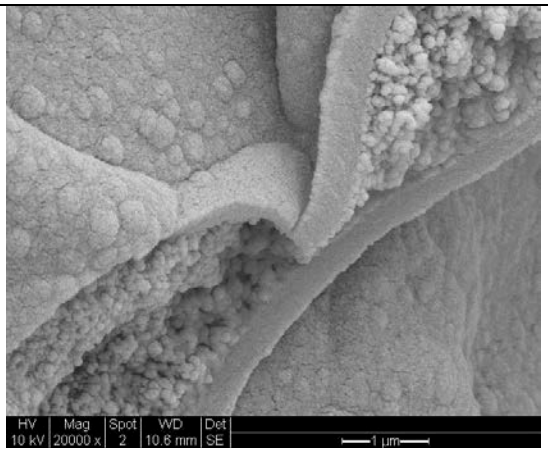

(d) S25, 20000X

Figure 4.22: Images of surfaces of various percentages of VTMS PHP at high magnification. (a) 5% VTMS. (b) 10% VTMS. (c) 15% VTMS. (d) 25% VTMS.

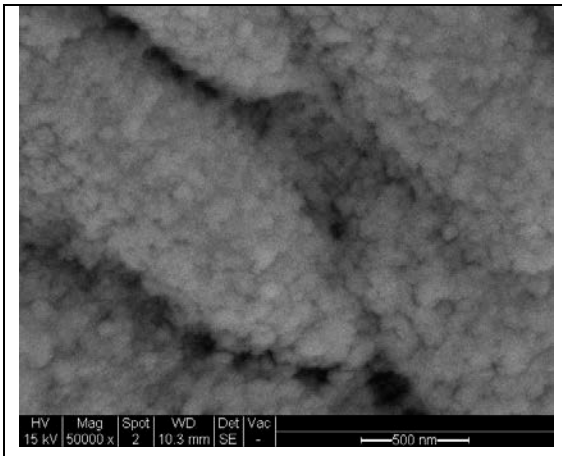

(a) S30, 50000X

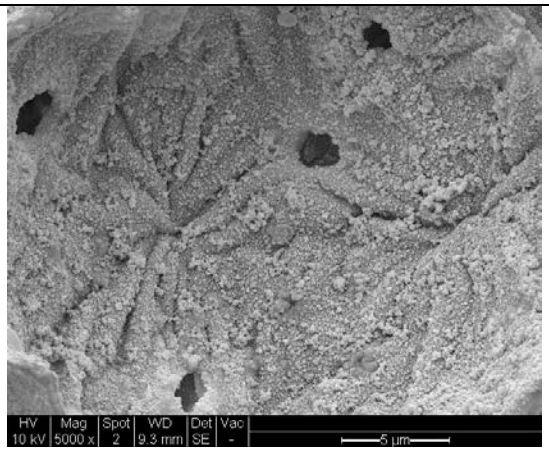

(b) S35, 5000X

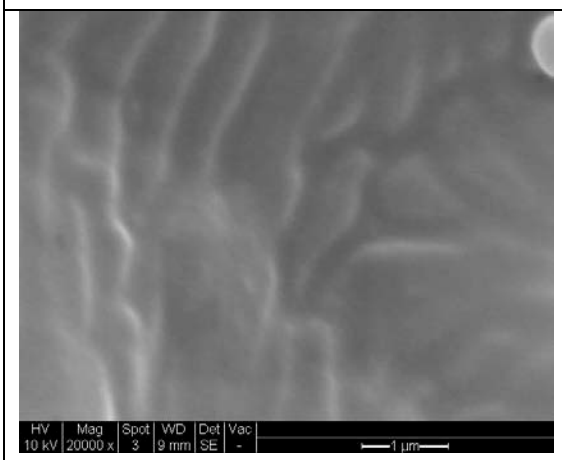

(c) S01, 20000X

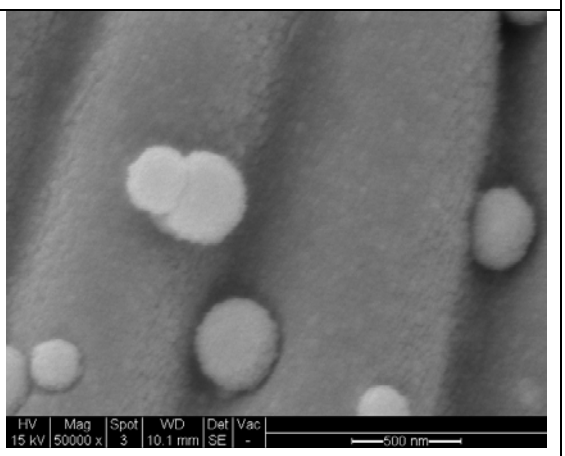

(d) S10M, 50000X

Figure 4.23: More images of surfaces of various percentages of VTMS PHP at high magnification. (a) 30% VTMS. (b) 35% VTMS. (c) Basic PHP: 0% VTMS. (d) 10% VTMS, Both initiators, aqueous and oil phase initiators are used.

In order to identify the elements in the sample, EDX (Energy Dispersive Analysis with X-Rays) was done on S5, the sample with the lowest percentage of VTMS, 5%. The result is presented in Figure 4.25 through Figure 4.28 based on the image in Figure 4.24. There is a presence of silica in the sample, confirming the incorporation of VTMS in the VTMS PHP.

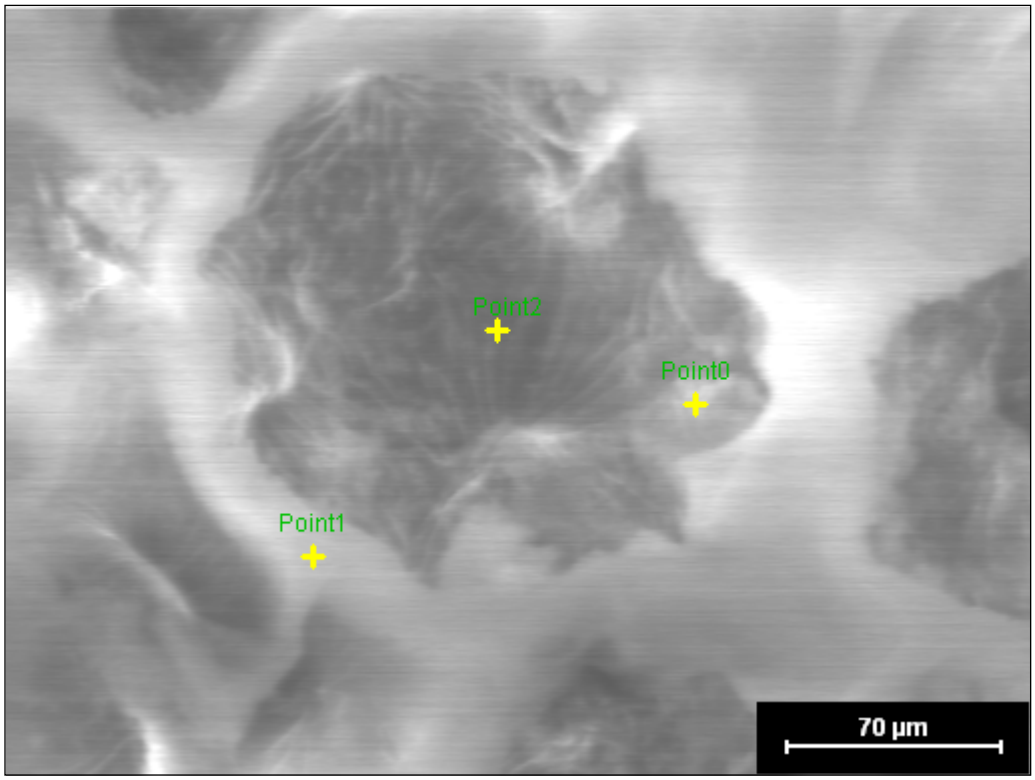

Figure 4.24: The image that corresponds to the EDX (S5).

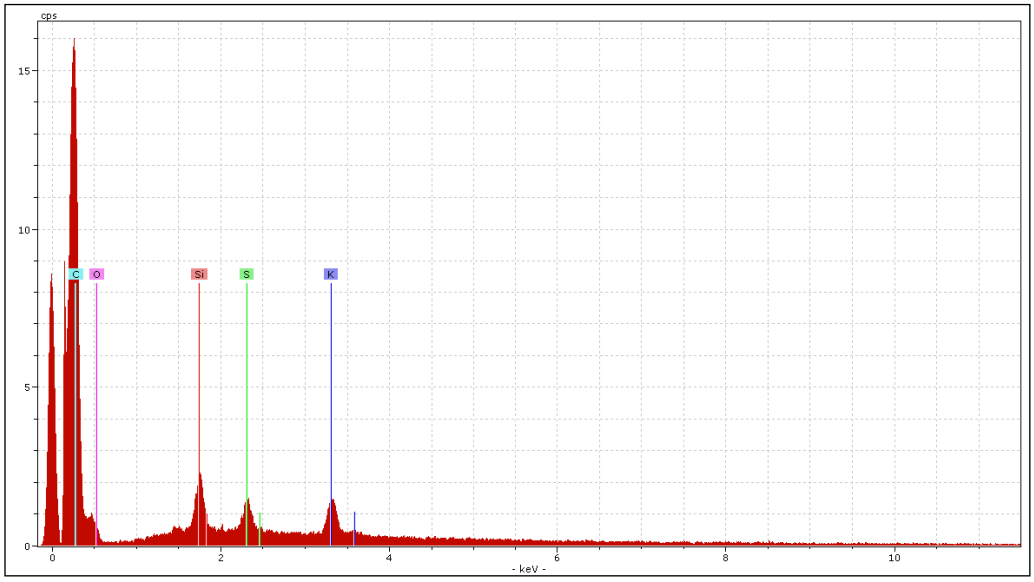

Figure 4.25: The whole area of image in Figure 4.24.

Table 4.6: EDX analysis for the whole area of the image.

Element	weight %	atomic %
Silicon	1.15	0.50
Potassium	0.93	0.29
Sulfur	0.65	0.25
Carbon	97.26	98.96

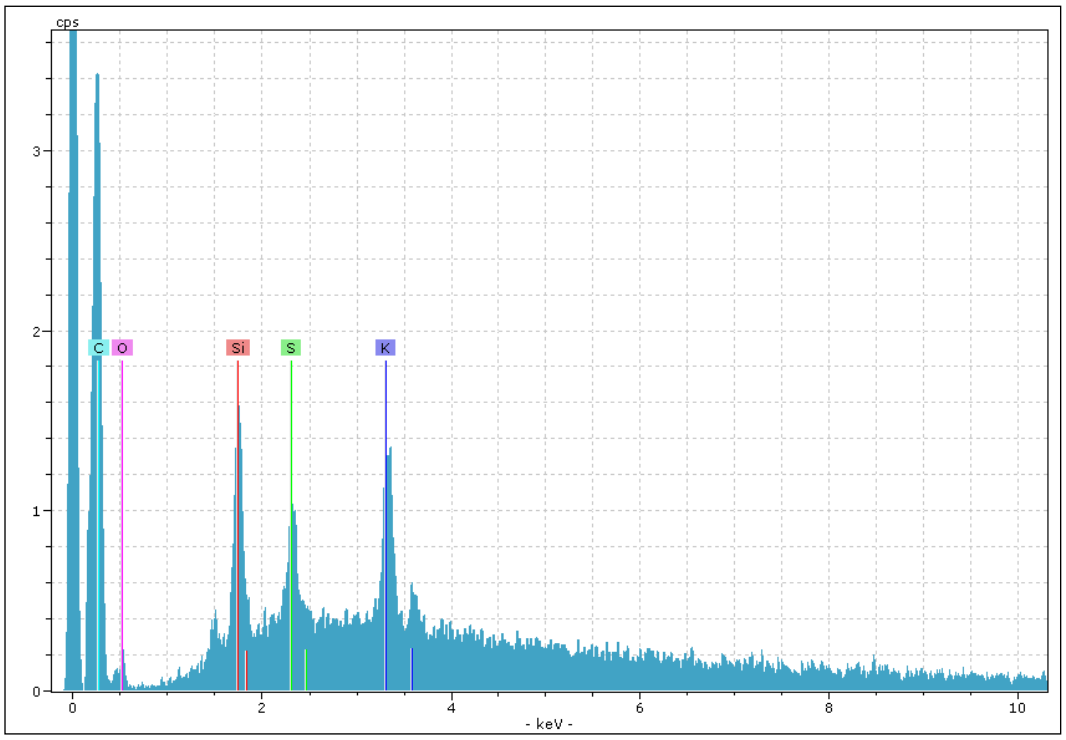

Figure 4.26: The EDX analysis for point 0, in the pore next to the wall (S5)

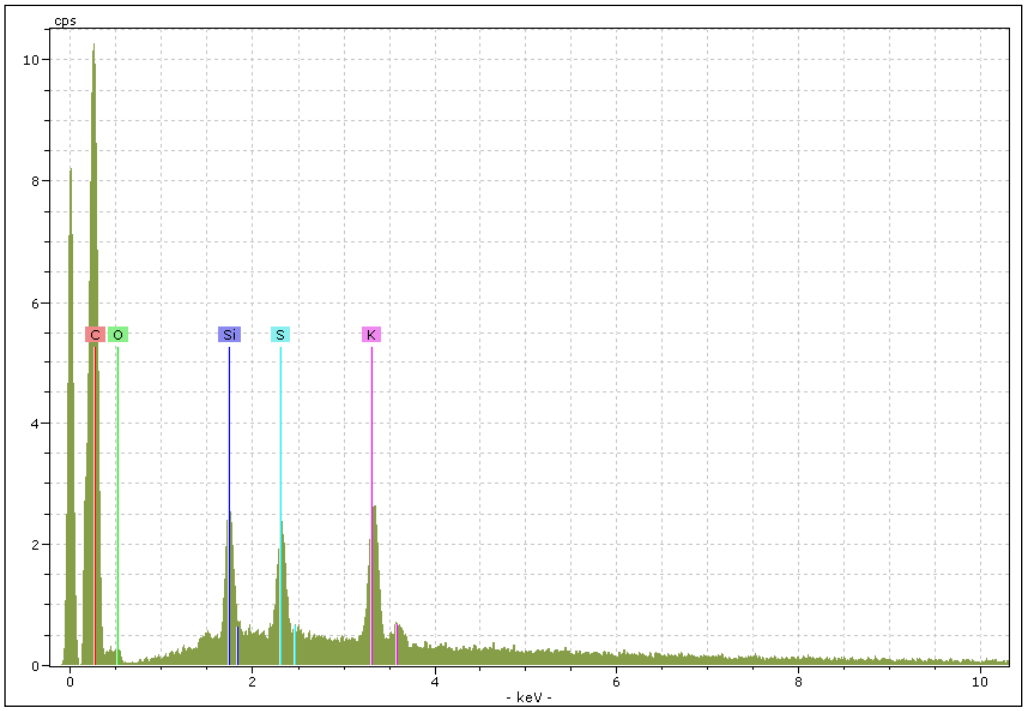

Figure 4.27: The EDX analysis for point 1, on the wall in between the pore (S5).

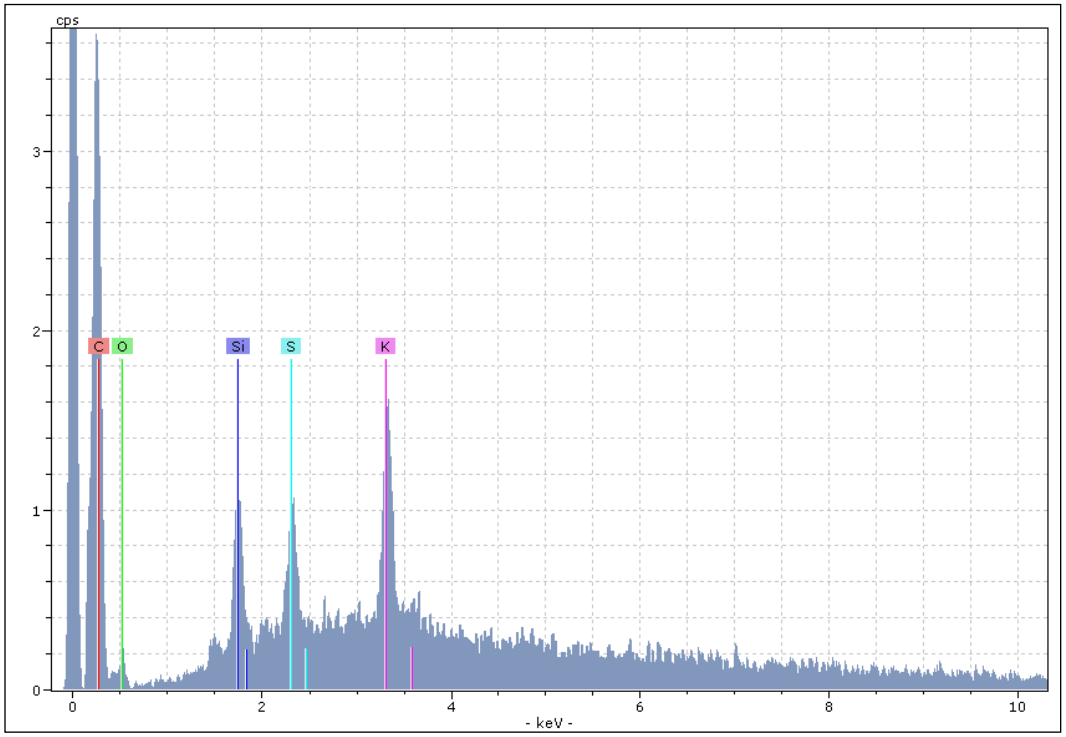

Figure 4.28: The EDX analysis for point 2, in the middle of the pore (S5).

Table 4.7: EDX analysis for 3 different points

	Point 0		Point 1		Point 2	
Element	weight %	atomic %	weight %	atomic %	weight %	atomic %
Silicon	32.32	37.89	23.88	28.72	25.61	30.79
Potassium	39.96	33.65	47.10	40.70	48.04	41.48
Sulfur	27.72	28.46	29.02	30.58	26.34	27.73

Table 4.7 indicates that there is silica in the pore and on the wall, i.e. in between the pores. The percentages of silica on the different sites of the pore itself and between the pore and the wall are different.

4.4.2 Effect of initiator – comparison to oil phase initiator.

The difference in the structure of 5% VTMS PHP produced with aqueous phase initiator and oil phase initiator is presented in Figure 4.29. The PHP produced with oil phase initiator still retains the typical PHP structure. Hence, the novel structure of PHP is contributed by aqueous phase initiator used in the making of VTMS PHP. Moreover, the VTMS PHP with aqueous phase initiator has more monodisperse and smaller pores compared to VTMS PHP produced with oil phase initiator. This is in agreement with the results produced by Williams et al. (1990). Thus, the VTMS emulsion with aqueous phase initiator is more stable than the one with oil phase initiator. This is further verified by the failure to produce higher percentage of VTMS PHP using oil phase initiator as discussed in the following paragraph.

There were attempts to produce VTMS PHP with 10% VTMS using oil phase initiator but there was no emulsion produced. Hence, further trial with higher percentage of VTMS was not done.

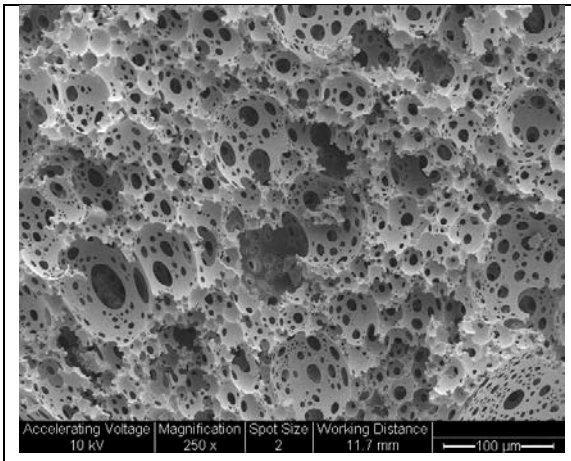

(a) S5-oil phase initiator, 250X.

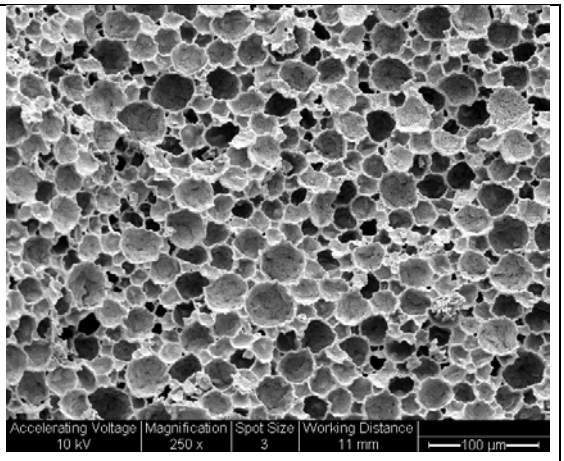

(b) S5- aqueous phase initiator, 250X.

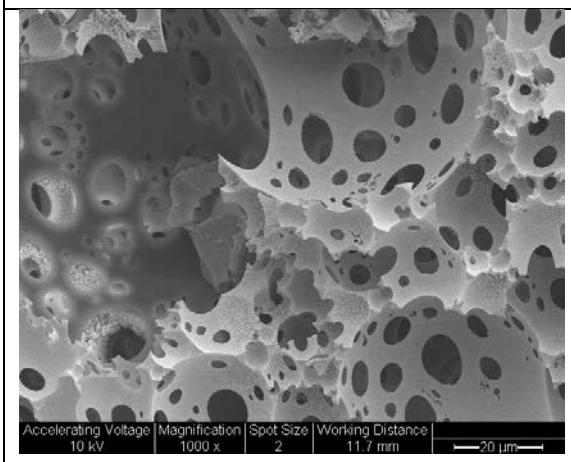

(c) S5-oil phase initiator, 1000X.

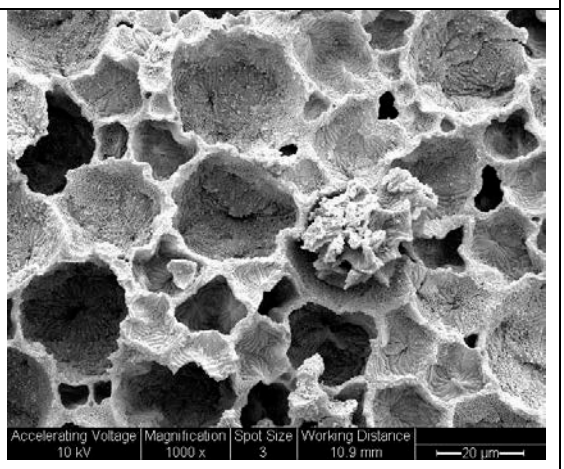

(d) S5- aqueous phase initiator, 1000X.

Figure 4.29: Images of silane PHP, aqueous phase initiator vs. oil phase initiator. Both are produced using 5% VTMS.

4.4.3 Effect on surface area and pore size distribution.

Study on the surface area and pore size distribution was done by analysing physisorption process of nitrogen as the adsorbate at liquid nitrogen temperature, 77K. Checking for reproducibility of the results was done as many as five runs depending on the standard errors.

4.4.3.1 Isotherm

The isotherms for silane (VTMS) PHP is as shown in Figure 4.30 to Figure 4.37. In summary, the initial part of the isotherm follows Type II isotherm, which corresponds to monolayer-multilayer adsorption. All samples exhibit irreversible isotherm since hysteresis was observed for all the samples, indicating the capillary condensation in mesopore structure as in type IV isotherm in the IUPAC classification (Sing et al., 1985; Gregg and Sing, 1982). Capillary condensation is said to occur when the adsorptive vapours condensed in the pores of the adsorbent/PHP at pressures less than the pressure of saturated vapour over the plane surface. Due to this vapour deposition, liquid layers formed on the capillary walls and merged to form menisci in capillaries. Porous solids often exhibit adsorption hysteresis; this indicates the mechanism of desorption is different to that of adsorption. All the isotherms exhibit stages of physisorption process in mesopores, which is monolayer-multilayer adsorption and capillary condensation. However, there is no limiting uptake observed for higher range of Ps/Po. The isotherm rises rapidly and exhibits vertical rise near Ps/Po=1, this indicates the presence of macropores and they are wide. The evidence for the presence of macropores in the samples is as discussed in section 4.4.3.3.

The hystereses looks like type H3 hysteresis which is often associated as aggregates of plate-like particles giving rise to slit-shaped pores (Sing et al., 1985). The higher the percentage of VTMS is, the narrower the hysteresis. S5 isotherm exhibits the widest hysteresis while the S40 isotherm exhibits the narrowest hysteresis amongst all the isotherms for VTMS PHPs. However, the hysteresis for S30 is wider than those for S15 and S20. This might be due to the more monodisperse pore of S30 as shown in section 4.4.1, which contributes to more mesopore distribution rather than macropore. The hysteresis is almost lost for S40 sample. This indicates the presence of more macropores than mesopores (Sing et al., 1985). This is discussed further in section 4.4.3.3. The comparisons of the isotherms are presented in Figure 4.38 to Figure 4.40.

Since all the isotherms appear to be Type H3 hysteresis loop, desorption branch is likely to yield a reliable estimate of pore size distribution due to the uncertainties inherent in the application of the Kelvin equation and the complexity of most pore

system (Sing et al., 1985). Nevertheless, the result for desorption branch is still presented and discussed in this thesis.

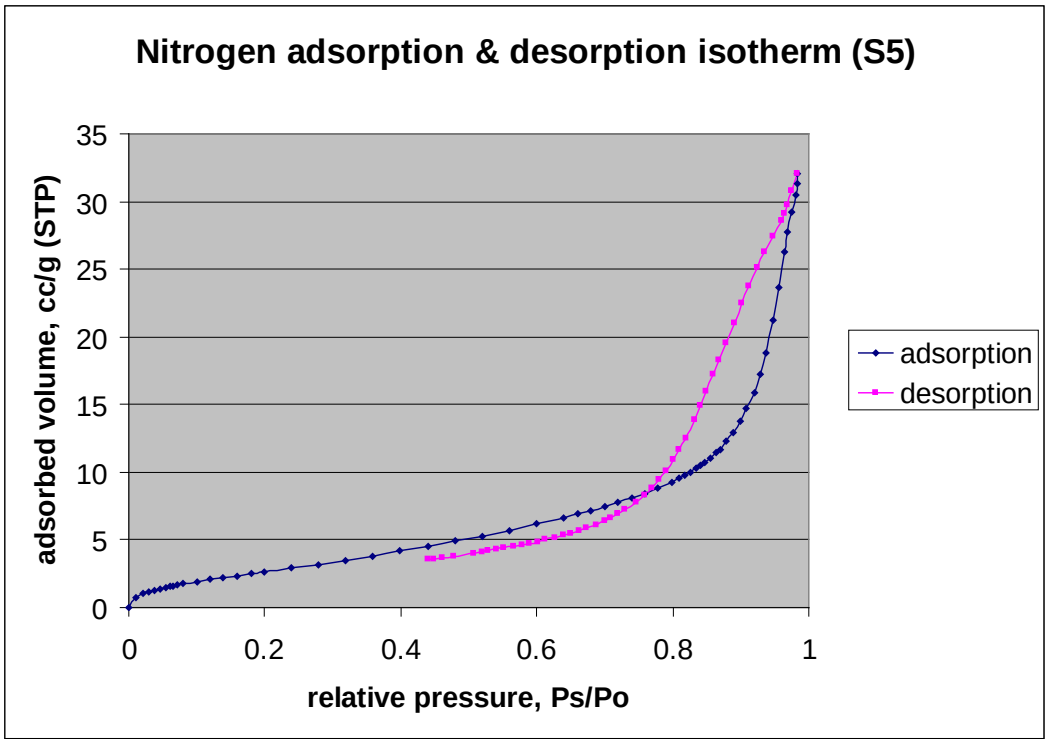

Figure 4.30: Isotherm plot for surface area and pore size analysis of 5% vinyl trimethoxy silane PHP.

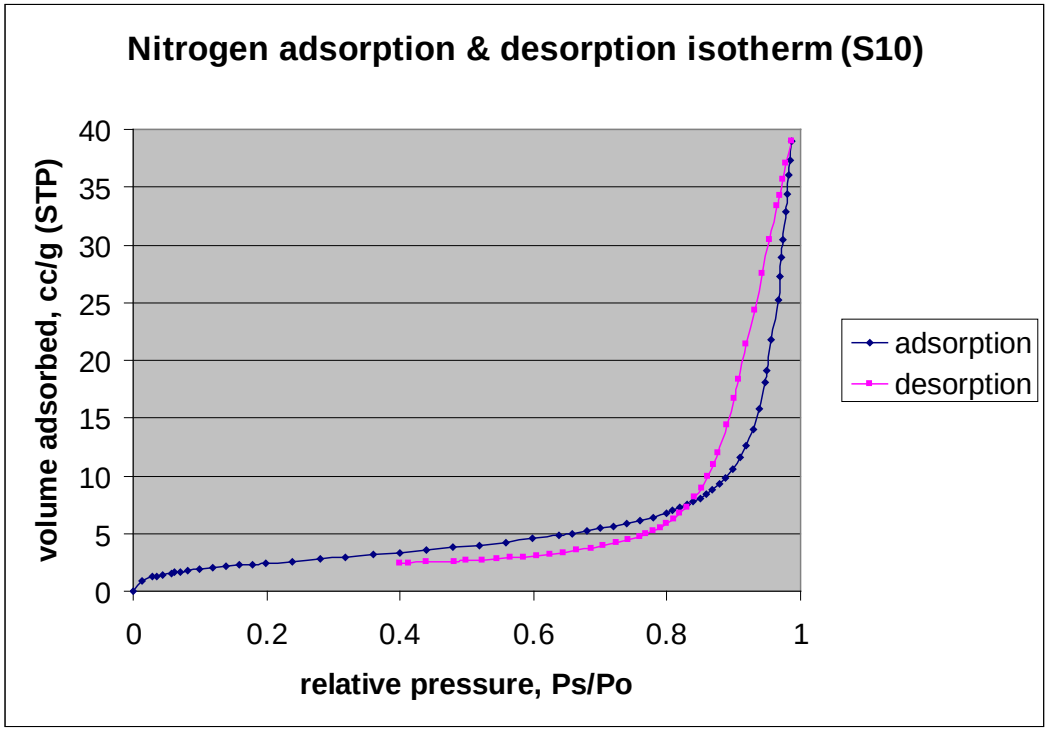

Figure 4.31: Isotherm plot for surface area and pore size analysis of 10% vinyl trimethoxy silane PHP.

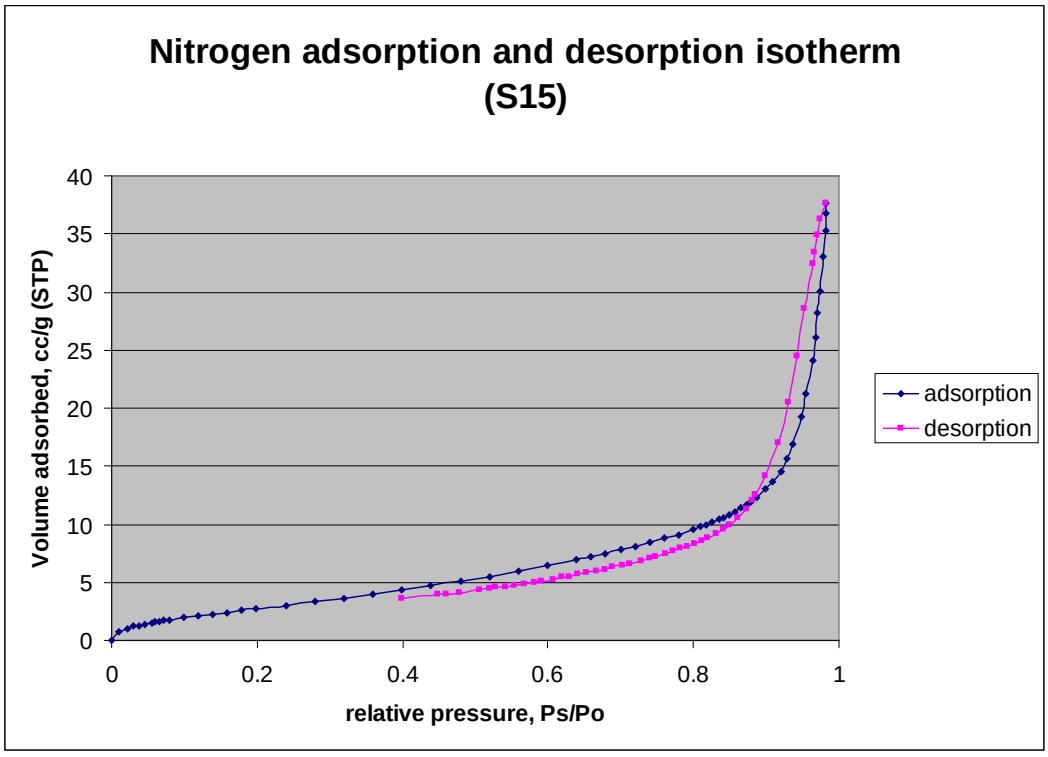

Figure 4.32: Isotherm plot for surface area and pore size analysis of 15% vinyl trimethoxy silane PHP.

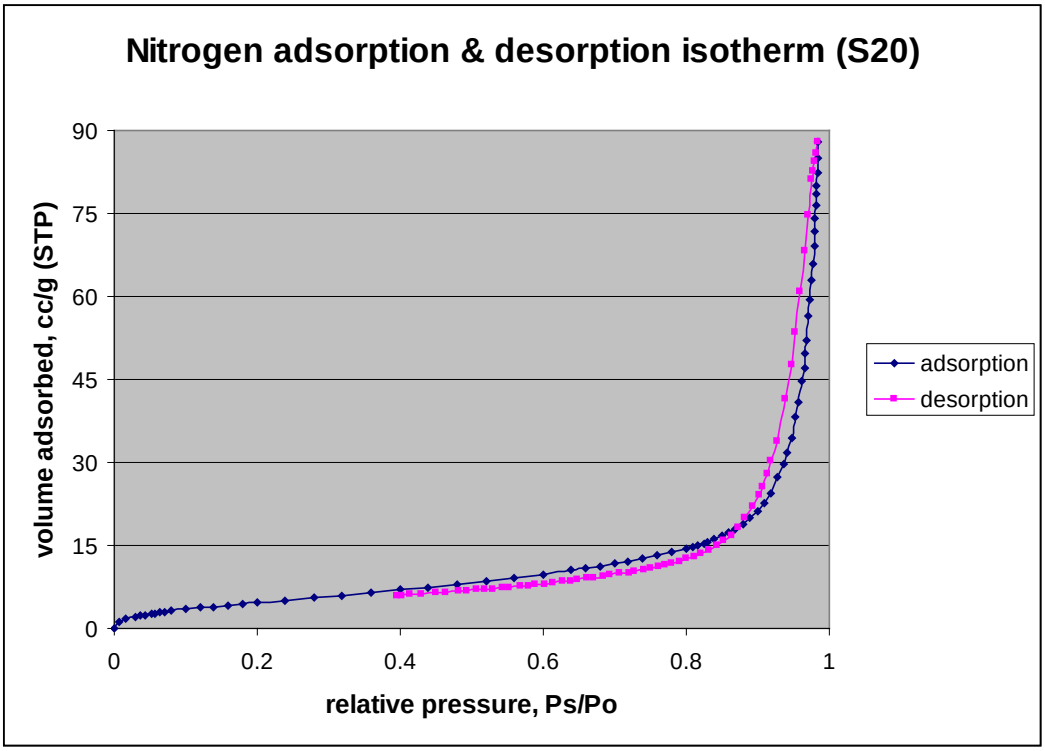

Figure 4.33: Isotherm plot for surface area and pore size analysis of 20% vinyl trimethoxy silane PHP.

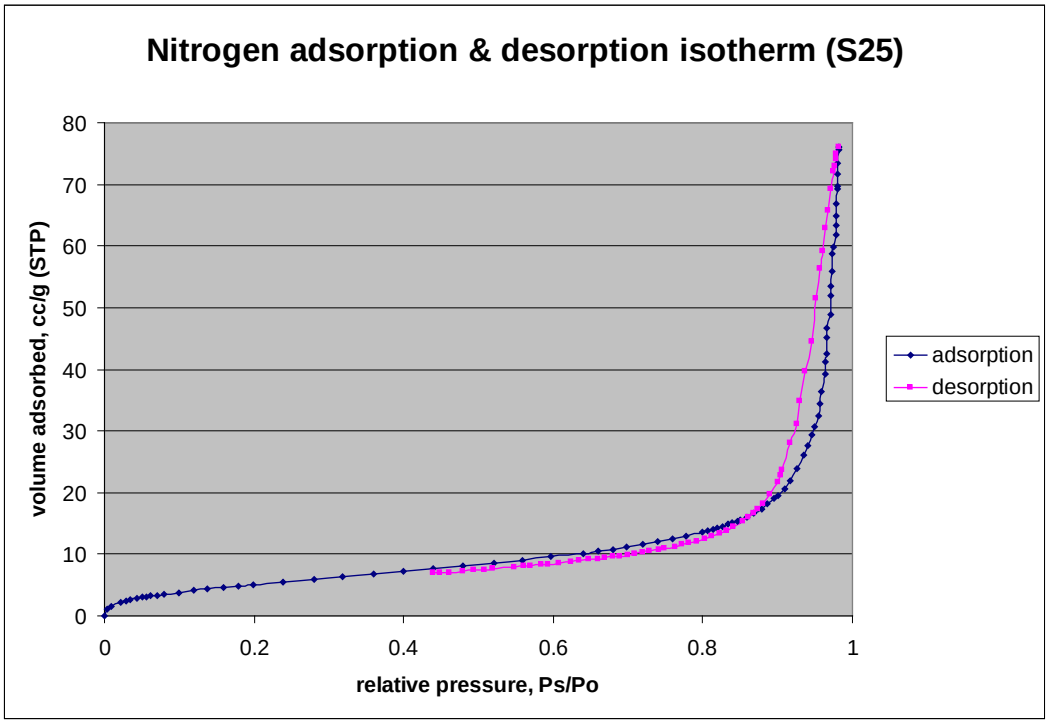

Figure 4.34: Isotherm plot for surface area and pore size analysis of 25% vinyl trimethoxy silane PHP.

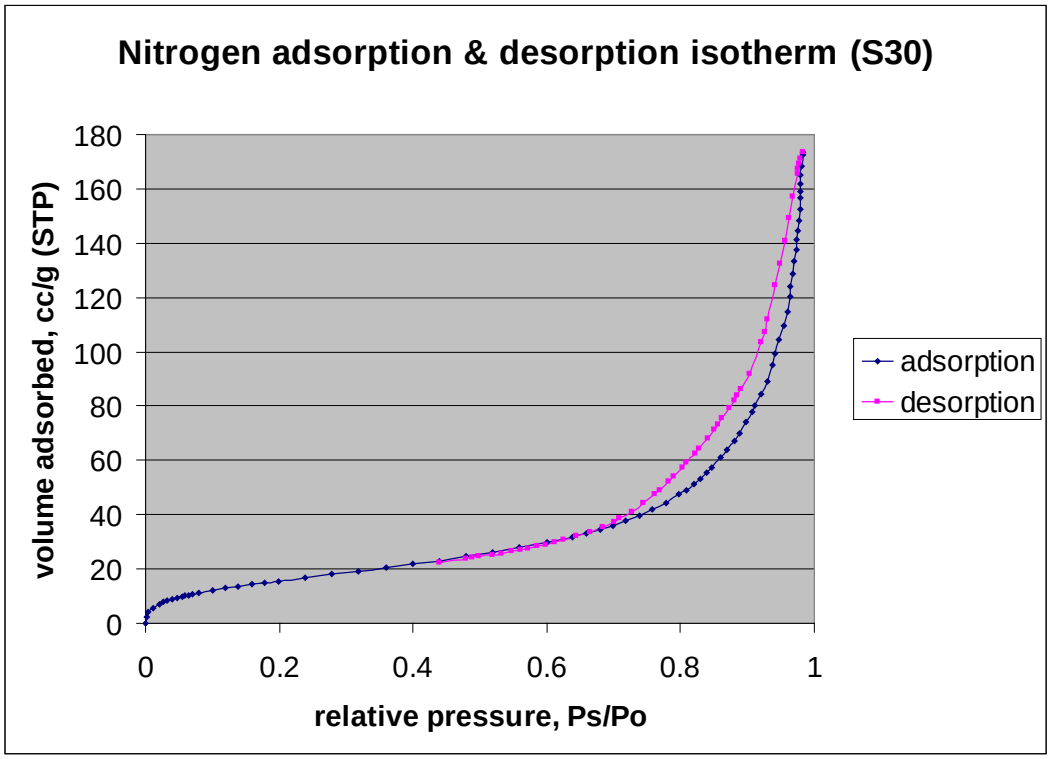

Figure 4.35: Isotherm plot for surface area and pore size analysis of 30% vinyl trimethoxy silane PHP.

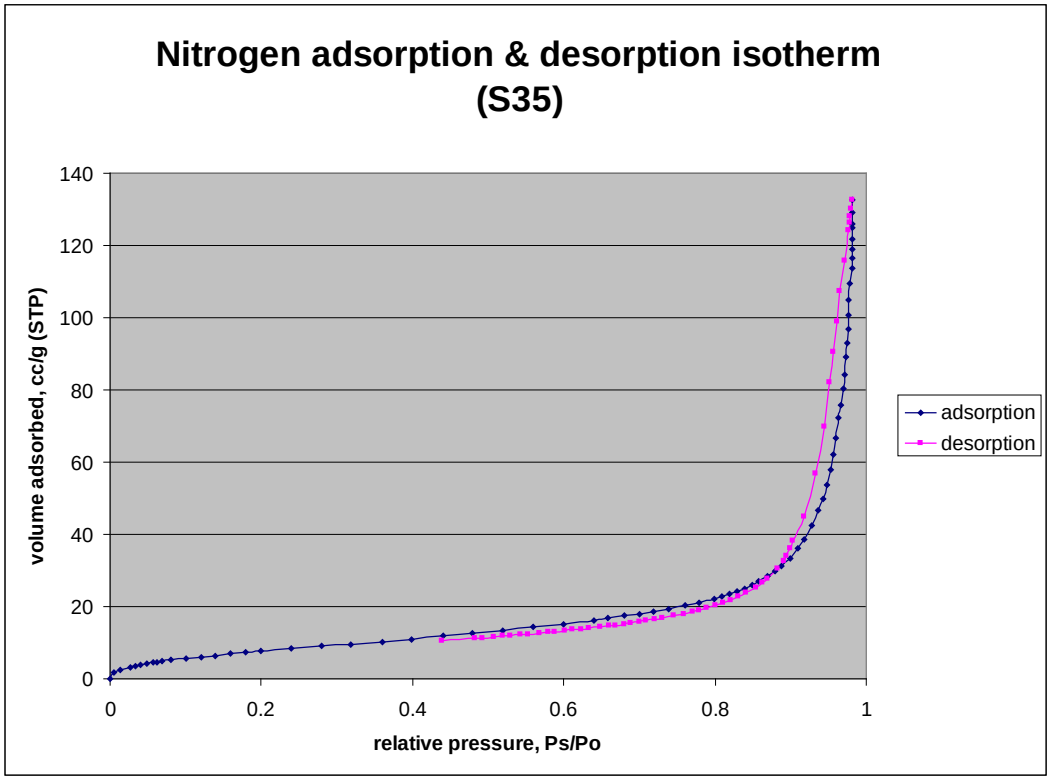

Figure 4.36: Isotherm plot for surface area and pore size analysis of 35% vinyl trimethoxy silane PHP.

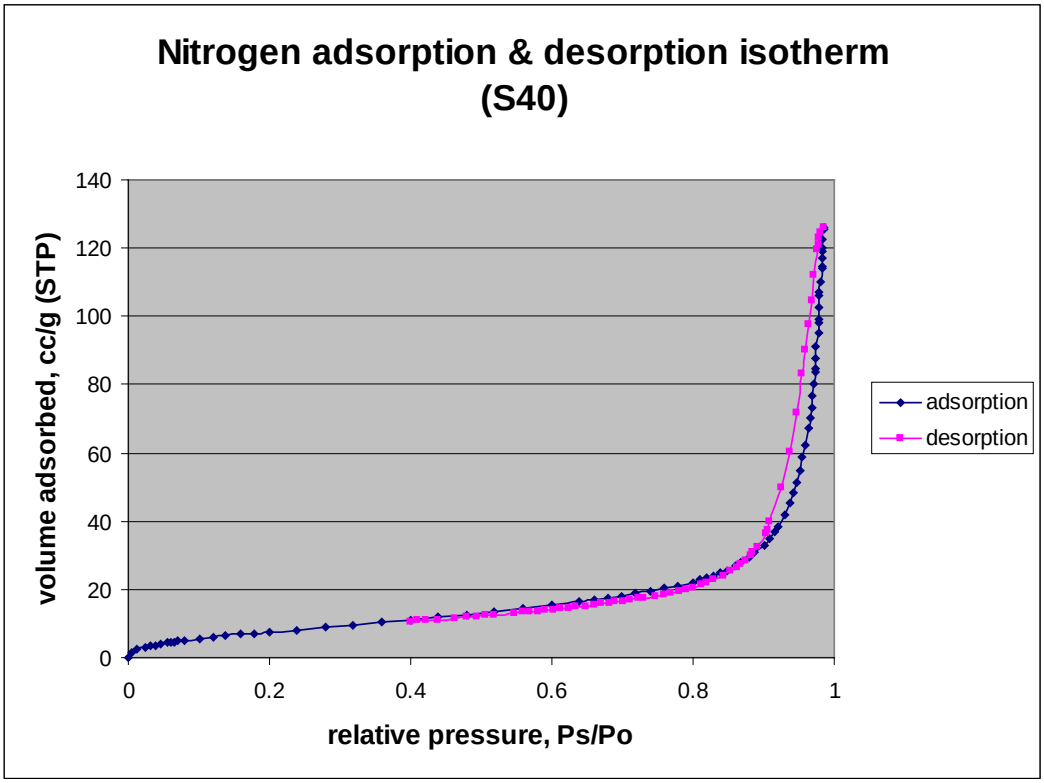

Figure 4.37: Isotherm plot for surface area and pore size analysis of 40% vinyl trimethoxy silane PHP.

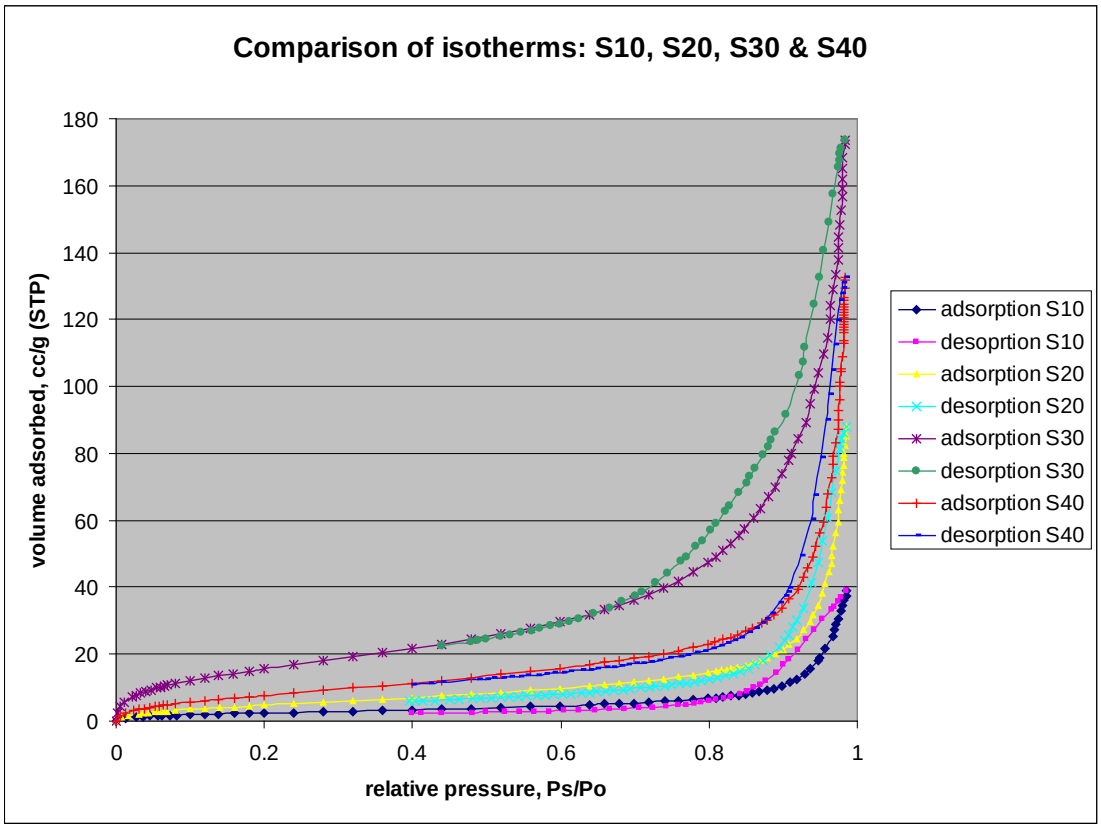

Figure 4.38: Comparison of isotherms, S10, S20, S30 & S40.

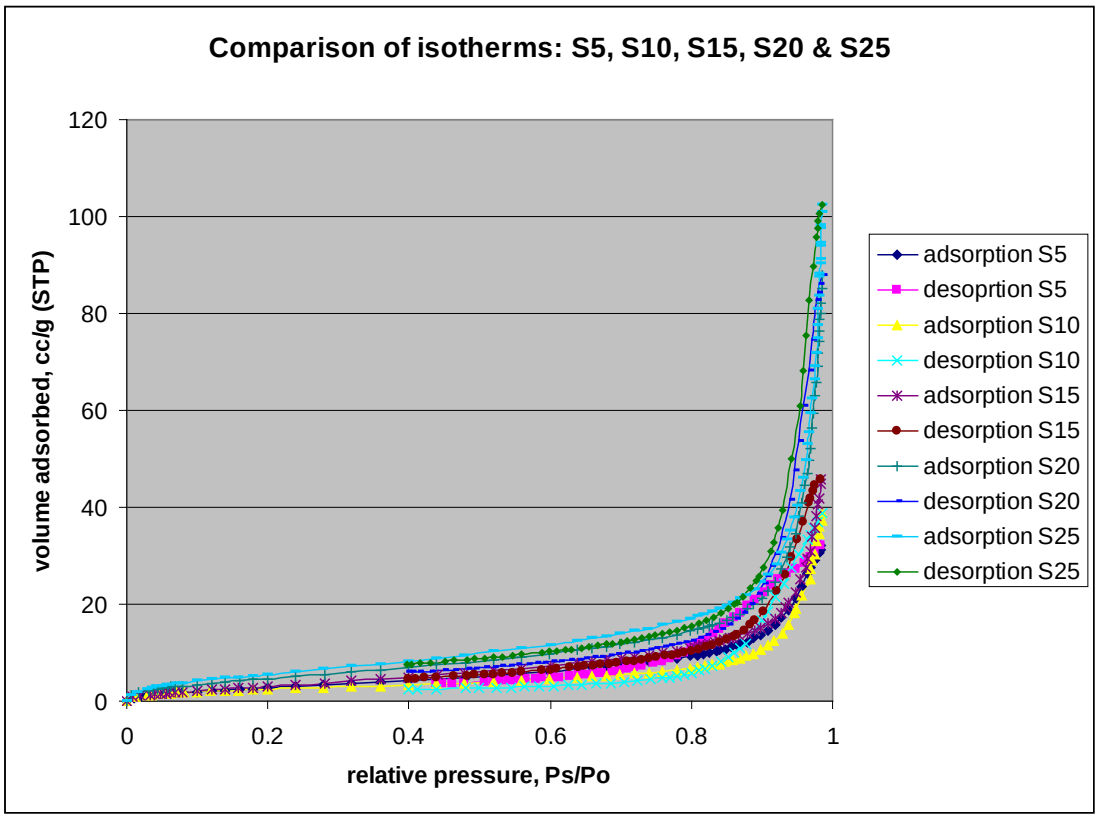

Figure 4.39: Comparison of isotherms, S5, S10, S15, S20 & S25.

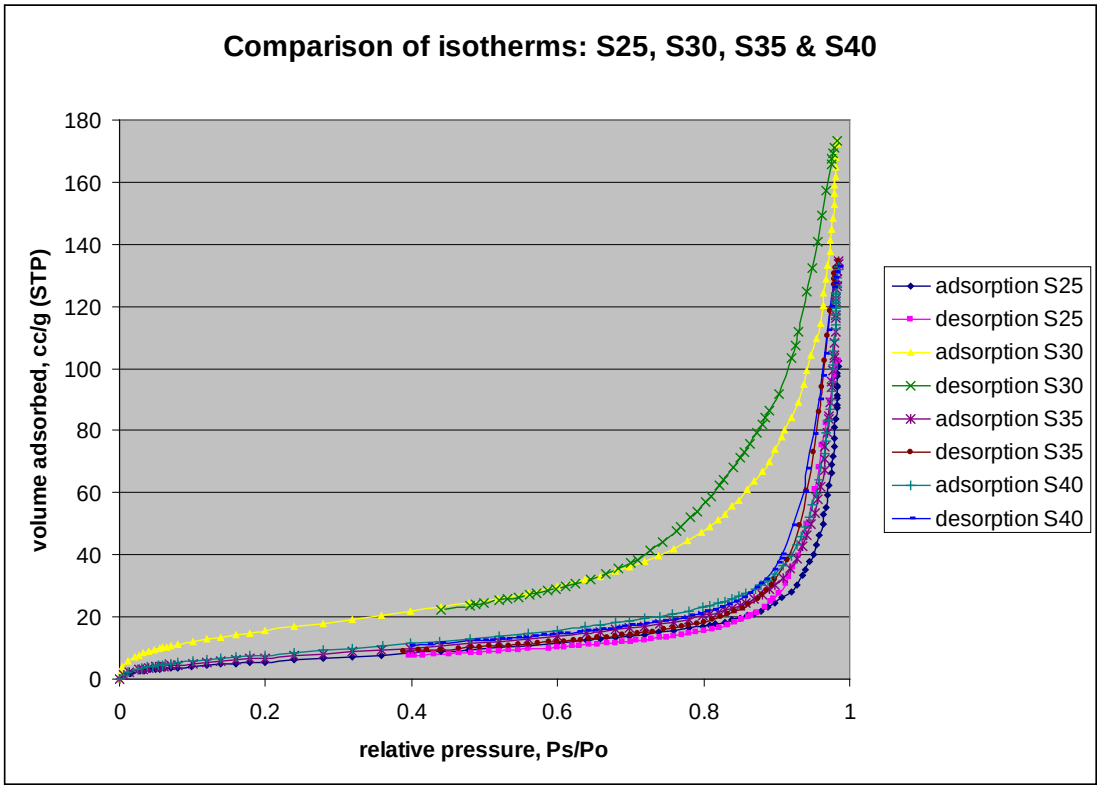

Figure 4.40: Comparison of isotherms, S25, S30, S35 & S40.

The isotherm for S5-O, the 5% VTMS PHP produced using oil phase initiator is presented in Figure 4.41. The comparison of isotherms between the two types of initiators is presented in Figure 4.42. The S5-O isotherm is similar to S5 isotherm, H3 type but with wider hysteresis. The isotherm exhibits stages of physisorption process in mesopores, which is monolayer-multilayer adsorption and capillary condensation. The wider hysteresis indicates the reduction in surface roughness (Northcott et al., 2007).

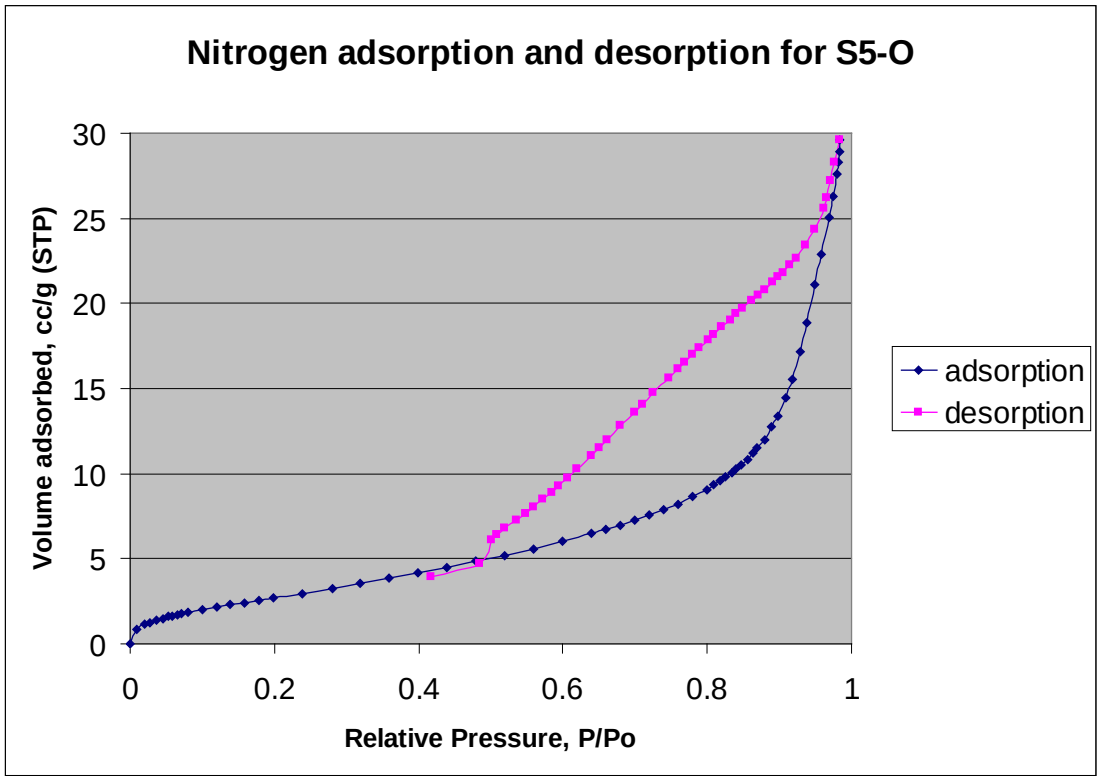

Figure 4.41: Isotherm plot for 5% vinyl trimethoxy silane PHP produced using oil phase initiator.

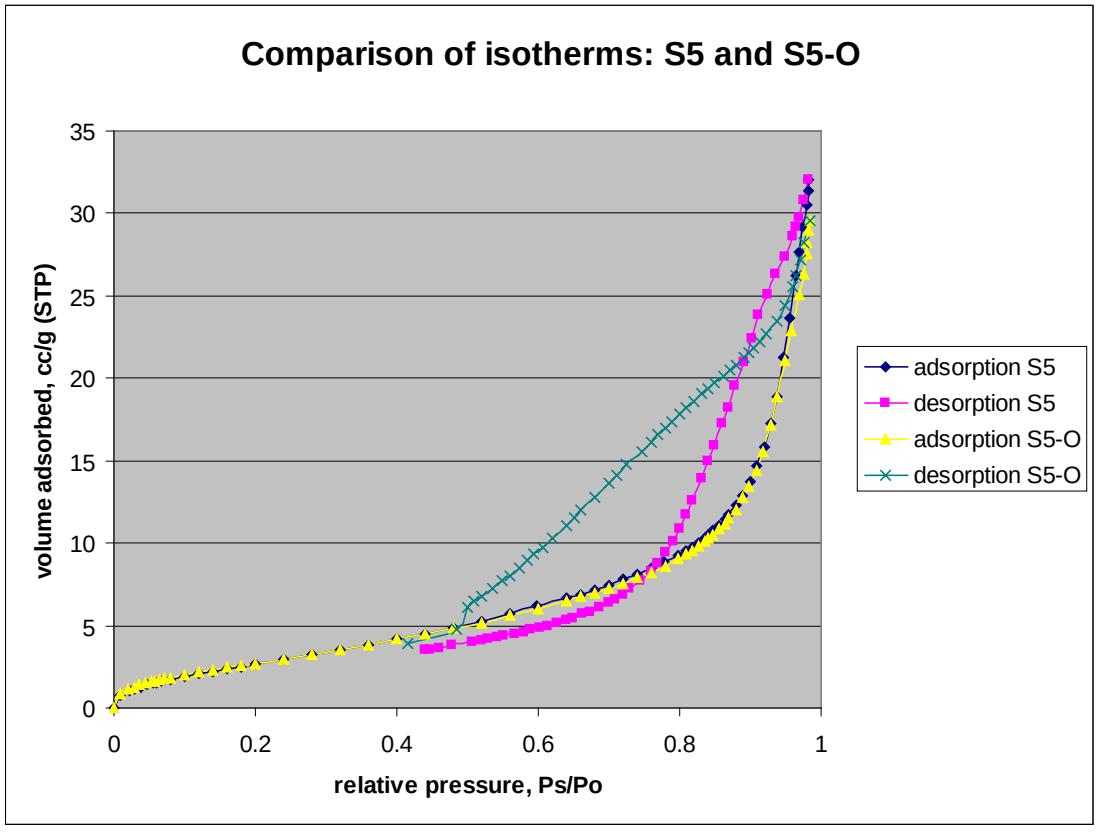

Figure 4.42: Comparison of isotherms, different type of initiators.

4.4.3.2 Surface area.

The surface area for various percentages of VTMS PHP and comparison to basic PHP is presented in Table 4.8 and Figure 4.43. Generally, it has been observed that the surface area of the PHP does not increase significantly with the increase in VTMS percentage except for S30 sample.

Table 4.8: Surface area of silane PHP

Sample name	Percentage silane, %	Surface area, m^2/g
S0	0	14.90
S5	5	8.58
S10	10	9.99
S15	15	11.02
S20	20	15.97
S25	25	18.02
S30	30	55.48
S35	35	27.51
S40	40	22.58

As shown in Table 4.8 and Figure 4.43, S30 has the highest surface area compared to the other silane PHPs. This result is consistent with the structure of the image shown previously in section 4.4.1, S30 is the most stable PHP with the most monodispersed pores amongst all VTMS PHPs. From the SEM image of S40 PHP, which is not stable with lots of coalescent pores, the low value of surface area is expected even though it has the highest VTMS percentage.

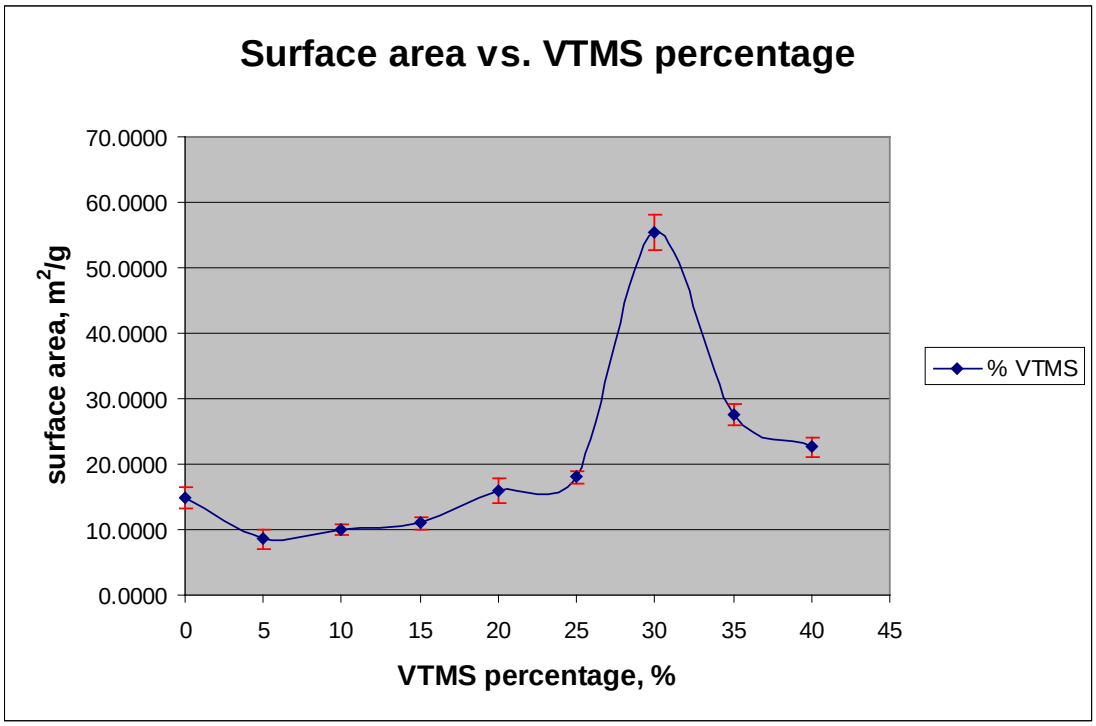

Figure 4.43: Plot of surface area for different percentages of vinyl trimethoxy silane PHPs with standard errors.

The standard errors observed in Figure 4.43 are small and acceptable. It was observed that S30 (30% VTMS) surface area is significantly different from all the other samples. The surface areas for S5, S10 and S15 do not differ significantly from one another due to overlapping error bars. The same conclusion can be made for S20 and S25. Comparing S30, S35 and S40, it has been observed that the surface areas differ significantly between one another due to non-overlapping error bars. The group of S5, S10 and S15 and another group of S20 and S25 differ from one another. These two groups also differ from S30, S35 and S40. The comparison is further elaborated by statistical analysis in the following paragraph.

Analysis of Variance (ANOVA) was performed to see how significant the differences are. At 5% significance level, it can be concluded that there are significant differences between the surface areas of the PHPs produced at several different percentages of VTMS. The differences are further analysed by Bonferroni test at 95.0% confidence intervals. The pairs that are different are S0 & S30, S0 & S35, S5 & S25, S5 & S30, S5 & S35, S5 & S40, S10 & S30, S10 & S35, S10 & S40, S15 & S30, S15 & S35, S15 & S40, S20 & S30, S20 & S35, S25 & S30, S25 & S35, S30 & S35, and S30 & S40. In summary, S30 differs significantly with all the other samples,

and only S30 and S35 differ significantly with basic PHP. The details of the model, hypothesis, significance level used and the results of this statistical analysis are presented in Appendix 1.

4.4.3.2.1 Effect of initiator on surface area

The results for surface area of VTMS PHPs with different phase initiators are presented in Table 4.9 and Figure 4.44. Further experiment on oil phase initiator using higher percentage of VTMS PHP was not carried out since several trials for 10 % VTMS result in failure.

Table 4.9: Suface area of 5% VTMS PHP, different phase initiators.

Sample name	initiator	Surface area, m^2/g
S5	Aqueous phase	10.00
S5-O	Oil phase	10.77

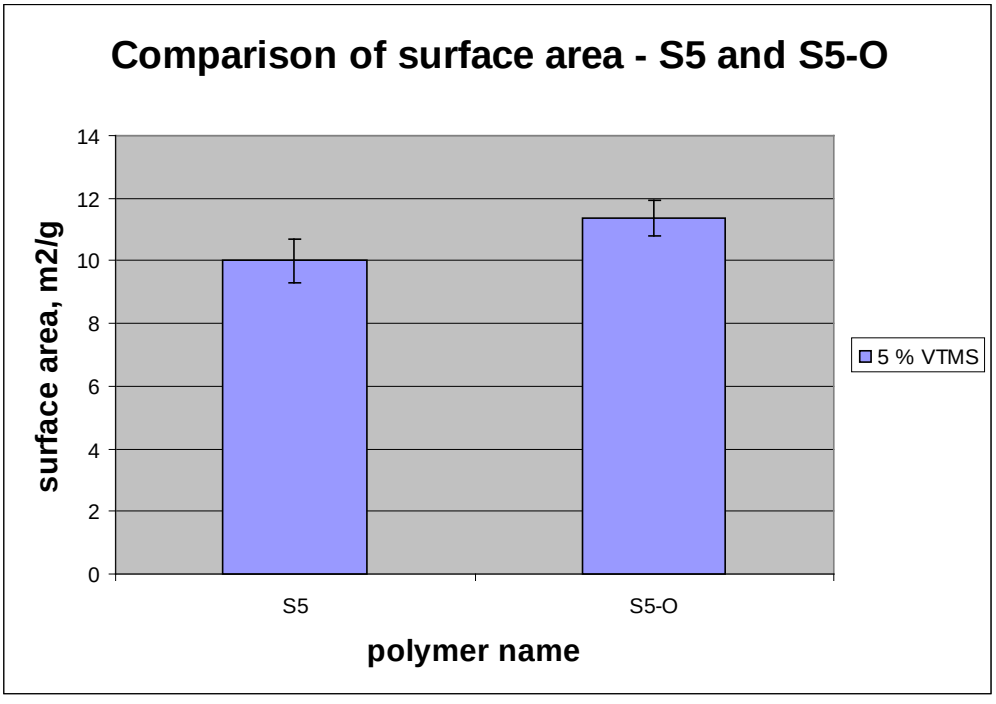

Figure 4.44: Comparison of surface area, aqueous phase initiator vs. oil phase initiator.

Two-sample T-test was performed to see whether the difference between the two means is significant or not. The result concludes that the means are not significantly different; there is no effect of type of initiator used on surface area of VTMS PHP produced at 5% VTMS. Detail of the analysis is presented in Appendix 1.

4.4.3.3 Pore size

The pore size distributions for various percentages of VTMS are presented in Figure 4.45 to Figure 4.52. The figures represent pore volume contribution of each individual pore diameter. In general, the pore size distributions for desorption curves for all VTMS PHPs are centred in the mesopore region. Only S5 has a monomodal pore size distribution centred in the low region of mesopore, 11 nm with a narrow distribution between 3.65 and 25 nm. S30 has bimodal distribution centred at 8 and 25 nm respectively, with a wider distribution between 3.65 and 50nm. The distribution centred at 8 nm exhibited higher differential pore volume compared to the one at 25 nm; this indicates the presence of more pores in the fine mesopore region. This result of S30 is consistent with the monodispersed pore as shown in section 4.4.1. A narrow distribution between 3.65 and 18 nm was also observed for the peak centred at 8 nm. S10 has a monomodal distribution centred at medium region of mesopore, 20 nm, but with wider distribution from 5 nm to 50 nm. S15 exhibits trimodal distribution in a wide distribution of pore size between 3.65 and 50 nm. S20 has a monomodal distribution covering a wide range, between 10 and 87 nm with the peak centred at 27 nm. S25 has a monomodal distribution between 4 and 71 nm with the peak centred at 30 nm. S35 has a big monomodal distribution with two small bimodal distributions in it with peaks of 21 and 30 nm, closed to one another and covering a wide pore size distribution, 3.65 nm to 71 nm. S40 could be described as having a monomodal distribution with the widest range, between 3.65 nm to 80 nm and centred at 30 nm.

There is no significant peak observed for any adsorption curves in the mesopore region. However all of the samples with the exception of S10, exhibits higher differential pore volumes in the region of fine mesopore, between 3.65 nm and 25 nm. S10, S20, S25, S30 and S35 have a monomodal distribution in the macropore region. S40 exhibits bimodal distribution, one in the mesopore region and another one in the macropore region.

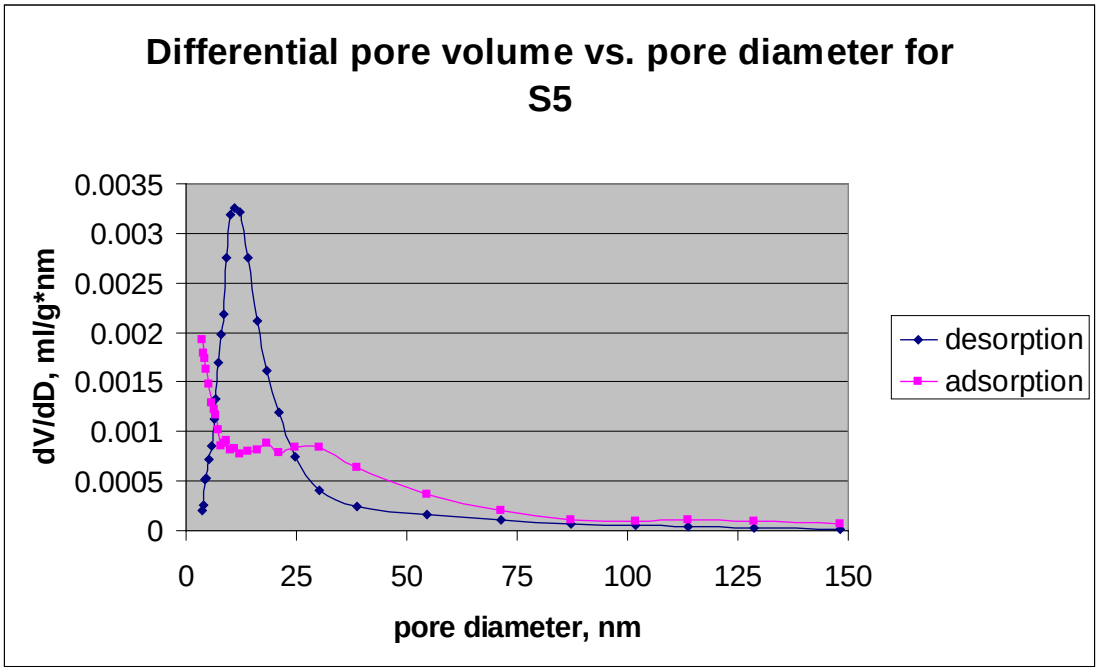

Figure 4.45: Plot of differential pore volume against pore diameter for S5, 5% vinyl trimethoxy silane.

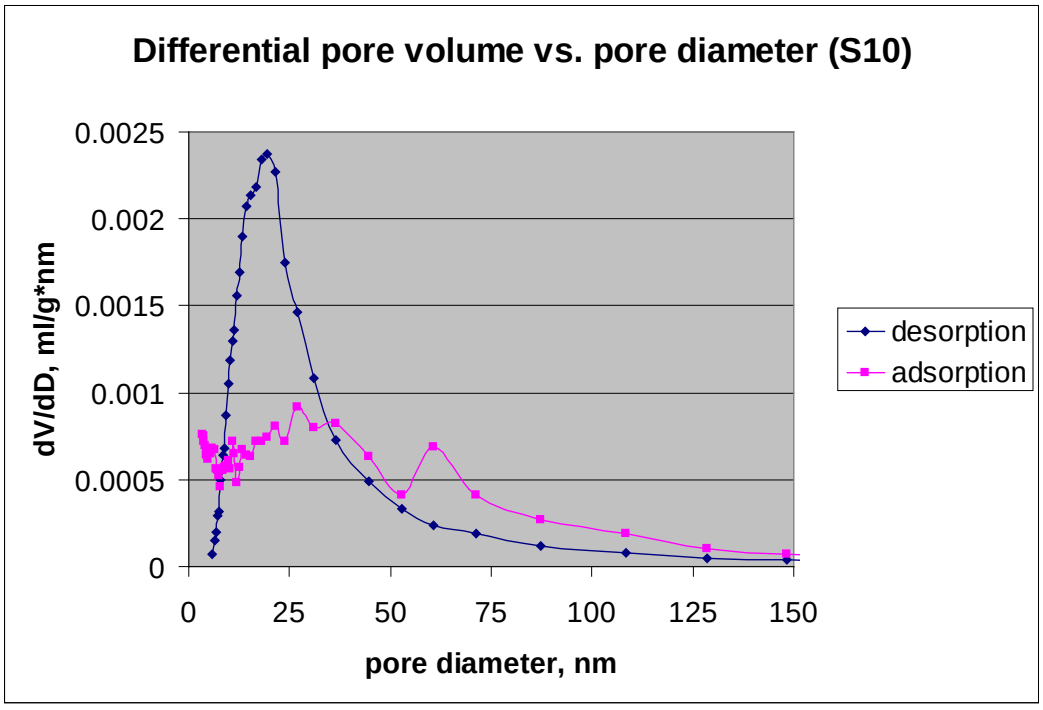

Figure 4.46: Plot of differential pore volume against pore diameter for S10, 10% vinyl trimethoxy silane.

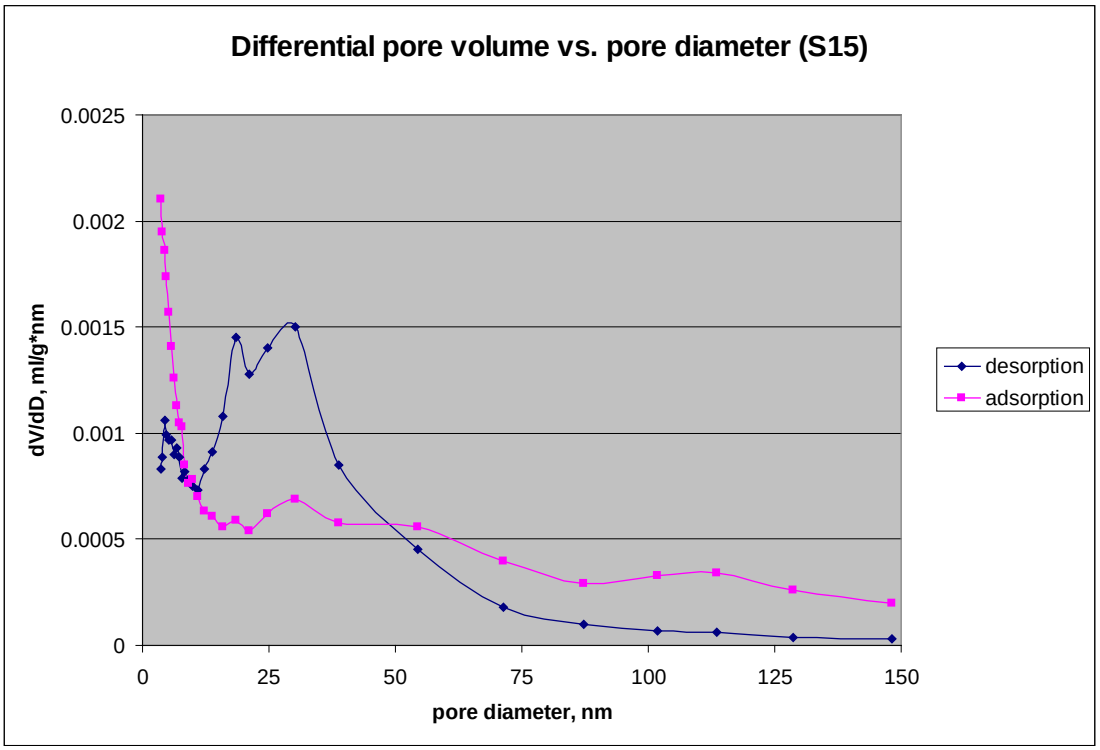

Figure 4.47: Plot of differential pore volume against pore diameter for S15, 15% vinyl trimethoxy silane.

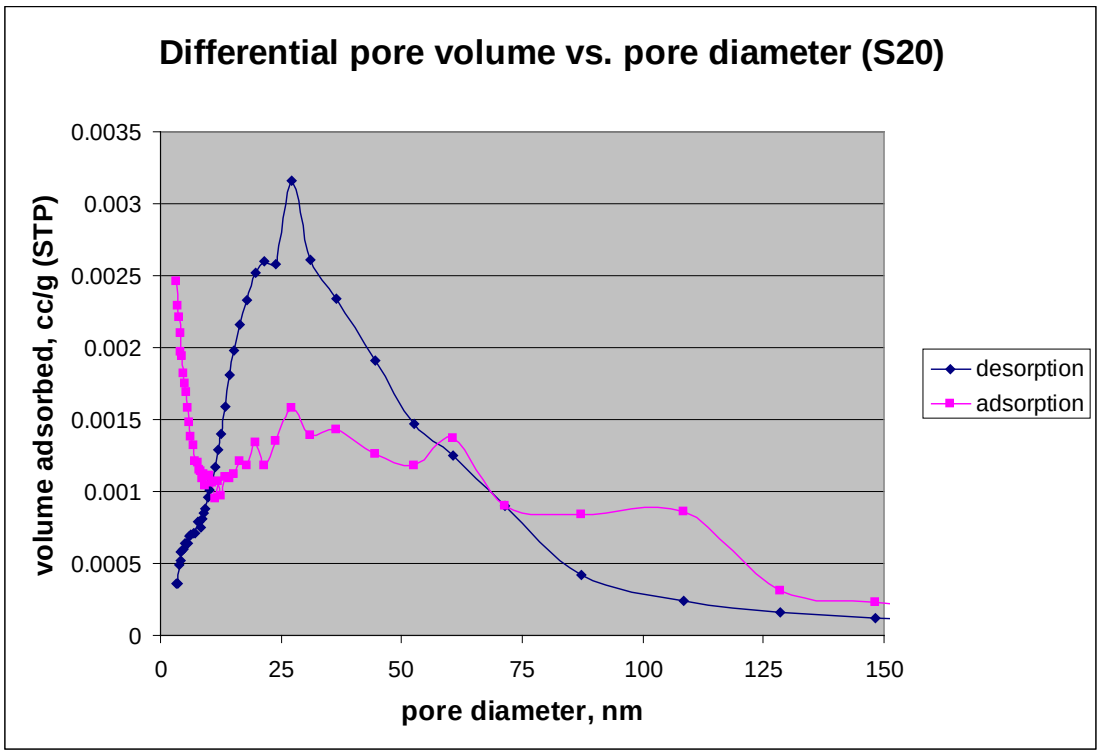

Figure 4.48: Plot of differential pore volume against pore diameter for S20, 20% vinyl trimethoxy silane.

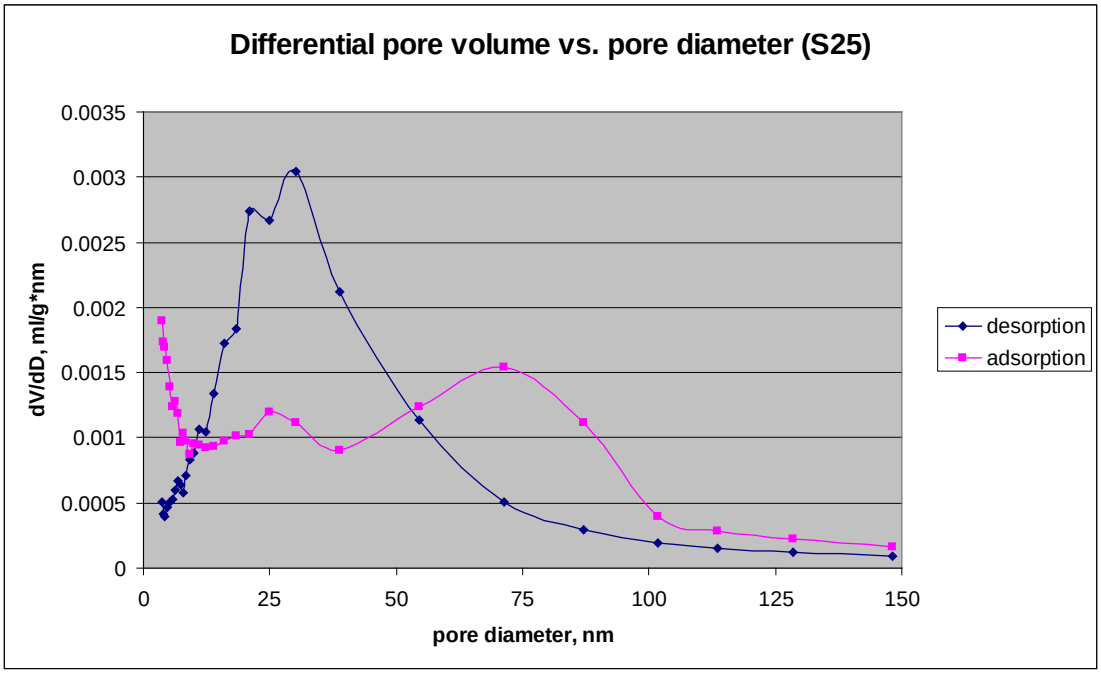

Figure 4.49: Plot of differential pore volume against pore diameter for S25, 25% vinyl trimethoxy silane.

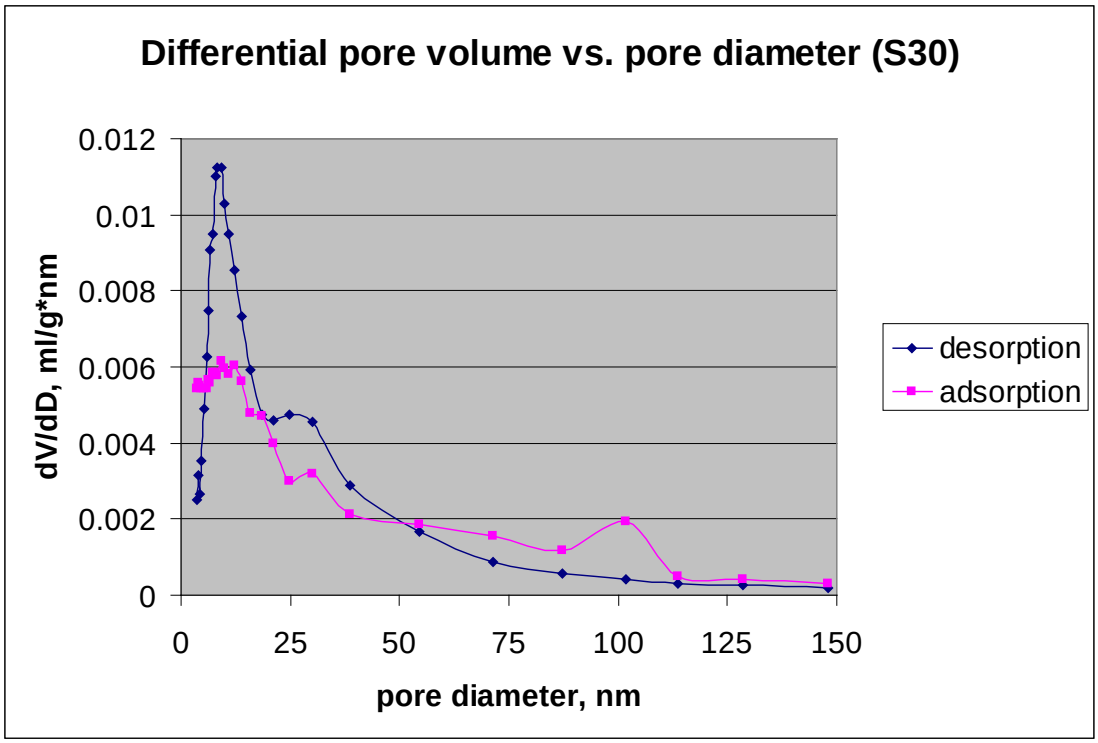

Figure 4.50: Plot of differential pore volume against pore diameter for S30, 30% vinyl trimethoxy silane.

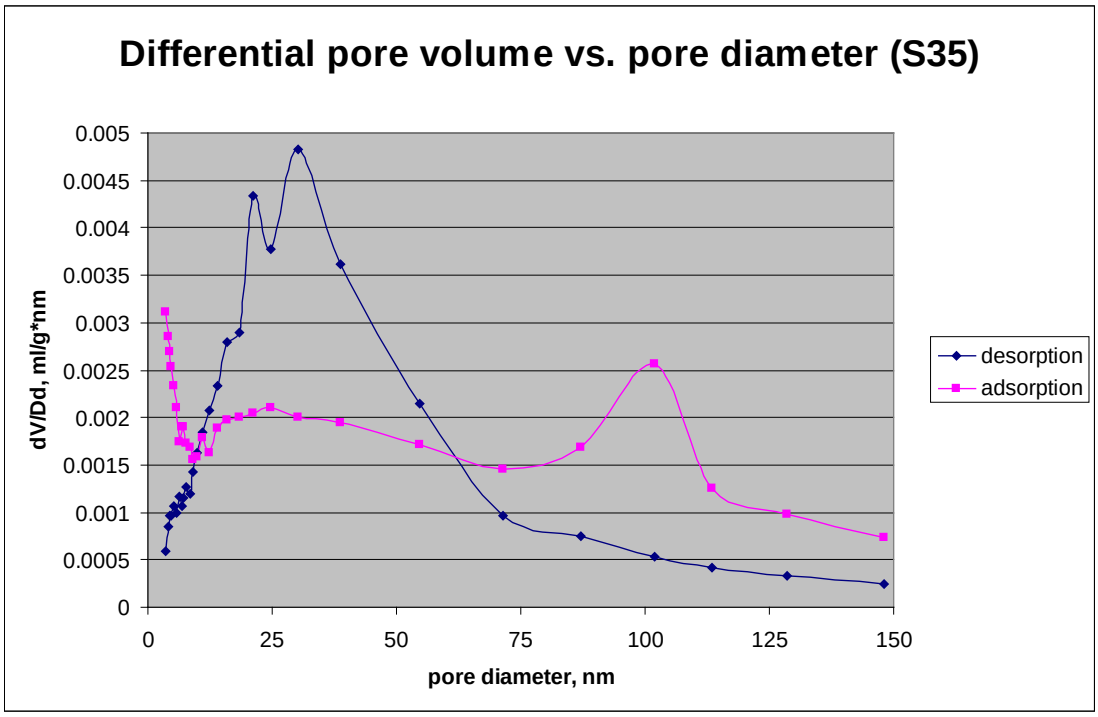

Figure 4.51: Plot of differential pore volume against pore diameter for S35, 35% vinyl trimethoxy silane.

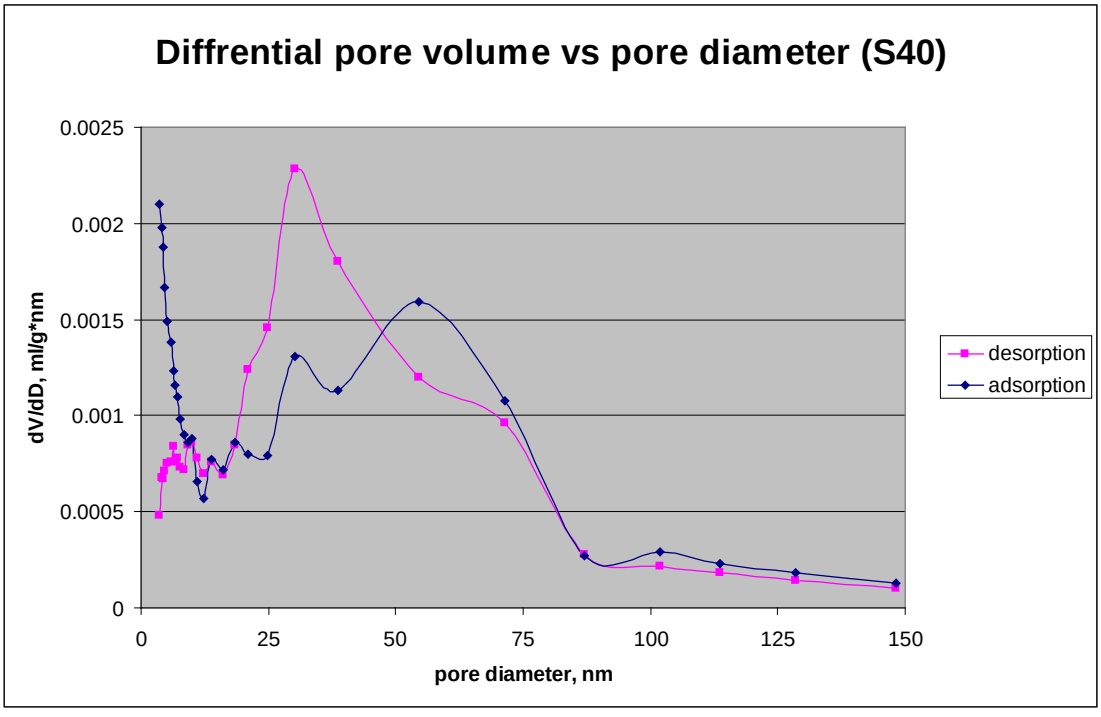

Figure 4.52: Plot of differential pore volume against pore diameter for S40, 40% vinyl trimethoxy silane.

4.4.3.4 Comparison of pore size distribution

Comparison of pore size distribution between different percentages of VTMS for desorption curve is presented in Figure 4.53 and Figure 4.54. The plot shows that the pore volumes are significantly contributed by the mesopore distribution. The highest peak of differential pore volume is observed for S30 PHP in the region of low value of mesopores, between 3.65 to 18.36 nm. The other peak observed in this low region is S5 peak but at a lower differential pore volume. S10 and S15 have the distribution centred at higher region of pore size with broader distribution, 4 to 60 nm ranges. The rest of the samples, S20, S25, S35 and S40 have the distribution shifted, covering from mesopore region to higher macropore region, from 20 to 87 nm.

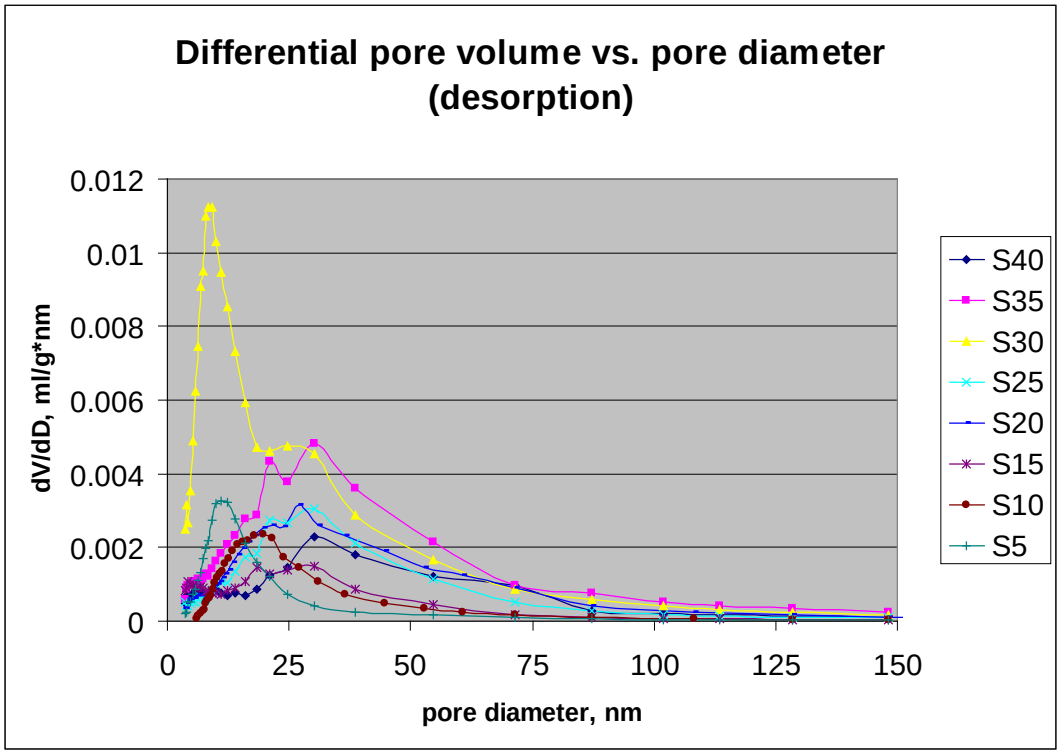

Figure 4.53: Plot of differential pore volume (desorption) against pore diameter for several percentages of VTMS.

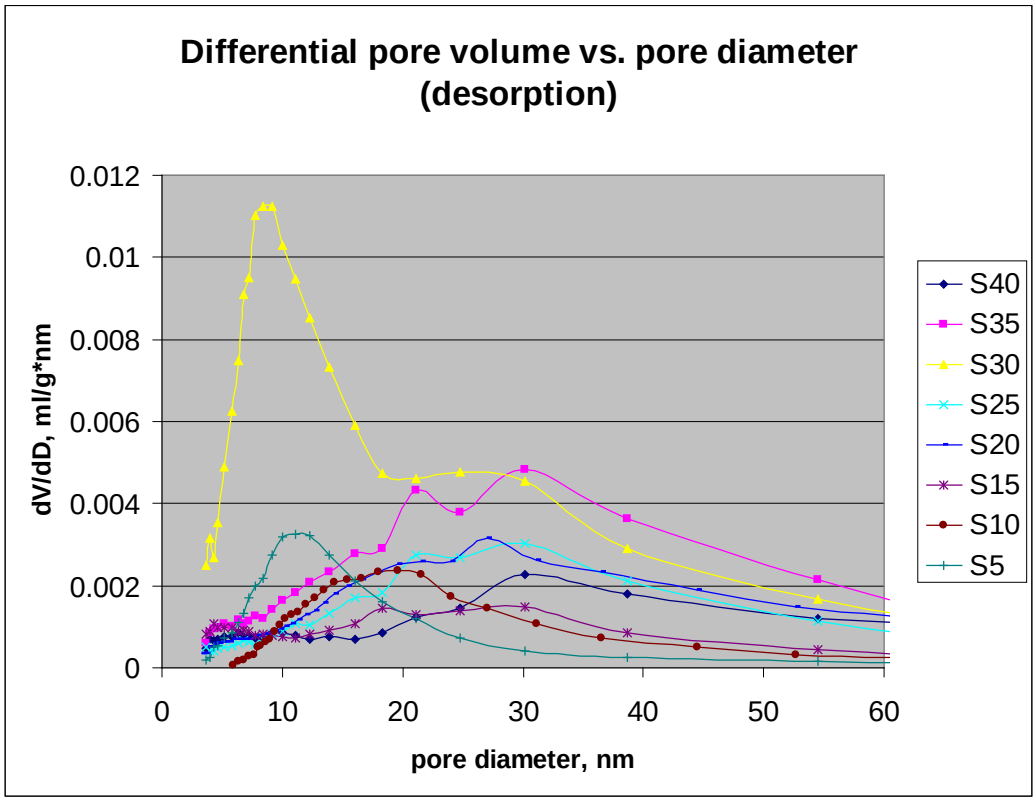

Figure 4.54: Plot of differential pore volume (desorption) against pore diameter at several percentages of VTMS for mesopores region.

Comparison of adsorption curves for different percentages of VTMS is presented in Figure 4.55. The highest pore volume distribution is observed for S30 sample whereas the lowest pore volume distribution is observed for S10 sample in the region of fine mesopore. S30 and S35 have a monomodal distribution in the macropore region. S40 has bimodal distribution, one in the region of mesopore and one in the macropore region.

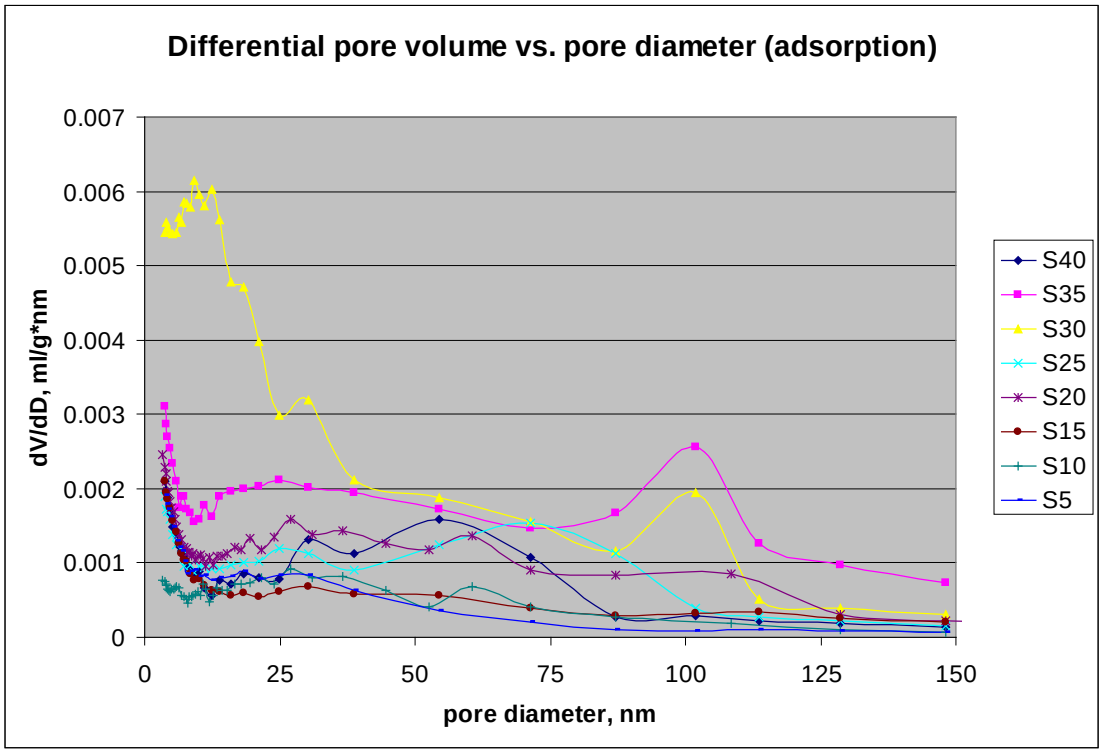

Figure 4.55: Plot of differential pore volume (adsorption) against pore diameter of several percentages of VTMS.

Comparison of pore volume in the mesopore region for all VTMS samples is presented in Table 4.10, Table 4.11, Table 4.12 and Figure 4.56. In summary, desorption curve results in higher total pore volume compared to adsorption curve. The highest total pore volume for desorption curve and adsorption curve is observed for S30 and the lowest total pore volume is observed for S15. Both curves also exhibit S5 with the highest percentage of total pore volume in the mesopore region compared to the others. This indicates that S5 pores are significantly contributed by the mesopore region rather than the macropore region.

In summary, desorption curves indicate that the pore volumes are significantly contributed by the mesoporous pores rather than the macroporous pores. Adsorption curves indicate that the pore volumes are significantly contributed by the macroporous pores, with the exception of S5, S10 and S30.

Table 4.10: Comparison of pore volume for VTMS PHPs.

Sample name	Desorption pore volume, ml/g			Adsorption pore volume, ml/g		
	mesopore	% of mesopore	Total	mesopore	% of mesopore	Total
S5	0.0453	85.0	0.0533	0.0340	65.9	0.0516
S10	0.0518	79.2	0.0654	0.0329	53.3	0.0617
S15	0.0444	72.8	0.0610	0.0290	42.7	0.0679
S20	0.0930	63.2	0.1471	0.0613	42.5	0.1445
S25	0.0800	64.6	0.1239	0.0422	34.1	0.1240
S30	0.2116	74.2	0.2854	0.1558	56.2	0.2773
S35	0.1301	58.1	0.2238	0.0800	33.1	0.2424
S40	0.0561	52.0	0.1078	0.0417	39.0	0.1062

Table 4.11: Comparison of desorption mesopore volume for VTMS PHPs.

Sample name	Mesopore volume, ml/g	Range of average pore size, nm	% pore volume
S5	0.0082	3.48 - 9.54	15.4
	0.0371	9.54 - 44.01	69.6
S10	0.0021	5.78 - 9.99	3.2
	0.0497	9.99 - 49.29	76.0
S15	0.0054	3.48 – 9.54	8.8
	0.0390	9.54 - 44.01	63.9
S20	0.0047	3.19 - 9.99	3.2
	0.0883	9.99 - 49.29	60.0
S25	0.0036	3.48 - 9.54	2.9
	0.0764	9.54 - 44.01	61.6
S30	0.0461	3.48 - 9.54	16.2
	0.1655	9.54 - 44.01	58.0
S35	0.0067	3.48 - 9.54	3.0
	0.1234	9.54 - 44.01	55.1
S40	0.0045	3.48 - 9.54	4.2
	0.0516	9.54 - 44.01	47.8

Table 4.12: Comparison of adsorption mesopore volume for VTMS PHPs.

Sample name	Mesopore volume, ml/g	Range of average pore size, nm	% pore volume
S5	0.0075	3.48 - 9.54	14.6
	0.0265	9.54 - 44.01	51.3
S10	0.0042	3.19 - 9.99	6.8
	0.0287	9.99 - 49.29	46.5
S15	0.0079	3.48 - 9.54	11.6
	0.0211	9.54 - 44.01	31.1
S20	0.0102	3.19 - 9.99	7.1
	0.0511	9.99 - 49.29	35.4
S25	0.0075	3.48 - 9.54	6.1
	0.0347	9.54 - 44.01	28.0
S30	0.0344	3.48 - 9.54	12.4
	0.1214	9.54 - 44.01	43.8
S35	0.0126	3.48 - 9.54	5.2
	0.0675	9.54 - 44.01	27.8
S40	0.0079	3.48 - 9.54	7.4
	0.0338	9.54 - 44.01	31.9

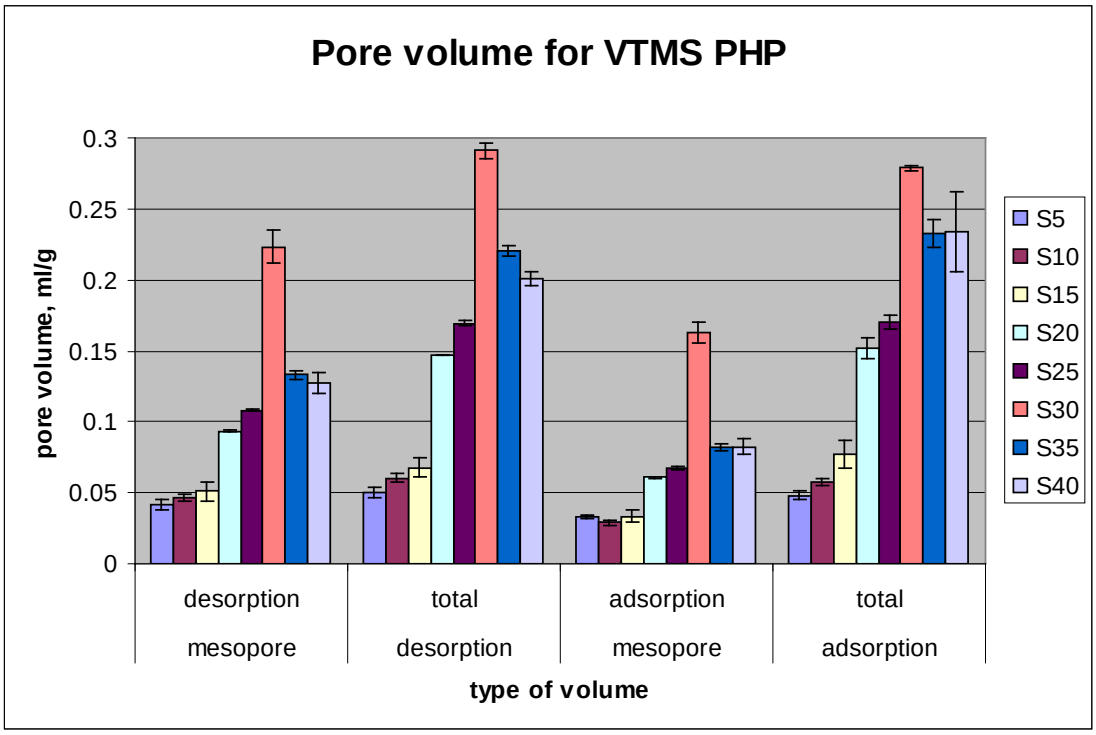

Figure 4.56: Comparison of pore volume for VTMS PHPs.

In order to further study the significant difference between the pore volumes, statistical analysis, ANOVA at 5 % significance level was performed. The results conclude that there exist significant differences between the pore volumes of all types of pore volumes. The results of Bonferroni test, pairwise comparison at 95.0% confident intervals are summarised in Table 4.13.

Further comparison was done on pore size distributions of 5% VTMS PHPs produced using oil phase initiator, S5-O and aqueous phase initiator, S5. The comparison is presented in Figure 4.57 through Figure 4.59. Desorption curves for both samples show monomodal distribution in the region of fine mesopore, below 25 nm. The desorption curves of both samples show that the pore volumes are significantly contributed by the fine size mesopore. There was no peak observed in the adsorption curve of S5; however the curve exhibit higher differential pore volume in the region of less than 10 nm pore. S5-O exhibits bimodal distributions in the region of mesopores, with peaks centred at 4 nm and 21 nm.

Table 4.13: Bonferroni pairwise comparison for all types of pore volumes of VTMS PHP.

Type of pore volumes	Pairs that are difference
Desorption mesopore	S0 & S30, S0 & S35, S0 & S40, S5 & S20, S5 & S25, S5 &S30, S5 & S35, S5 & S40, S10 & S20, S10 & S25, S10 & S30, S10 & S35, S10 & S40, S15 & S20, S15 & S25, S15 & S30, S15 & S35, S15 & S40, S20 & S30, S20 & S35, S20 & S40, S25 & S30, S30 & S35, S30 & S40.
Total desorption	S0 & S5, S0 & S20, S0 & S25, S0 & S30, S0 & S35, S0 & S40, S5 & S20, S5 & S25, S5 &S30, S5 & S35, S5 & S40, S10 & S20, S10 & S25, S10 & S30, S10 & S35, S10 & S40, S15 & S20, S15 & S25, S15 & S30, S15 & S35, S15 & S40, S20 & S30, S20 & S35, S20 & S40, S25 & S30, S30 & S35, S30 & S40.
Adsorption mesopore	S0 & S5, S0 & S10, S0 & S15, S0 & S30, S0 & S40, S5 & S20, S5 & S25, S5 & S30, S5 & S35, S5 & S40, S10 & S20, S10 & S25, S10 & S30, S10 & S35, S10 & S40, S15 & S20, S15 & S25, S15 & S30, S15 & S35, S15 & S40, S20 & S30, S20 & S35, S20 & S40, S25 & S30, S25 & S40, S30 & S35, S30 & S40.
Total adsorption	S0 & S20, S0 & S25, S0 & S30, S0 & S35, S0 & S40, S5 & S20, S5 & S25, S5 & S30, S5 & S35, S5 & S40, S10 & S20, S10 & S25, S10 & S30, S10 & S35, S10 & S40, S15 & S20, S15 & S25, S15 & S30, S15 & S35, S15 & S40, S20 & S30, S20 & S35, S20 & S40, S25 & S30, S25 & S35, S25 & S40, S30 & S35, S30 & S40.

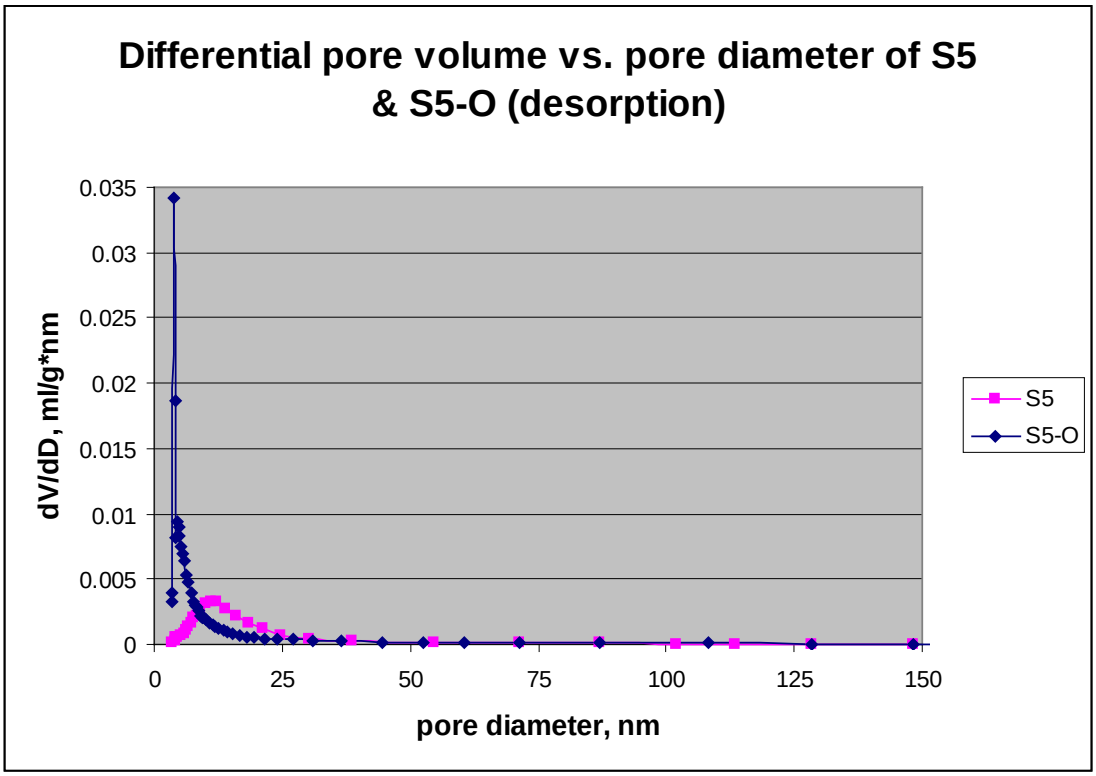

Figure 4.57: Plot of differential pore volume against pore diameter for 5% VTMS. Comparison between aqueous phase initiator and oil phase initiator.

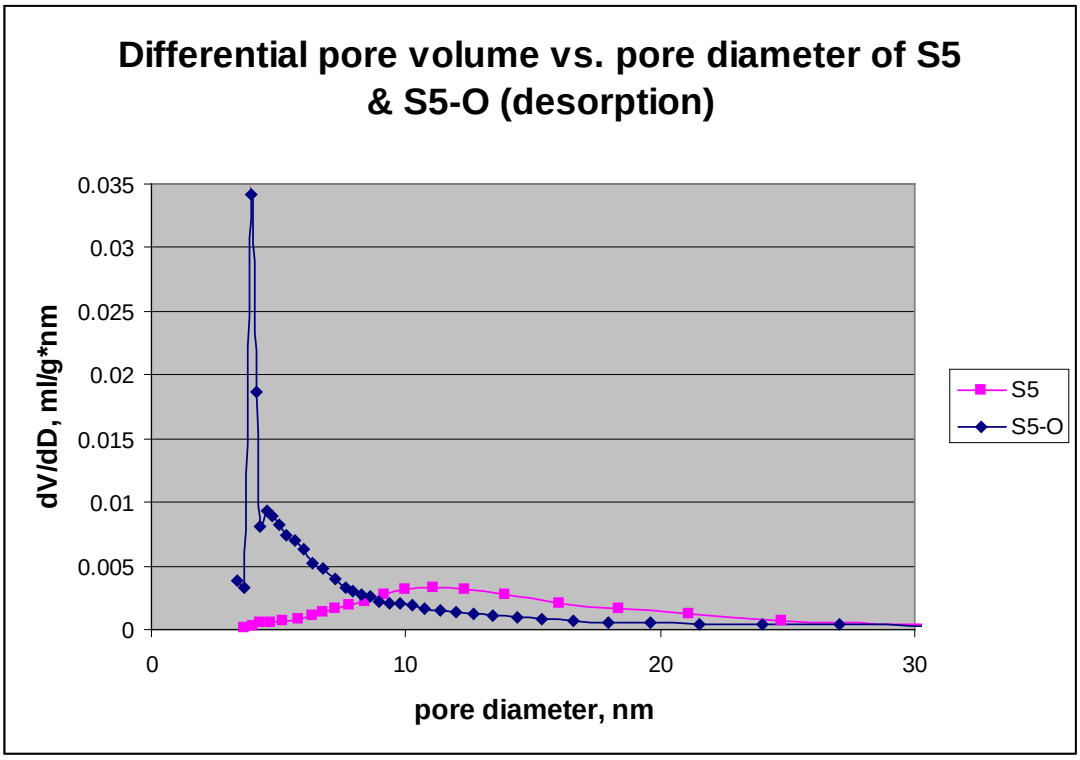

Figure 4.58: Plot of desorption differential pore volume against pore diameter for 5% VTMS in mesopore region. Comparison between aqueous phase initiator and oil phase initiator

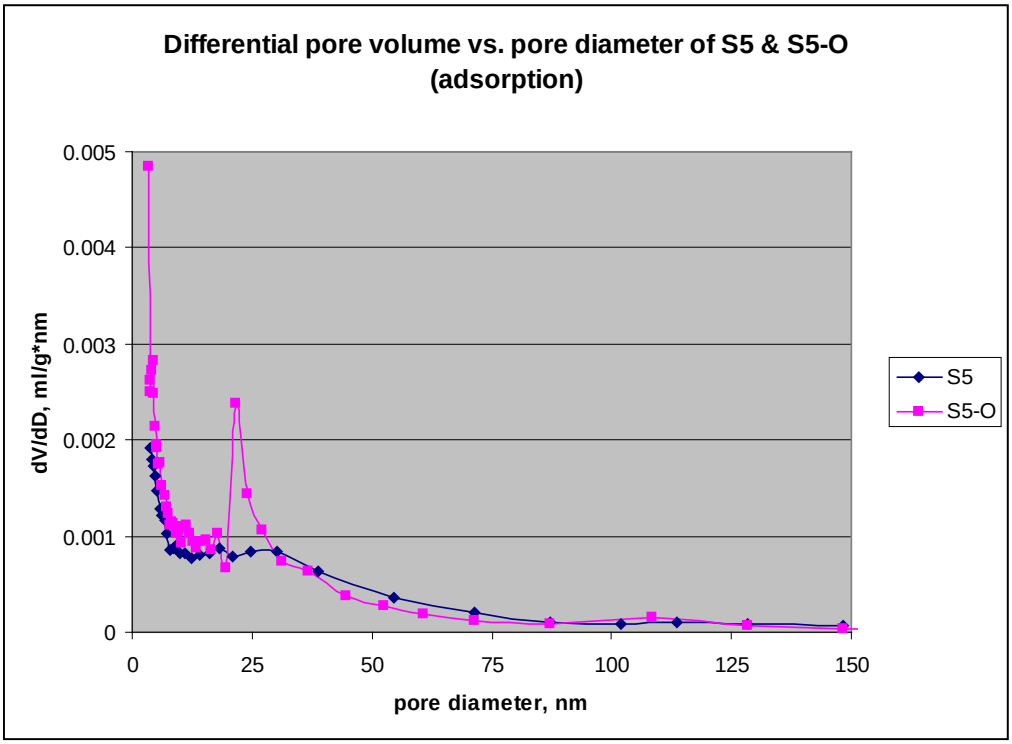

Figure 4.59: Plot of adsorption differential pore volume against pore diameter for 5% VTMS. Comparison between aqueous phase initiator and oil phase initiator.

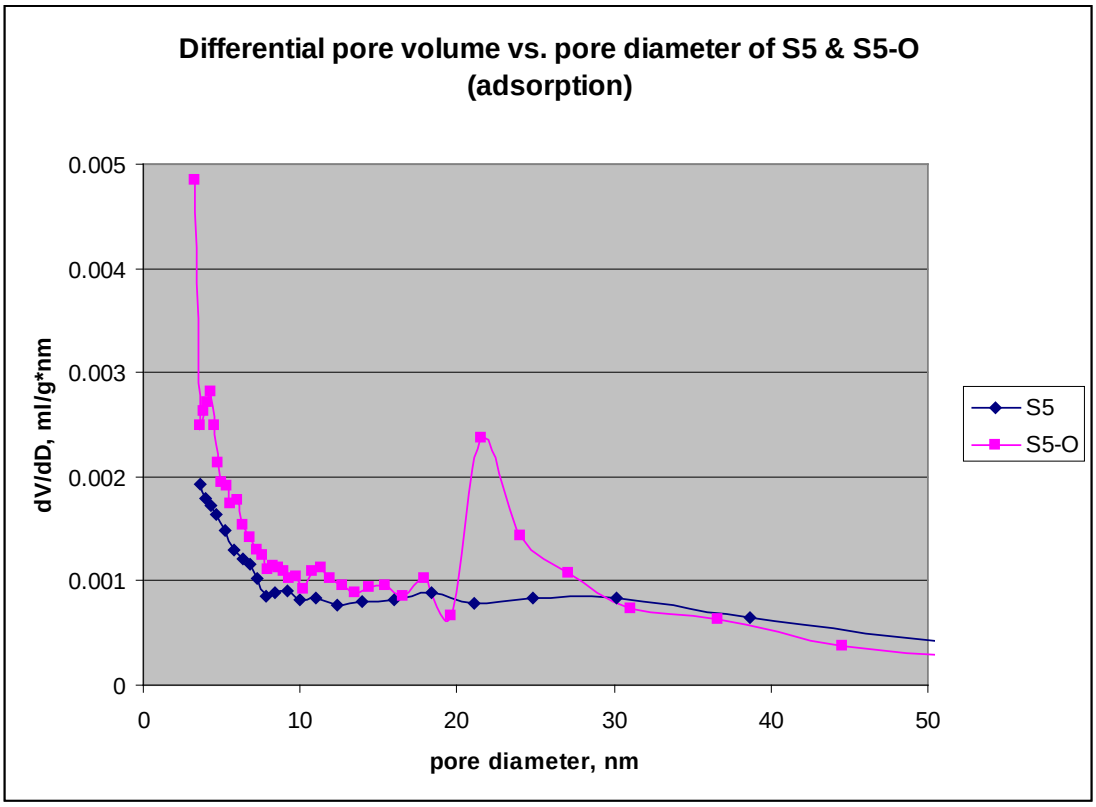

Figure 4.60: Plot of adsorption differential pore volume against pore diameter for 5% VTMS in mesopore region. Comparison between aqueous phase initiator and oil phase initiator.

Total pore volumes of desorption and adsorption curves are presented in Table 4.14 and Figure 4.61. The percentages of the mesopore region are also high. Thus, the total pore volumes for both desorption and adsorption curves for both samples are significantly contributed by the mesopores. Desorption curves exhibit higher percentages of mesopore volumes compared to adsorption curves. Comparing mesopore volumes and total pore volumes of both desorption and adsorption curves in Table 4.14, S5-O has higher pore volumes than S5. However, comparing the standard error bars of the volumes in Figure 4.61, the pore volumes of both samples do not differ significantly except for total desorption pore volumes.

Two-sample T-test was performed and the result concludes that at 5% significance level, the means are equal. There is no effect of type of initiator used on all types of pore volumes of VTMS PHP produced with 5% silane.

Table 4.14: Comparison of pore volume for S5 and S5-O.

Sample name	Desorption pore volume			Adsorption pore volume		
	mesopore ml/g	% mesopore	Total, ml/g	mesopore ml/g	% mesopore	Total, ml/g
S5	0.0416	83.40	0.0499	0.0326	67.70	0.0482
S5-O	0.0509	83.92	0.0607	0.0389	73.90	0.0527

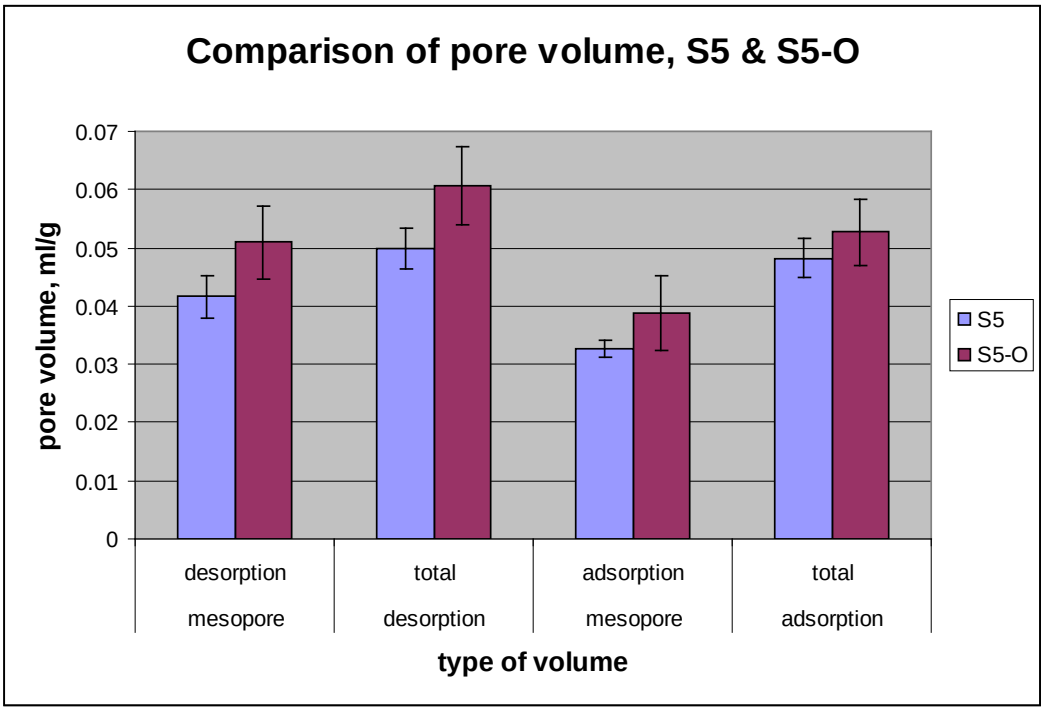

Figure 4.61: Comparison of pore volumes of S5 & S5-O

4.4.4 FTIR Analysis.

The spectra from the lowest to the highest percentage of VTMS successfully incorporated into the HIPE are shown in Figure 4.62 through Figure 4.66. There was a significant difference in the peak produced with the increase of VTMS, specifically at the band of 920 to 1250 cm -1. This range of absorption is attributed to asymmetric vibration of –Si–OCH_3 (Barzin et al., 2006; Rodriguez-Fernandez and Gilbert, 1997). The peak is divided into two peaks at this band, as listed in Table 4.15. The rest of the peaks are similar to the peaks observed in basic PHP as is discussed in section 4.5.3. It

has been observed that for the bands lower than 905 cm^{-1}, the transmittance intensity decreased with the increase in the percentage of VTMS. Thus, the changes in peaks intensity confirmed the success of functionalizing VTMS into the HIPE.

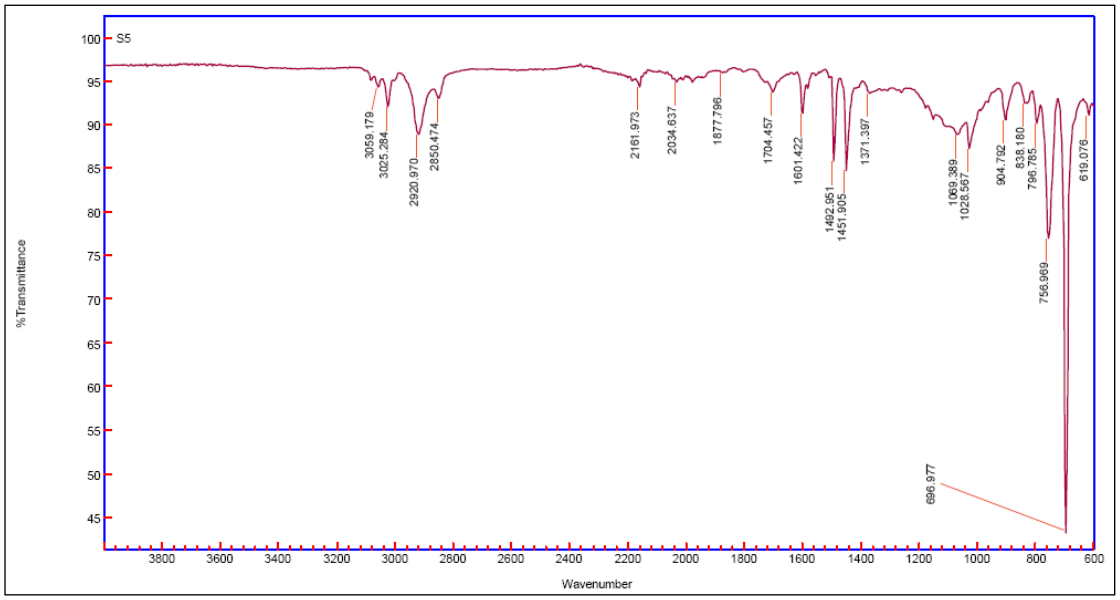

Figure 4.62: FTIR spectrum for S5, 5% VTMS PHP

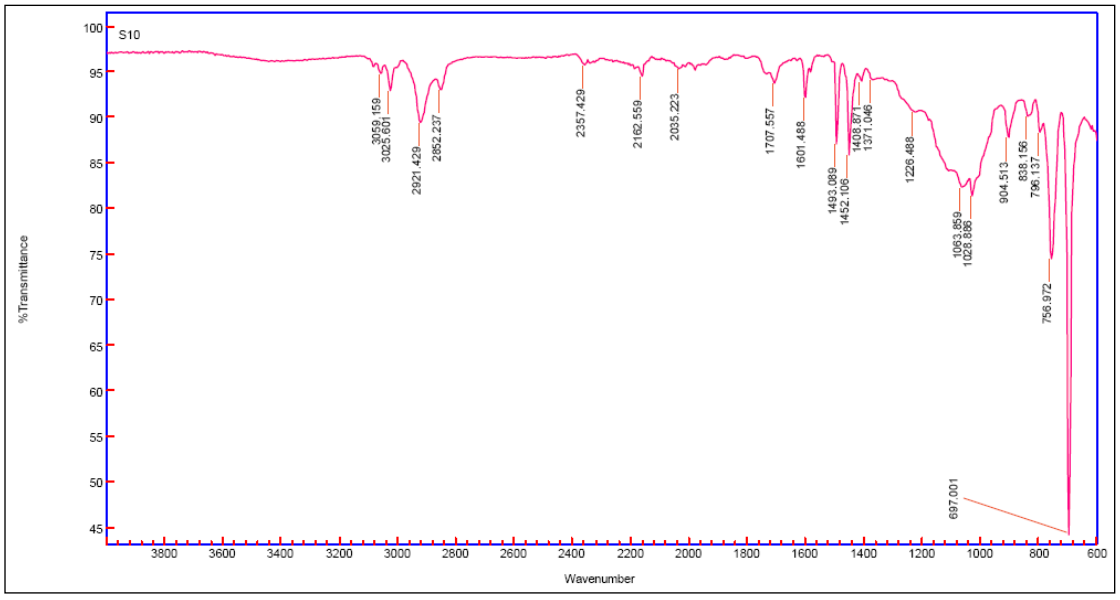

Figure 4.63: FTIR Spectrum for S10, 10% VTMS PHP.

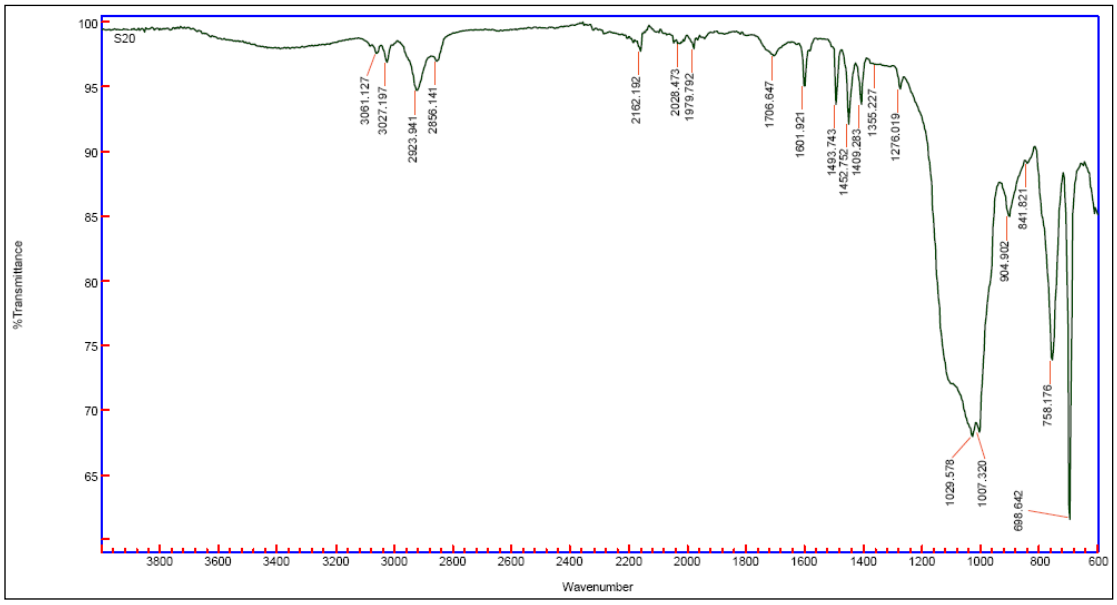

Figure 4.64: FTIR Spectrum for S20, 20% VTMS PHP.

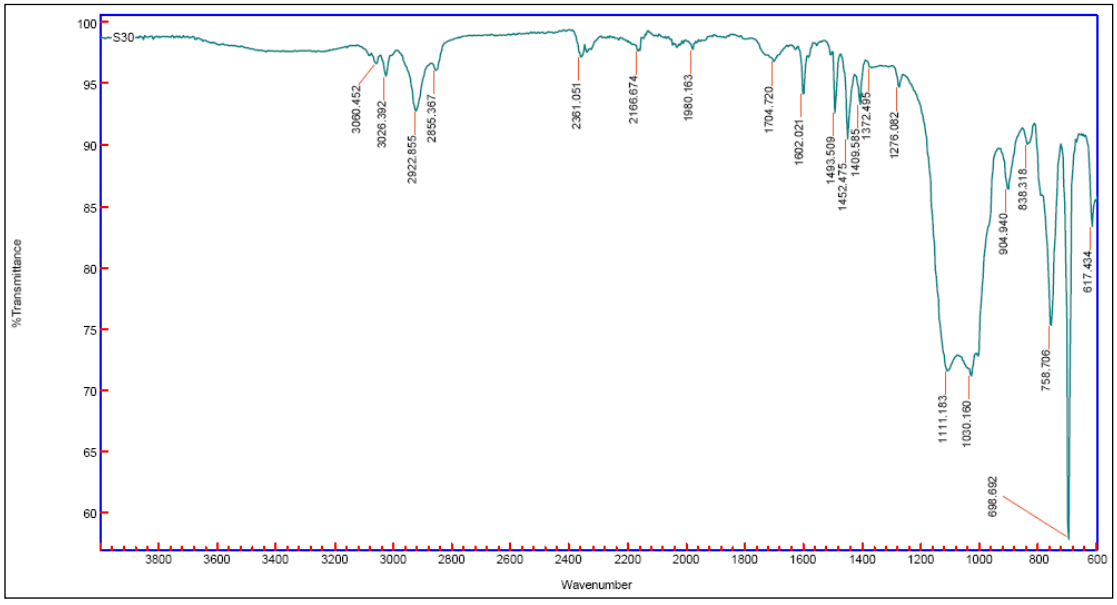

Figure 4.65: FTIR Spectrum for S30, 30% VTMS PHP.

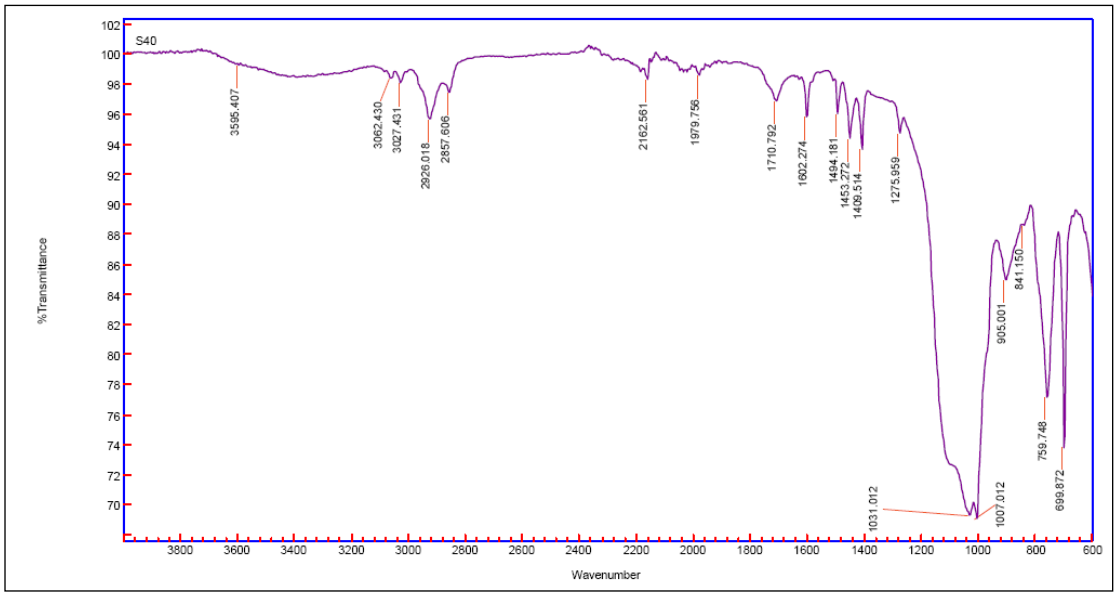

Figure 4.66: FTIR Spectrum for S40, 40% VTMS PHP.

Table 4.15: Two peaks in the stretching band of 920 to 1250 cm $^{-1}$.

Sample name	Wavenumber of the peak, cm $^{-1}$.	
S5	1069.389	1028.567
S10	1063.859	1028.886
S20	1029.578	1007.230
S30	1111.183	1030.160
S40	1031.012	1007.012

There was a significant difference in the peaks of –Si–OCH_3 produced in the band range of 920 – 1250 cm $^{-1}$. The absorption intensity for S40 is the strongest and the absorption intensity for S5 is the weakest. The higher is the percentage of VTMS, the stronger is the absorption intensity as was observed in Figure 4.67.

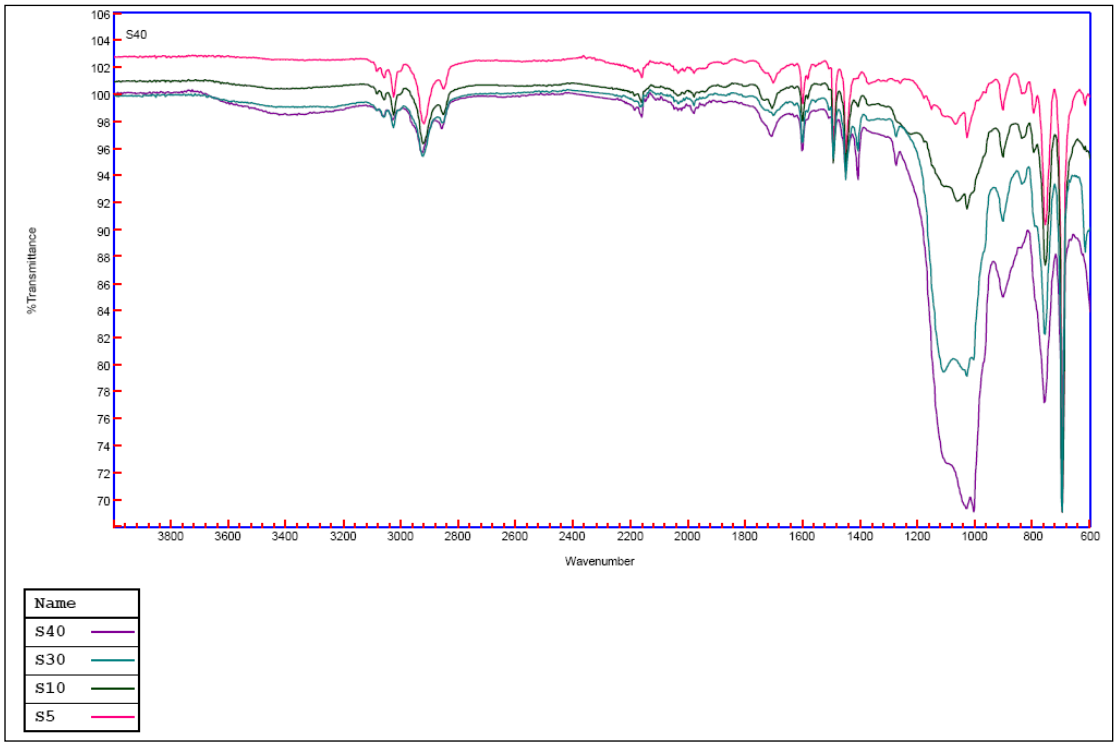

Figure 4.67: FTIR spectrum for VTMS PHPs – comparison.

4.4.5 Effect of surfactant

Span 85 and a mixed of Span 80 and Span 85 were used in different percentages to prepare VTMS PHP in the effort to get a stable emulsion. The weight percentages of SPAN 80 to SPAN 85 that were tried are 75:25 and 50:50. Combination of 0.5 weight percent of aqueous phase initiator and 0.5 weight percent of oil phase initiator was also tried. None of the trials produce a stable emulsion after the mixing. Upon leaving the liquid product in the oven overnight at 60 C, the product turned into gel form.

4.5 *Basic PHP*

In order to investigate the factors that contribute to the coral-like pores of the polymer with banana-like strand, further experiments were done on basic PHP (0% VTMS). Therefore, several basic PHPs at the same and different composition were

also prepared. The summary of the basic PHPs experiments is presented in Table 4.16.

Table 4.16: The basic PHPs experiments. S01-S03 & S05 – S07 with 68% styrene, S04 with 78% styrene.

Sample name	Phase Composition, %		Dosing & mixing time, min	
	Oil phase	Aqueous phase	Dosing	Mixing
S01	20	80	10	50
S02	20	80	10	20
S03	20	80	5	1
S04, 78% styrene	20	80	10	50
S05	10	90	10	50
S06	15	85	10	50
S07	20	80	10	5

4.5.1 Morphology

Generally, except for S04, the banana-like strand is less apparent in basic PHP even though the pore shape is still similar; coral-like with no interconnects in the pore. The structure appears to be more like a closed pore. The images are shown in Figure 4.68 and Figure 4.69. The pore shape for VTMS PHP and basic PHP produced from 20 % oil phase with 68% styrene and 80 % aqueous phase is similar. Upon increasing the percentage of styrene in the oil phase to 78% while keeping the oil and aqueous phase composition the same, the interconnect pores are started to be seen, i.e. S04. S04 has no banana-like strand amongst all the basic PHPs produced. Thus, the coral-like structure was produced due to the phase composition of 20:80 of oil to aqueous phase ratio but with 68% styrene in the oil phase. For the PHP with highest aqueous phase of 90%, S05, the emulsion is less stable, with many coalescent pores. For the least mixing time, S03, the emulsion is the least stable, thus there are many coalescent pores and the pore size is the biggest.

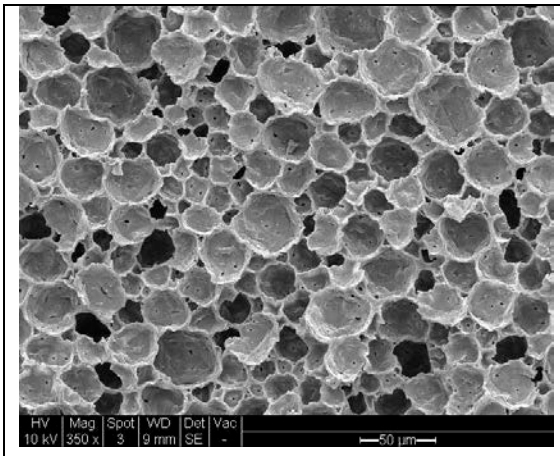

(a) S01, 350 X magnification.

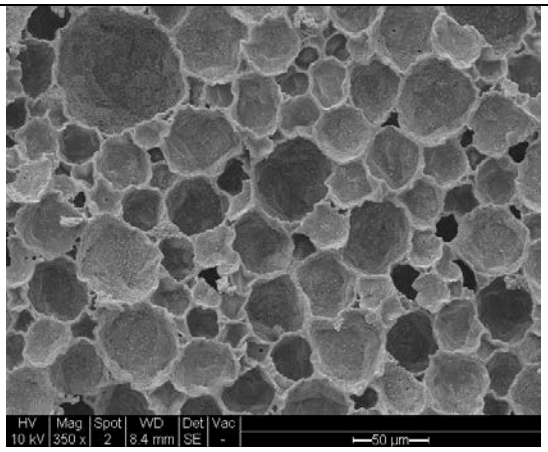

(b) S02, 350X magnification.

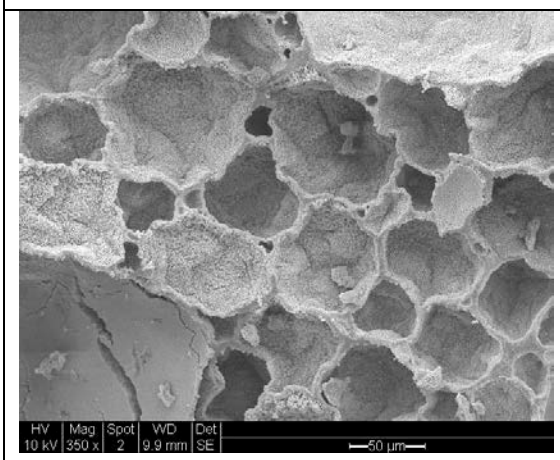

(c) S03, 350X magnification.

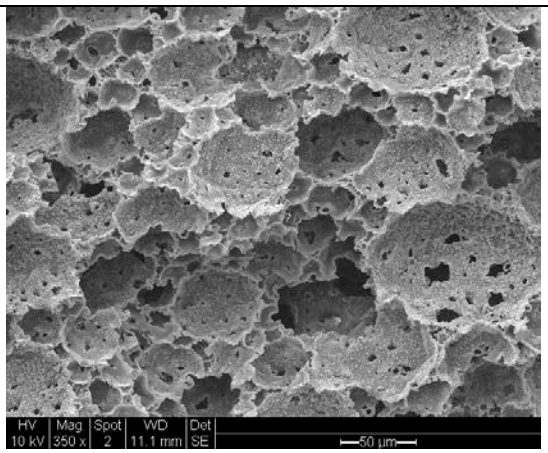

(d) S04, 350X magnification.

S01 – S03, 68 % styrene.

S03 – 68% styrene, lowest mixing time, the least stable, many coalescent pores, bigger pores.

S04 – 78% styrene, interconnect pores are observed.

Figure 4.68: Comparison of several basic PHPs.

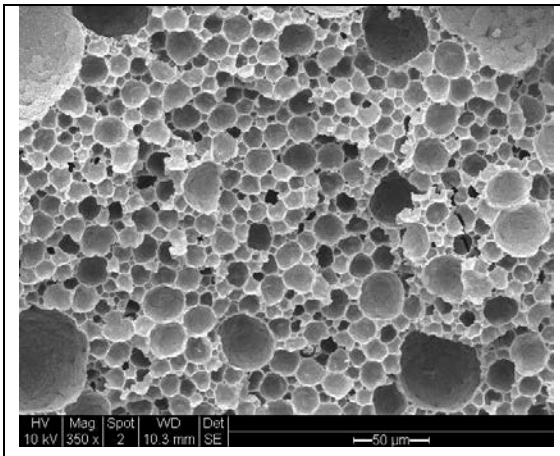

(a) S05, 350X.

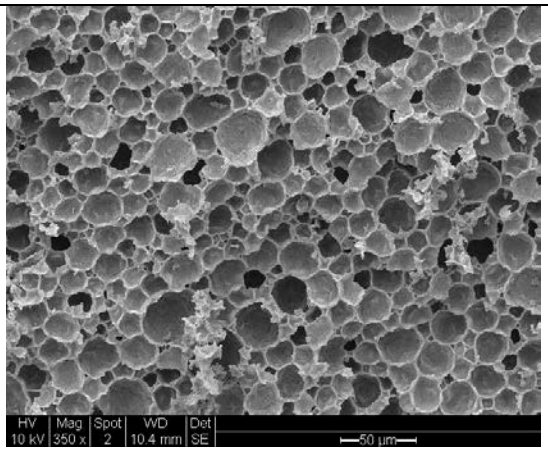

(b) S06, 350X.

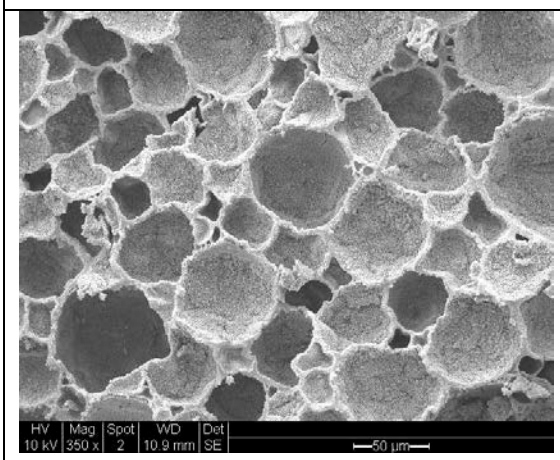

(c) S07, 350X.

S05 – S07, 68 % styrene.

S05 – 68% styrene, (90%) highest aqueous phase percentage – many coalescent pores.

S07 - big pores – due to mixing time, 10 min dosing, 5 min mixing.

Figure 4.69: More comparison of basic PHPs.

Further comparison was done at higher magnification of the images as presented in Figure 4.70 and Figure 4.71. Presence of spherical particles was observed on the surface of S02, S03, S04 and S07. Few spherical particles could be observed on the surface of S01 but none was observed on S05 and S06. This was further confirmed by the images at higher magnification in Figure 4.72 and Figure 4.73. The most spherical particles were spotted on S03 and S07; none was observed on S05 and S06.

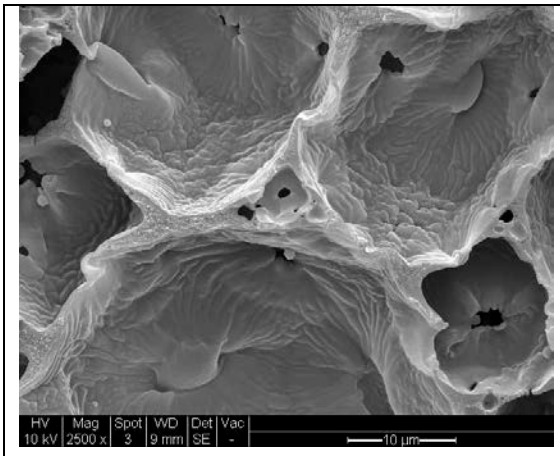

(a) S01, 2500X magnification.

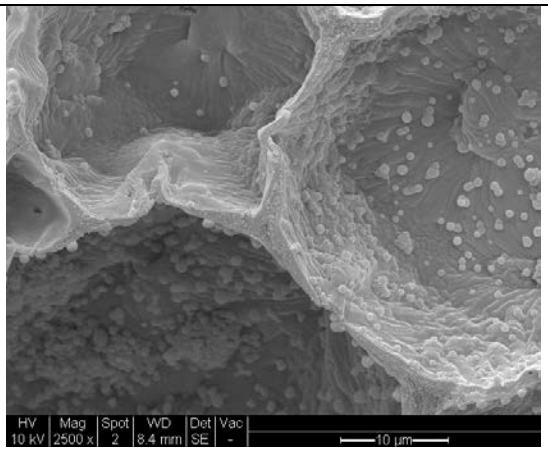

(b) S02, 2500X magnification.

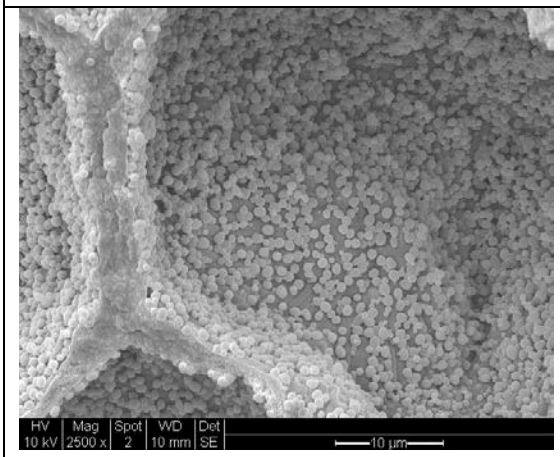

(c) S03,2500X magnification.

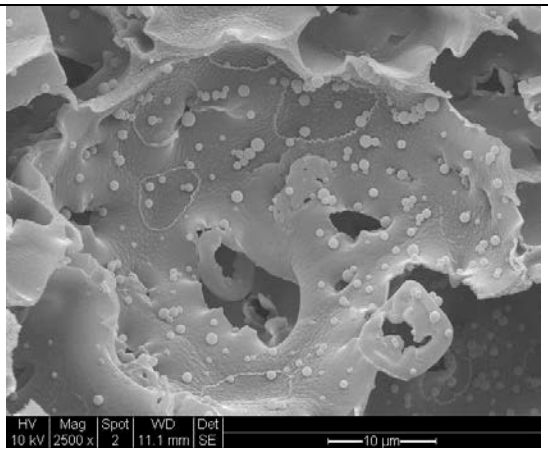

(d) S04, 2500X magnification.

Figure 4.70: Various basic PHPs at 2500X magnification.

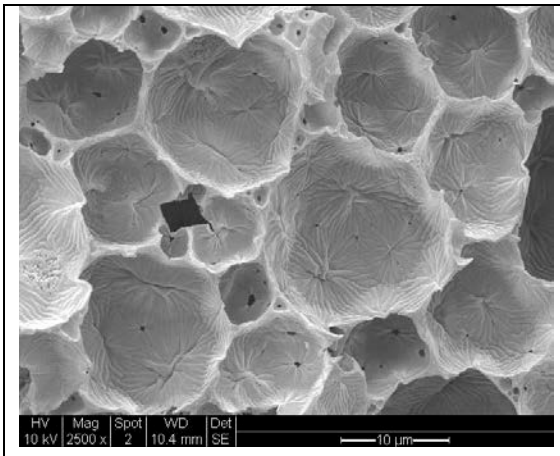

(a) S05, 2500X.

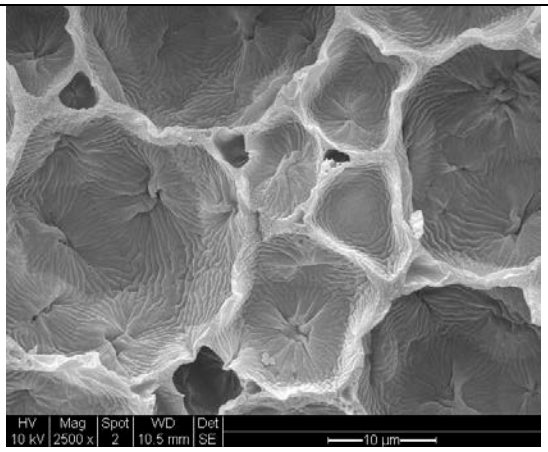

(b) S06, 2500X.

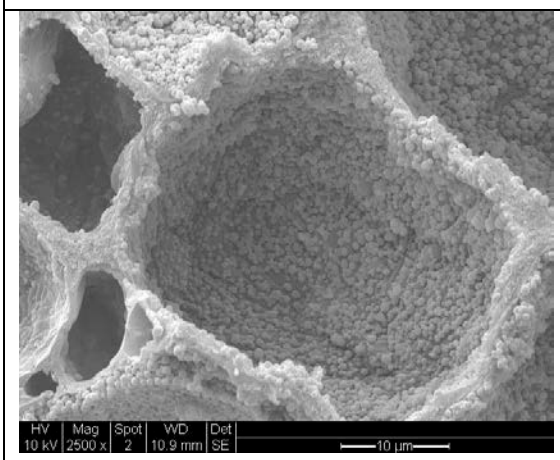

(c) S07, 2500X.

Figure 4.71: More images of various basic PHPs at 2500X magnification.

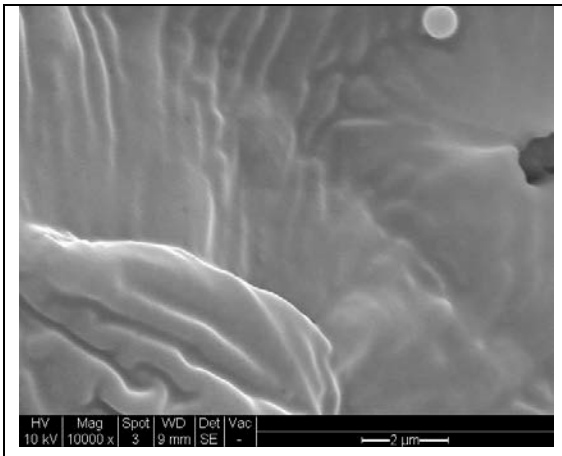

(a) S01, 10000X.

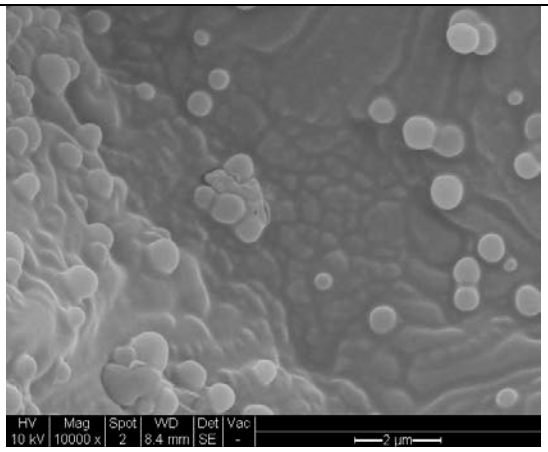

(b) S02, 10000X.

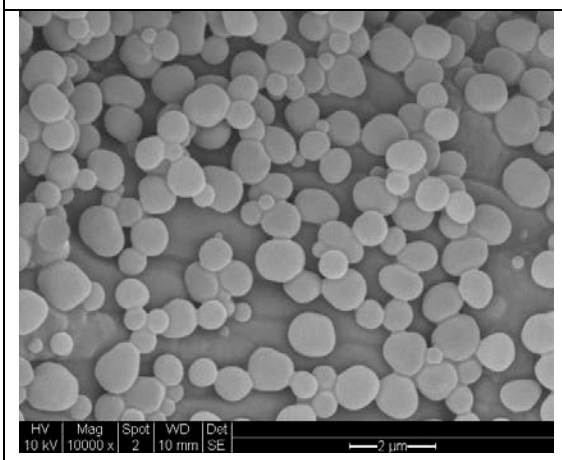

(c) S03, 10000X.

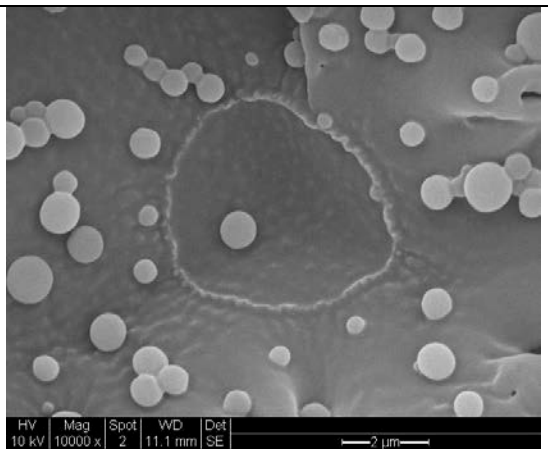

(d) S04, 10000X.

Figure 4.72: Structure of various basic PHPs at 10000X magnification.

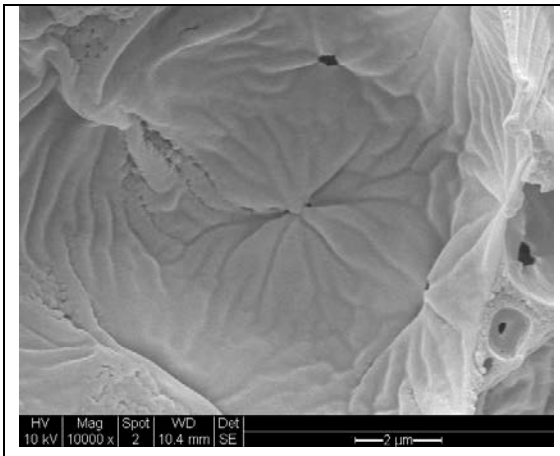

(a) S05, 10000X.

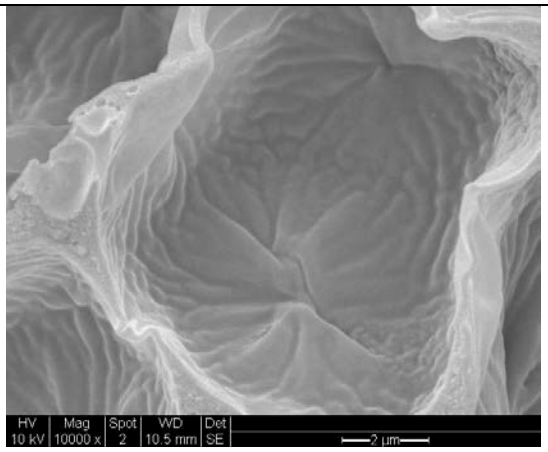

(b) S06, 10000X.

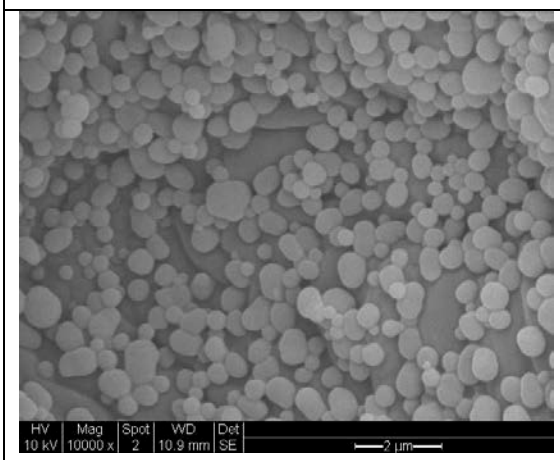

(c) S07, 10000X.

Figure 4.73: More images of various basic PHPs at 10000X magnification.

Comparison on the wall structure of the basic PHPs is as shown in Figure 4.74 and Figure 4.75. The walls look like they contain agglomerated particles.

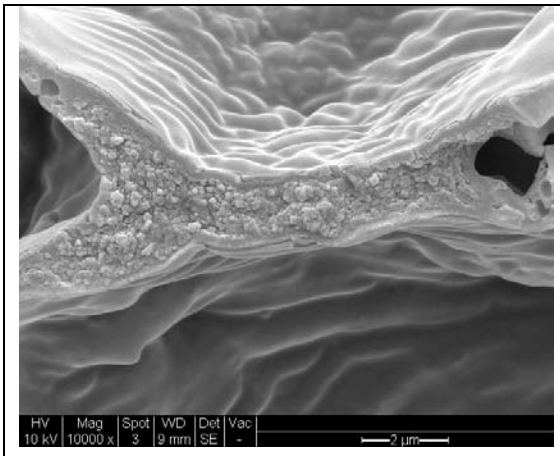

(a) S01, 10000X.

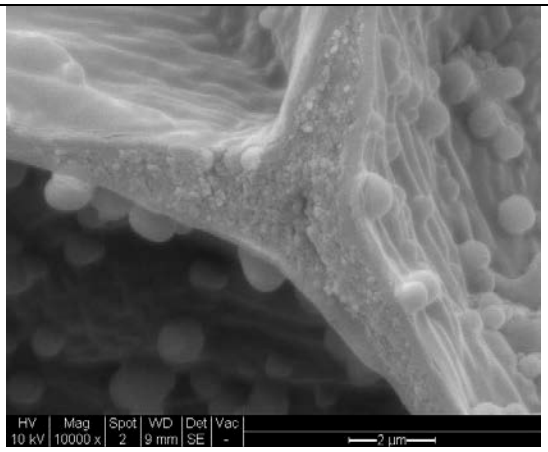

(b) S02, 10000X.

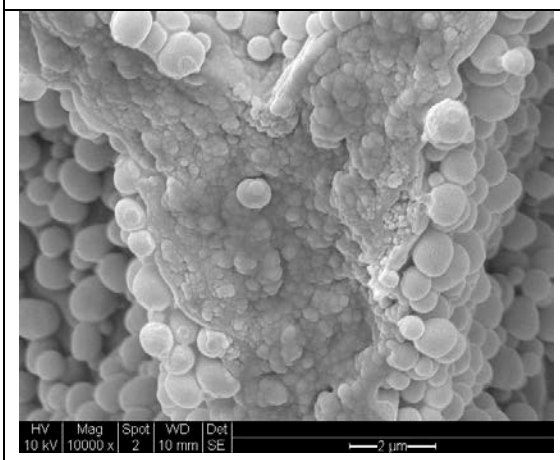

(c) S03, 10000X.

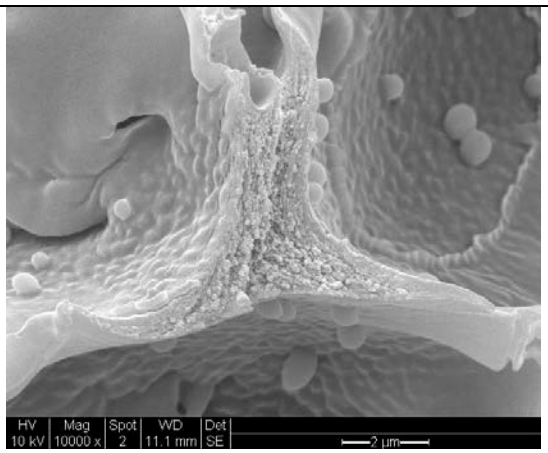

(d) S04, 10000X.

Figure 4.74: Wall structure of various basic PHPs.

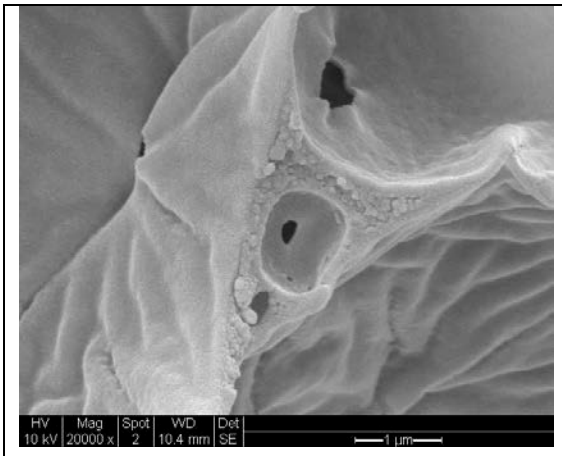

(a) S05, 20000X.

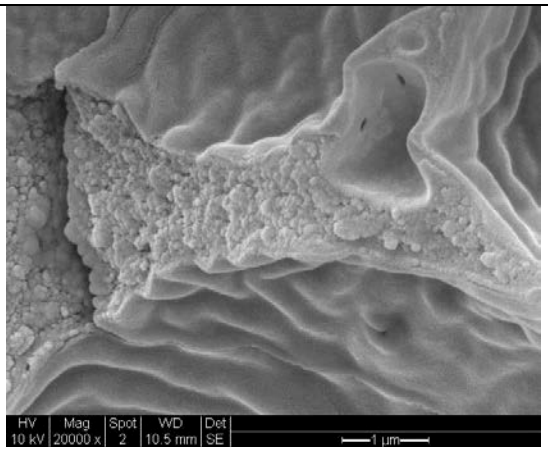

(b) S06, 20000X.

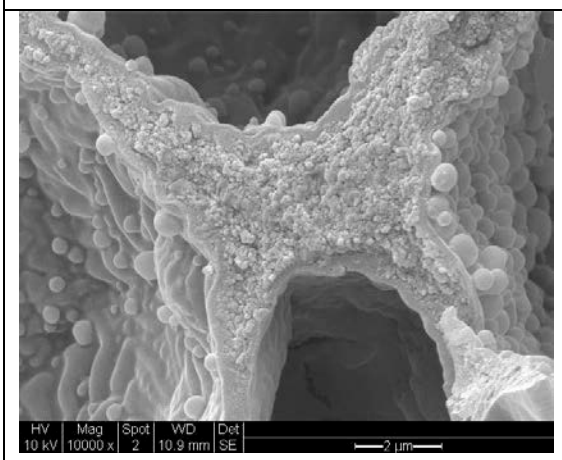

(c) S07, 10000X

Figure 4.75: More images of wall structure of various basic PHPs.

4.5.2 Surface area and pore size distribution.

Study on the surface area and pore size distribution was done by analysing physisorption process of nitrogen as the adsorbate at liquid nitrogen temperature, 77K. Checking for reproducibility of the results was done using as many as five runs.

4.5.2.1 Isotherm

The isotherms for several different basic polymers are presented in Figure 4.76 through Figure 4.82. In general, the isotherms are similar to those of VTMS polymer

except for the less steep slope and wider hysteresis. The initial part of all the isotherms follow Type II isotherm, which corresponds to monolayer-multilayer adsorption. All samples exhibit irreversible isotherm since hysteresis was observed for all the samples, indicating the capillary condensation in mesopore structure as in type IV isotherm in the IUPAC classification (Sing et al., 1985; Gregg and Sing, 1982). The presence of adsorption hysteresis indicates the mechanism of desorption is different to that of adsorption and has always been associated with porous materials. All the isotherms exhibit stages of physisorption process in mesopores, which is monolayer-multilayer adsorption and capillary condensation. However, there is no limiting uptake observed for higher range of Ps/Po. The isotherm rises rapidly near Ps/Po=1, which indicates the presence of macropores.

All hystereses are Type H3 hysteresis as classified by (Sing et al., 1985) which associated with aggregates of plate-like particles giving rise to slit-shaped pores. S03, S04 and S07 have narrower hysteresis compared to S01, S02, S05 and S06. As discussed previously in section 4.4.3.1, due to Type H3 hysteresis, only adsorption branch result of pore size distribution is reliable even though results of both adsorption and desorption branches are discussed here.

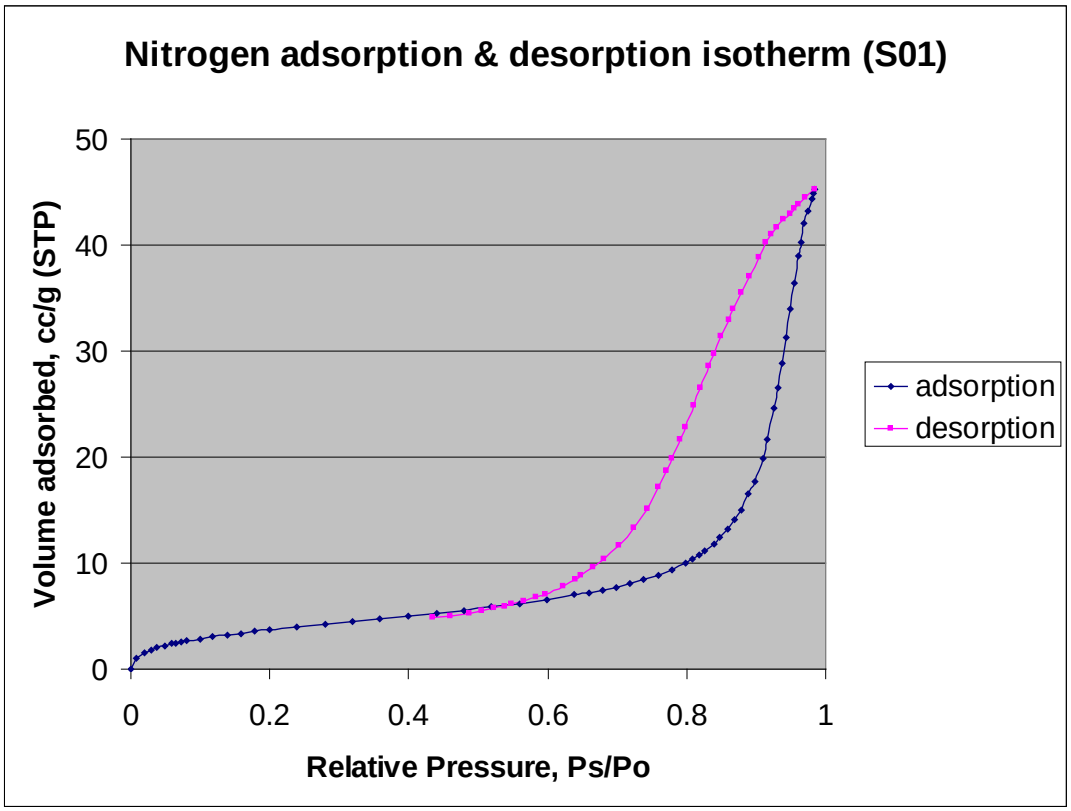

Figure 4.76: Isotherm plot for surface area and pore size analysis of S01 PHP

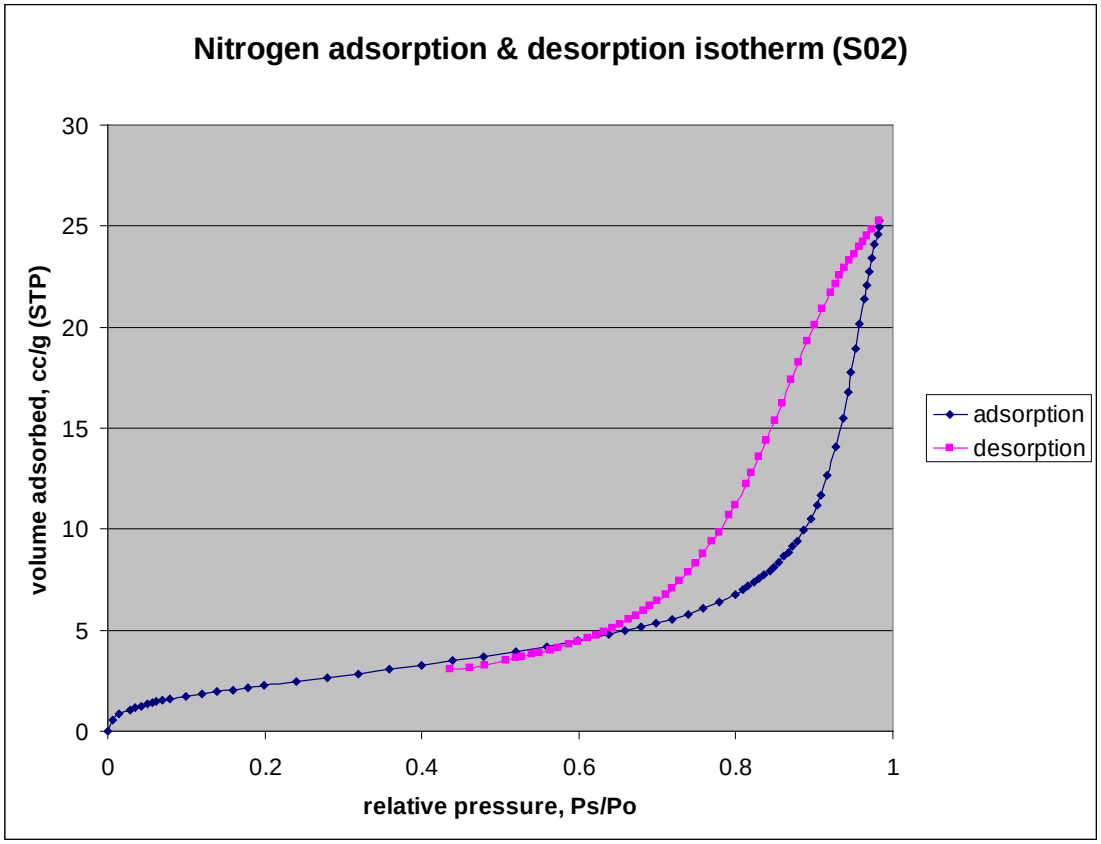

Figure 4.77: Isotherm plot for surface area and pore size analysis of S02 PHP

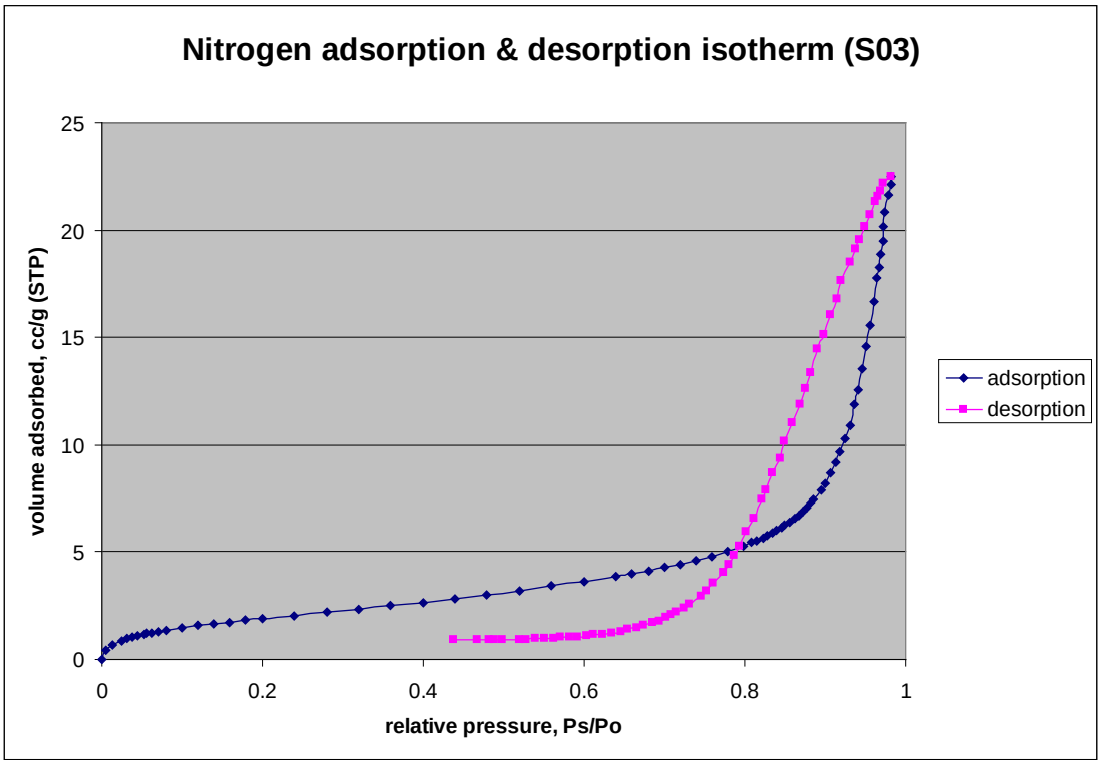

Figure 4.78: Isotherm plot for surface area and pore size analysis of S03 PHP

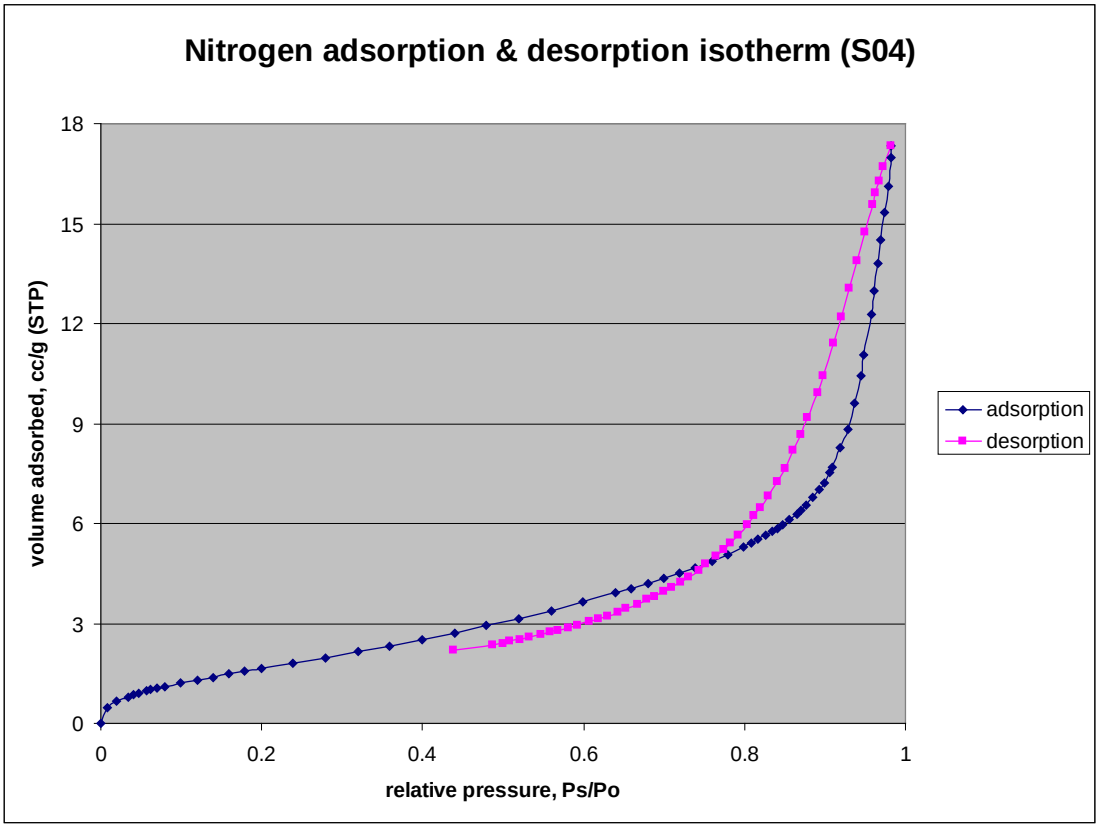

Figure 4.79: Isotherm plot for surface area and pore size analysis of S04 PHP

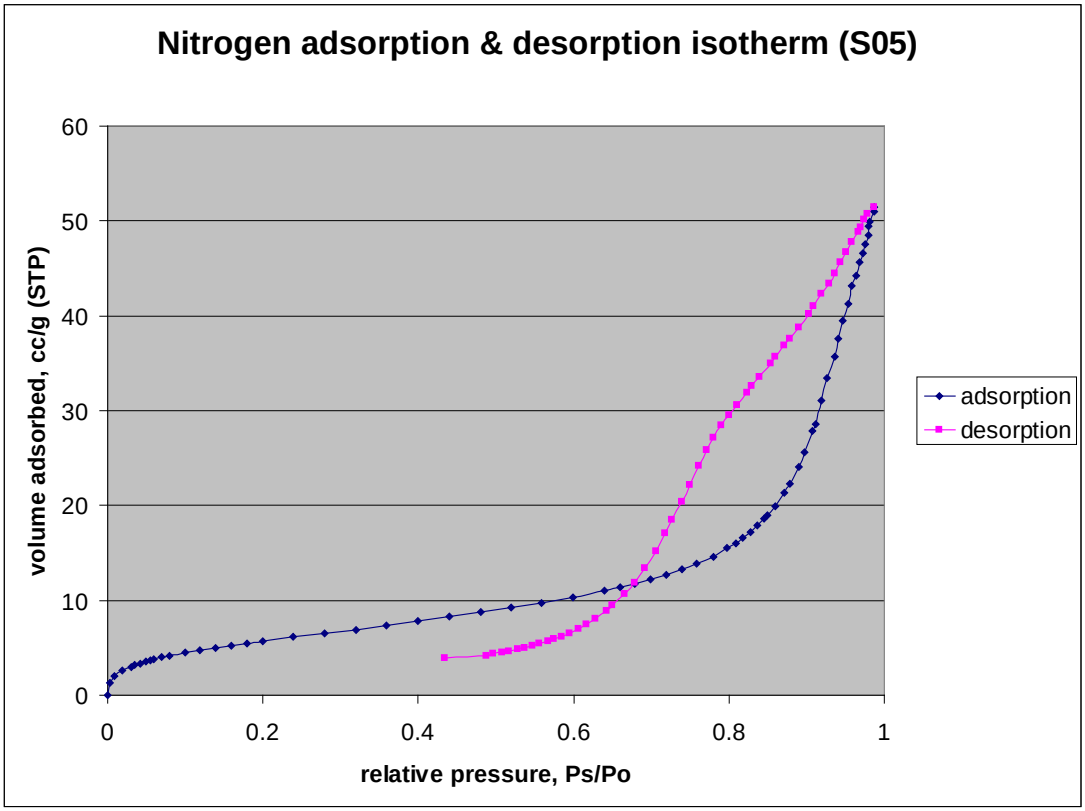

Figure 4.80: Isotherm plot for surface area and pore size analysis of S05 PHP.

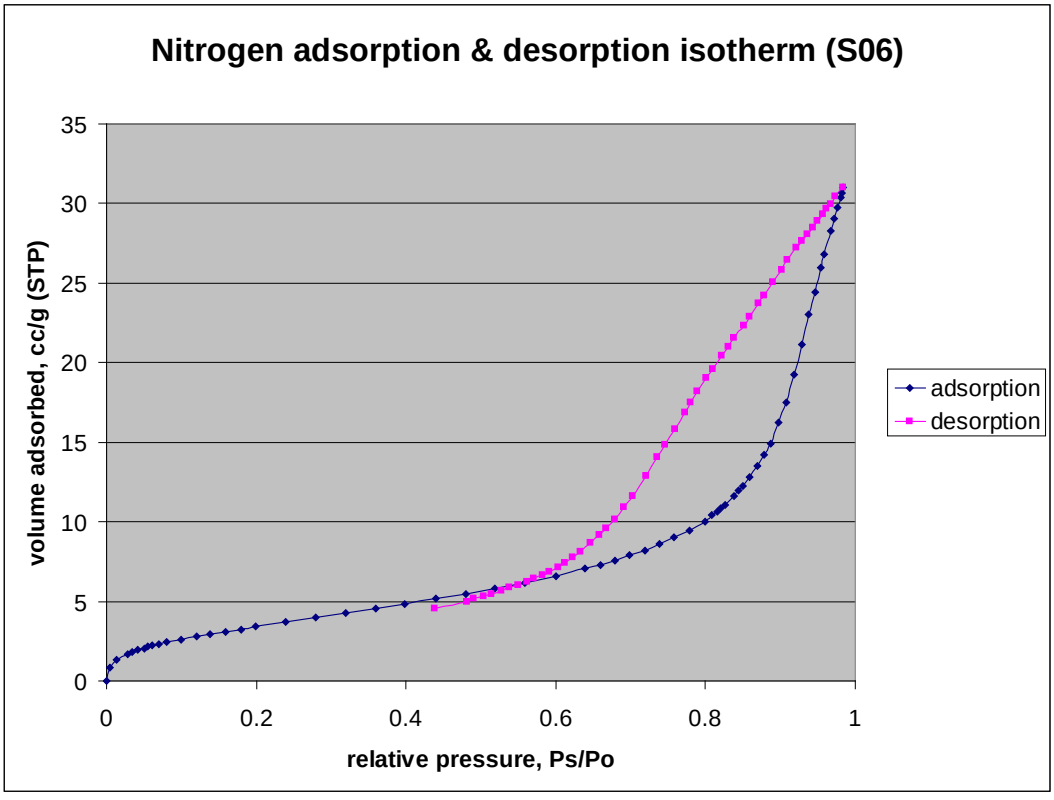

Figure 4.81: Isotherm plot for surface area and pore size analysis of S06 PHP

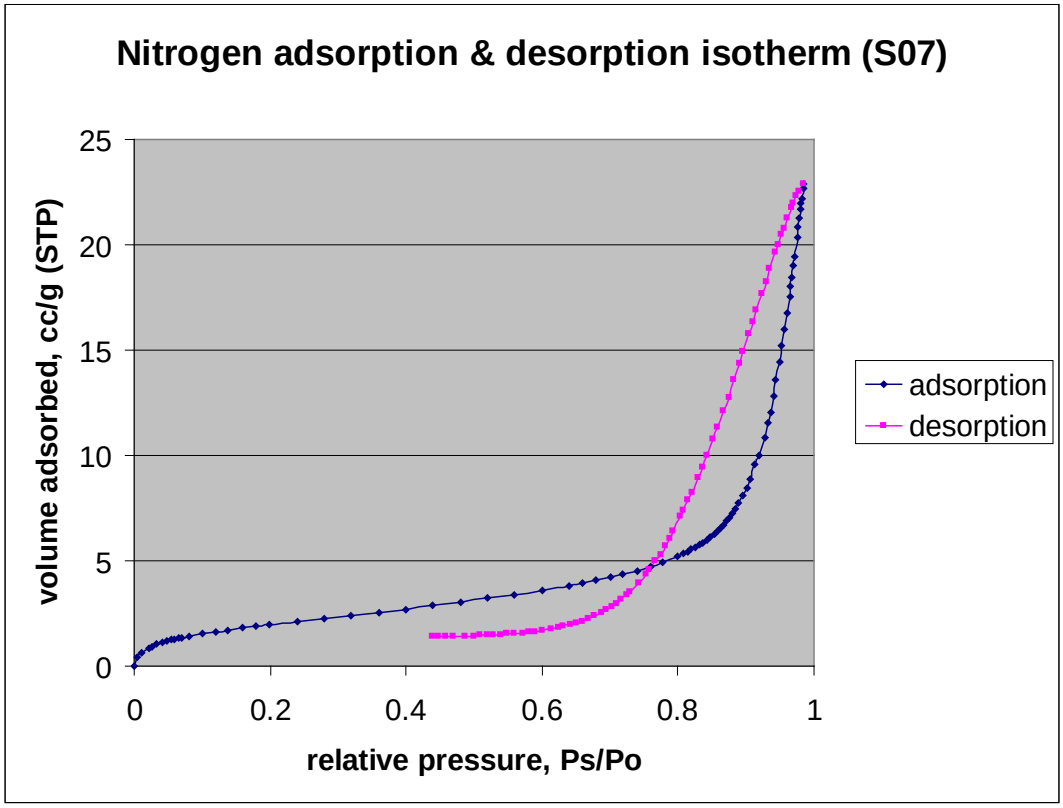

Figure 4.82: Isotherm plot for surface area and pore size analysis of S07 PHP.

4.5.2.2 Surface area

The surface areas of seven different basic PHPs are presented in Figure 4.83. The highest surface area belongs to S01 while the lowest surface area belongs to S04. Further comparisons based on certain parameters are discussed in the following paragraphs.

The results for surface area of basic PHPs produced by different percentages of oil phase are presented in Table 4.17. It has been observed that the lowest percentage of oil phase gives the highest surface area.

Statistical analysis, ANOVA concluded that there is no significant difference in the surface area of the polymers produced at three different percentage of oil phase.

Table 4.17: Surface areas for basic PHPs with different percentage of oil phase.

sample name	oil phase	surface area, m^2/g
S05	10	12.71
S06	15	12.02
S01	20	14.90

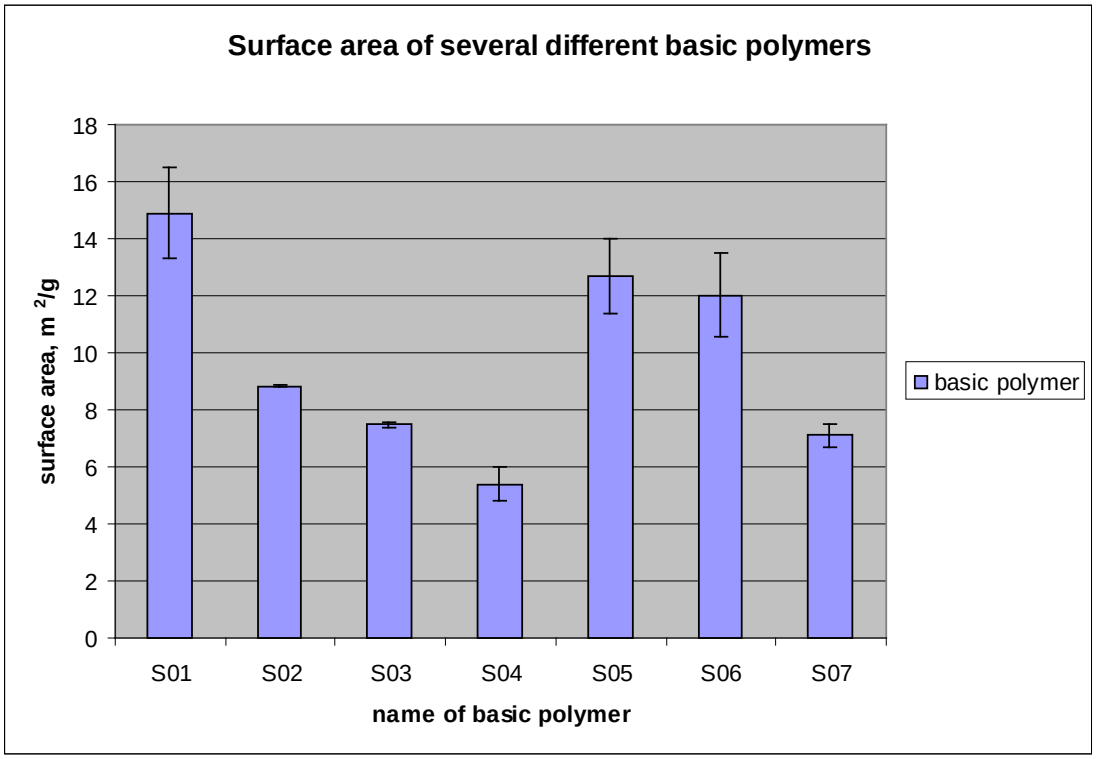

Figure 4.83: Surface area of several different basic PHPs.

The results for surface areas of basic PHPs produced by different mixing times are presented in Table 4.18 and Figure 4.84. The higher the total mixing time, the higher is the surface area.

Statistical analysis, ANOVA at 5 % significance level was further performed to check for significant difference. The results concluded that there are significant differences in the surface area of the polymers produced at four different mixing times. These differences are further analysed by Bonferroni test at 95.0% confident intervals. The pairs that are difference are between mixing time of 6 & 60 minutes, 15 & 60 minutes, 30 & 60 minutes.

Table 4.18: Surface areas for basic PHPs with different total mixing time (dosing + mixing time)

Sample name	Total mixing time, min	surface area, m^2/g
S01	60	14.90
S02	30	8.84
S07	15	7.10
S03	6	7.47

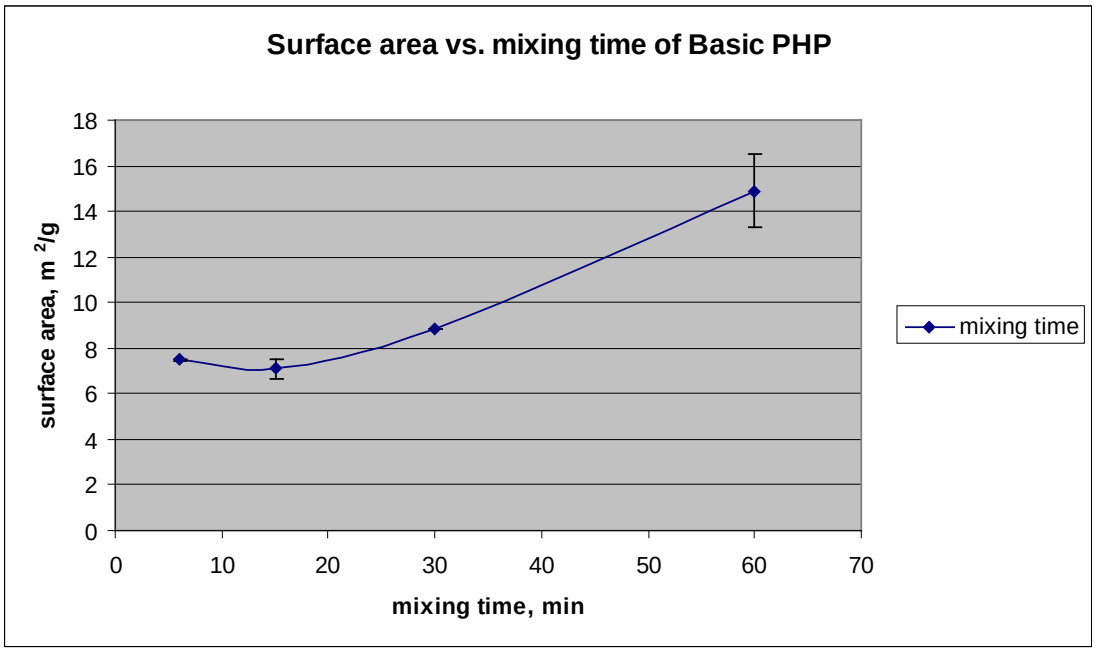

Figure 4.84: The plot of surface area as a function of mixing time.

The results for surface area of basic PHPs with two different percentages of styrene in the oil phase are presented in Table 4.19. Comparing the two samples, the one with 68% styrene has a higher surface area.

T-test at 5% significance level was performed and the result concluded that there is effect of styrene percentage on surface area of basic PHP. The two means are significantly different from one another.

Table 4.19: Surface areas for basic PHPs with two different percentages of styrene.

sample name	% styrene	surface area, m^2/g
S01	68	14.90
S04	78	5.40

4.5.2.3 Pore size distribution

The pore size distributions of each basic PHP for both desorption and adsorption curves are presented in Figure 4.85 through Figure 4.91. In summary, for desorption curve, all of the samples are having the same profile of pore size distributions. They are monomodal distributions in the range of mesoporous pores. The peaks for each sample are summarised in Table 4.20; the peaks are in the region of fine mesopore. Thus, desorption pore volumes are significantly contributed by the mesoporous pores. For adsorption curves, all the distribution profiles look similar. Details of these profiles are further discussed in section 4.5.2.4.

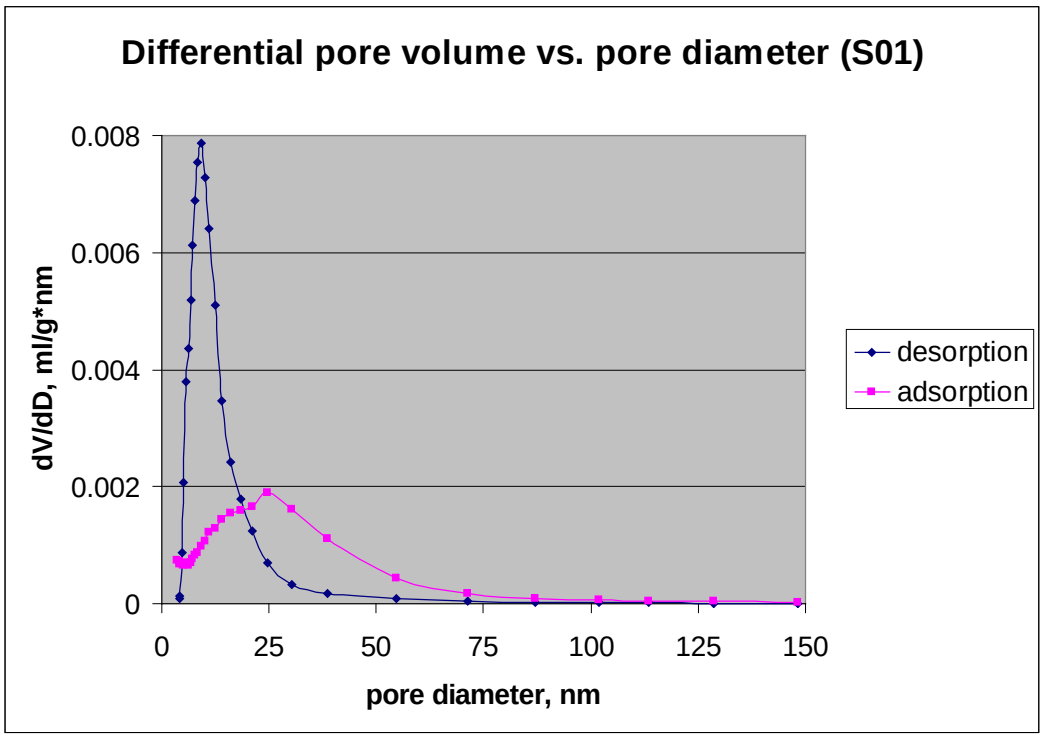

Figure 4.85: Pore size distribution for S01.

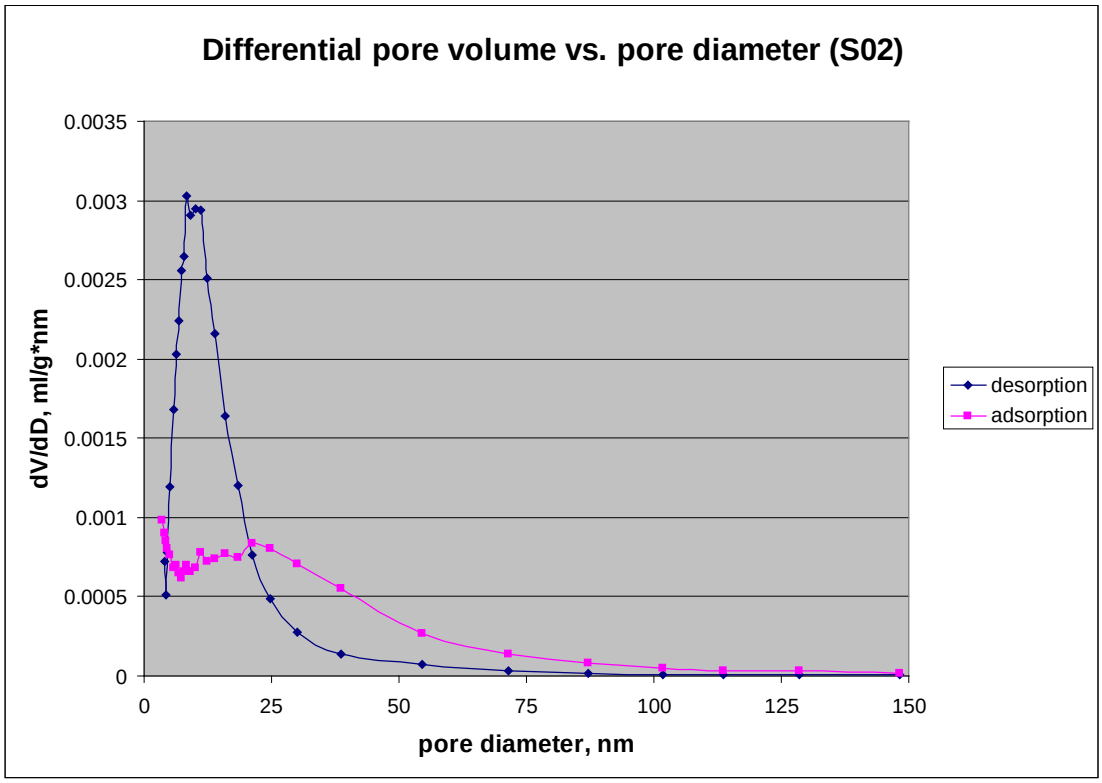

Figure 4.86: Pore size distribution, S02.

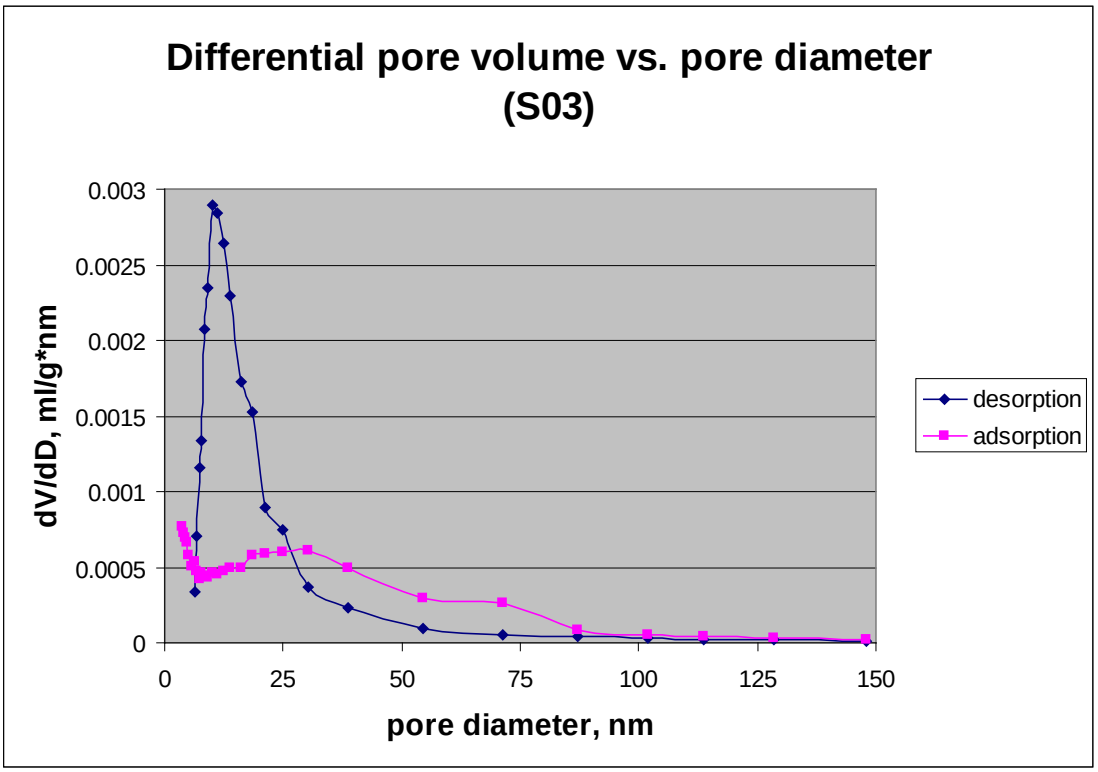

Figure 4.87: Pore size distribution, S03.

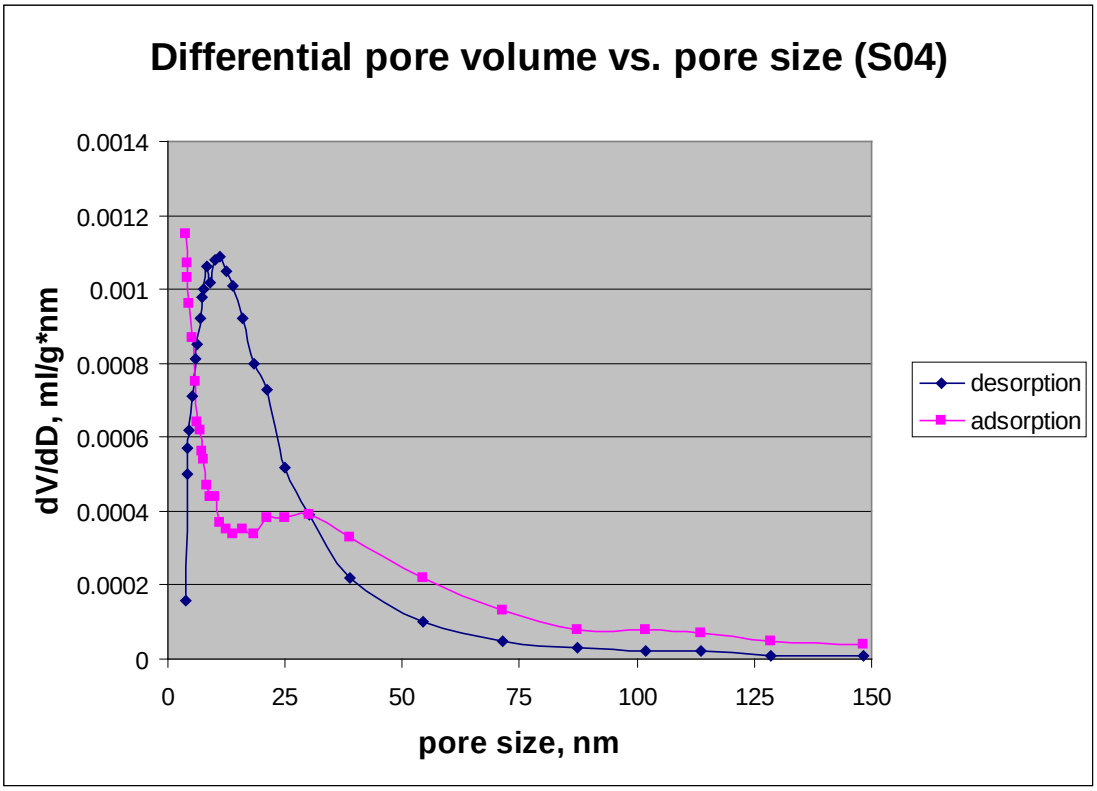

Figure 4.88: Pore size distribution, S04.

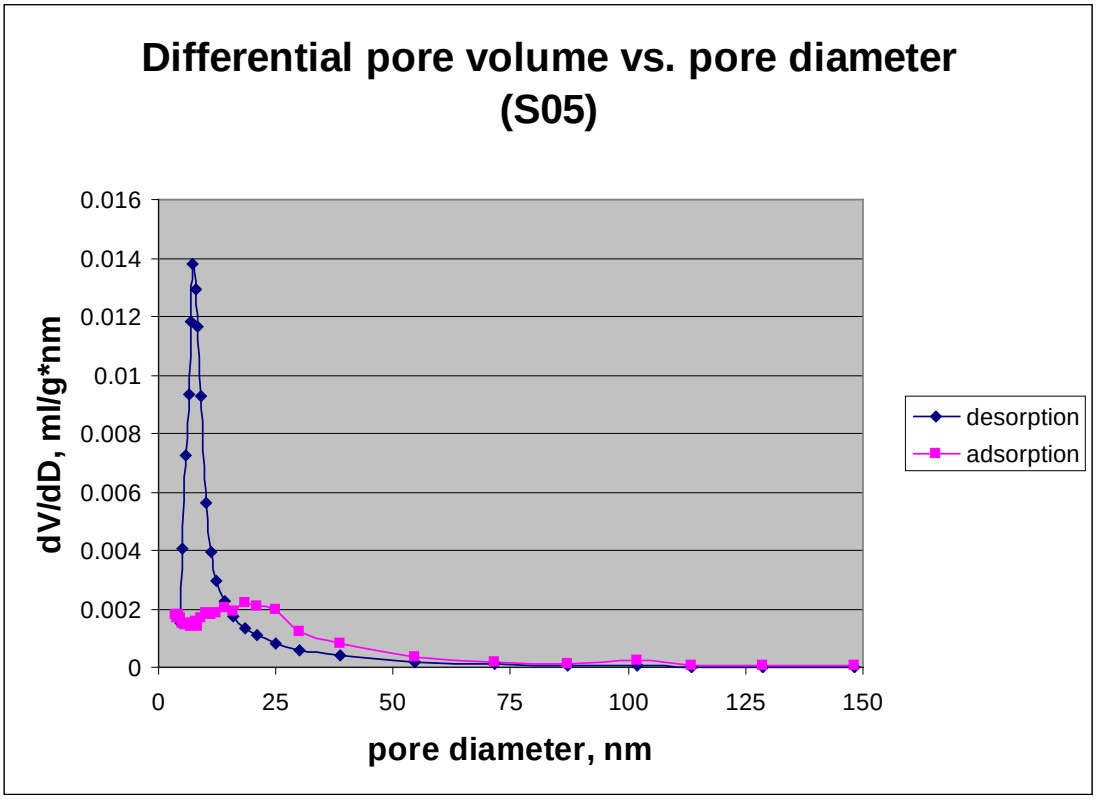

Figure 4.89: Pore size distribution, S05

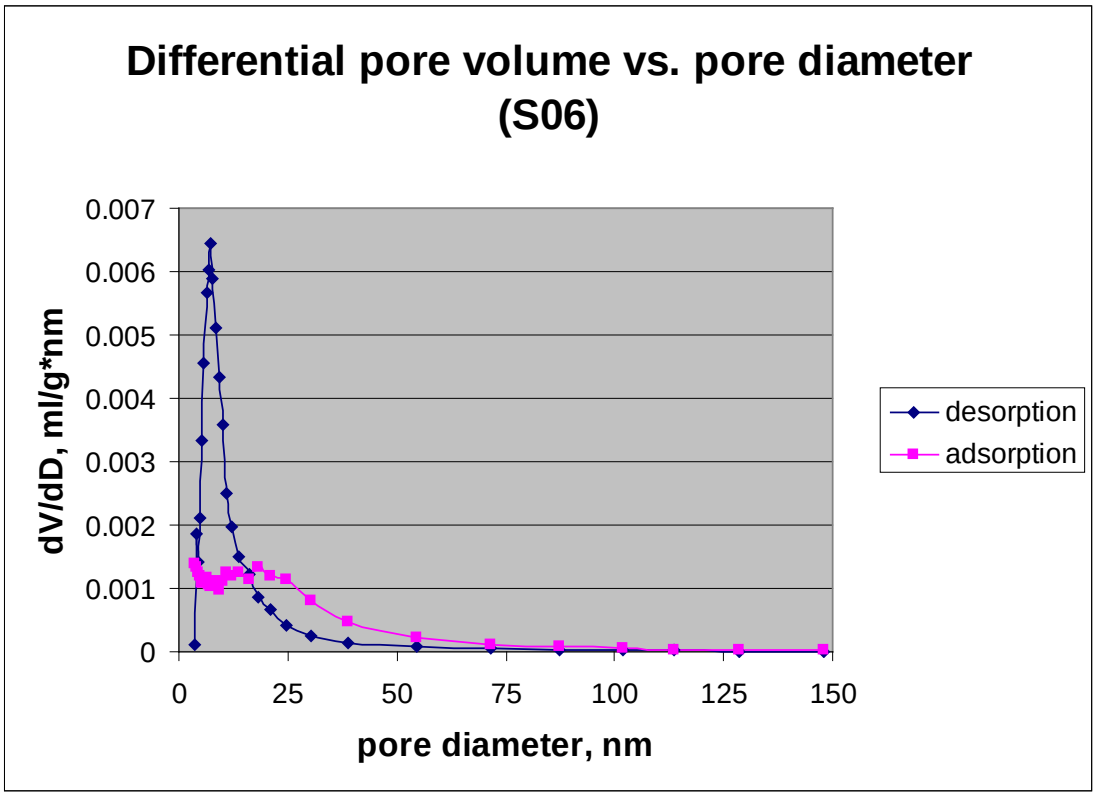

Figure 4.90: Pore size distribution, S06.

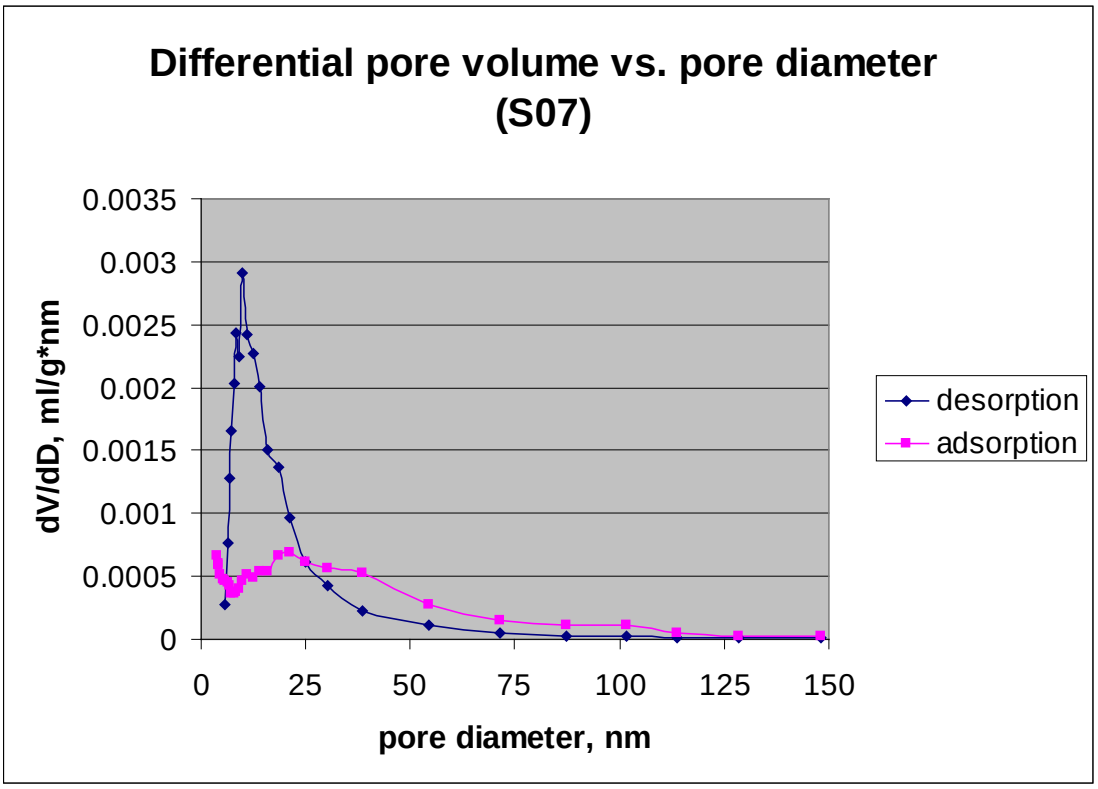

Figure 4.91: Pore size distribution, S07.

Table 4.20: Peaks for monomodal distribution of desorption curves.

Sample name	Peak, nm
S01	9.15
S02	10.01
S03	10.01
S04	10.01
S05	7.24
S06	7.24
S07	10.01

4.5.2.4 Comparison of pore size distribution

The pore size distributions for desorption curves of different kinds of basic PHPs are compared in Figure 4.92 and Figure 4.93. All of them have monomodal distribution in the range of 3 to 30 nm. S05 has the highest peak followed by S01, S06, S02, S03, S07 and S04. Thus, S05 should have the highest desorption pore volume and S04 should be the one with the minimum desorption pore volume. This is confirmed by the results presented in Table 4.21. Hence, desorption pore volumes are significantly contributed by the mesoporous pores.

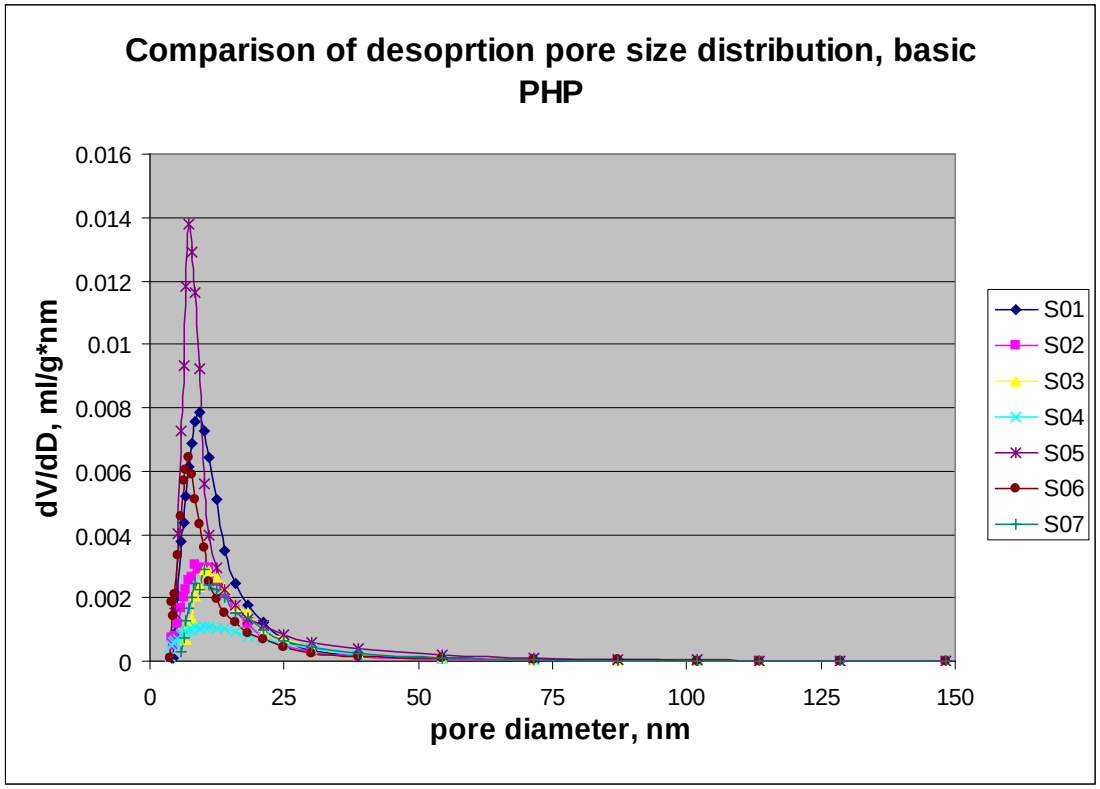

Figure 4.92: Comparison of desorption pore size distribution for basic PHP.

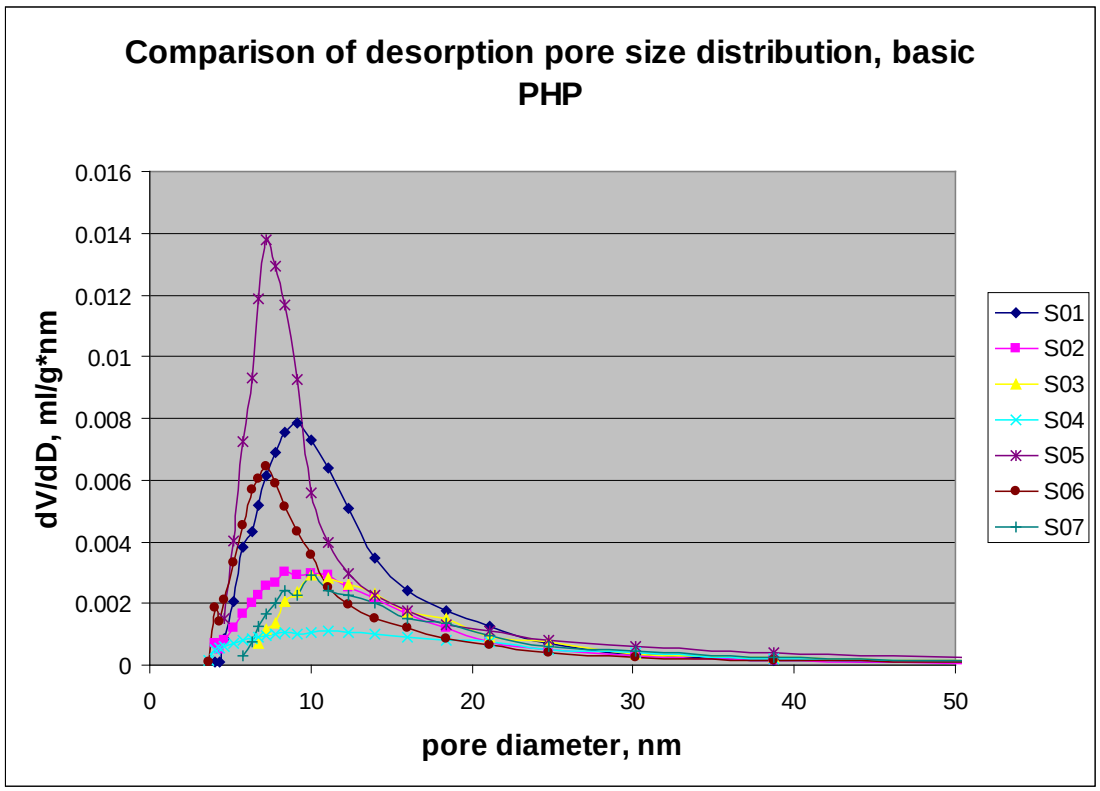

Figure 4.93: Comparison of desorption pore size distribution for basic PHPs in mesopore range.

Comparison of adsorption pore size distributions between different kinds of basic PHPs are presented in Figure 4.94 and Figure 4.95. All of them are monomodal distributions in the mid region of mesoporous range and not in the fine region. Similar to desorption curves, S05 has the highest peak here, followed by S01, S06, S02, S07, S03 and S04. This result agrees with the adsorption pore volumes listed in Table 4.21. Thus, the adsorption pore volumes are significantly contributed by mesoporous pores.

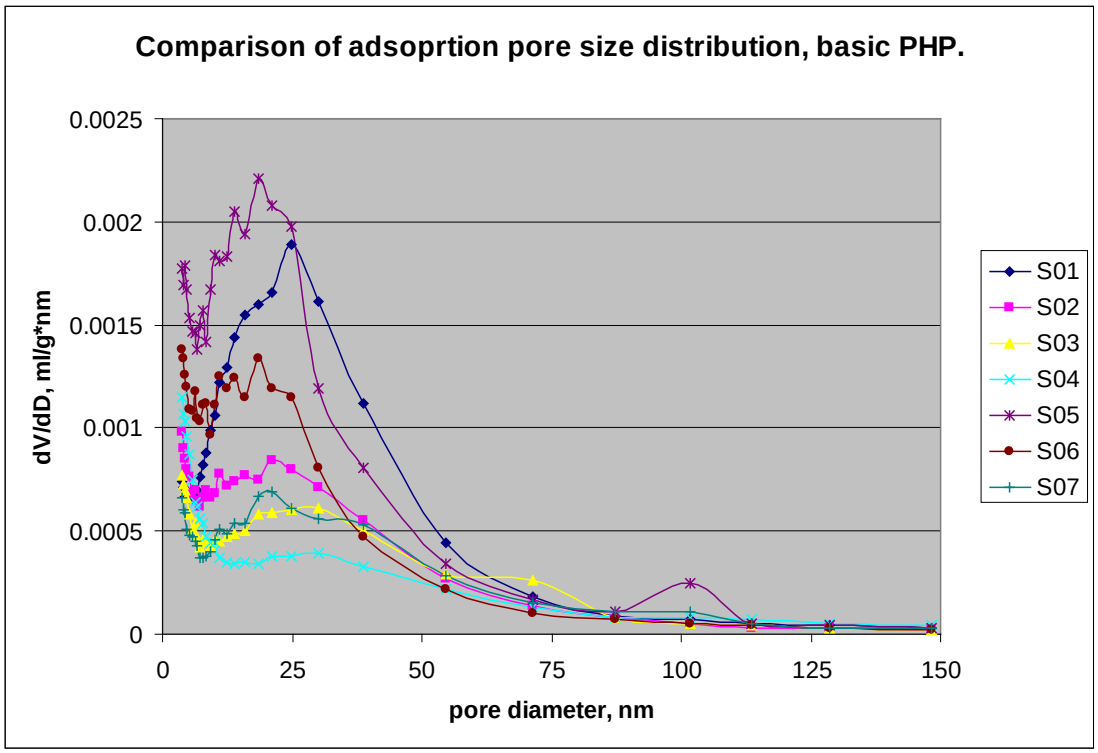

Figure 4.94: Comparison of adsorption pore size distribution for basic PHPs.

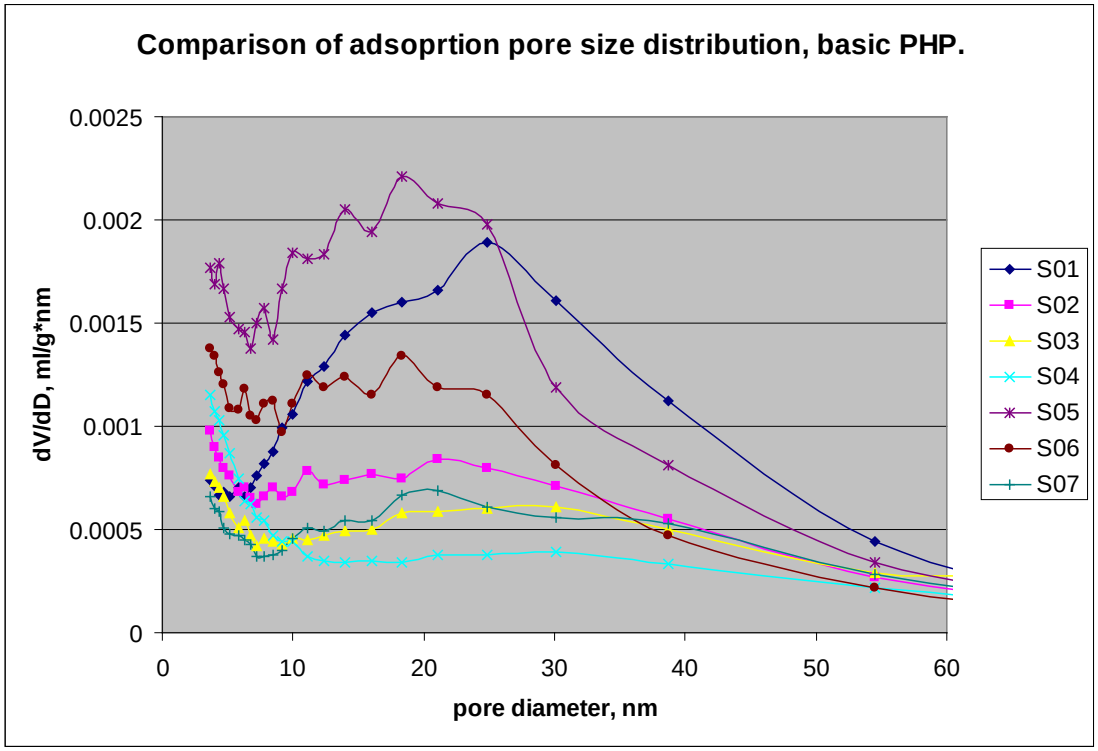

Figure 4.95: Comparison of adsorption pore size distribution for basic PHPs in mesopore range.

Comparison of pore volumes between basic PHPs having different percentage of oil phase is presented in Figure 4.96 and Figure 4.97. S05, the one with the lowest percentage of oil phase has the highest peak while S01 the one with the highest oil phase percentage has the second highest peak. S06, the one with the medium oil phase percentage has the lowest peak. These results of both desorption and adsorption curves are in agreement with the pore volumes listed in Table 4.21.

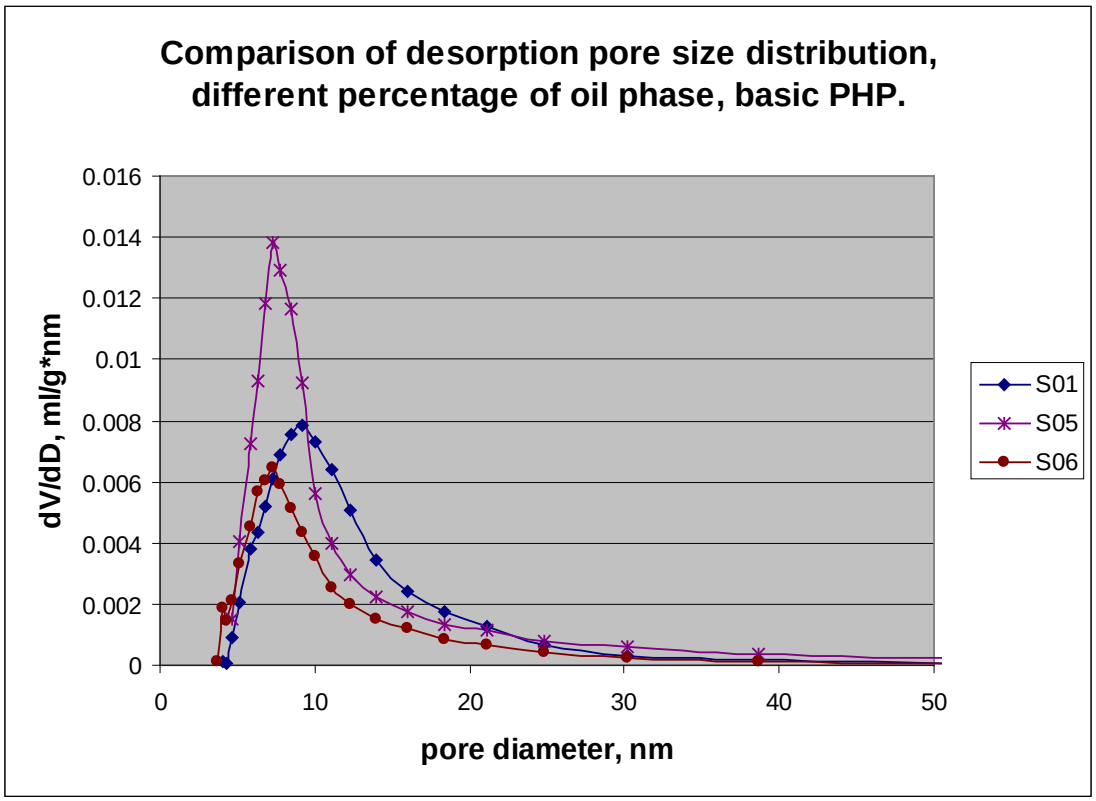

Figure 4.96: Comparison of desoprtion pore size distribution – samples with different percentage of oil phase.

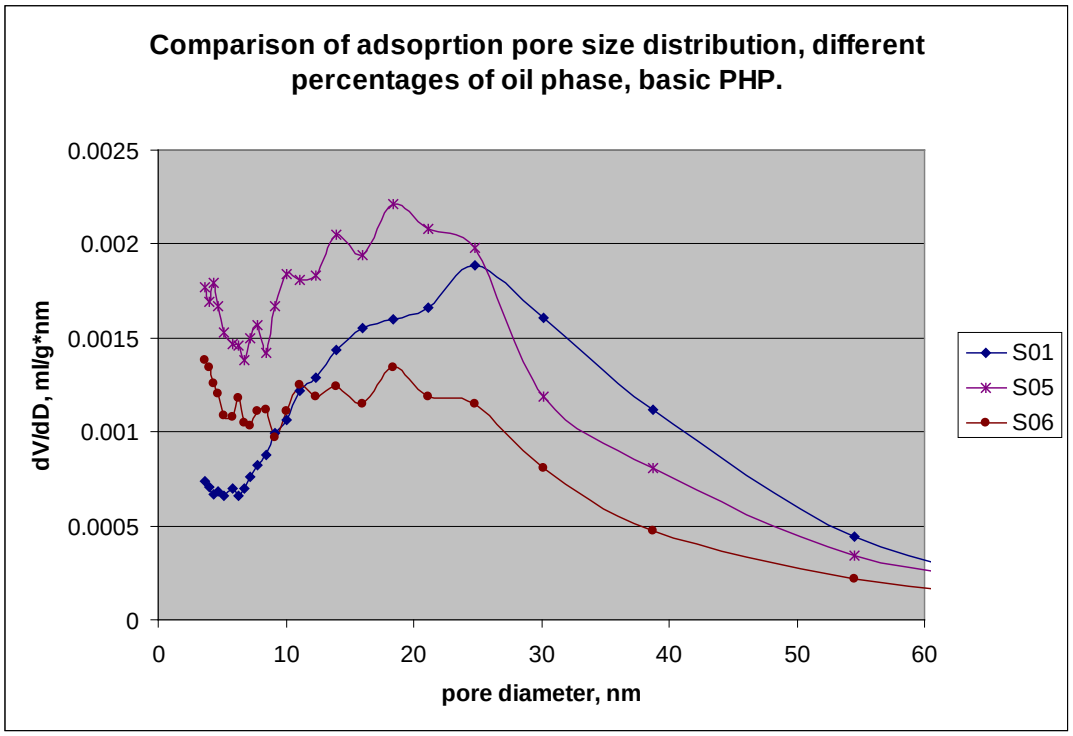

Figure 4.97: Comparison of adsorption pore size distribution – samples with different percentage of oil phase.

Comparison of pore volumes between basic PHPs having different mixing times is presented in Figure 4.98 and Figure 4.99. S01, the one with the highest mixing time of 60 minutes is the only one exhibits significant difference in the peak height. The rest of the samples have similar peaks. This agrees with the results listed in Table 4.21.

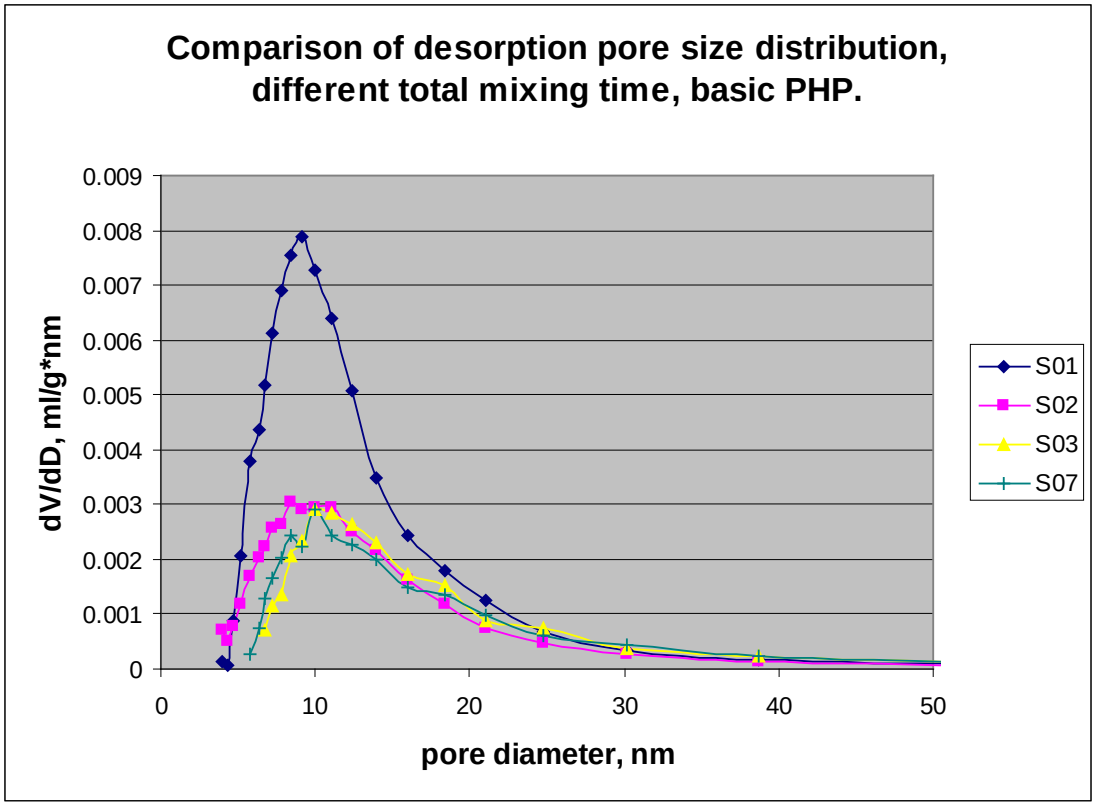

Figure 4.98: Comparison of desorption pore size distribution – samples of different mixing time.

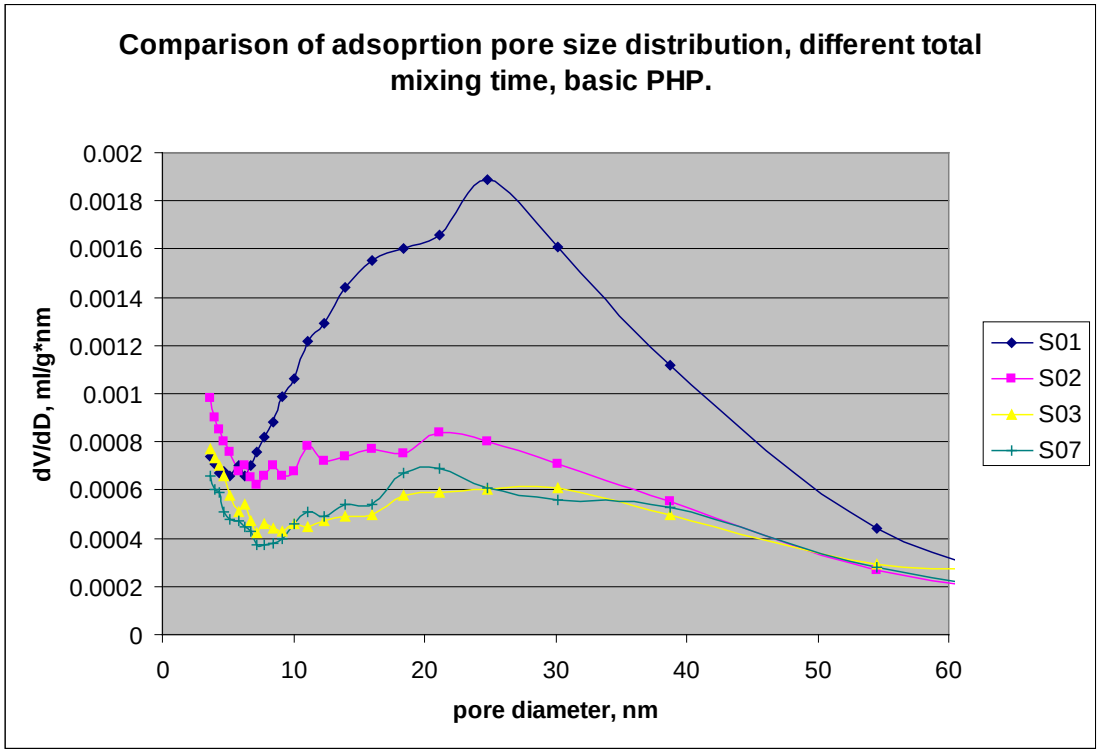

Figure 4.99: Comparison of adsorption pore size distribution – samples of different mixing time.

The comparison of pore size distributions between the two samples with different percentages of styrene is presented in Figure 4.100 and Figure 4.101. It has been observed that the two samples differ significantly between one another. S01 is the one with the highest peak and S04 is the one with the lowest peak. This has been verified by desorption and adsorption pore volumes. Further statistical analysis of two-sample t-test was performed at 5% significance level. The results conclude that the means are not equal, i.e. there is effect of styrene percentage on all types of pore volume of basic PHP.

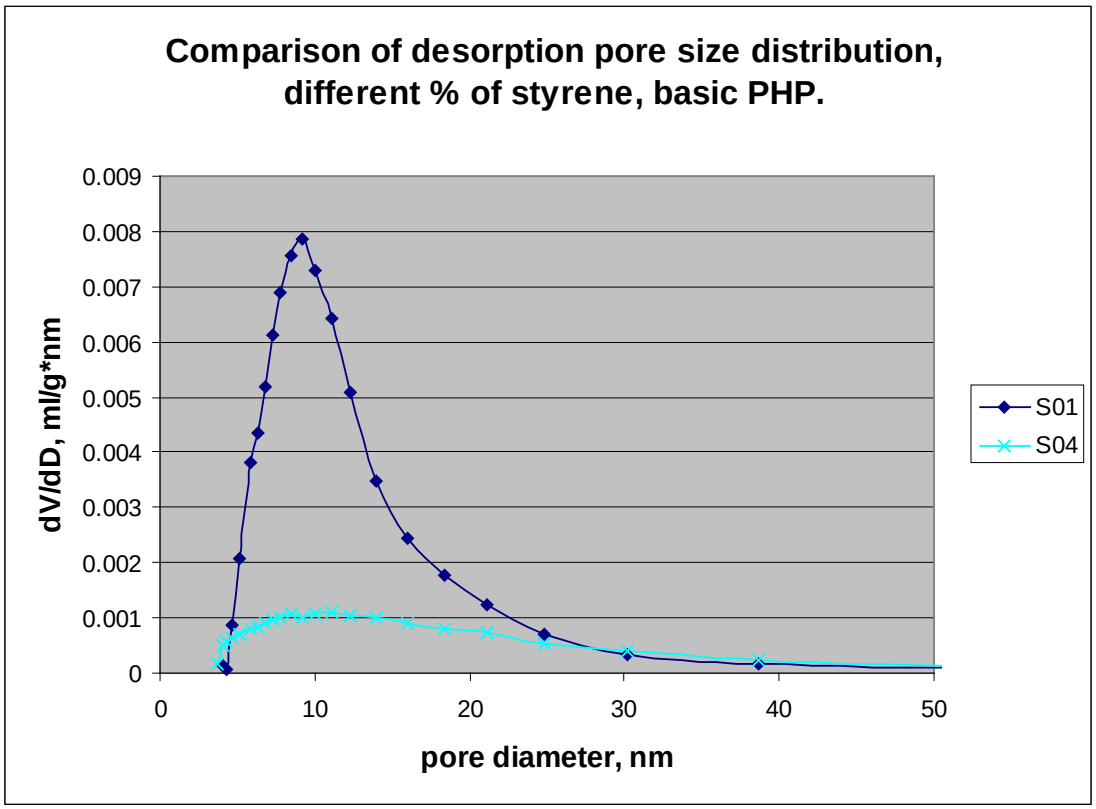

Figure 4.100: Comparison of desorption pore size distribution – samples with different percentage of styrene.

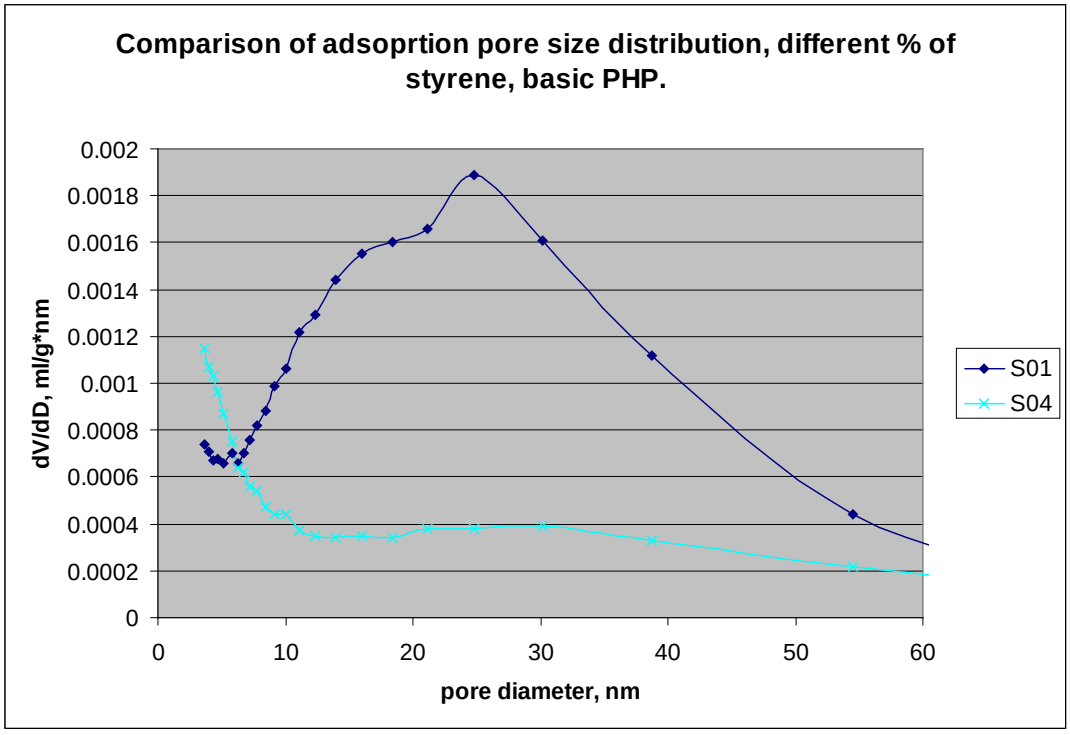

Figure 4.101: Comparison of adsorption pore size distribution - samples with different percentages of styrene.

Total pore volumes of desorption and adsorption curves for basic PHPs are presented in Table 4.21. The highest desorption pore volume, adsorption pore volume and total pore volume belongs to S05 and S01, the basic PHP with the least percentage of oil phase with 68% styrene. S04, the one with 78% styrene in the oil phase has the lowest desorption pore volume, adsorption pore volume and total pore volume. From the percentages of pore volumes listed in Table 4.21, it can be concluded that pore volumes are significantly contributed by the mesoporous pores. Comparison of pore volumes of several basic PHPs are presented in Figure 4.102.

Table 4.21 : Total pore volumes of basic PHPs.

Sample name	Desorption pore volume, ml/g			Adsorption pore volume, ml/g		
	mesopore	% of mesopore	Total	mesopore	% of mesopore	Total
S01	0.0813	95.2	0.0853	0.0647	83.5	0.0775
S02	0.0400	93.4	0.0428	0.0318	79.2	0.0401
S03	0.0598	92.6	0.0646	0.0460	72.6	0.0635
S04	0.0281	86.3	0.0326	0.0208	64.0	0.0325
S05	0.0736	90.7	0.0811	0.0611	81.8	0.0748
S06	0.0485	92.0	0.0528	0.0398	81.3	0.0489
S07	0.0508	91.7	0.0554	0.0399	74.3	0.0536

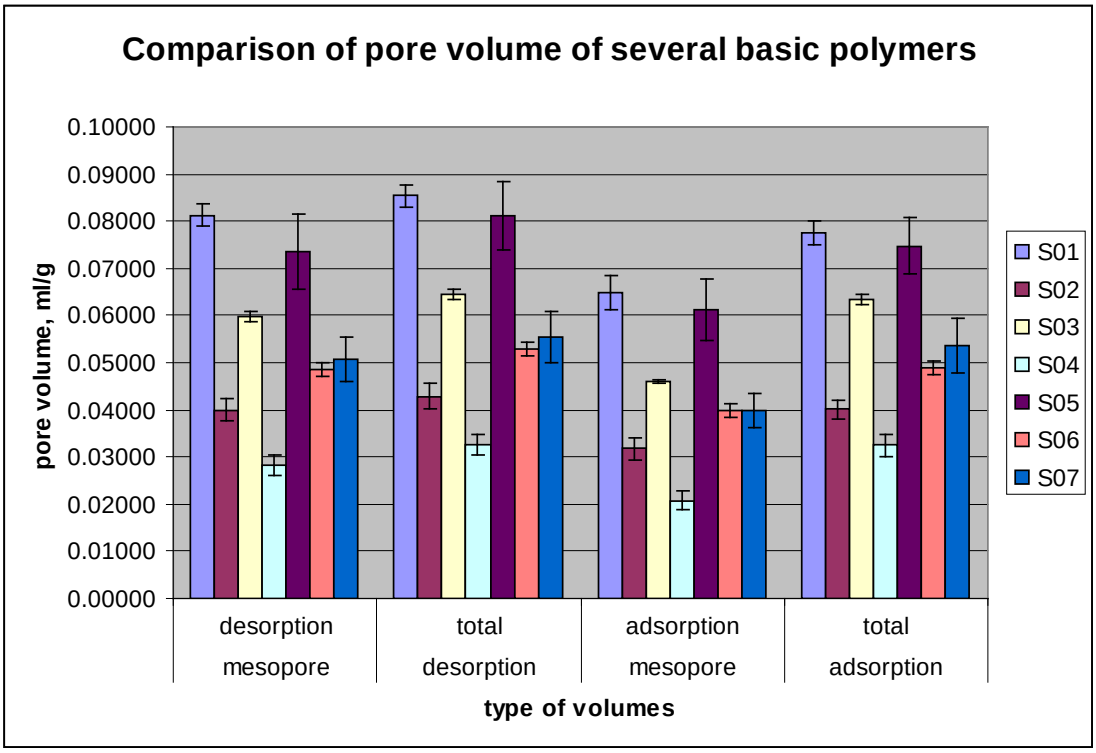

Figure 4.102: Comparison of pore volumes of several basic PHPs.

4.5.3 FTIR analysis

The spectrum for basic PHP S01 is presented in Figure 4.103. There were several absorption peaks for the band lower than 1000 cm^{-1}. The peak at 697.189 cm^{-1} is very strong, followed by medium intensity peak at 757.32 cm^{-1}, and weak intensity peaks at 796.985, 838.846 and 904.611 cm^{-1}. The very intense peaks at 697 and 757 cm^{-1} are attributed to out-of-plane C–H bends of the aromatic ring (Bhagiyalakshmi et al., 2010; Vinodh et al., 2010; Jiang and Zeng, 2009). The weak peaks of 797 and 905 cm^{-1} are attributed to phenyl rings (Mercier et al., 2000). According to Hubbard et al. (1998), 797 and 838 cm^{-1} bands are attributed to phenyl ring while 905 cm^{-1} is attributed to a mixed band of weak monosubstituted phenyl ring, medium to weak disubstituted phenyl ring and strong vinyl group. Three peaks are observed in the region of 1000 to 1300 cm^{-1}, 1028.63 is attributed to monosubstituted phenyl ring (Mercier et al., 2000), 1057.99 (Mercier et al., 2001) and 1181.320 cm-1 (Choudhary et al., 2000) belongs to C–O stretch. These bands disappeared after incorporation of VTMS and bindzil. An absorption peak at 1738.833 cm^{-1} is attributed to C=O stretch carbonyl group, (Leber et al., 2007; Mercier et al., 2001; Choudhary et al., 2000).

Mixed band with absorption peaks at 1367.583, 1451.893, 1492.860 are attributed to aromatic ring backbone –CH– bending vibration (Vinodh et al., 2010). 1601.042 cm^{-1} corresponds to bands of C=C in aromatic ring from styrene unit (Vinodh et al., 2010). Absorption peaks of 2850.435 and 2920.689 cm^{-1} are attributed to C–H stretching vibration of methyl and methylene groups (Rubino et al., 2010; Vinodh et al., 2010; Shi et al., 2009; Herrera et al., 2005). 3025.345 and 3059.288 cm^{-1} absorption peaks are due to =C–H stretch in aromatic rings (Ungureanu et al., 2007).

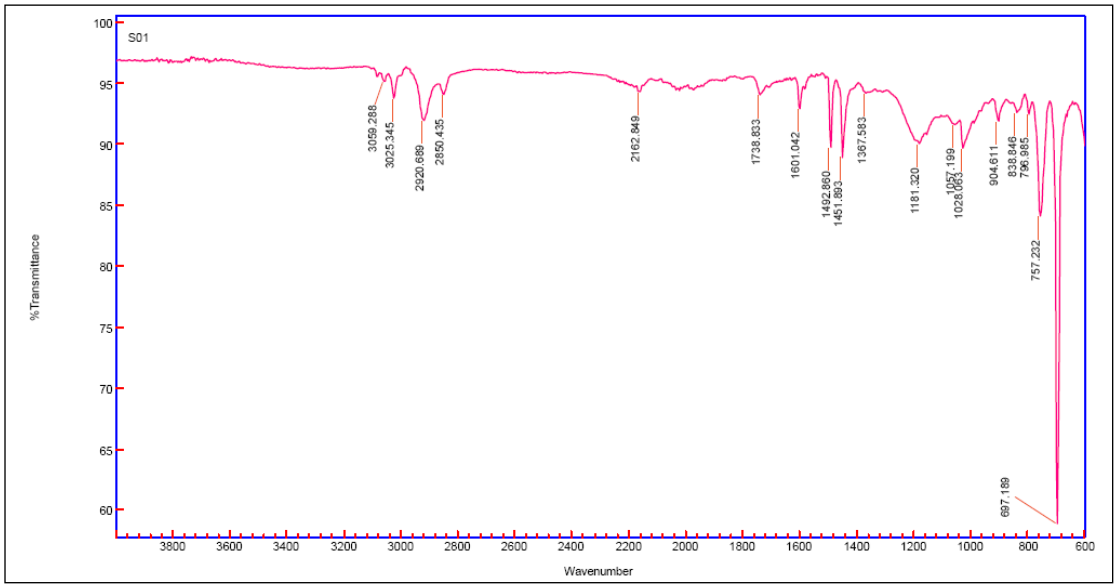

Figure 4.103: FTIR Spectrum of basic PHP, S01.

4.6 *Silica or Bindzil PHP – second phase.*

4.6.1 Morphology

The images of both B10 and B30 PHPs are presented in Figure 4.104. It has been observed that the pores of B30 are bigger than the pores of B10. It appears that B10 has higher porosity and has more interconnecting pores than B30. Higher magnifications of both PHPs show the presence of spherical particles. The wall structures of both PHPs look similar. Some closed pores could also be observed in B30 image (c).

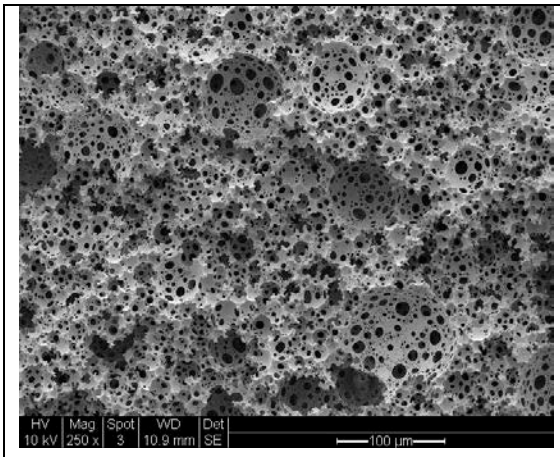

(a) B10 X250, smaller pore but bigger and more interconnect

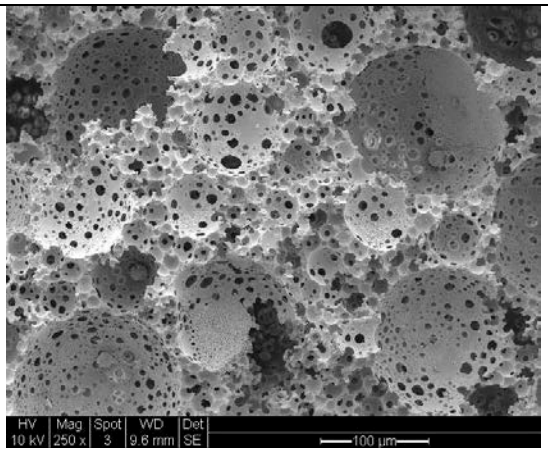

(b) B30 X250, bigger pores but smaller and less interconnect.

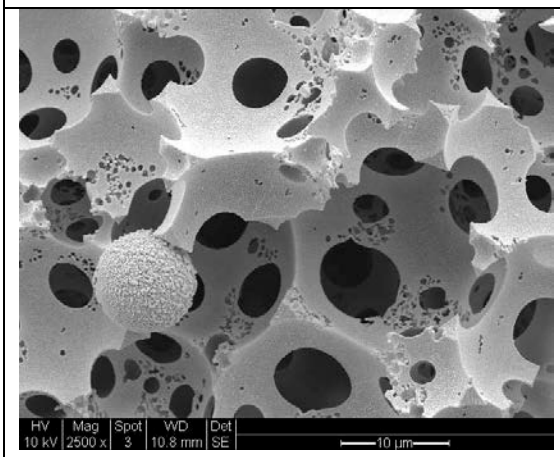

(c) B10 at higher magnification showing presence of spherical particles.

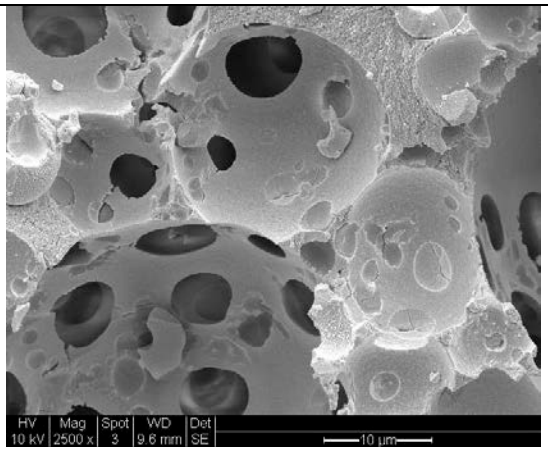

(d) B30 at higher magnification showing presence of spherical particles.

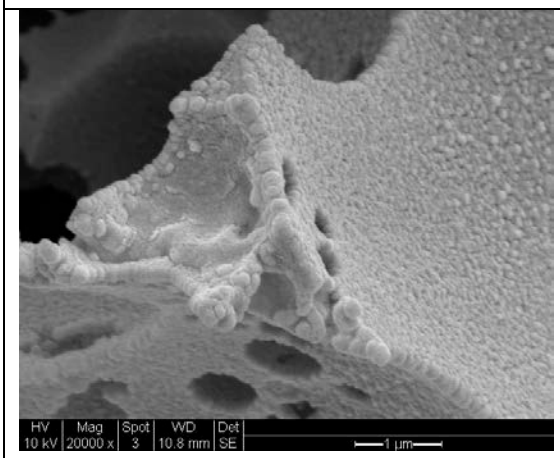

(e) B10, wall structure.

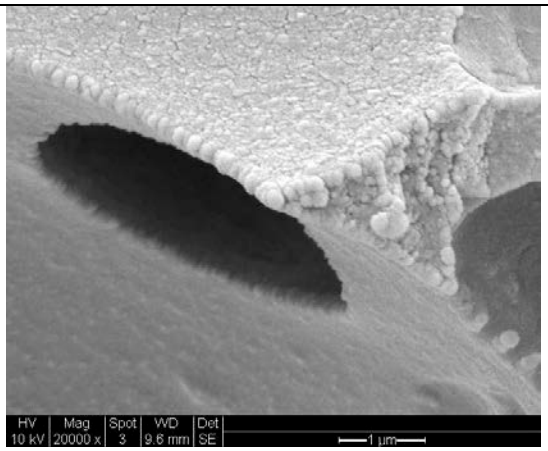

(f) B30, wall structure.

Figure 4.104: Comparison of the images between B10 & B30.

4.6.2 Surface area and pore size distribution

The surface area and pore size distribution are analysed by physisorption process of nitrogen as the adsorbate at liquid nitrogen temperature, 77K.

4.6.2.1 Isotherm

The nitrogen adsorption and desorption isotherms for B10 and B30 PHPs are presented in Figure 4.105 and Figure 4.106 respectively. Both are reversible type IV isotherm with no limiting values as Ps/Po approaches 1. Both have the same adsorption isotherm but with a slight difference in hysteresis. B10 has a narrower part of hysteresis especially in the initial part of it compared to B30. These isotherms are less steep and wider compared to VTMS PHP isotherms. Both hysteresis are Type H4 loop and often been associated with narrow slit-like pores (Sing et al., 1985). Comparison of B10 and B30 isotherms is presented in Figure 4.107.

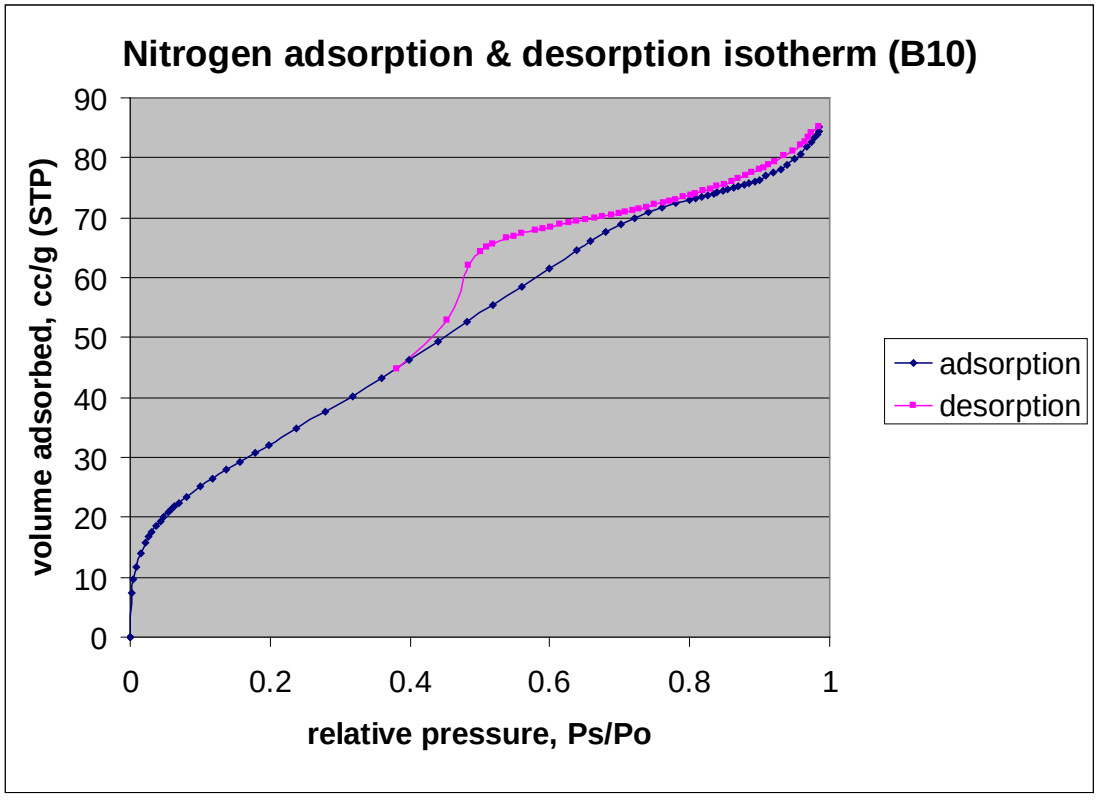

Figure 4.105: Isotherm plot for surface area and pore size analysis of B10 PHP.

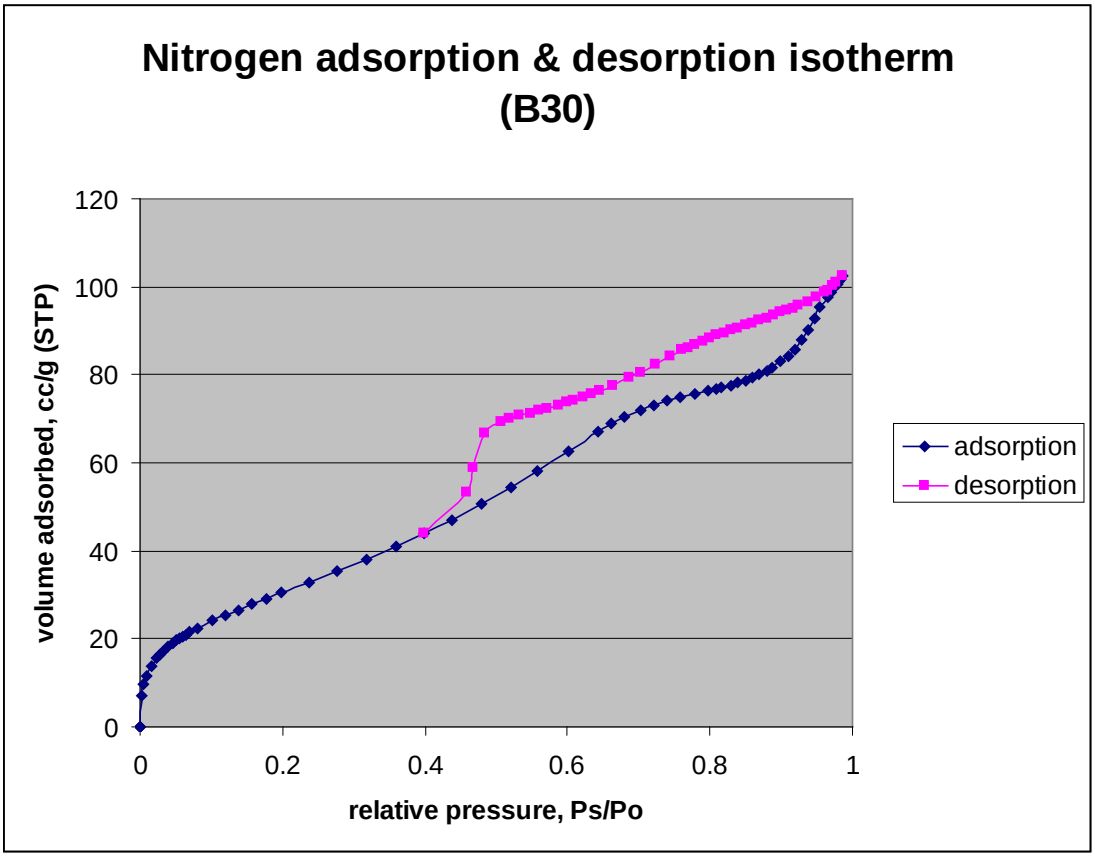

Figure 4.106: Isotherm plot for surface area and pore size analysis of B30 PHP.

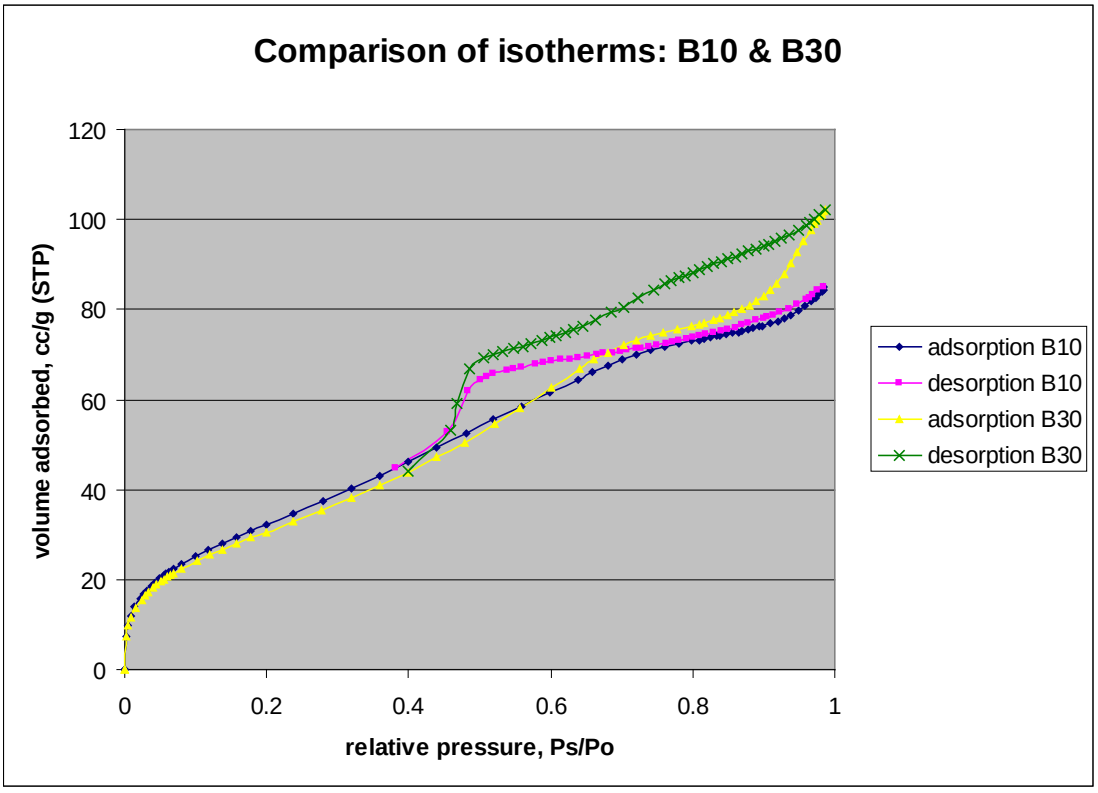

Figure 4.107: Comparison of isotherms, B10 & B30 PHP.

4.6.2.2 Surface area.

The surface area for Bindzil 10 and Bindzil 30 PHPs is presented in Table 4.22 and Figure 4.108. The standard errors of both PHPs are small and acceptable. The two values do not differ significantly as expected due to the overlapping of both standard errors. Statistical analysis, T-test at 5% significance level concludes that there is no significant difference between surface area of B10 and B30 PHP.

Table 4.22: Surface area for B10 and B30 PHP.

Sample name	Surface area, m^2/g	Standard error
B10	118.35	2.22
B30	113.39	3.07

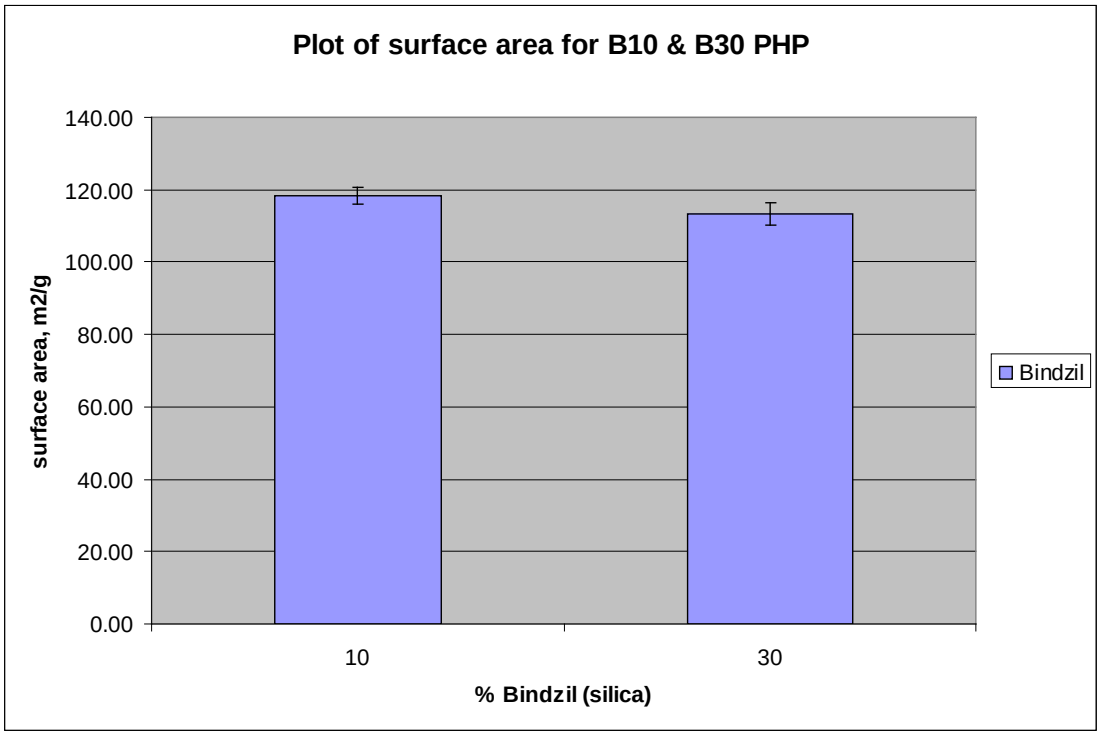

Figure 4.108: Plot of surface area of B10 and B30 PHP.

4.6.2.3 Pore size distribution.

The pore size distribution for binzil (silica) PHP is presented in Figure 4.109 through Figure 4.112. The figures represent pore volume contribution of each

individual pore diameter. In general, 90% of pore volumes of both adsorption and desorption curves for both silica PHPs are contributed by mesopores. This is confirmed by the values listed in Table 4.25. Specifically, both curves exhibit higher differential pore volume for fine pore diameters of mesopore. Thus, pore volume is significantly contributed by lower value range of mesopores. From both desorption and adsoprtion curve, more than 50% of pore volume is contributed by mesopore of size 4 nm and less. This result is presented further in Table 4.23 and Table 4.24.

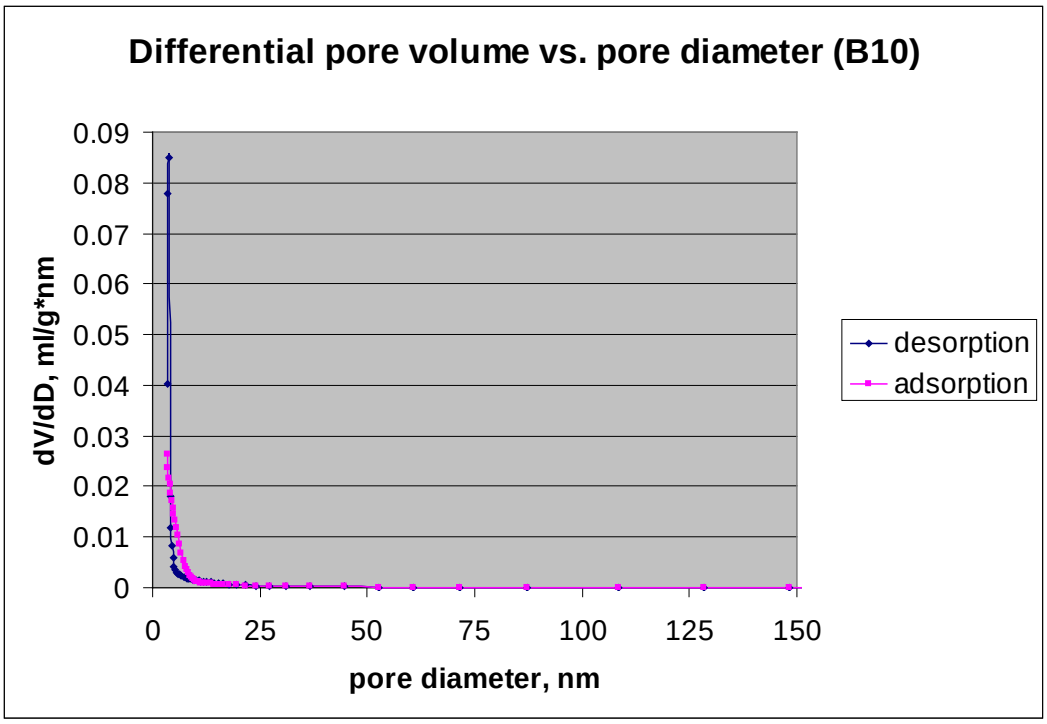

Figure 4.109: Pore size distribution for B10 PHP.

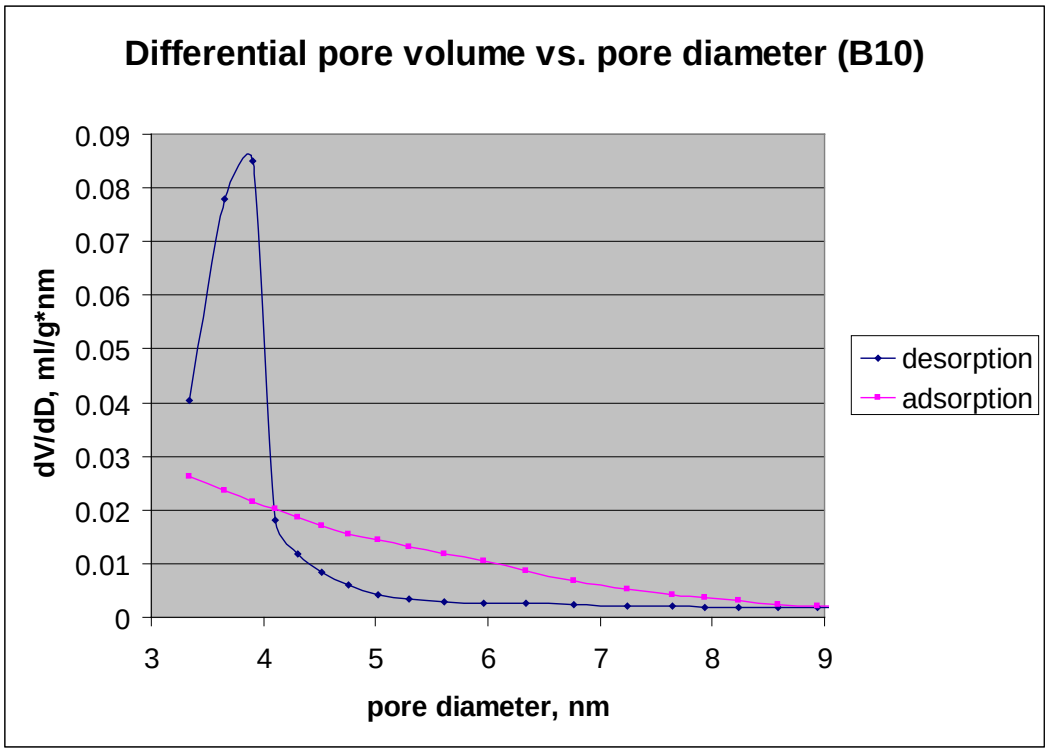

Figure 4.110: Pore size distribution for low range mesopores of B10 PHP.

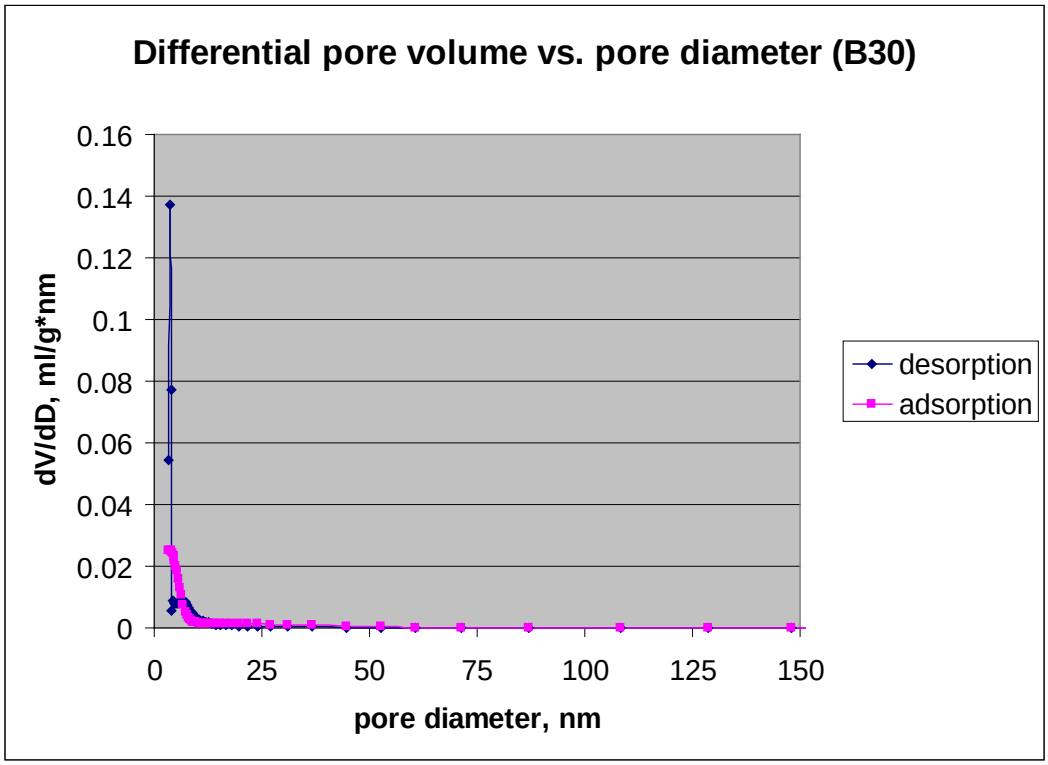

Figure 4.111: Pore size distribution for B30 PHP.

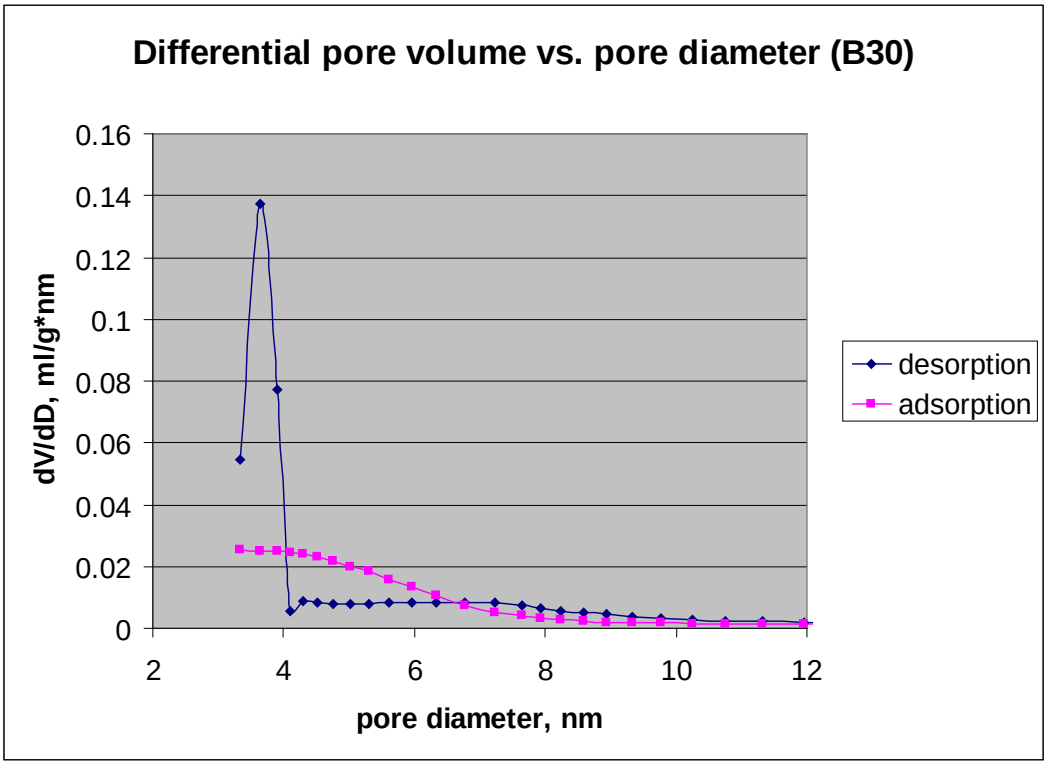

Figure 4.112: Pore size distribution for low range mesopores of B30 PHP.

Table 4.23: Desorption pore size distribution.

Sample name	mesopore volume, ml/g	Range of average pore size, nm	% pore volume
B10	0.0535	3.19 – 4.00	54.71
	0.0383	4.00 – 49.29	39.16
B30	0.0761	3.19 – 4.00	52.09
	0.0341	4.00 – 49.29	42.87

Table 4.24: Adsorption pore size distribution.

Sample name	Pore volume, ml/g	Range of average pore size, nm	% pore volume
B10	0.0600	3.19 – 7.50	67.02
	0.0218	7.50 – 49.29	24.38
B30	0.0720	3.19 – 7.50	56.09
	0.0436	7.50 – 49.29	33.97

4.6.2.4 Comparison of pore size distribution.

The comparison of pore volume distribution in the low value of mesopore was done and presented in Figure 4.113 and Figure 4.114. Desorption and adsorption pore volumes for both B10 and B30 PHPs are significantly contributed by low value of mesopores, for desorption curve, below 4 nm and for adsorption curve, below 8 nm.

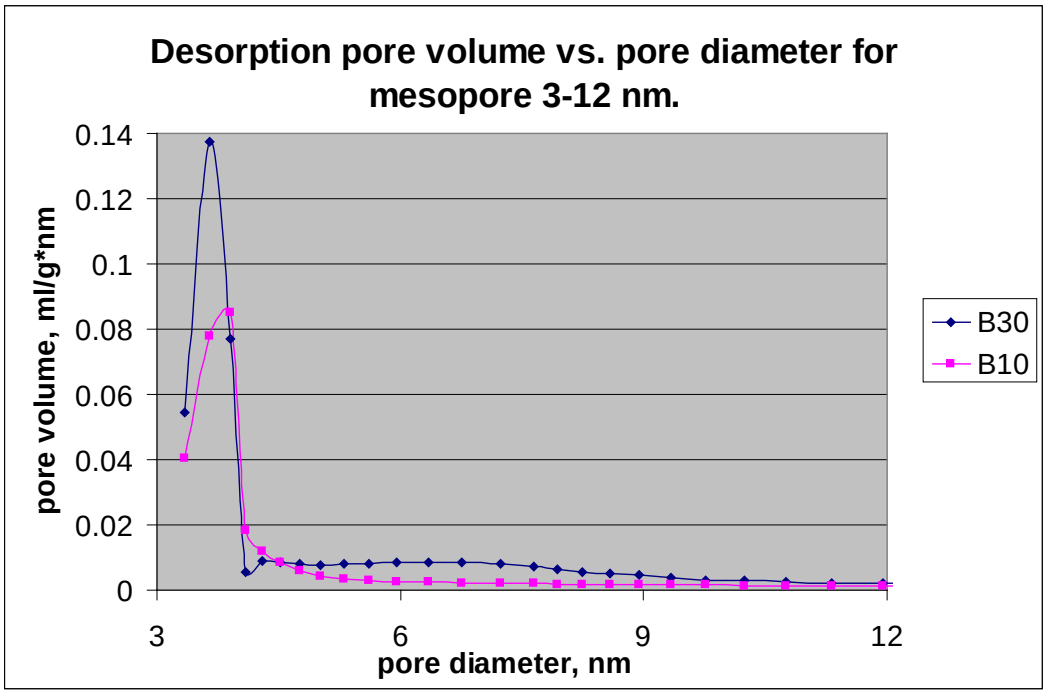

Figure 4.113: Desorption pore size distribution for silica/bindzil PHP, comparison between B10 & B30.

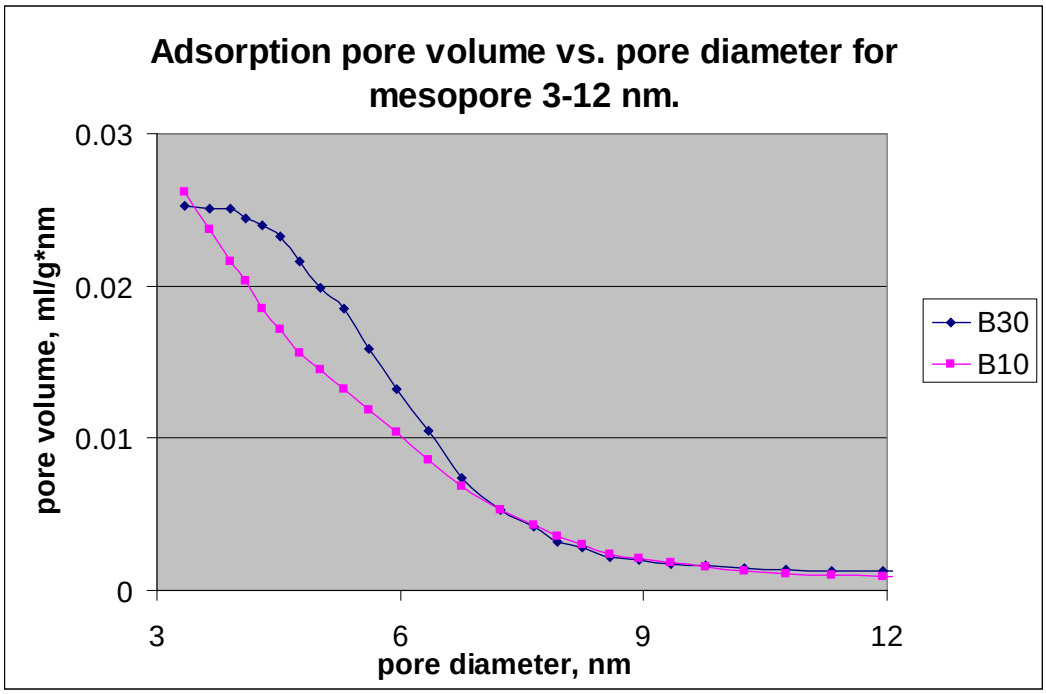

Figure 4.114: Adsorption pore size distribution for silica/bindzil PHP, comparison between B10 & B30.

Further comparison between B10 and B30 are presented in Table 4.25. Both samples, B10 and B30 differ significantly from one another for all type of pore volumes due to non-overlapping error bars, as presented in Figure 4.115.

Statistical analysis, two sample T-test was further performed to check how significant the difference is. The result conclude that there is significant difference between desorption mesopore volumes of B10 and B30 and between total desorption pore volumes of B10 and B30. However, the difference between adsorption mesopore volumes of B10 and B30 is not significant. On the other hand, there is significant difference between total adsorption pore volumes of B10 and B30.

Table 4.25: Total desorption and adsorption mesopore volume.

Sample name	Desorption pore volume			Adsorption pore volume		
	mesopore	%	Total, ml/g	mesopore	%	Total, ml/g
B10	0.0834	92.36	0.0903	0.0753	89.87	0.0838
B30	0.1176	93.77	0.1255	0.0961	87.03	0.1104

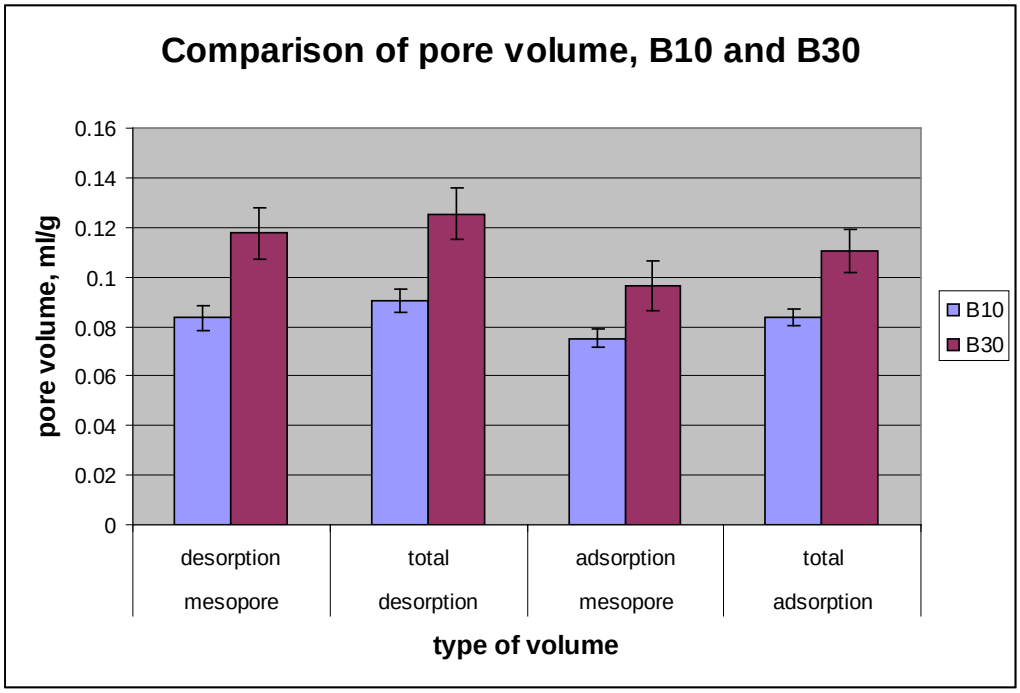

Figure 4.115: Comparison of pore volume, B10 and B30.

4.6.3 FTIR Spectrum

The result for FTIR spectrum of B10 and B30 is presented in Figure 4.116 and Figure 4.117 respectively. There was a strong absorption intensity of siloxane, –Si–O–Si stretching vibration at 1092.384 and 1083.404 cm^{-1} for B10 and B30 respectively, in a broad band of 980 to 1200 cm^{-1} (Gamys et al., 2010; Hilonga et al., 2010; Mustafa et al., 2010; Prud'homme et al., 2010; Alemdar et al., 2009; Shi et al., 2009; Yang et al., 2009; Kim and Jang, 2000).

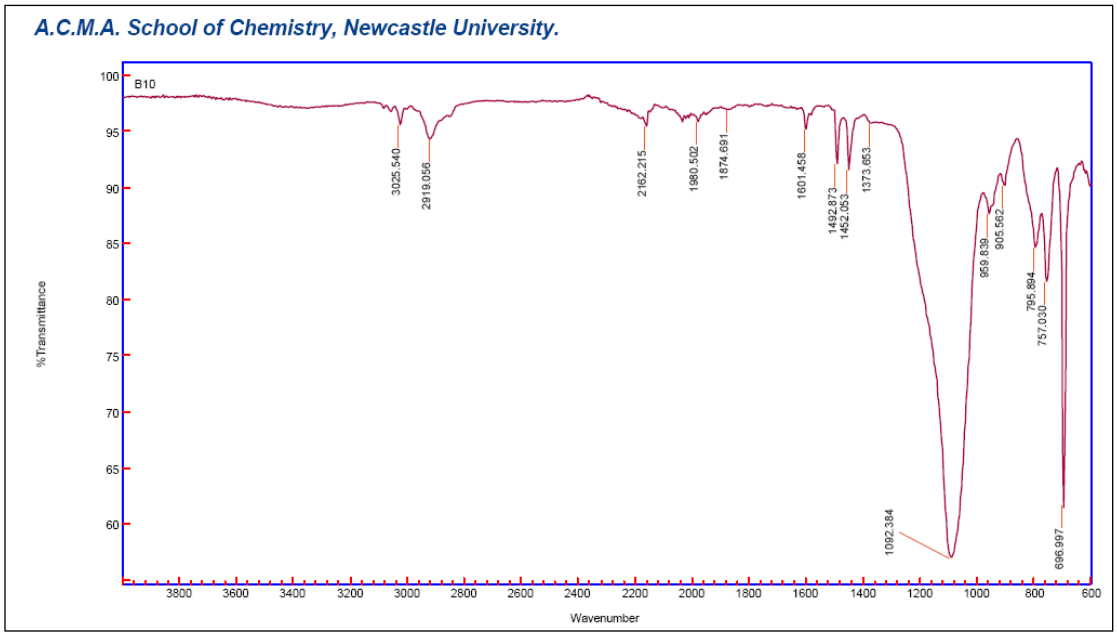

Figure 4.116: FTIR spectrum for B10 PHP.

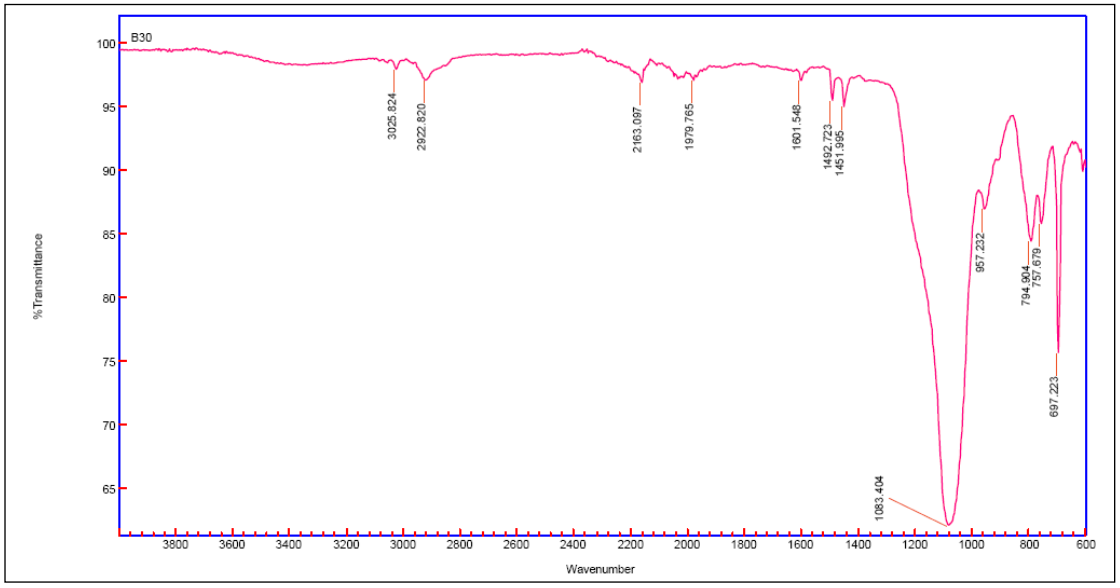

Figure 4.117: FTIR spectrum for B30 PHP.

The comparison of PHPs with different percentage of silica in aqueous solution is presented in Figure 4.118. The two spectra look similar to one another. Comparing these spectra to the basic PHP spectrum, it was observed that the peaks at 1028, 1057 and 1181 cm $^{-1}$ disappeared and was replaced by a strong peak of siloxane. Both spectra have additional peak at 959.839 and 957.232 for B10 and B30 respectively. These peaks are attributed to siloxane linkages (Kim and Jang, 2000). Thus, this

confirmed that the bindzil (silica) was successfully incorporated into the HIPE. The rest of the absorption bands are similar to the bands observed in basic PHP.

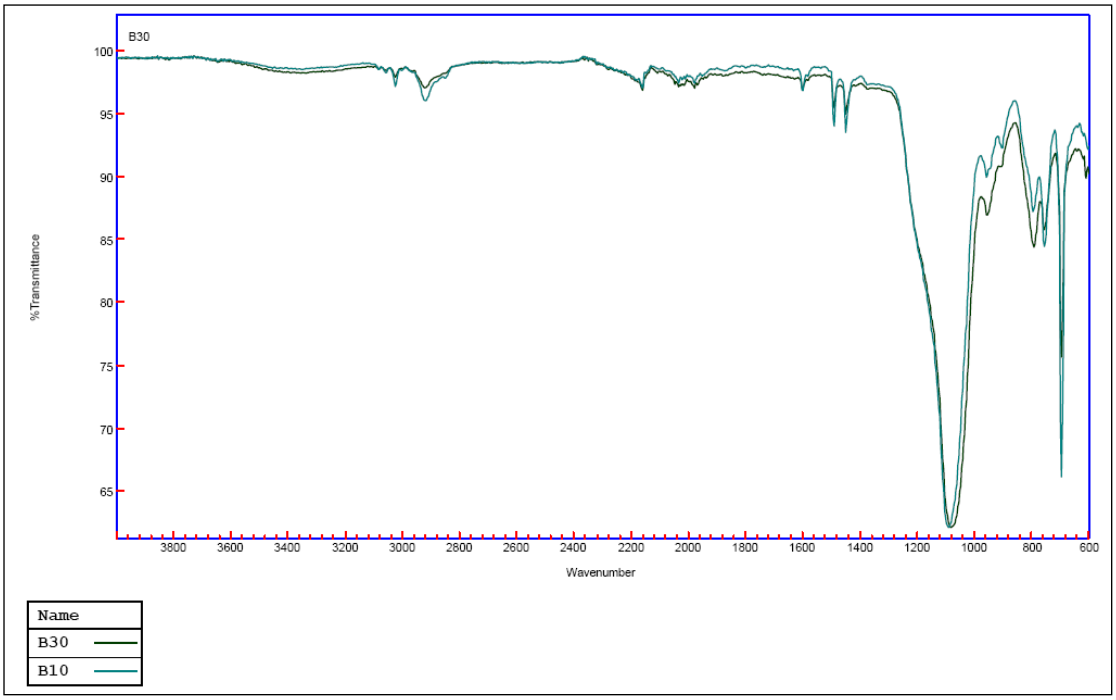

Figure 4.118: FTIR Spectrum for B10 and B30 PHP: comparison

4.6.4 Effect of phase initiator

Study on silica PHP was further done by using the aqueous phase initiator instead of oil phase initiator. There was emulsion produced after the mixing; however; the product was only partly polymerised after leaving it overnight in the oven at 60 °C. The product was a cylindrical solid polymer surrounded by white slurry. Upon drying both parts of the product in the oven at 60 °C, study on the morphology of the products was done by SEM analysis. The images of several different areas for the liquid part after drying are presented in Figure 4.119 through Figure 4.122. All the images are irregular in shape and very different from any image observed of different types of PHPs. The images for the solid cylindrical part are presented in Figure 4.123. The images look knobbly with no pore, which is similar to the image of silane-silica PHP as discussed in section 4.7.1. In conclusion, preparation of bindzil or silica PHP through aqueous phase initiator is a failure; further study need to be done.

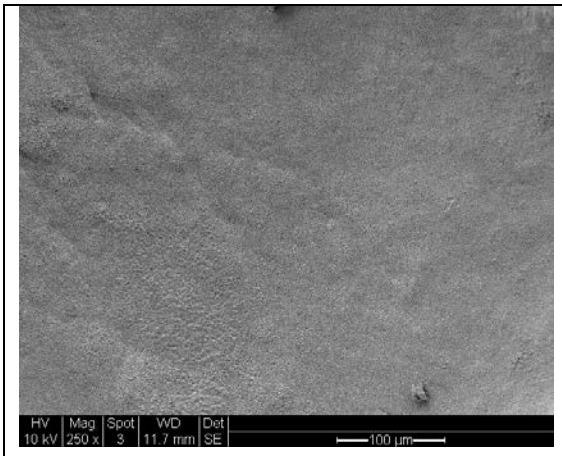

(a) B10a

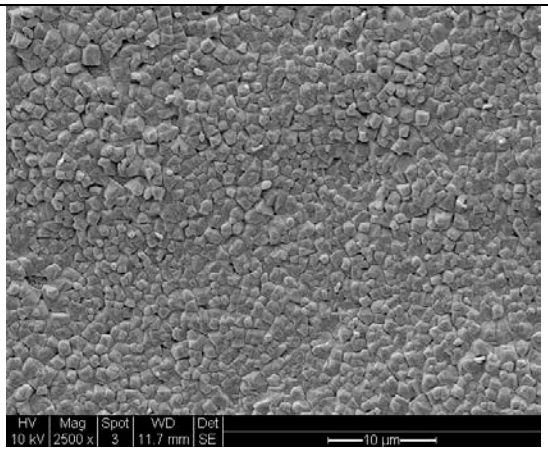

(b) B10a

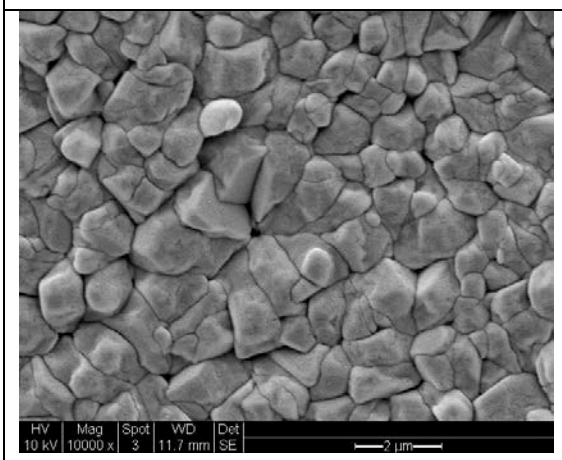

(c) B10a

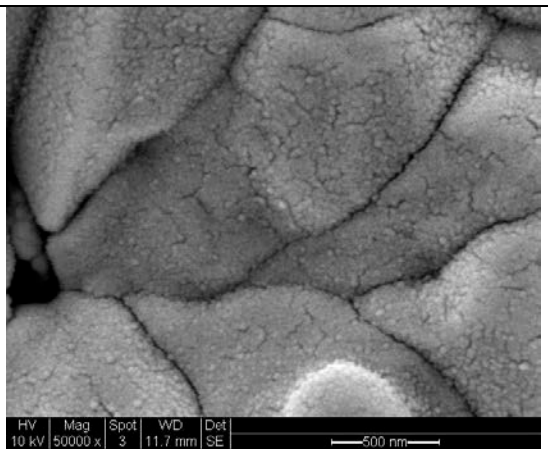

(d) B10a

Figure 4.119: SEM images of the liquid part after drying in the oven at 60 °C

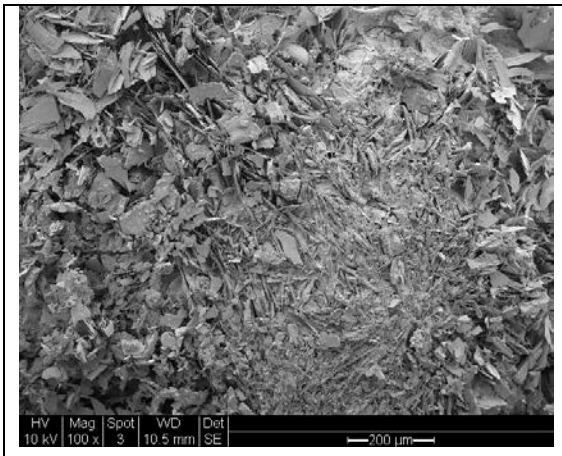

(a) B10a another area

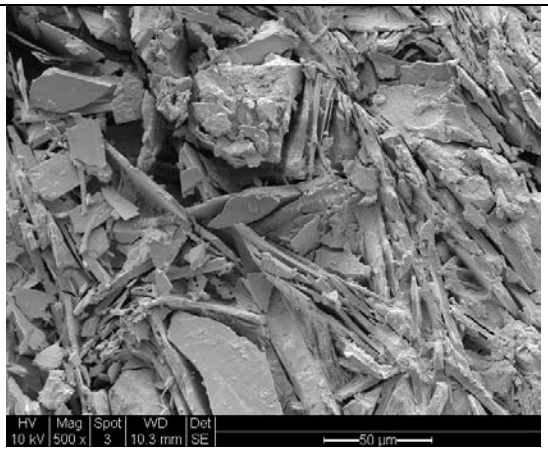

(b) B10a

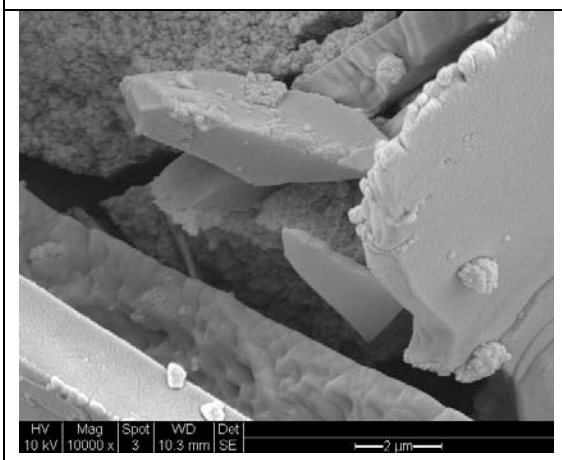

(c) B10a

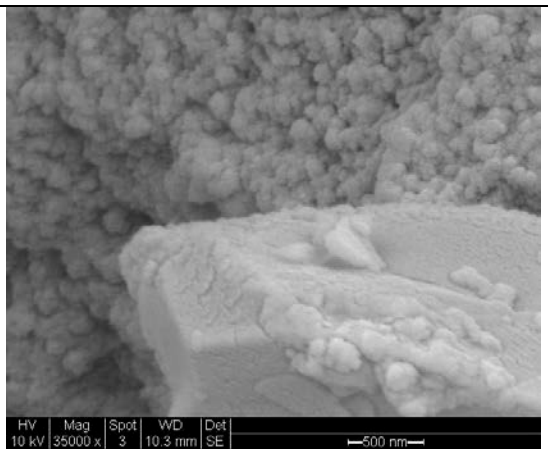

(d) B10a

Figure 4.120: Another area of SEM images of the liquid part after drying in the oven at 60 °C.

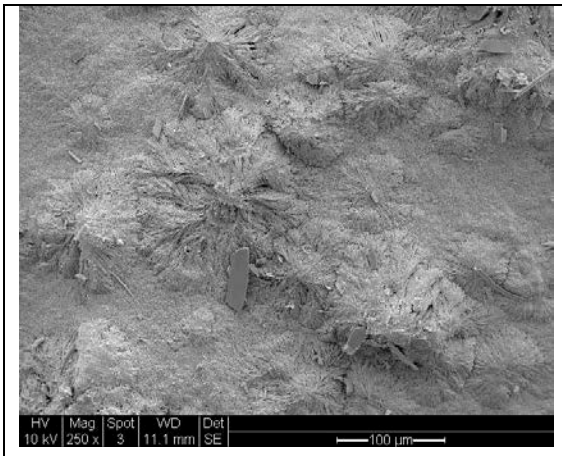

(a) B10a, another area

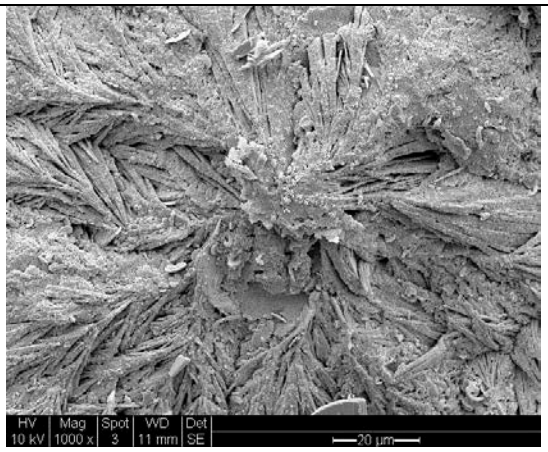

(b) B10a

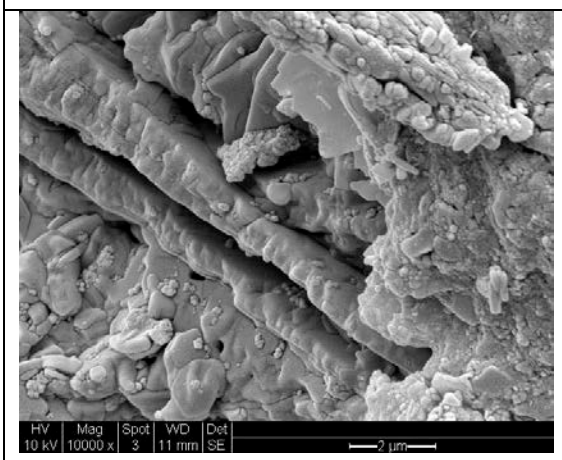

(c) B10a

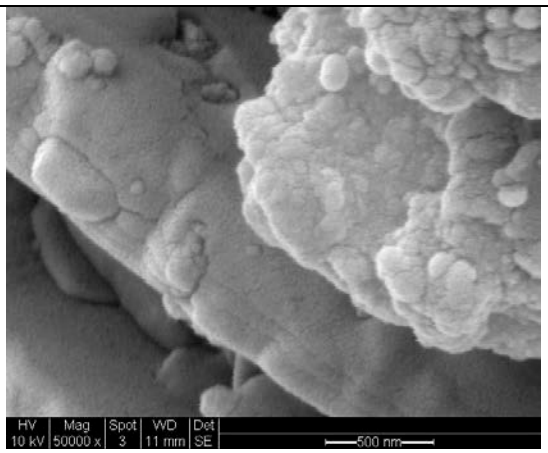

(d) B10a

Figure 4.121: Another area of SEM images of the liquid part after drying in the oven at 60 °C.

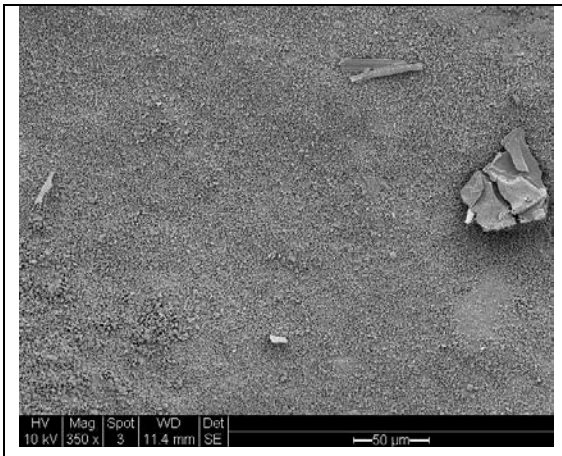

(a) B10a, another area.

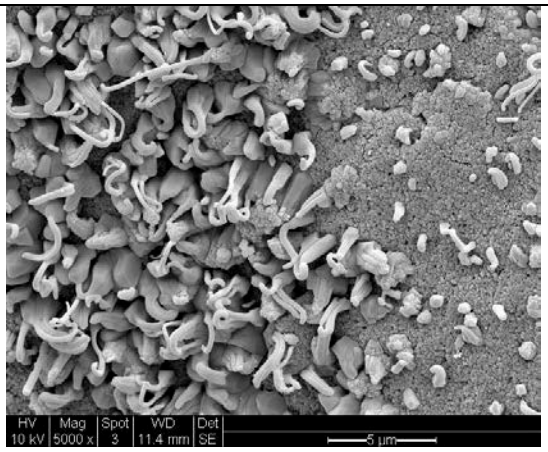

(b) B10a

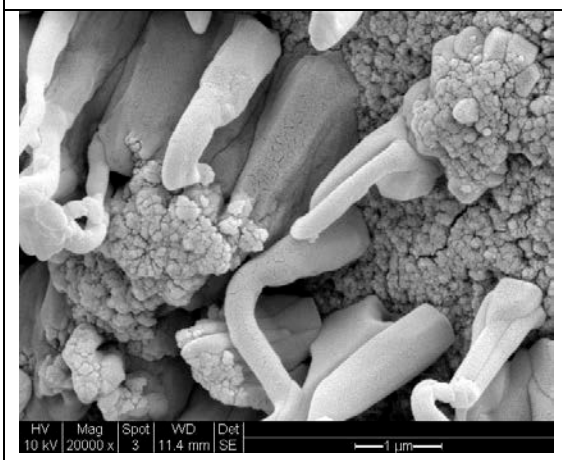

(c) B10a

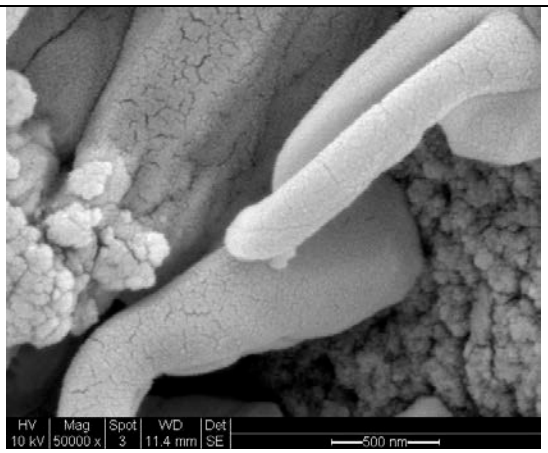

(d) B10a

Figure 4.122: Another area of SEM images of the liquid part after drying in the oven at 60 °C.

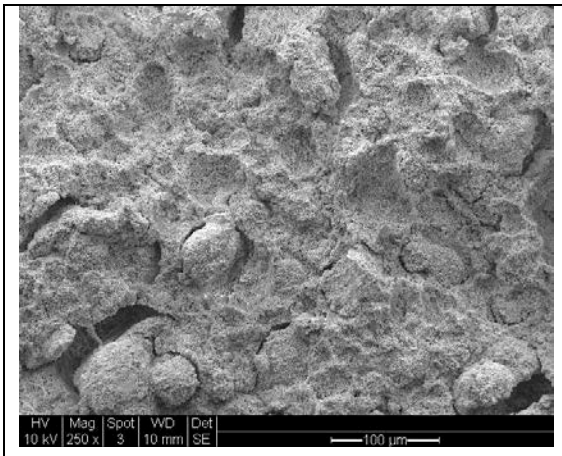

(a) B10b solid part

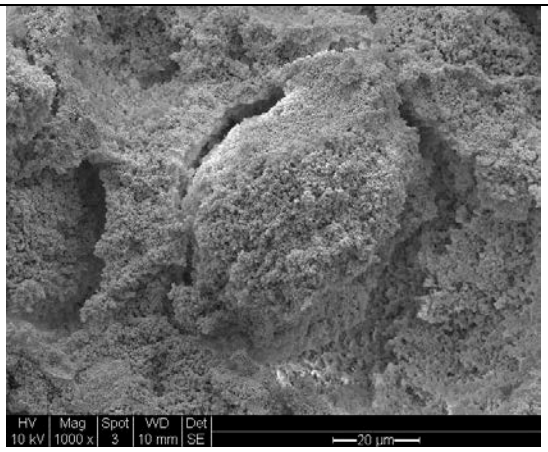

(b) B10b, 1000 magnifications.

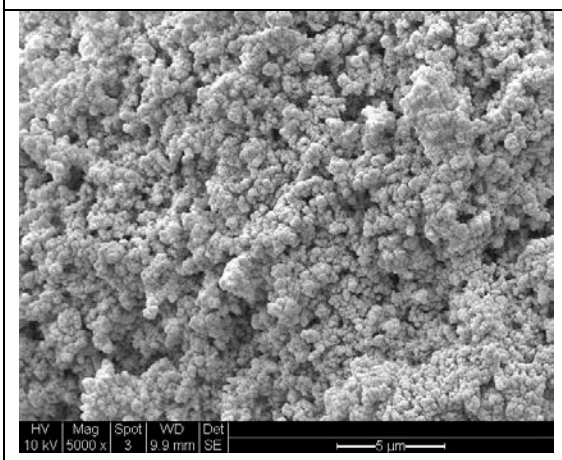

(c) B10b, 5000 magnifications.

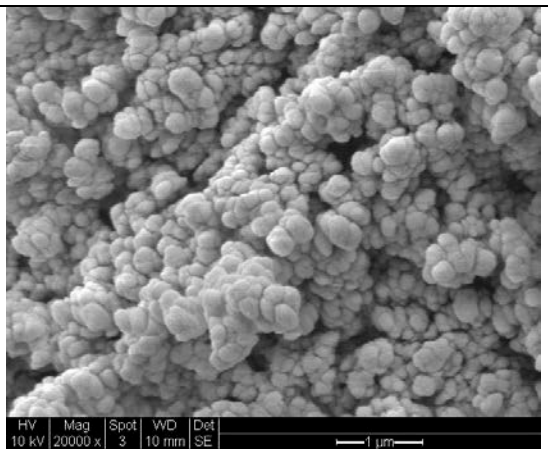

(d) B10b, 20000 magnifications.

Figure 4.123: SEM images of the solid cylindrical part after drying in the oven at 60 °C.

Further study on both parts of the product was done using EDX (Energy Dispersive Analysis with X-Rays). The images correspond to the analysis are presented in Figure 4.124. The results for EDX analysis are presented in Figure 4.125, Figure 4.126, Figure 4.127 and Table 4.26. The EDX results show the presence of silica in both liquid and solid parts of the product. The distribution in liquid part is not homogeneous since two different areas have different percentages of elements.

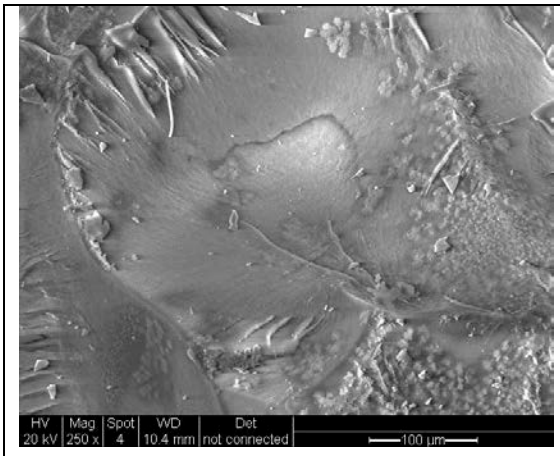

(a) B10a e-1

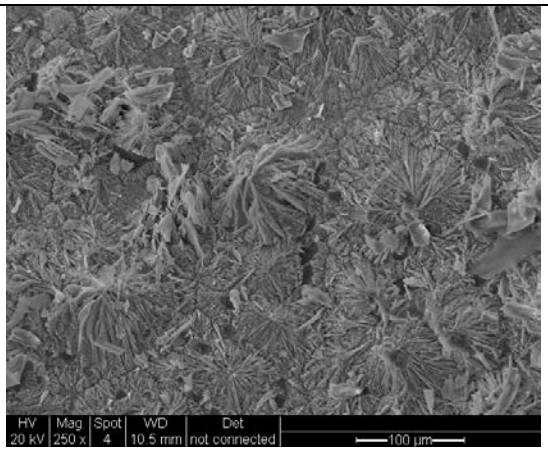

(b) B10a e-2

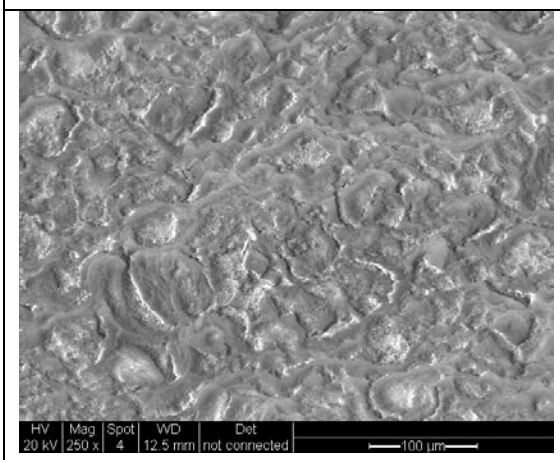

(c) B10b e-1

(a) B10a e-1, an area of dried liquid part.
(b) B10a e-2, another area of dried liquid part.
(c) B10b e-1, an area of solid cylindrical part.

Figure 4.124: The images used in EDX analysis.

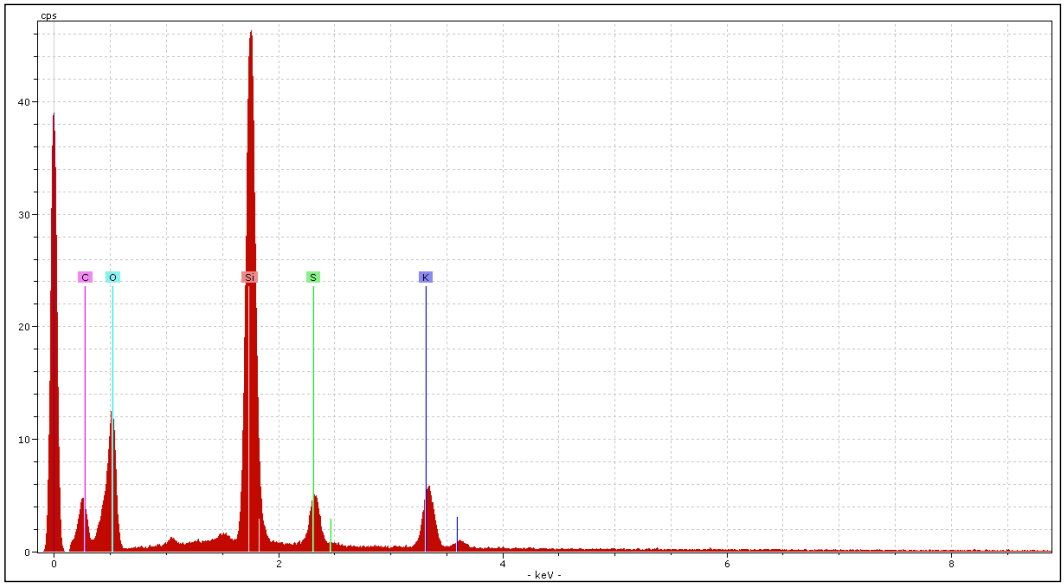

Figure 4.125: Spectrum for B10a e-1, a dried liquid part.

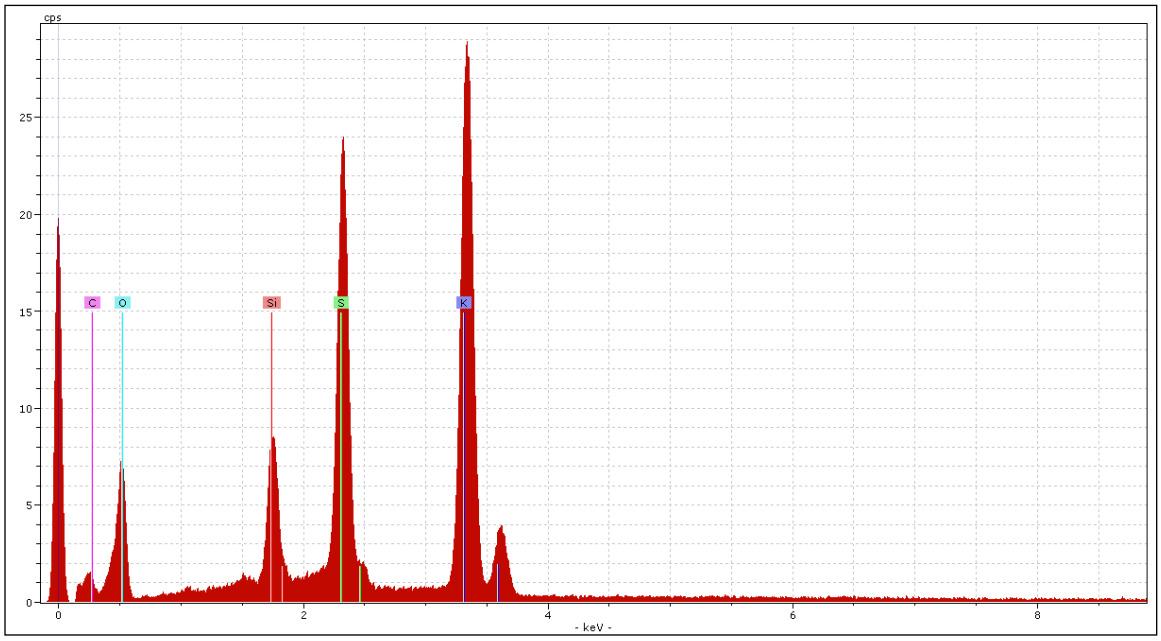

Figure 4.126: Spectrum for B10a e-2, another area of dried liquid part.

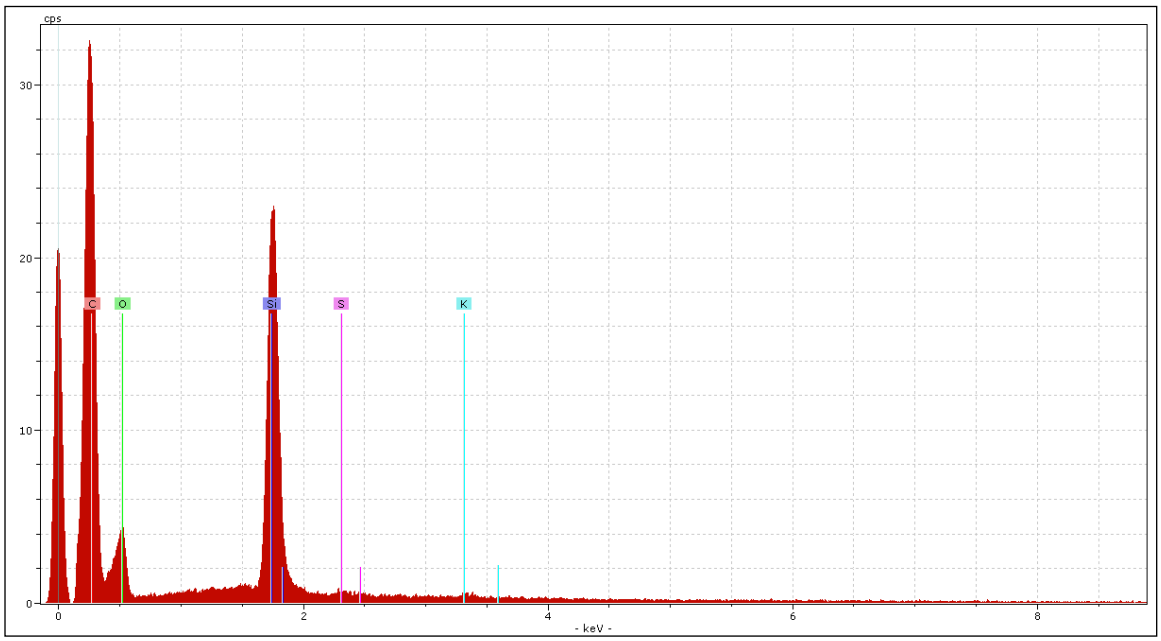

Figure 4.127: Spectrum for B10b e-1, solid cylindrical part.

Table 4.26: Summary of EDX results for two different parts of B10, produced with aqueous phase initiator.

Element	B10a e-1		B10a e-2		B10b e-1	
	weight %	atomic %	weight %	atomic %	weight %	atomic %
Silicon	23.13	15.47	2.18	1.40	11.18	5.65
Sulfur	3.38	1.98	7.62	4.27	34.46	30.55
Potassium	5.35	2.57	10.50	4.83	53.84	63.59
Oxygen	68.13	79.98	79.68	89.49	0.23	0.10
Carbon	0.00	0.01	0.01	0.01	0.29	0.10

4.6.4.1 FTIR analysis.

The FTIR results for both liquid (B10a) and solid (B10b) parts are presented in Figure 4.128 and Figure 4.129 respectively. Generally all the bands look the same except for some differences in intensity of the absorption bands and disappearance of some of the bands. In the lower absorption band of 697 cm^{-1}, B10a has the stronger absorption intensity than B10b. B10a has stronger absorption intensity at 757 cm^{-1} but has weaker absorption intensity at 796 cm^{-1}. Peaks of 697 and 757 cm^{-1} are attributed to out-of-plane C–H bends of the aromatic ring whereas 796 cm^{-1} is attributed to phenyl ring. The peaks at 906 (phenyl ring) and 960 cm^{-1} (–Si–O–Si linkages) disappeared in B10b. B10a exhibit stronger absorption intensity for aromatic ring in the bands of 1452 to 1603 cm^{-1} and 2853 to 3060 cm^{-1}. Absorption bands of 2853 and 3060 cm^{-1} disappeared from the B10b spectrum, leaving weak peaks of 2925.502 and 3026.921 cm^{-1}. This indicates the weak presence of C–H stretching vibration of methyl and methylene groups, and =C–H stretch of aromatic rings in B10b. Both B10a and B10b have strong absorption intensity for siloxane, –Si–O–Si stretching vibration at 1102.172 cm^{-1} and 1070.776 cm^{-1}, respectively. Thus the presence of –Si–O–Si stretching vibration in both parts is quite significant.

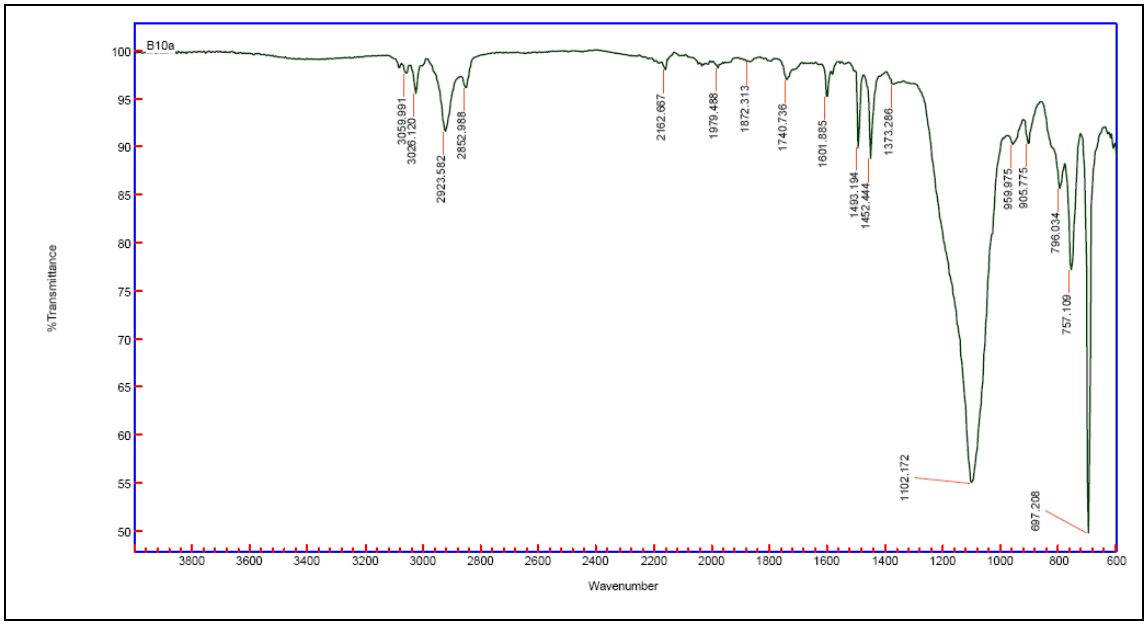

Figure 4.128: FTIR spectrum for B10a, the liquid part, dried in the oven at 60 °C.

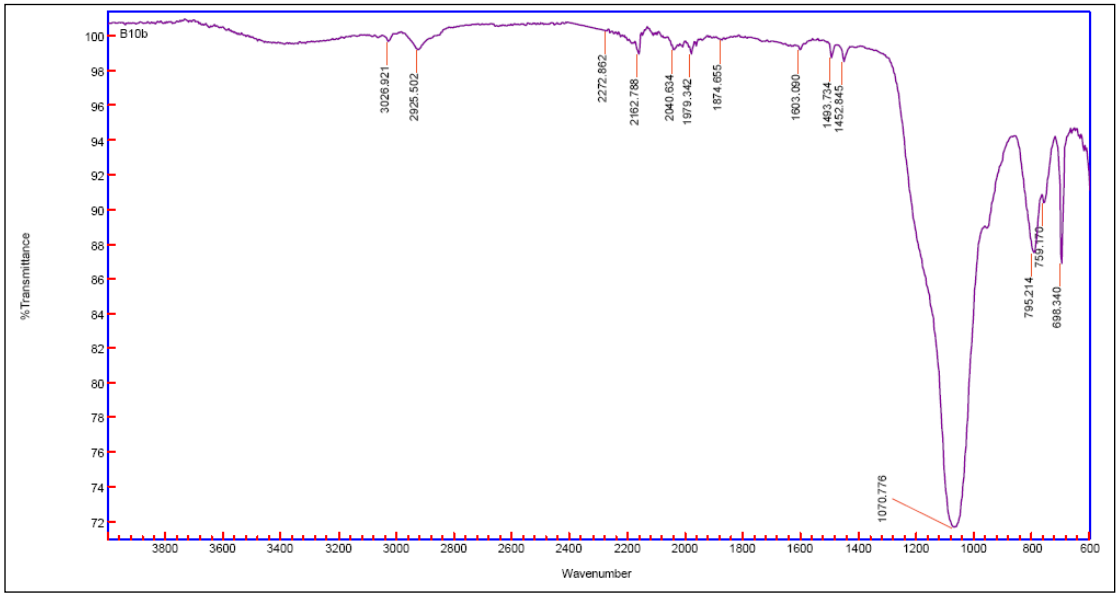

Figure 4.129: FTIR spectrum of solid cylindrical part.

4.7 *Silane + Silica (VTMS- Bindzil) PHP*

Further study was done by incorporating the bindzil solution (silica) and vinyl trimethoxy silane (VTMS) through the aqueous phase and the oil phase respectively.

4.7.1 Morphology

The morphology of the VTMS-Bindzil PHPs is presented in Figure 4.130, Figure 4.131 and Figure 4.132. The images show that there was no pore obtained; instead the structure is best described as knobbly.

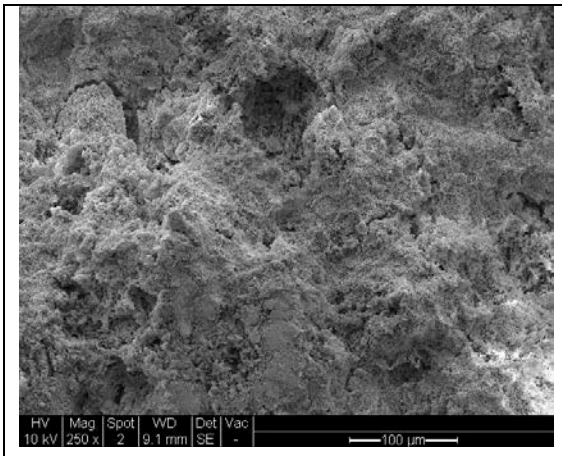

(a) S10B10

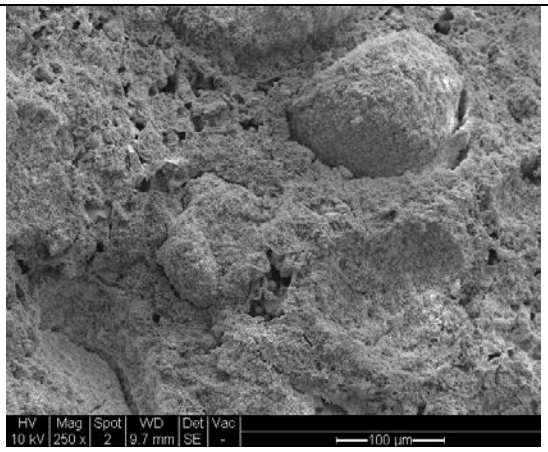

(b) S15B10

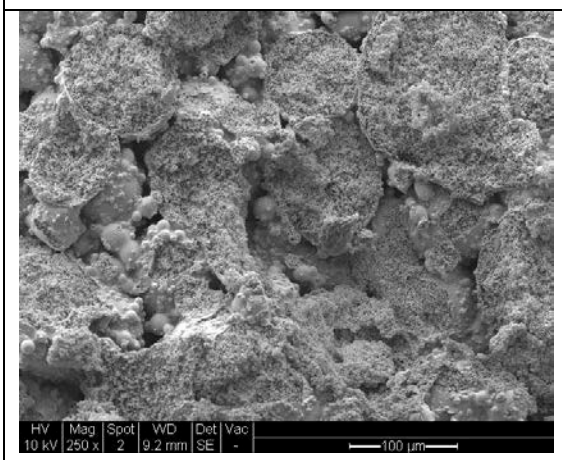

(c) S20B10

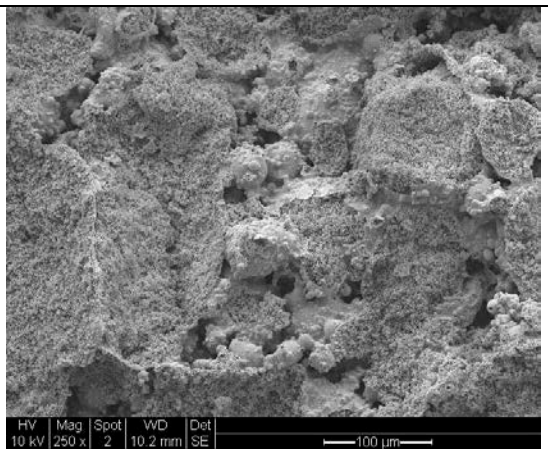

(d) S25B10

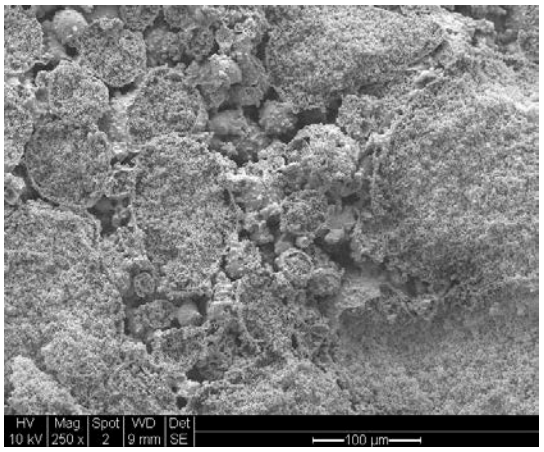

(e) S30B10

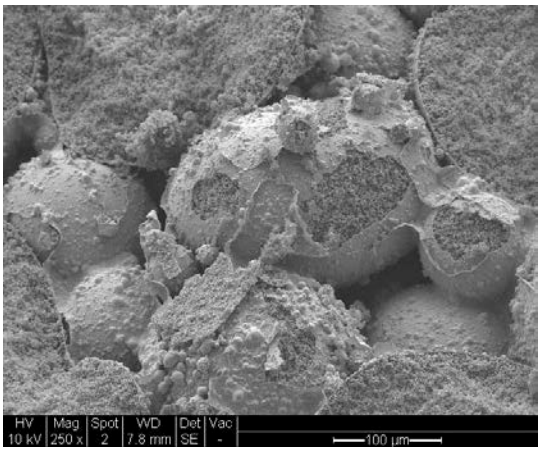

(f) S35B10

Figure 4.130: Various PHPs with different percentages of vinyl trimethoxy silane and bindzil.

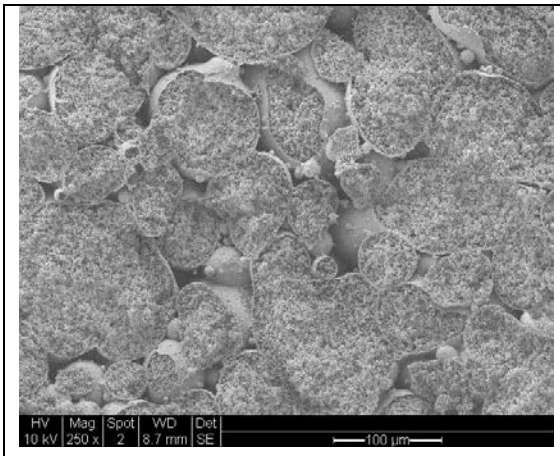

(a) S40B10

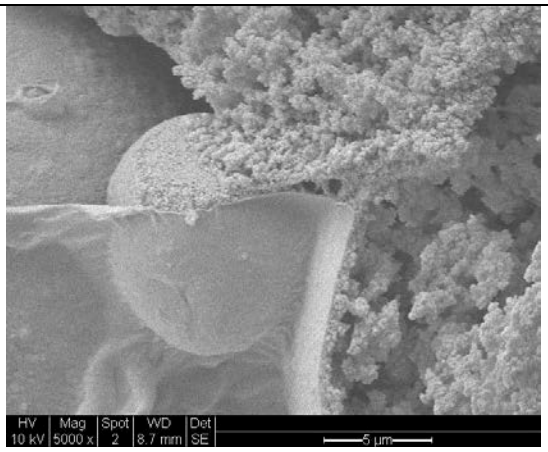

(b) S40B10X5000, skin and structure underneath

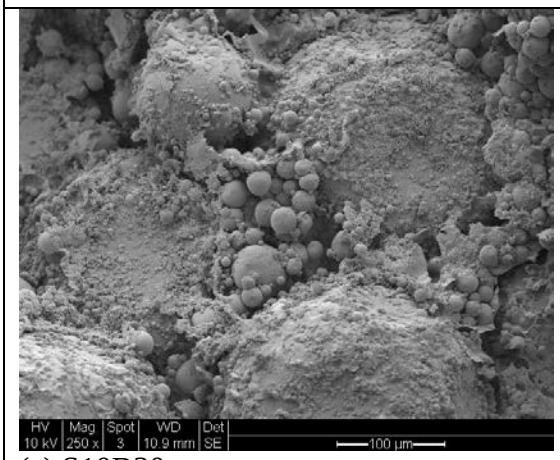

(c) S10B30

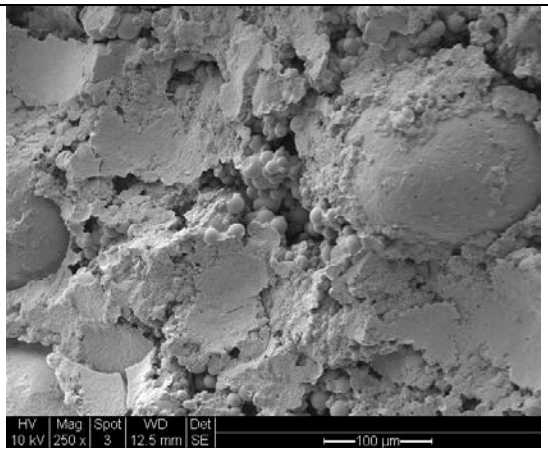

(d) S30B30

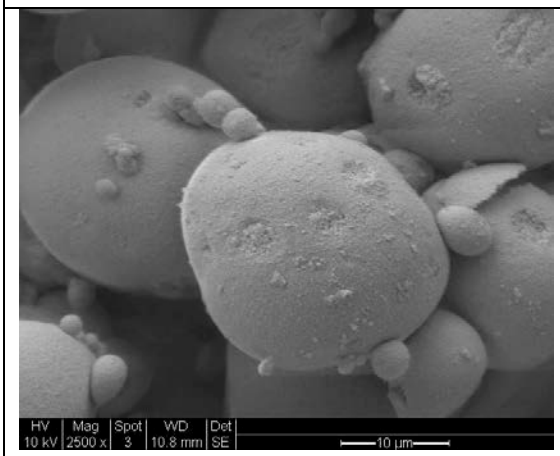

(e) S10B30

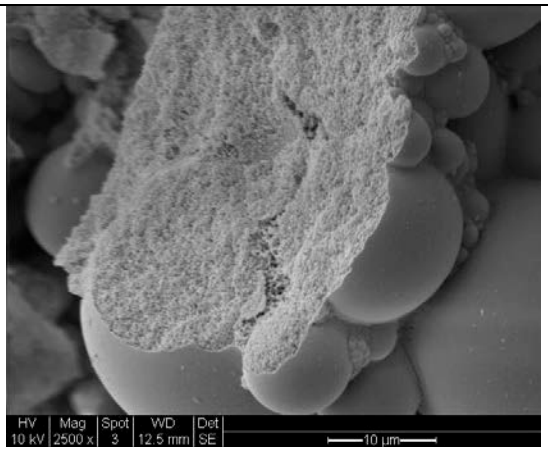

(f) S30B30

Figure 4.131: Various PHPs with different percentages of vinyl trimethoxy silane and bindzil at several magnifications.

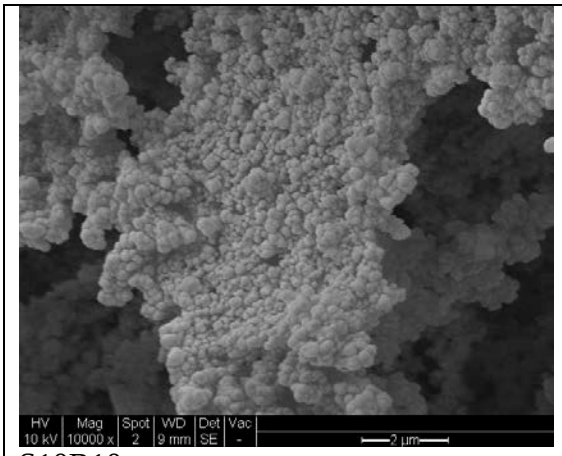

S10B10

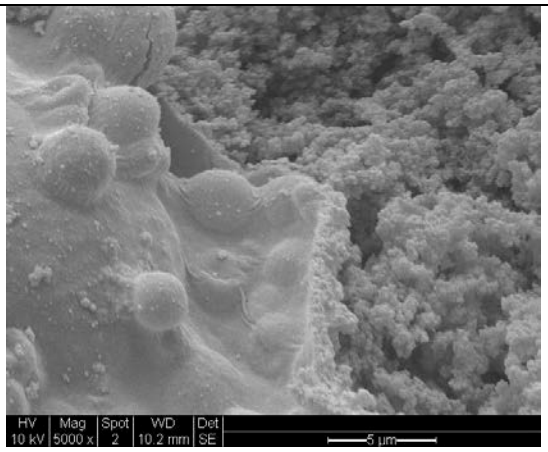

S25B10

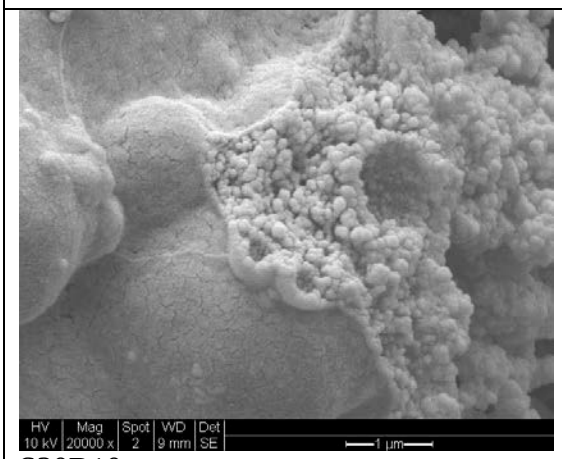

S30B10

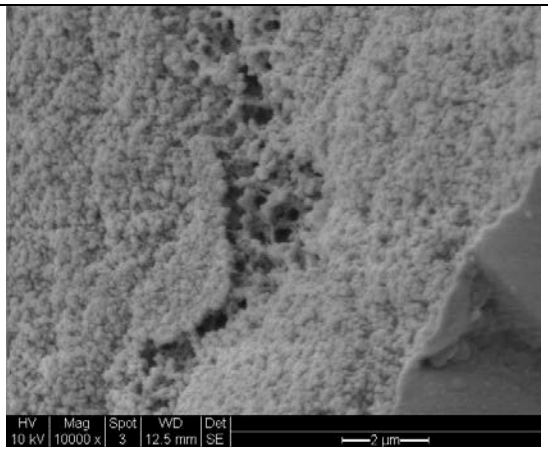

S30B30

Figure 4.132: Various PHPs with different percentages of vinyl trimethoxy silane and bindzil at several higher magnifications.

4.7.2 Surface area and pore size distribution.

Surface area and pore size distribution was analysed by nitrogen adsorption and desorption isotherm at 77K.

4.7.2.1 Isotherm.

The isotherms for all VTMS-Bindzil PHPs are presented in Figure 4.133 to Figure 4.140. All the isotherms exhibit monolayer-multilayer physisorption process. All of the isotherms are steep, similar to the isotherms of VTMS (silane) PHP with narrow Type H3 hysteresis, except for S10B30. As discussed previously in section

4.4.3.1, due to Type H3 hysteresis, only adsorption branch result of pore size distribution is reliable even though results of both adsorption and desorption branches are discussed here.

The isotherm for S10B30 has the widest hysteresis among all the isotherms. The S10B30 isotherm resembles more of B30 isotherm which is type H4 loop, as discussed in section 4.6.2.1 but with steeper curve.

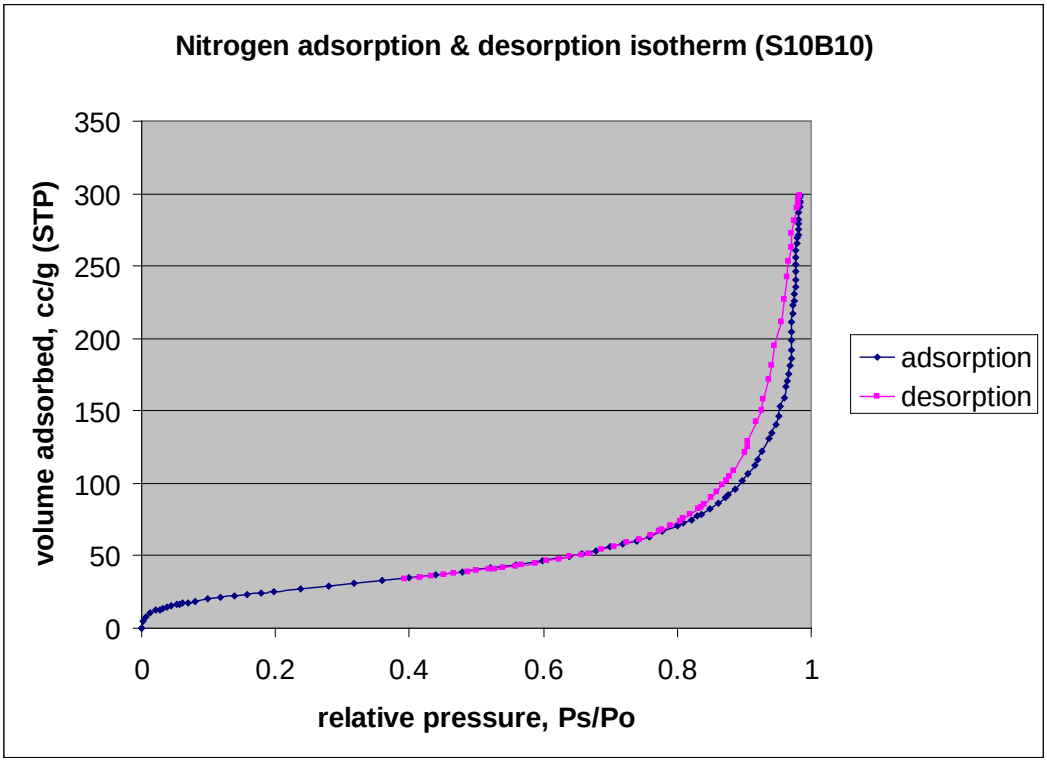

Figure 4.133: Plot of nitrogen adsorption and desorption S10B10 PHP (10% VTMS, Bindzil 10)

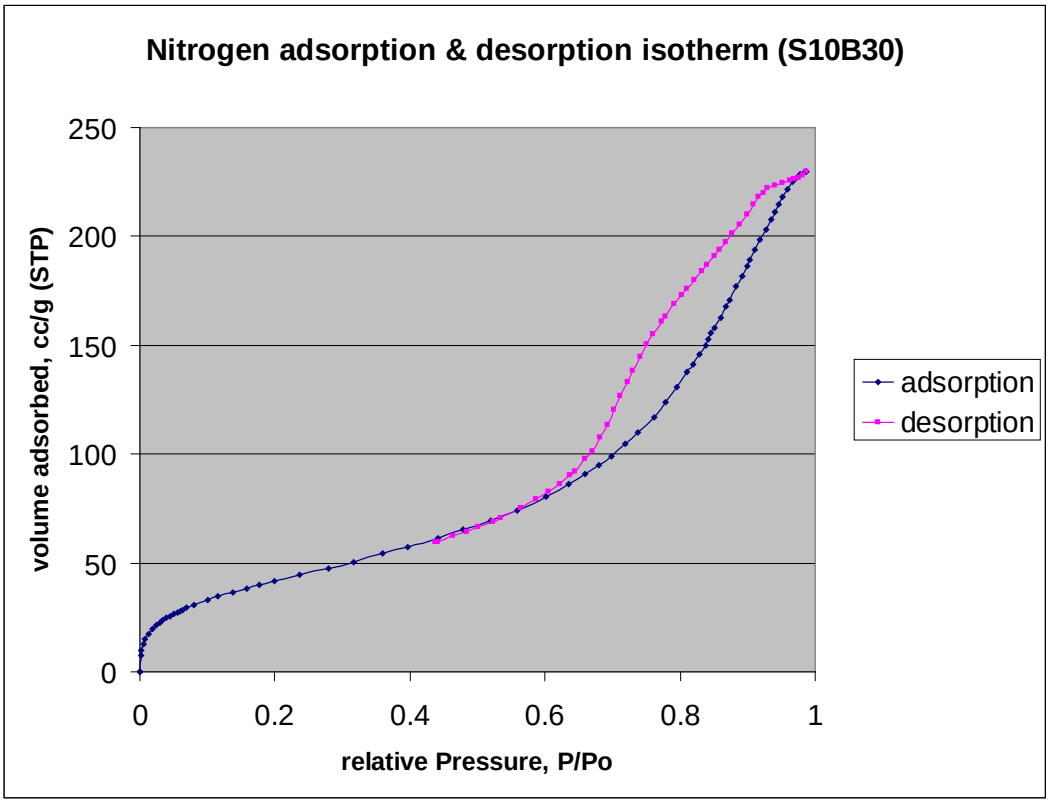

Figure 4.134: Plot of nitrogen adsorption and desorption S10B30 PHP (10% VTMS, Bindzil 30)

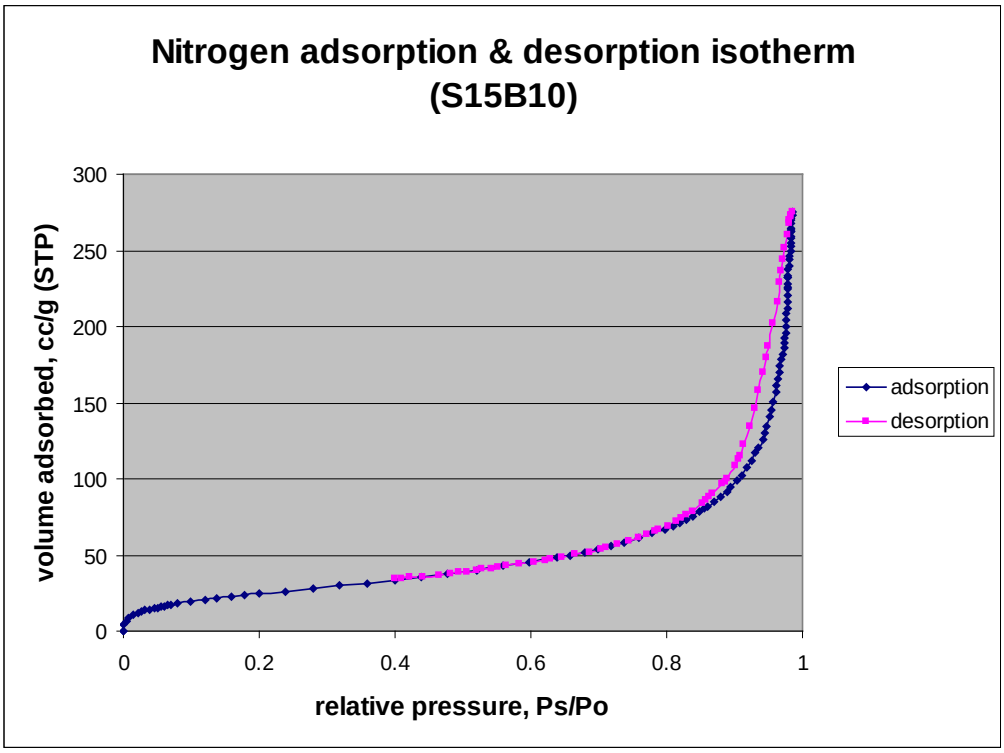

Figure 4.135: Plot of nitrogen adsorption and desorption S15B10 PHP (15% VTMS, Bindzil 10)

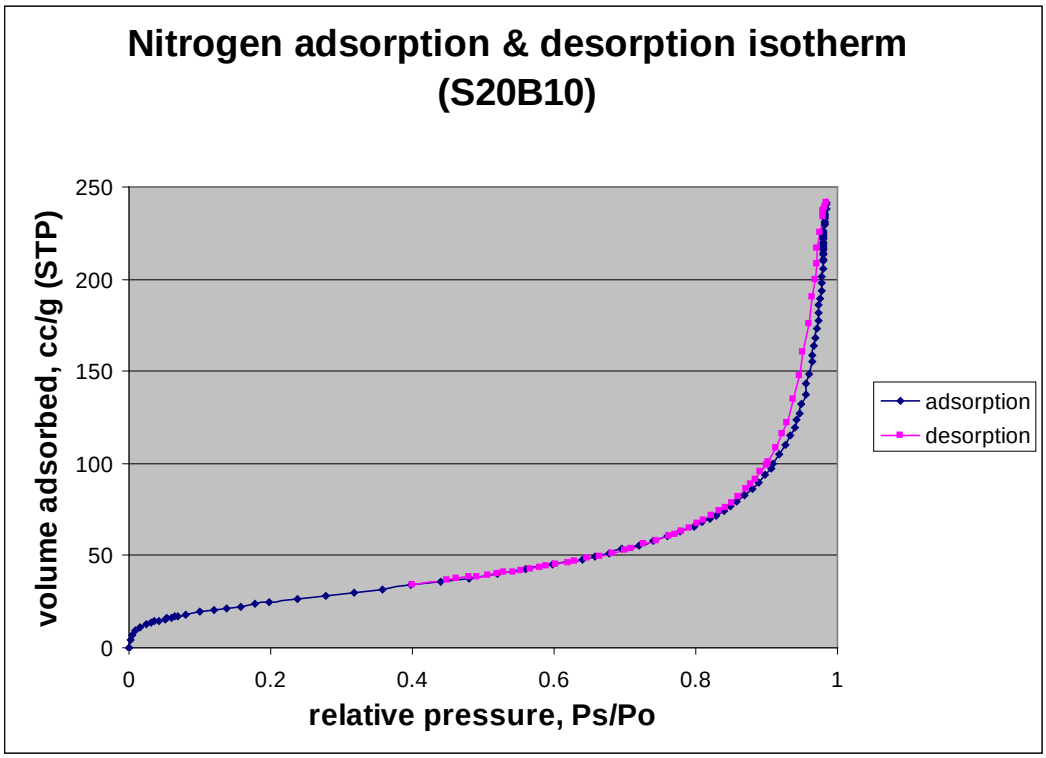

Figure 4.136: Plot of nitrogen adsorption and desorption S20B10 PHP (20% VTMS, Bindzil 10)

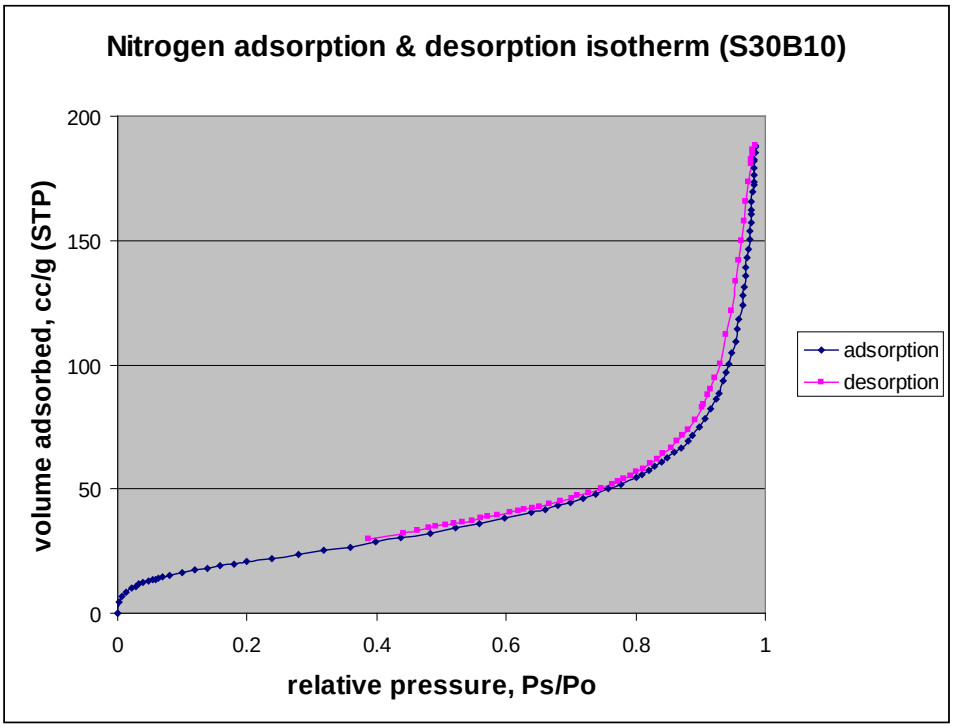

Figure 4.137: Plot of nitrogen adsorption and desorption S30B10 PHP (30% VTMS, Bindzil 10)

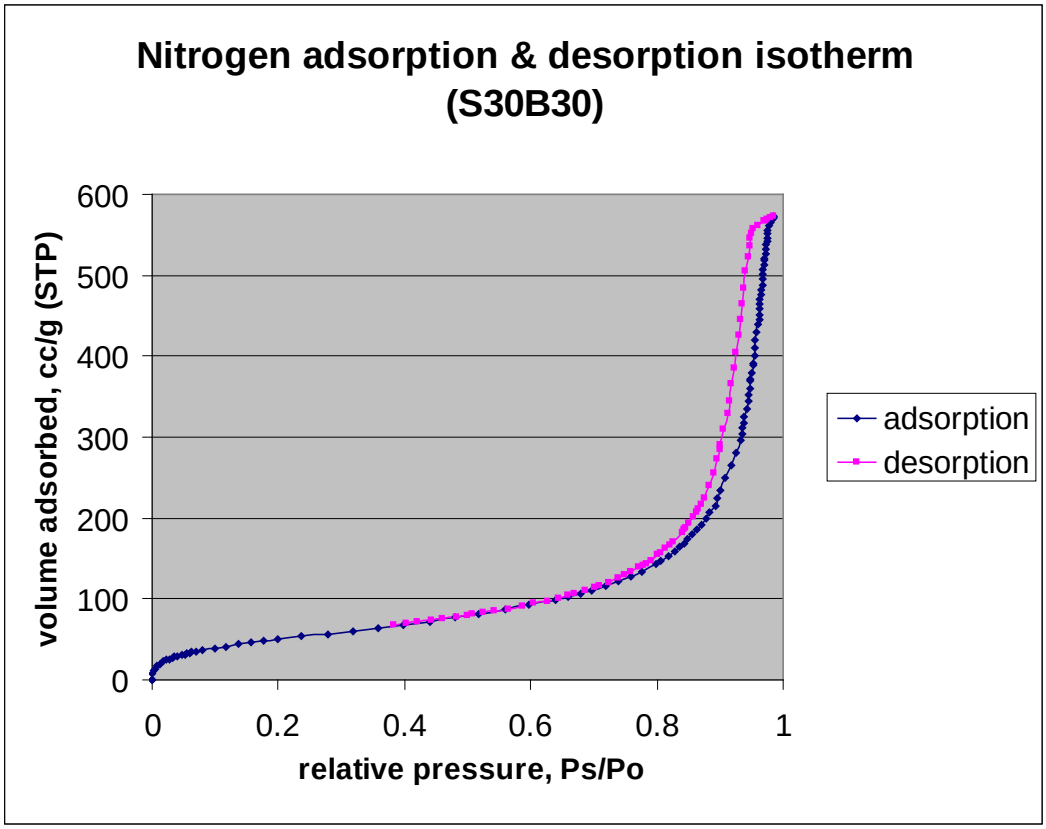

Figure 4.138: Plot of nitrogen adsorption and desorption S30B30 PHP (30% VTMS, Bindzil 30)

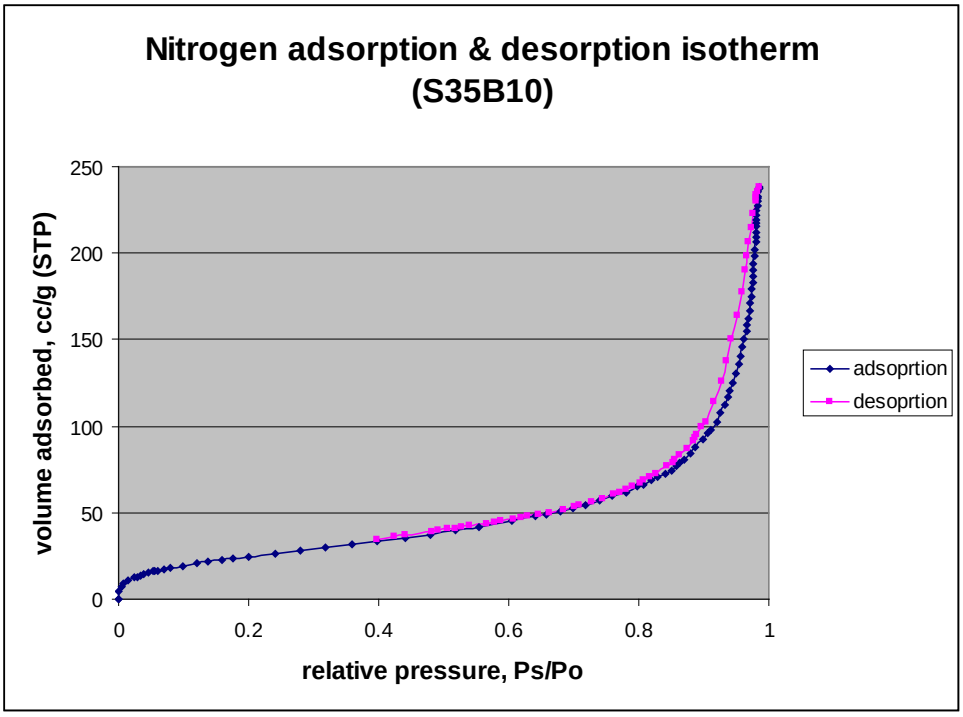

Figure 4.139: Plot of nitrogen adsorption and desorption S35B10 PHP (35% VTMS, Bindzil 10)

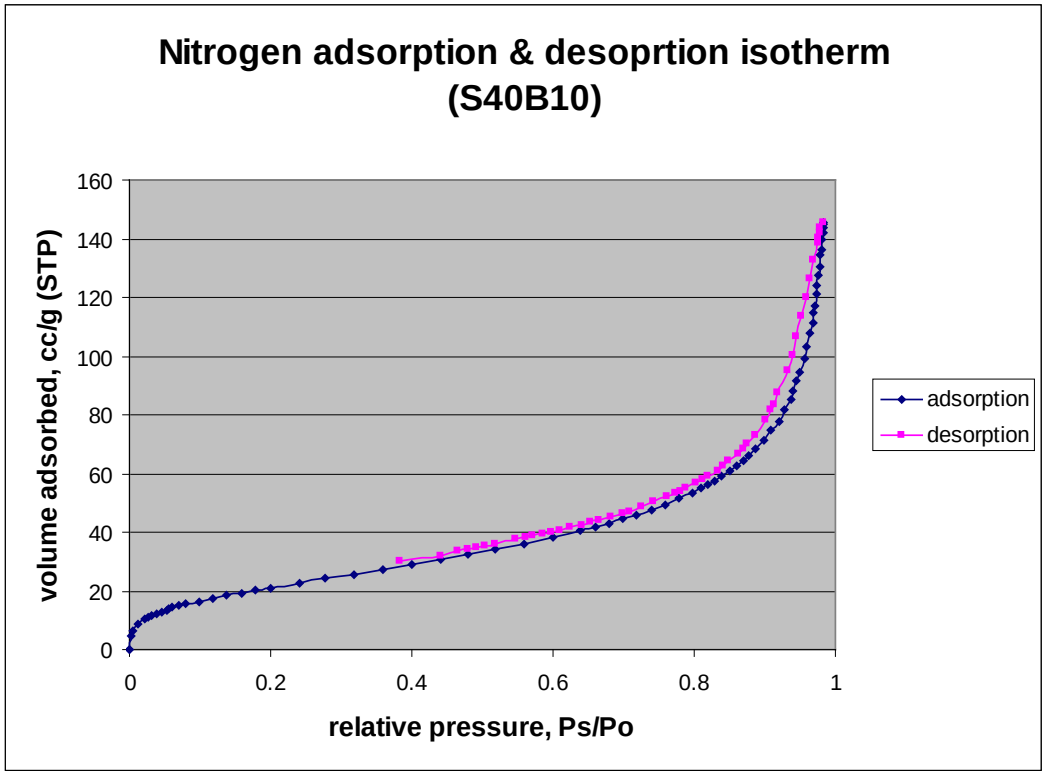

Figure 4.140: Plot of nitrogen adsorption and desorption S40B10 PHP (40% VTMS, Bindzil 10)

4.7.2.2 Surface area.

The results for surface areas of different percentages of VTMS and bindzil PHPs are presented in Table 4.27, Figure 4.141 and Figure 4.142 . Contribution to the surface area dominantly comes from incorporating the Bindzil. This was observed in the surface area of S10B30 and S30B30, the PHPs with 30% percentages of bindzil. The highest surface area was observed for S30B30.

Table 4.27: Surface area of VTMS-Binzil PHPs

sample name	surface area, m^2/g
S10B10	94.59
S10B30	154.32
S15B10	94.55
S20B10	90.42
S25B10	72.52
S30B10	81.19
S30B30	192.33
S35B10	96.30
S40B10	82.32

There was a difference between the surface area of S10B30 and S30B30 and between these two samples to the rest of VTMS-Bindzil samples. There was no difference between the surface area of S10B10, S15B10, S20B10 and S35B10 due to overlapping error bars. Further comparison showed that there was also no difference between the surface area of S25B10, S30B10 and S40B10. The surface area of the group S10B10, S15B10, S20B10 and S35B10 differ from the surface area of the group S25B10, S30B10 and S40B10.

Statistical analysis, ANOVA concluded that there are significant differences in the surface area of VTMS-Bindzil polymer produced at significance level of 0.05. These differences are further analysed by Bonferroni test at 95.0% confident intervals. The pairs that are difference are presented in Table 4.28. In conclusion, surface area of S30B30 differs significantly from the rest of VTMS-Bindzil PHPs.

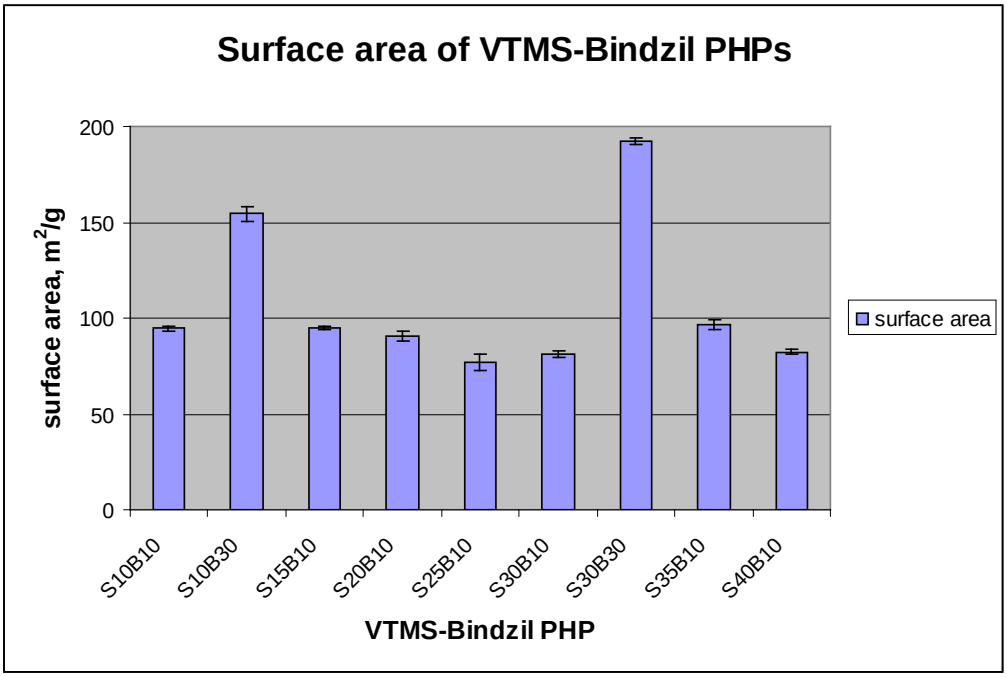

Figure 4.141: Surface area of several VTMS-Bindzil PHPs.

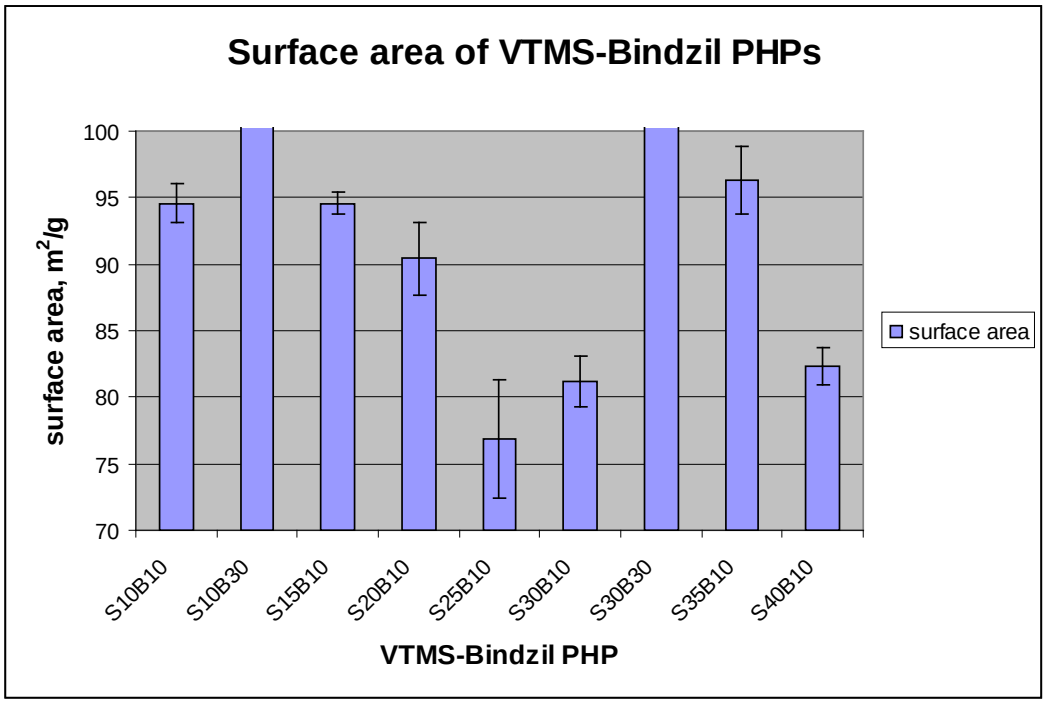

Figure 4.142: A closed-up presentation of standard errors.

Table 4.28: Pairs of VTMS-Bindzil PHPs with significant difference in surface area.

VTMS -Bindzil PHP	
S10B10	S10B30
S10B10	S30B30
S10B30	S15B10
S10B30	S20B10
S10B30	S25B10
S10B30	S30B10
S10B30	S30B30
S10B30	S35B10
S10B30	S40B10
S15B10	S30B30
S20B10	S30B30
S25B10	S30B30
S30B10	S30B30
S30B30	S35B10
S30B30	S40B10

4.7.2.3 Pore size distribution.

Pore size distributions of all VTMS-bindzil samples are presented in Figure 4.143 through Figure 4.159. Desorption pore size distributions for S10B10 and S15B10 exhibit monomodal distribution in mesopore range. S10B30 has monomodal distribution between 3 nm to 10 nm centred at 7 nm while S30B30 has a wide monomodal distribution covering the whole range of mesopore from 3nm to 50 nm with a peak at 25nm for desorption curve. S25B10, S30B10, S35B10 and S40B10 exhibit monomodal distribution within a narrow distribution of 3.34 – 4.1 nm with a peak centred at 3.65 nm. S20B10 exhibits no significant peak, but have high differential pore volume in the mesopore region of the desorption curve. For adsorption curve, none of the samples exhibit significant peak in the mesopore region. S15B10 have several small multimodal distributions and a monomodal distribution in the macropore region, between 60 nm and 125 nm.

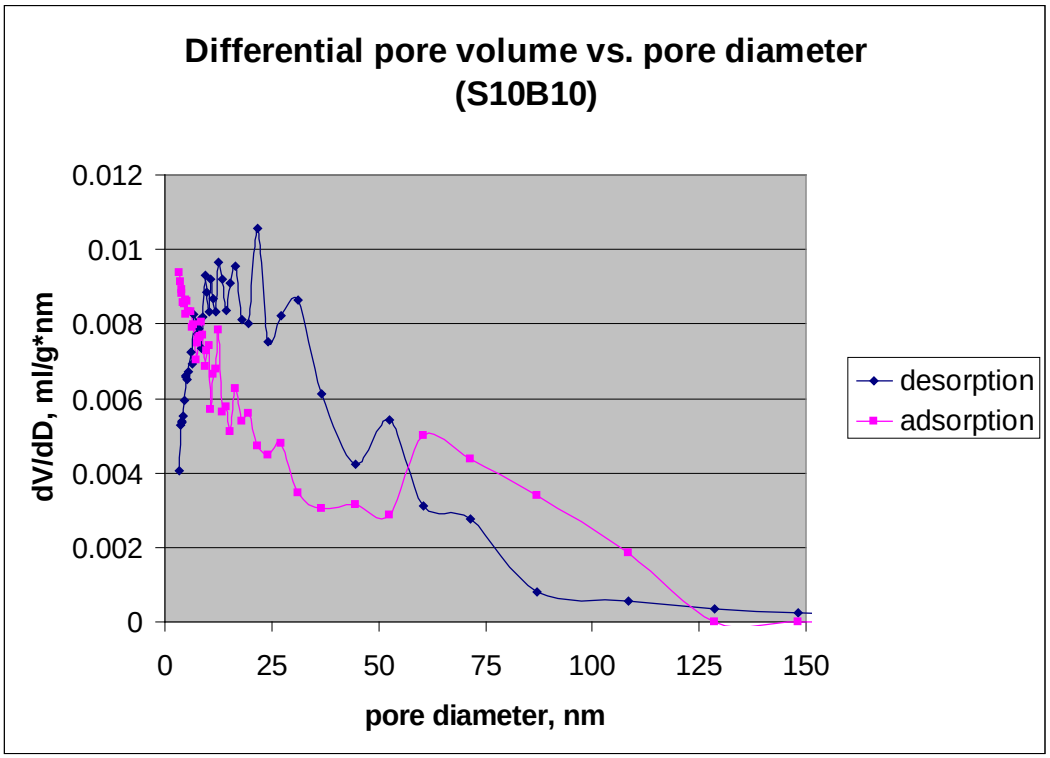

Figure 4.143: Pore size distribution of S10B10 PHP.

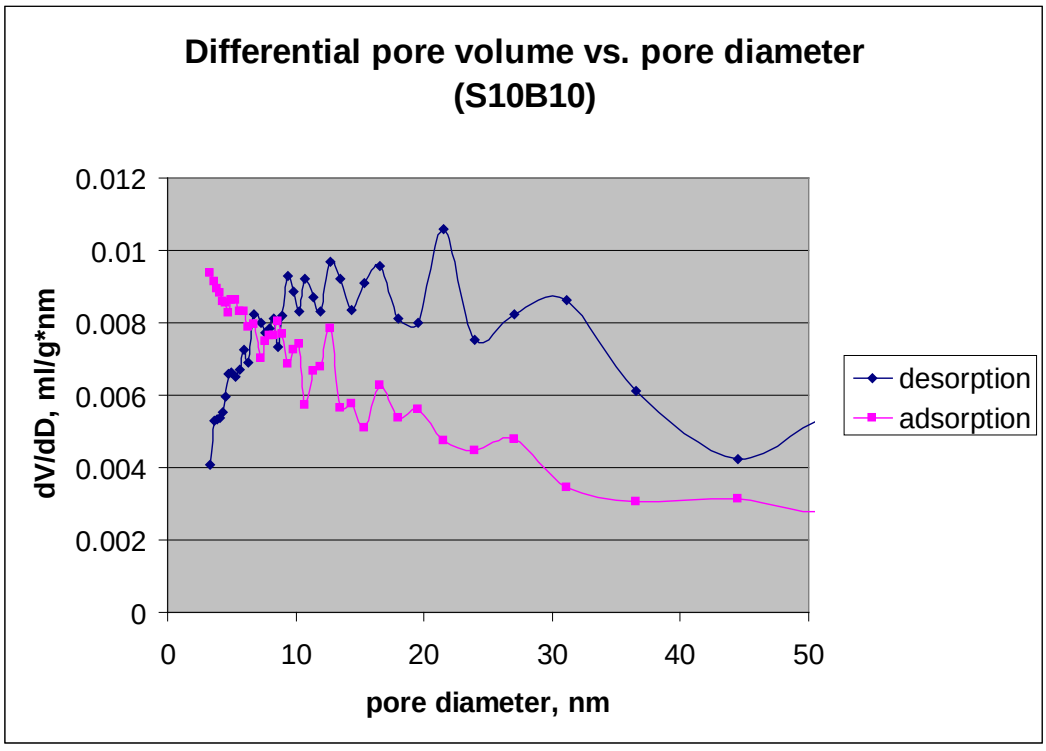

Figure 4.144: Pore size distribution for mesopores of S10B10 PHP

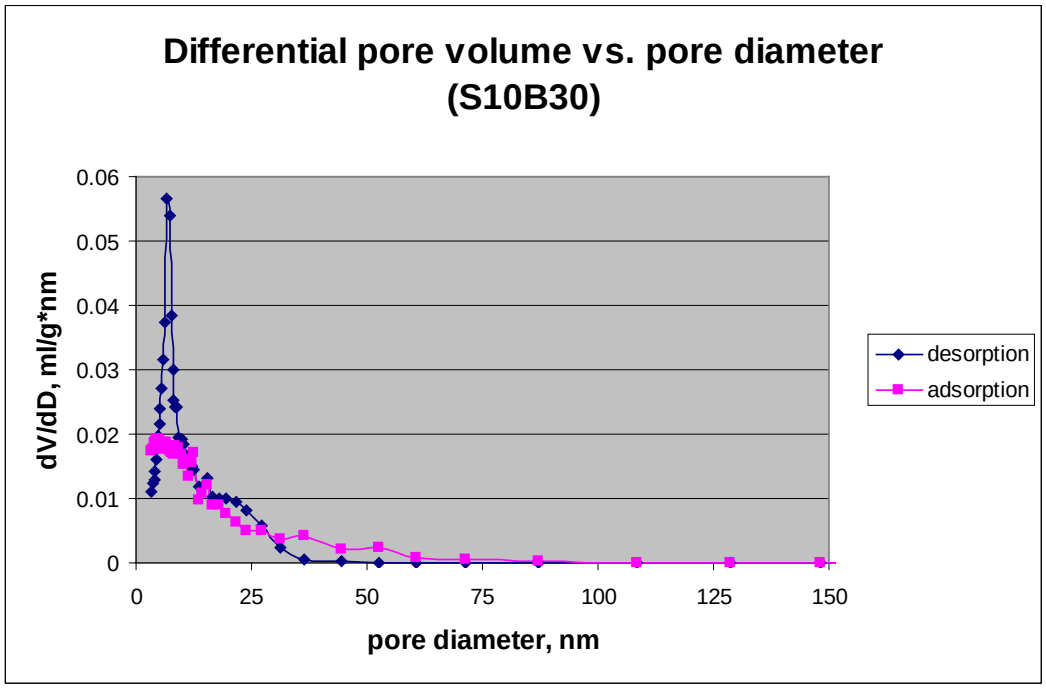

Figure 4.145: Pore size distribution of S10B30 PHP.

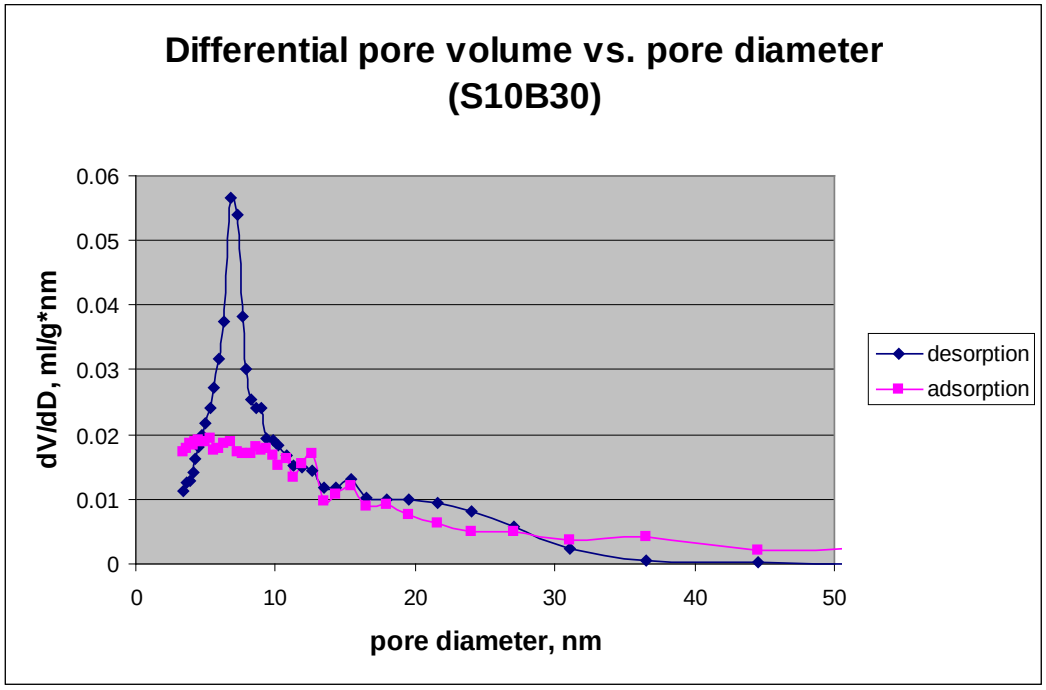

Figure 4.146: Pore size distribution for mesopores of S10B30 PHP.

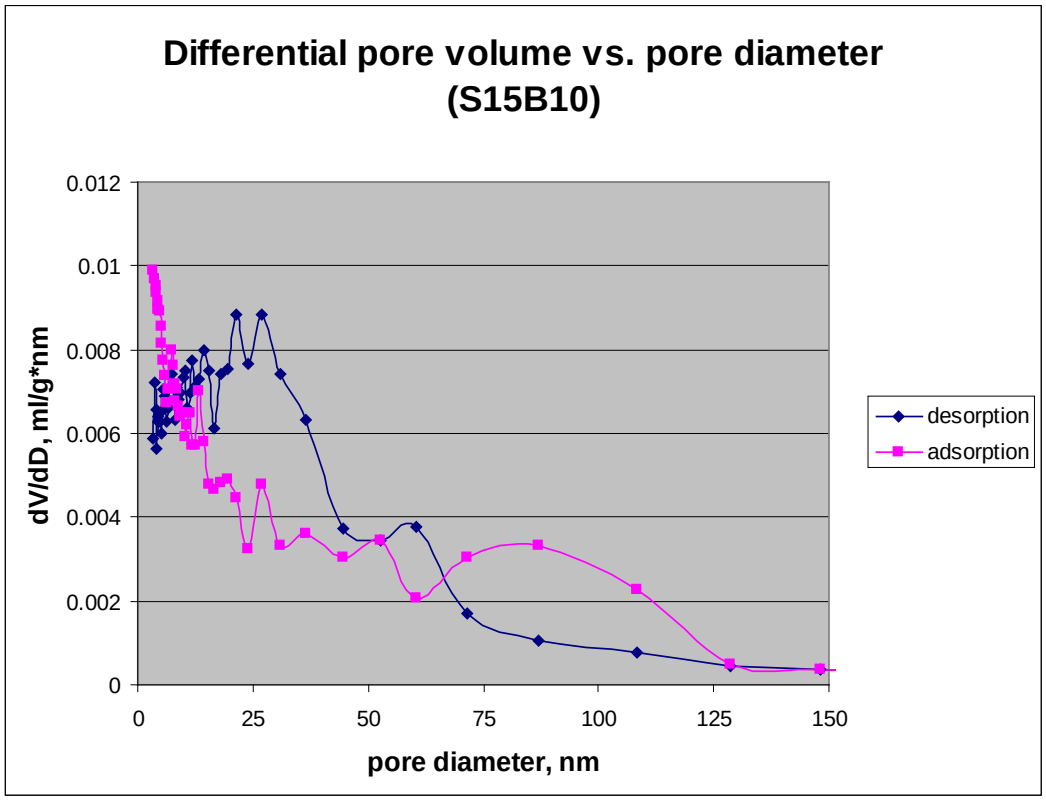

Figure 4.147: Pore size distribution of S15B10 PHP.

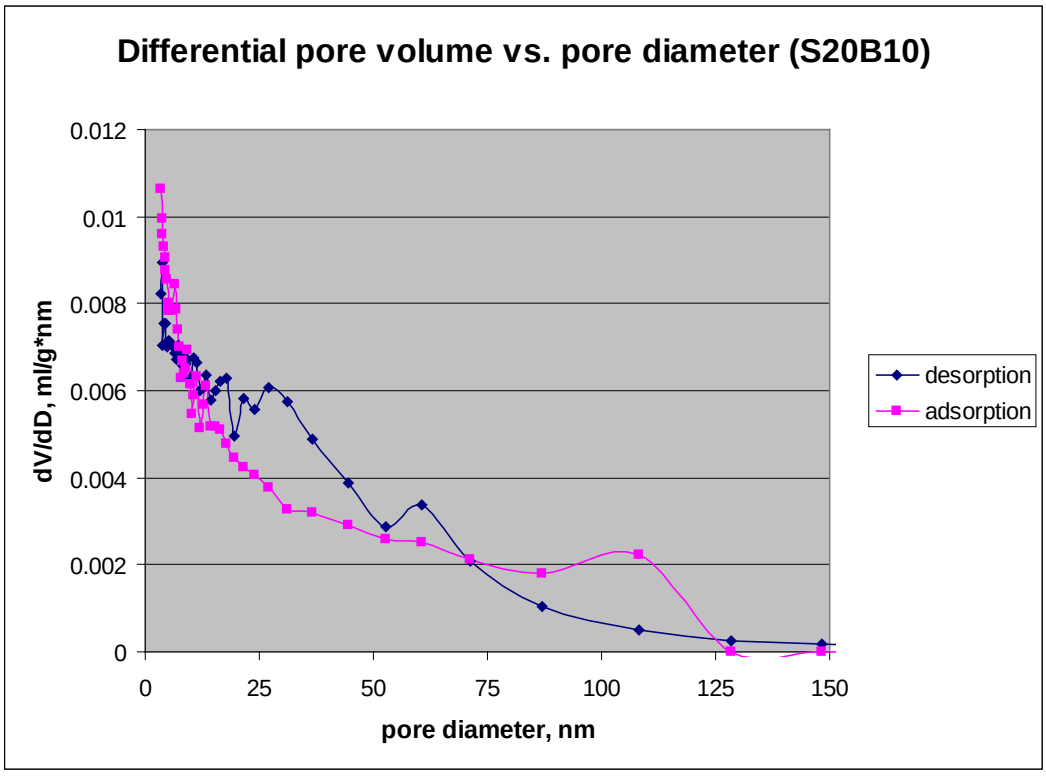

Figure 4.148: Pore size distribution of S20B10 PHP.

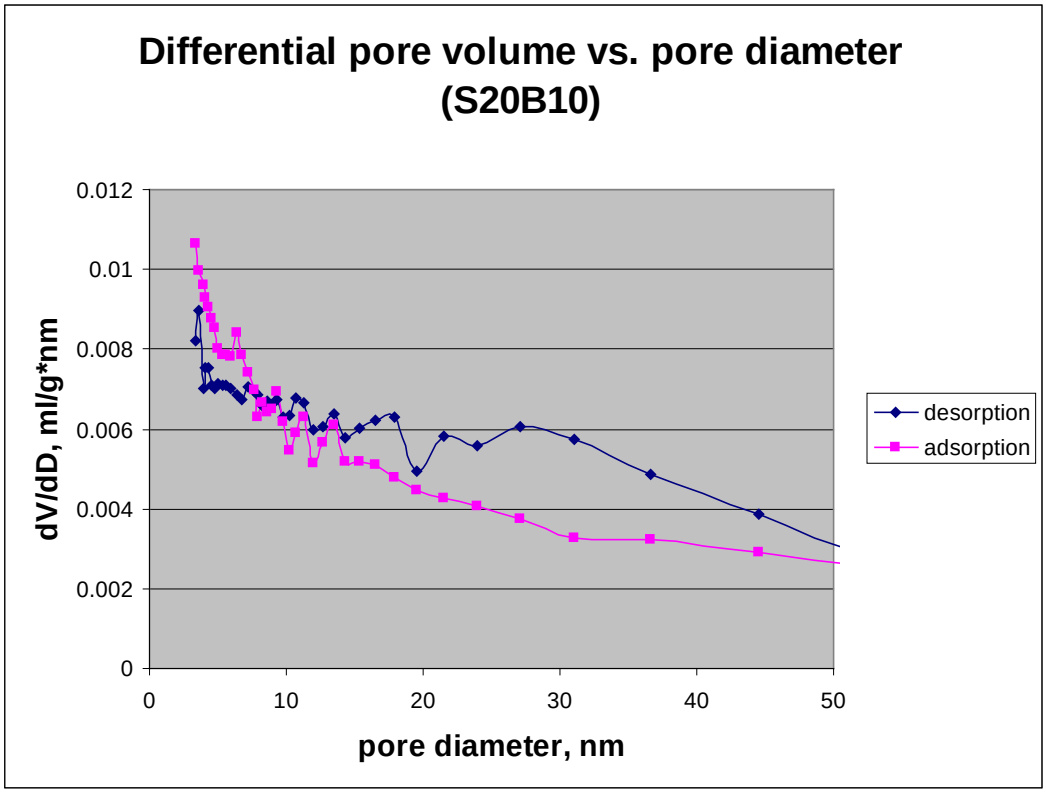

Figure 4.149: Pore size distribution for mesopores of S20B10 PHP.

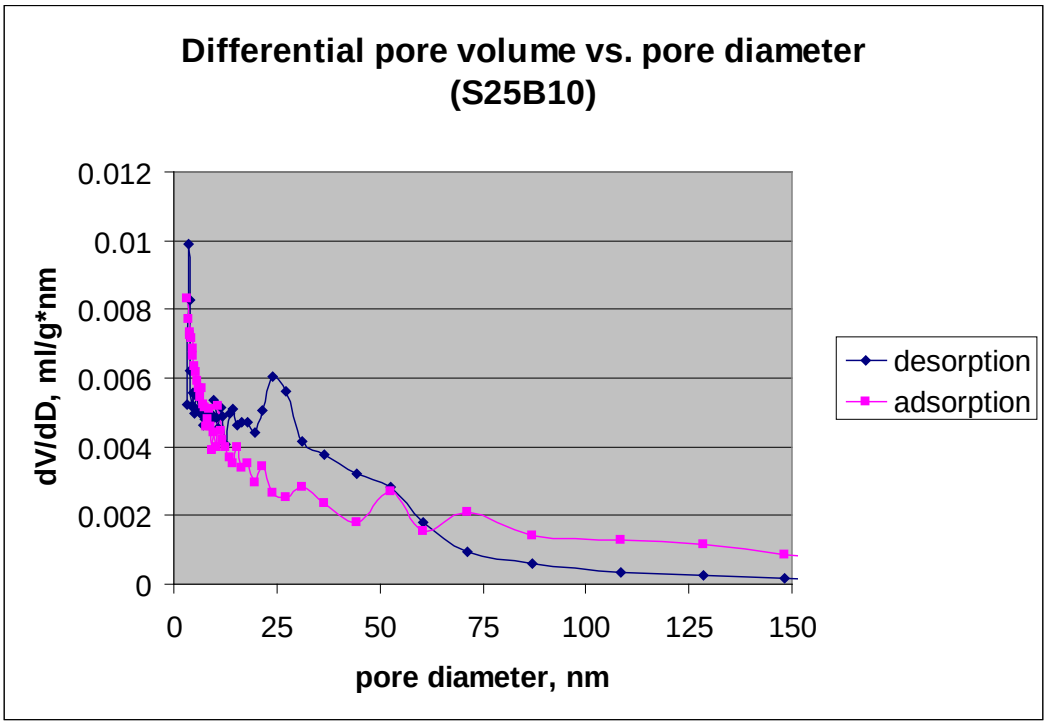

Figure 4.150: Pore size distribution of S25B10 PHP.

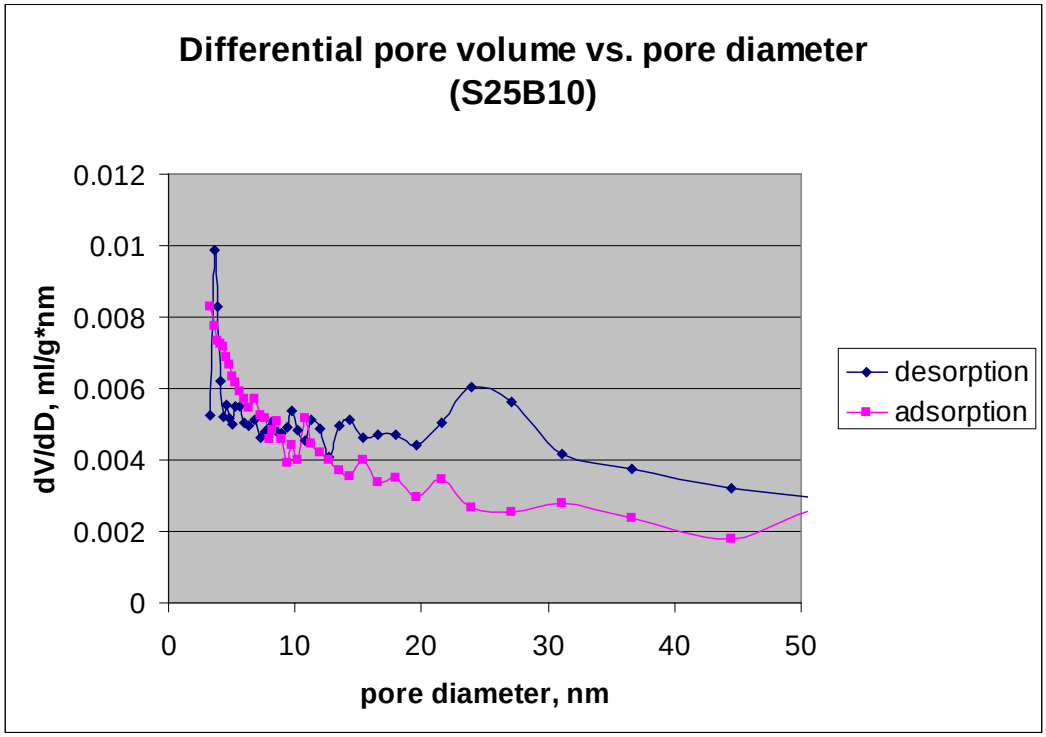

Figure 4.151: Pore size distribution for mesopores of S25B10 PHP.

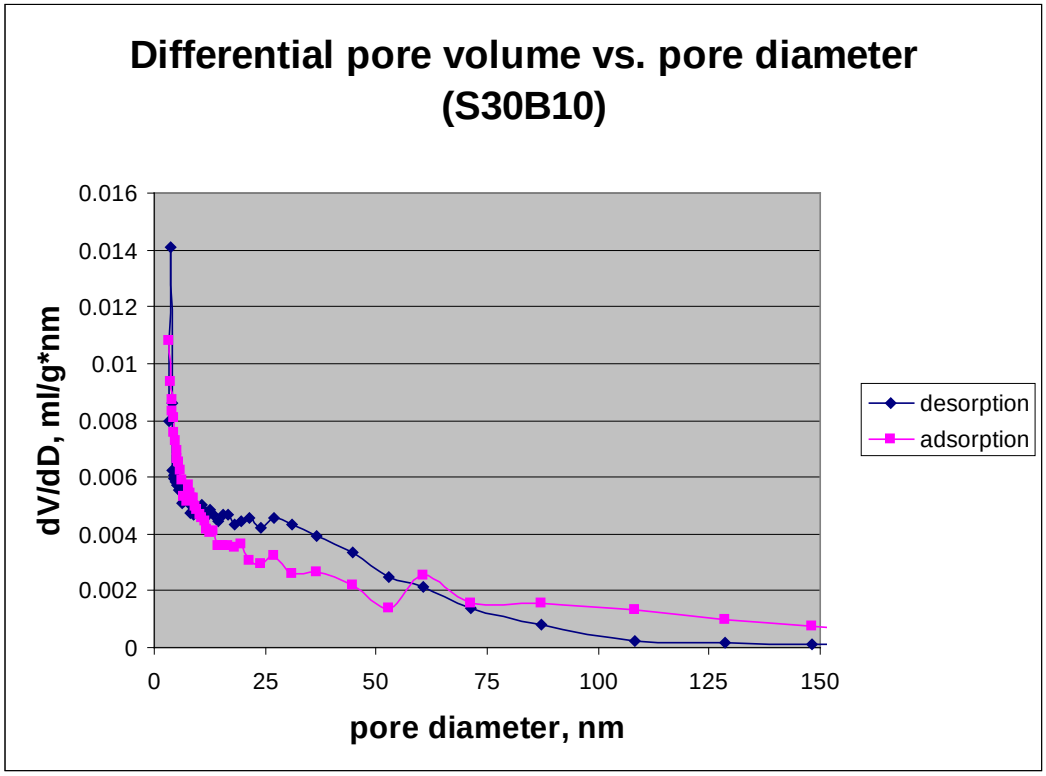

Figure 4.152: Pore size distribution of S30B10 PHP.

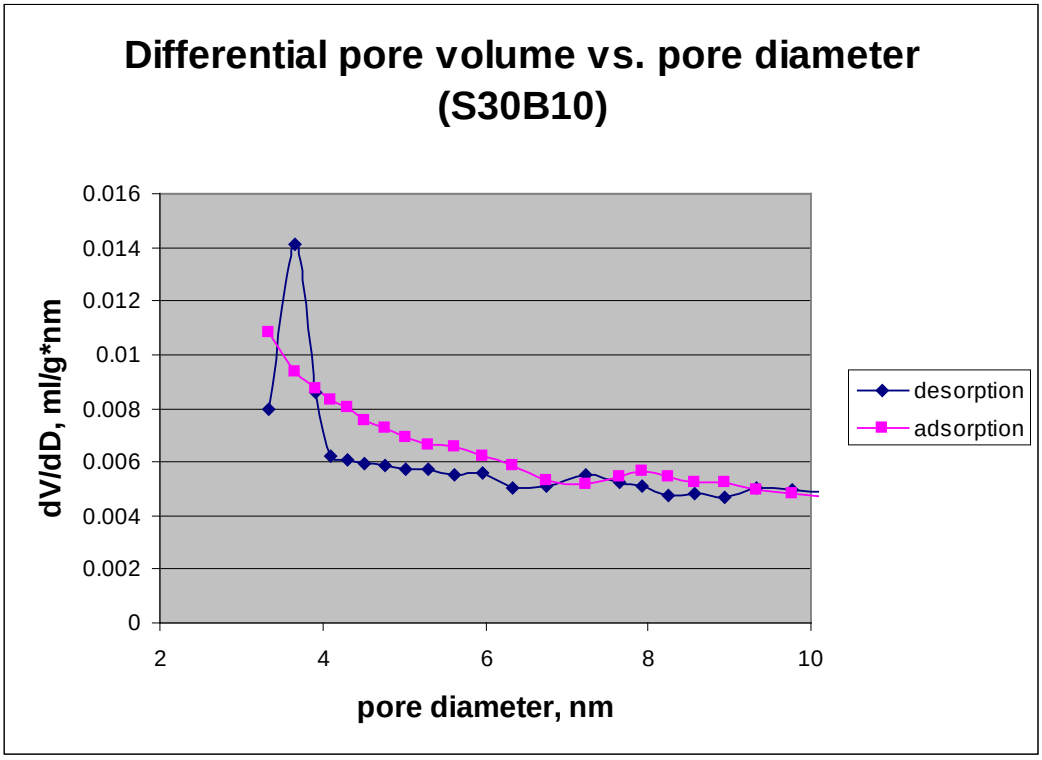

Figure 4.153: Pore size distribution for fine mesopores of S30B10 PHP.

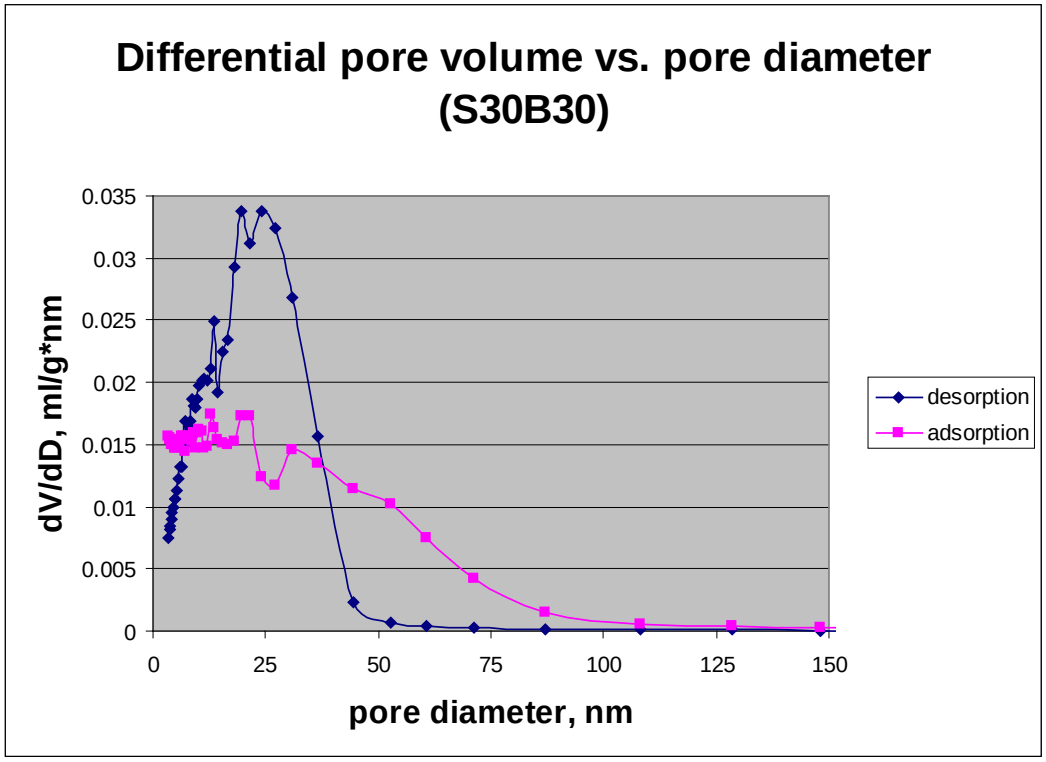

Figure 4.154: Pore size distribution of S30B30 PHP.

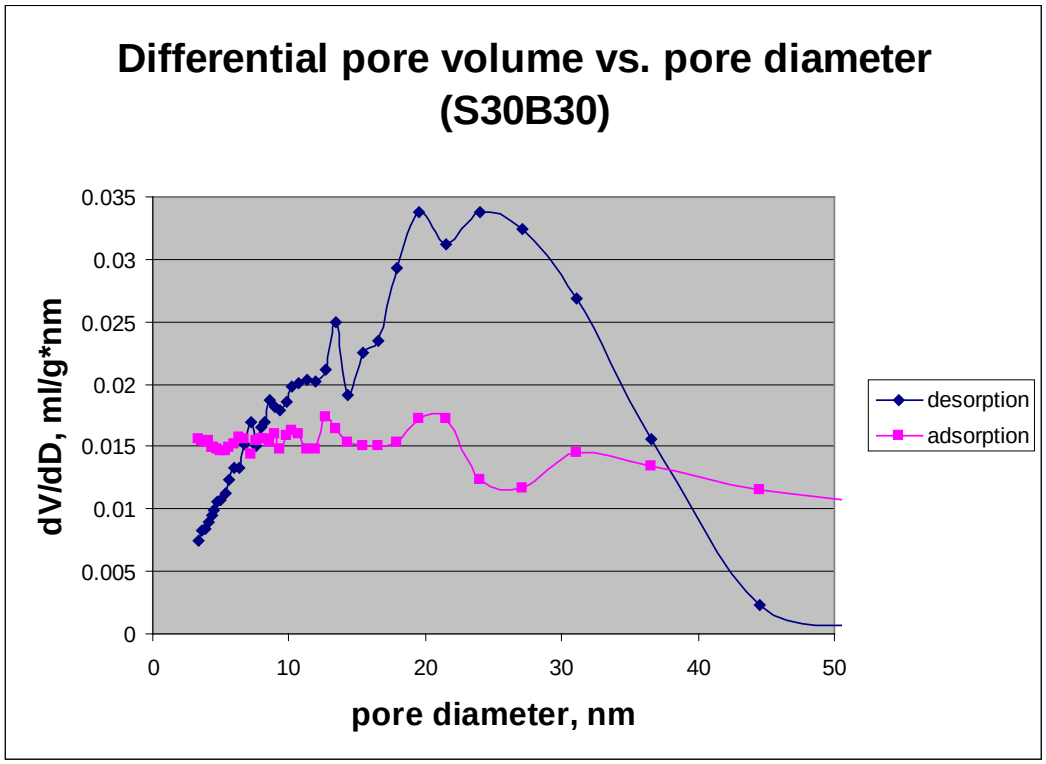

Figure 4.155: Pore size distribution for mesopores of S30B30 PHP.

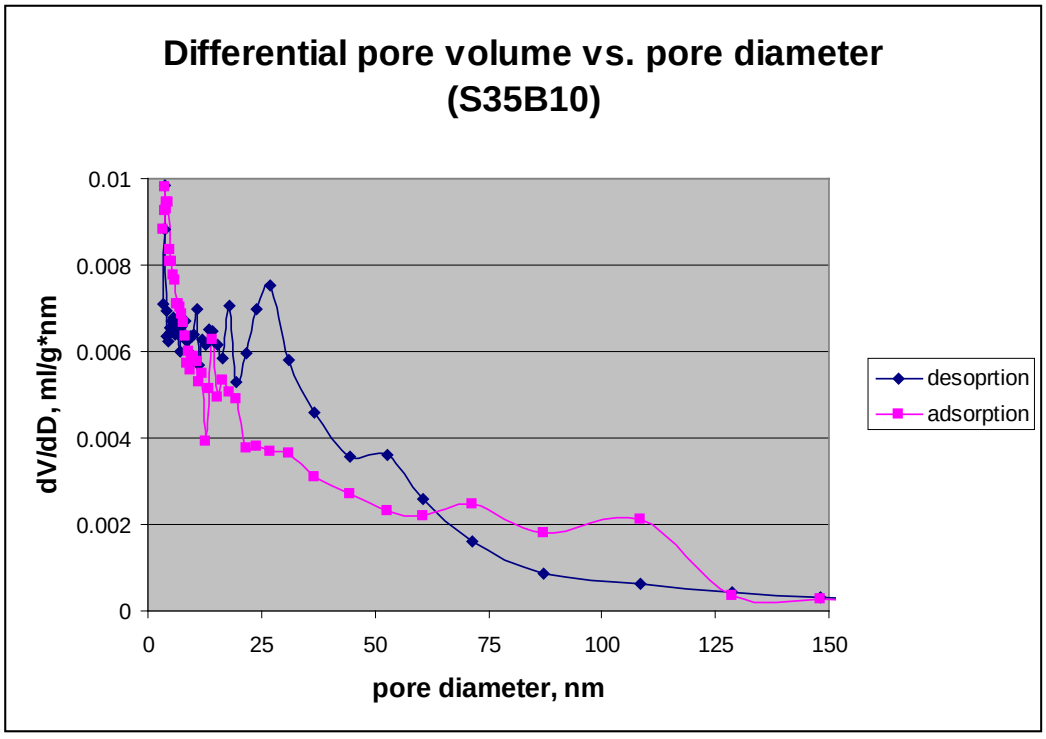

Figure 4.156: Pore size distribution of S35B10 PHP.

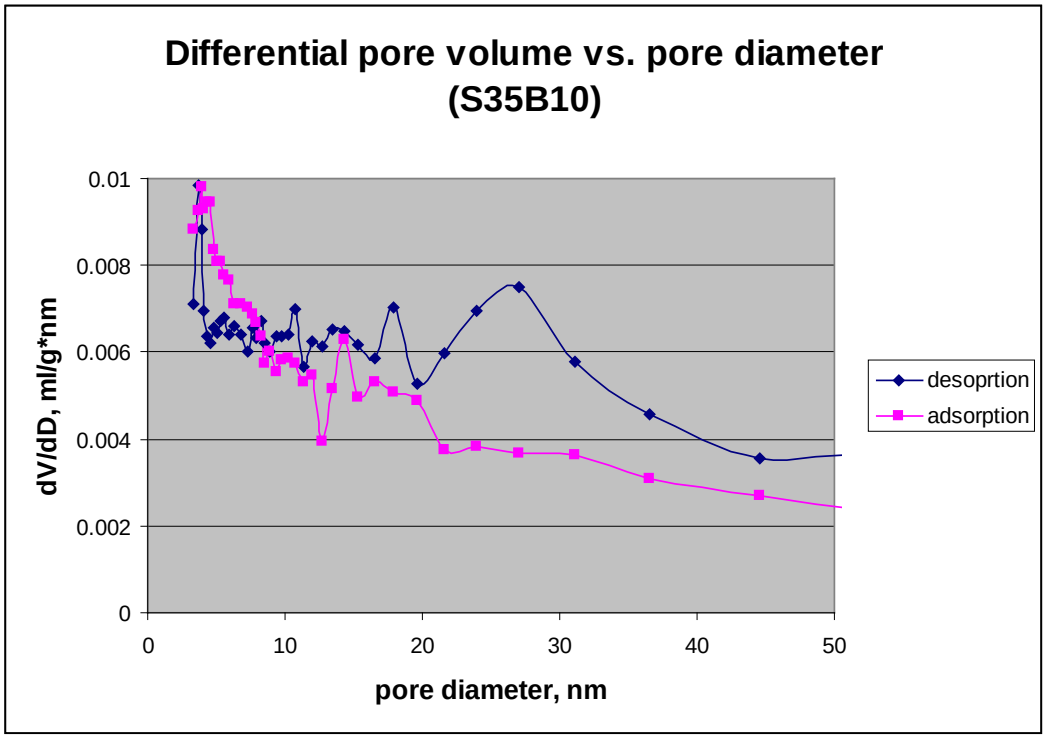

Figure 4.157: Pore size distribution of S35B10 PHP in mesopore region.

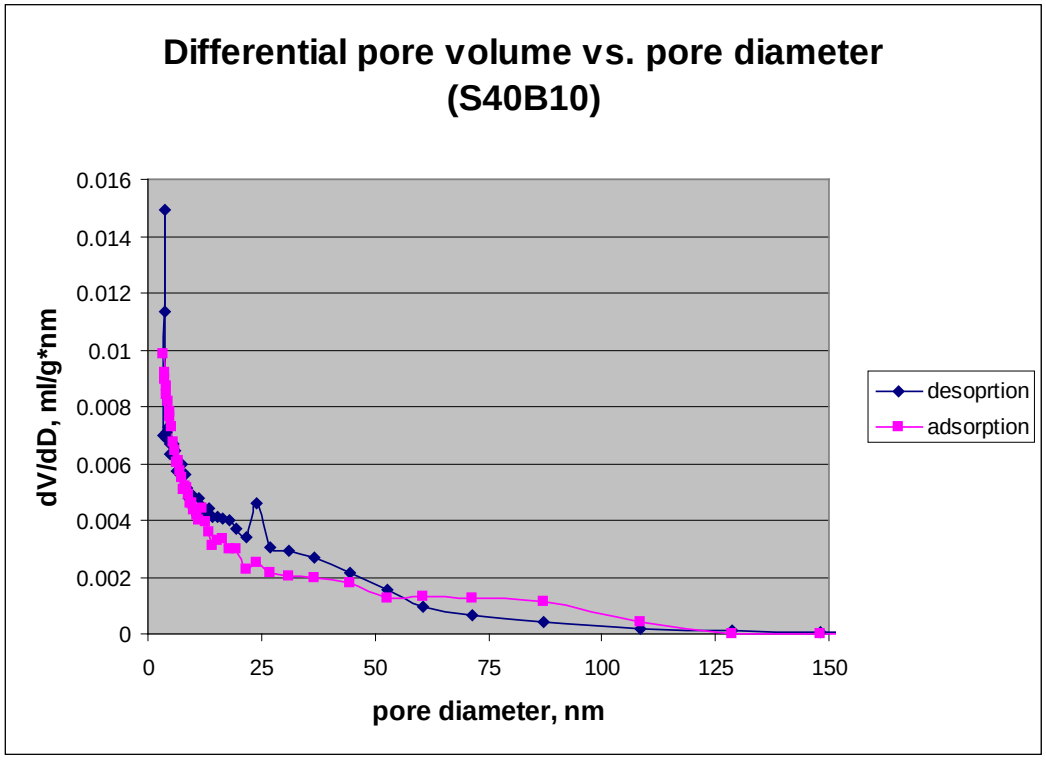

Figure 4.158: Pore size distribution of S40B10 PHP.

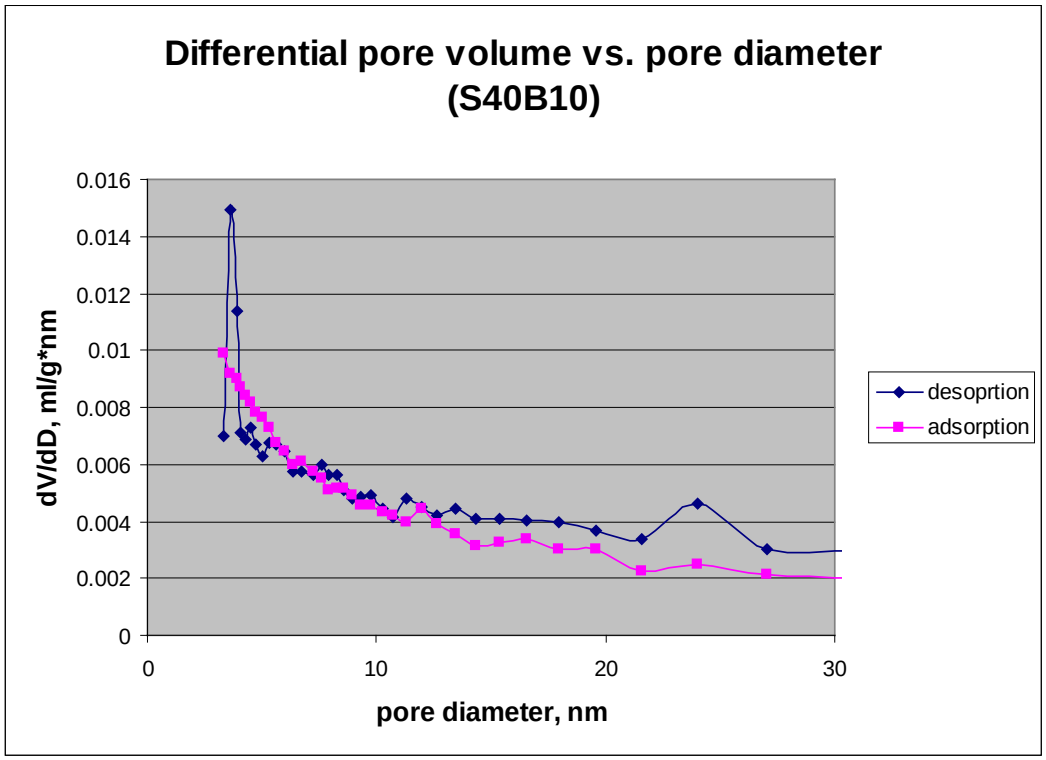

Figure 4.159: Pore size distribution of S40B10 PHP in low mesopore region.

4.7.2.4 Comparison of pore size distribution.

The results for pore volume in the mesopore range and total pore volume of the samples are presented in Table 4.29. For desorption curve, contribution of the mesopore range to the porosity of the samples is quite significant due to the high percentages of pore volumes in the mesopore region. The two highest contributions are from S10B30 and S30B30 with more than 90%. The rest of the samples have about 70% contribution from the mesopore range. On the other hand, adsorption curves exhibit a different result. Only S10B30 and S30B30 have pore volume contribution from the mesopore range more than 70%. The other samples have lower contribution of less than 60%, with S15B10 having the lowest contribution of only 35%.

Table 4.29: Desorption and adsorption pore volume for VTMS + Bindzil PHPs.

Sample name	Desorption pore volume			Adsorption pore volume		
	Mesopore, ml/g	% of mesopore	Total, ml/g	Mesopore, ml/g	% of mesopore	Total, ml/g
S10B10	0.3307	69.4	0.4764	0.2217	49.4	0.4492
S10B30	0.3953	99.1	0.3989	0.3485	90.9	0.3834
S15B10	0.3021	68.3	0.4421	0.2118	48.8	0.4335
S20B10	0.2540	67.9	0.3743	0.2039	57.1	0.3573
S25B10	0.2066	72.3	0.2858	0.1465	45.6	0.3213
S30B10	0.2026	71.1	0.2849	0.1592	49.3	0.3229
S30B30	0.8704	97.6	0.8923	0.6432	71.8	0.8959
S35B10	0.2577	68.2	0.3776	0.1980	53.8	0.3680
S40B10	0.1688	78.9	0.2141	0.1386	67.1	0.2065

Comparison of pore volumes of different VTMS-bindzil PHPs is presented in Figure 4.160. It has been observed that S30B30 has the highest pore volumes for all the types of pore volumes whereas S40B10 has the lowest of all types. It is clearly shown here the high contribution of mesopore range to pore volumes of S10B30 for both adsorption and desorption curves.

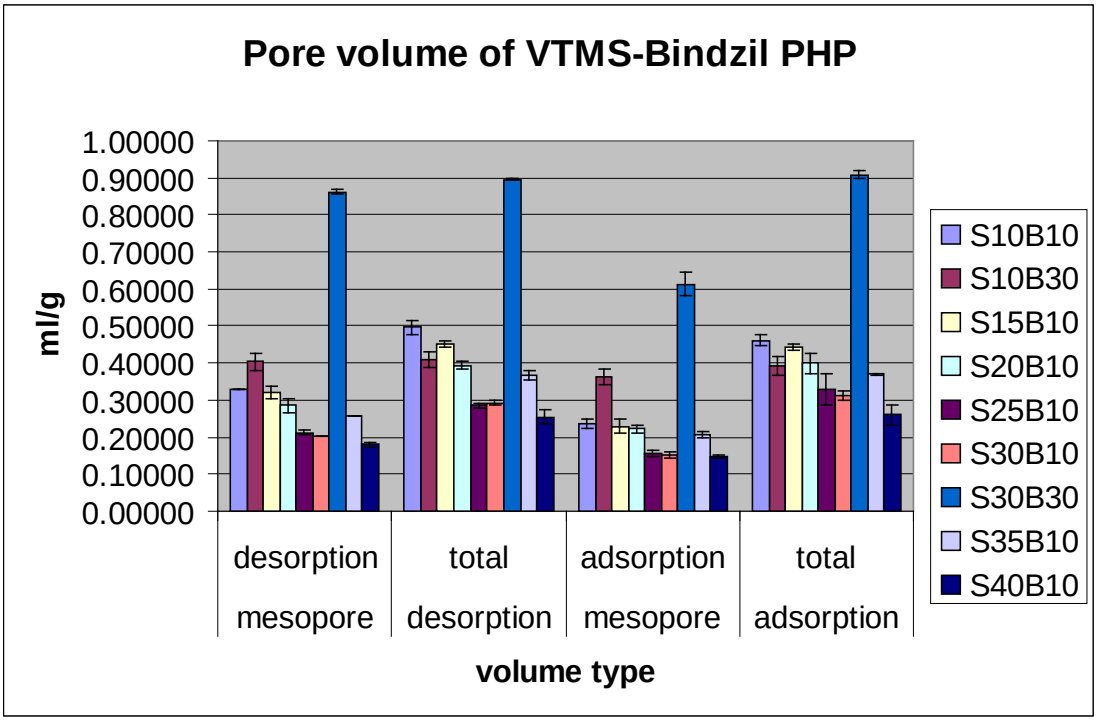

Figure 4.160: Plot of desorption and adsorption pore volume for VTMS-Bindzil PHPs.

4.7.3 FTIR Analysis

The spectra for several different VTMS-Binzil PHPs are presented in Figure 4.161 through Figure 4.164. All the spectra exhibit the strongest absorbance intensity in the absorbance band of 900 to 1280 cm^{-1} with the peak of about 1100 cm^{-1}. This band is attributed to –Si–OCH3 groups (Barzin et al., 2006; Rodriguez-Fernandez and Gilbert, 1997). Comparing the spectra to the spectrum of basic PHP S01, –Si–OCH3 band in silane-silica PHP spectra replaced the absorption peaks of 1028.063, 1057.199 and 1181.320 in the spectrum of basic PHP S01. Thus, VTMS was successfully incorporated into HIPE producing VTMS-Binzil PHP. The absorption peak 904.611 of basic PHP was shifted a little bit to 907 cm^{-1} with reduced intensity in VTMS-Binzil PHP. There is one more extra absorption peak at 960 cm^{-1} but vey weak; this peak is attributed to Si-O-Si linkages (Kim and Jang, 2000). These two absorption peaks appear very weak for S10B30, S30B10 and S30B30. S10B10 with the least percentage of VTMS and bindzil has the strongest absorption at these two peaks of 907 and 960 cm^{-1}. These two peaks appear in a mixed band with split peaks. The

absorption peaks of 697 and 757 in basic PHP still retain the same absorption peak since the shift is very small, about 1 cm^{-1}, but the intensity reduced. The peak at 838.846 disappeared at all in VTMS-Binzil PHP but the peak at 796.985 shifted a little bit to the lower wavenumber with higher intensity. The rest of the absorption peaks bigger than 1280 cm^{-1} still appear as they are in basic PHP but with reduced intensity. The intensity reduction is very apparent for S30B30, the one with highest percentage of VTMS and bindzil.

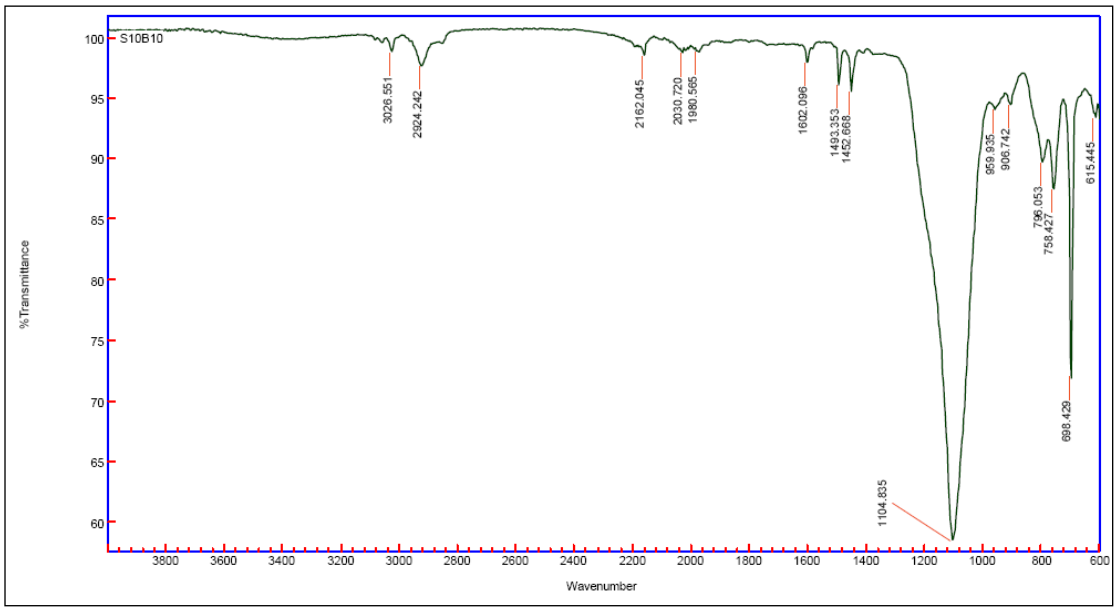

Figure 4.161: Spectrum of VTMS-bindzil PHP (S10B10).

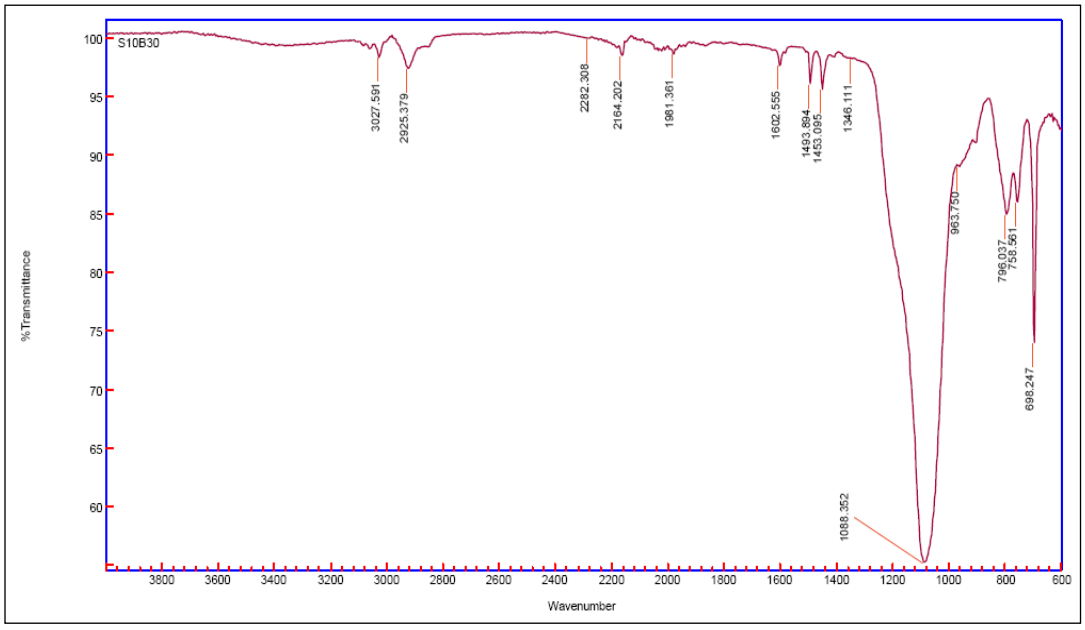

Figure 4.162: Spectrum of VTMS-bindzil PHP (S10B30).

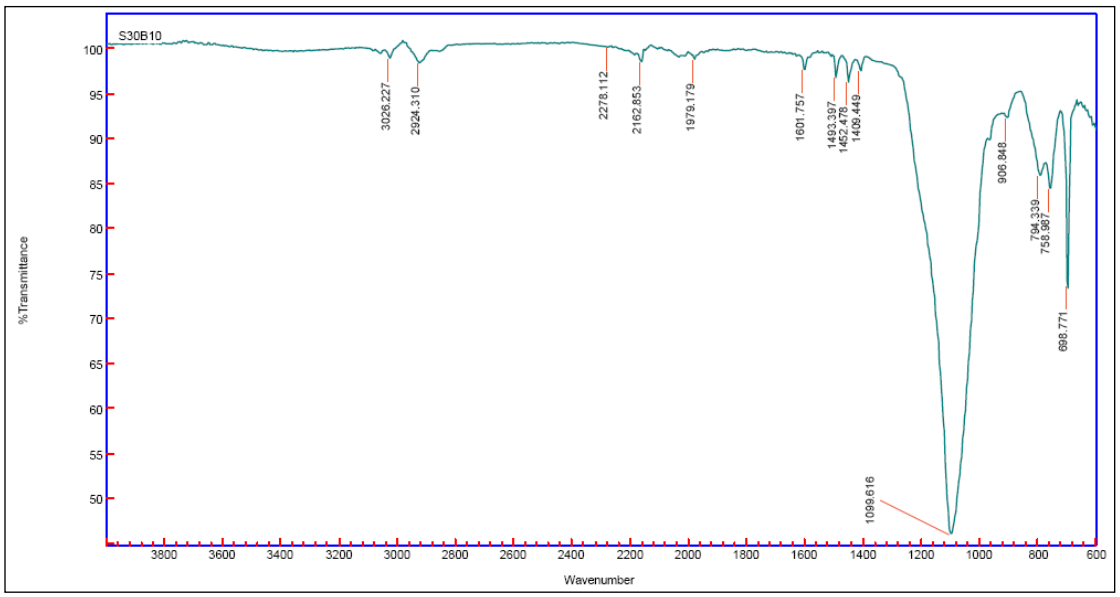

Figure 4.163: Spectrum of VTMS-bindzil PHP (S30B10).

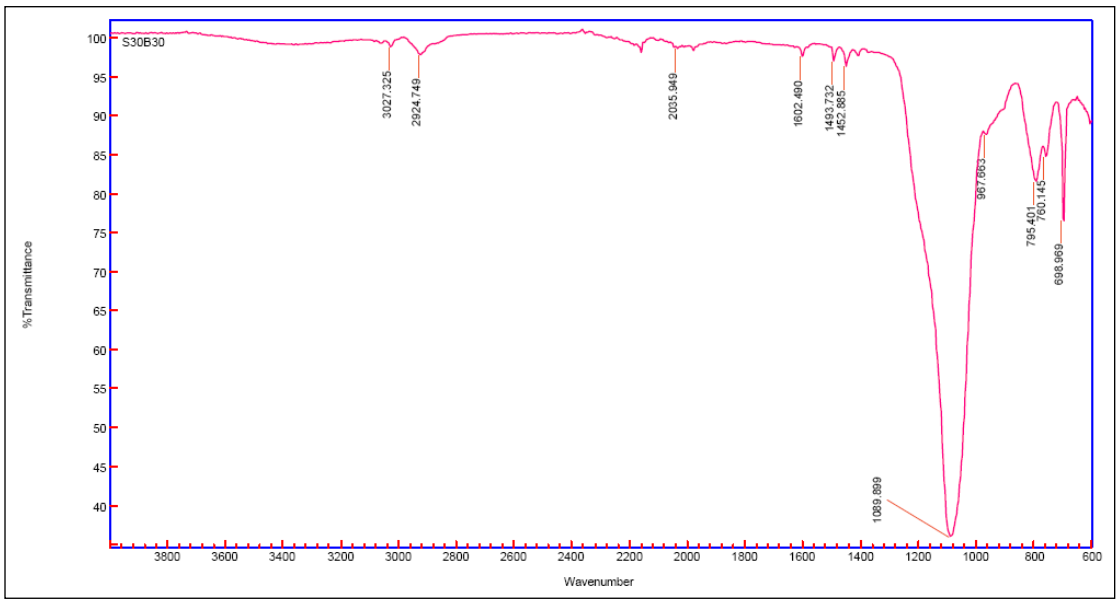

Figure 4.164: Spectrum for VTMS-bindzil PHP (S30B30)

Comparison of the four spectra of VTMS-bindzil PHP is presented in Figure 4.165. In the absorbance band of 900 to 1280 cm-1, S10B10 spectrum exhibits the strongest absorption intensity, followed by S10B30, and then by S30B10 and S30B30. The spectra of S30B10 and S30B30 are similar; their peak intensities are almost the same and overlapping on one another.

Comparing the spectrum of S30B30 to the spectra of S30 and B30, S30B30 has the strongest absorption peak in the band of 900 to 1280 cm^{-1}. This might be due to overlapping of –Si–O-CH_3 and Si–O–Si bands in this region.

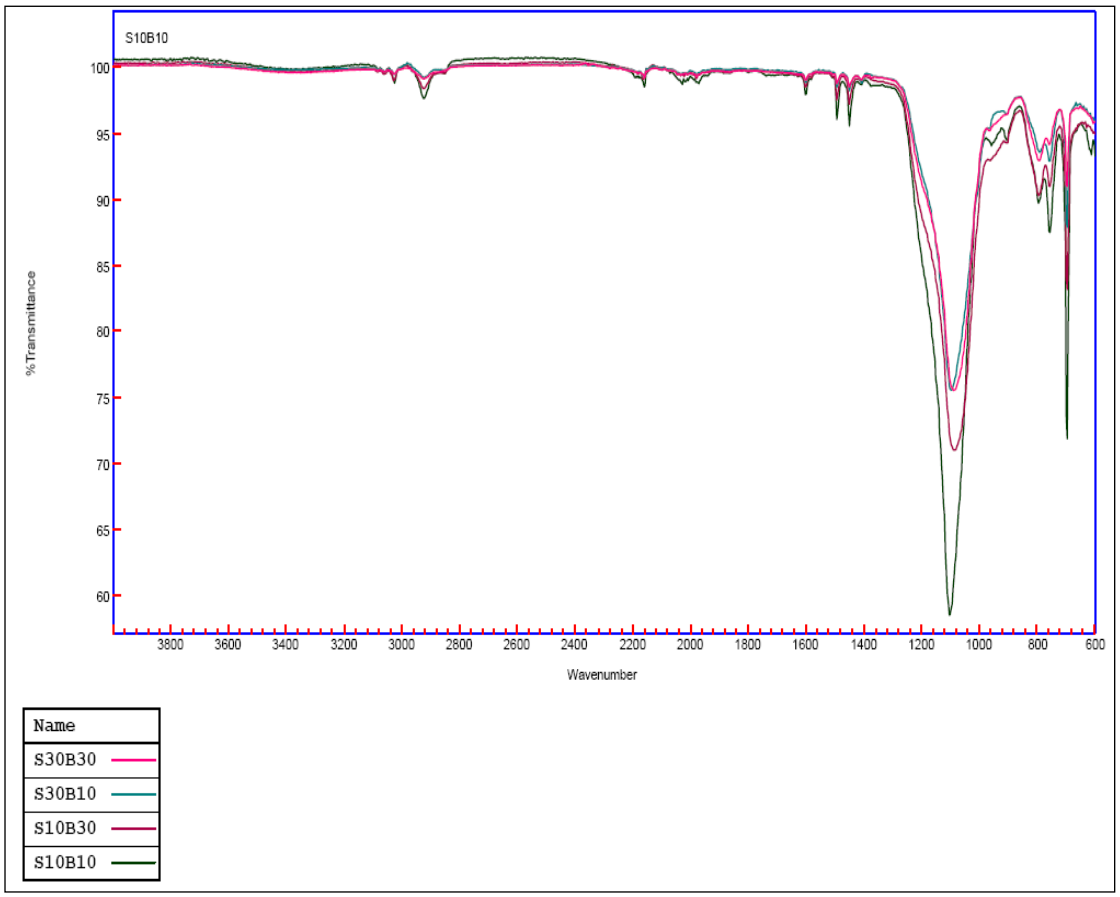

Figure 4.165: Comparison of four VTMS-Bindzil PHPs

4.8 *Microporosity*

A check on the presence of the micropore volumes was done by doing t-Plot analysis using Harkin-Jura equation. None of the samples showed the presence of micropore volumes. (Pores with widths not exceeding about 2 nm are called micropores, according to IUPAC).

4.9 *Sulphonation of PHP*

Sulphonation of PHP using thermal (via conventional oven) method and microwave irradiation was tried. Sulphonated Binzil PHPs were successfully produced using microwave irradiation and thermal methods. On the other hand, trials on VTMS PHPs using microwave irradiation were a failure, the PHPs burned and crumbled. Sulphonated VTMS PHP was successfully produced through thermal method, using a conventional oven only. The list of sulphonated PHPs produced are presented in Table 4.30.

Table 4.30: List of sulphonated PHPs.

sample name	% acid	soaking time, hr	microwave	thermal
B30A	98	2	/	
B30AN	98	2	/	
B30B	98	24	/	
B30BN	98	24	/	
B30C	98	24		95°C
B30CN	98	24		95°C
S30A	10	24		95°C
S30AN	10	24		95°C
S30B	98	24		95°C
S30BN	98	24		95°C

N=neutralised with Sodium Hydroxide, soaked in 1M NaOH for 3 hours.

4.9.1 Morphology

Morphology of sulphonated VTMS and Bindzil PHPs is presented by SEM images in Figure 4.166. Cracks could be observed on the structure of sulphonated PHPs. The sulphonated PHPs still retain the pore shape of VTMS and Bindzil PHPs. S30BN, sulphonated VTMS in 98% sulphuric acid has more cracks compared to S30AN, sulphonated VTMS in 10% sulphuric acid. Sulphonated Bindzil PHPs produced through microwave irradiation, B30AN and B30BN have more cracks

compared to sulphonated Bindzil PHP produced through thermal method, B30CN. The cracks in morphology of B30BN, soaked for 24 hours in sulphuric acid are more apparent compared to the cracks in morphology of B30AN, soaked for 2 hours in sulphuric acid.

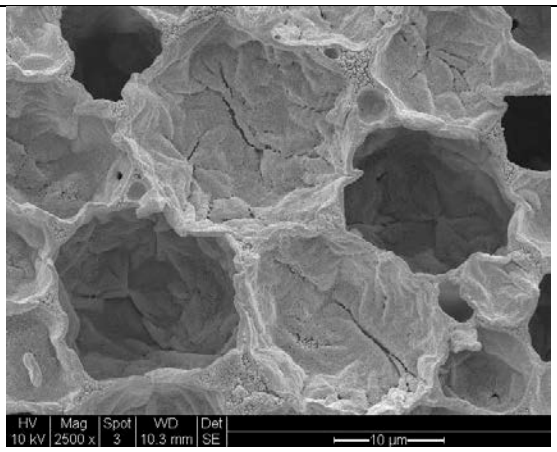

(a) S30AN, X2500

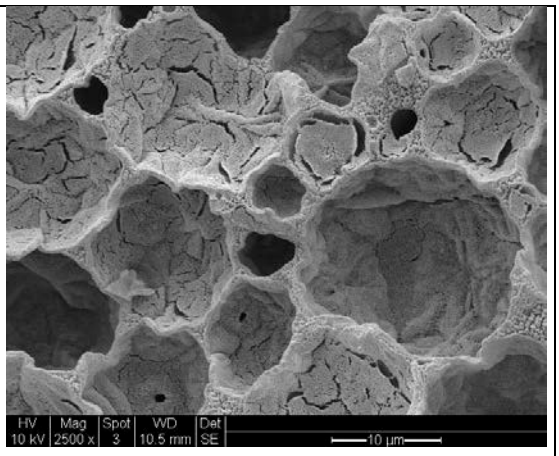

(b) S30BN, X2500

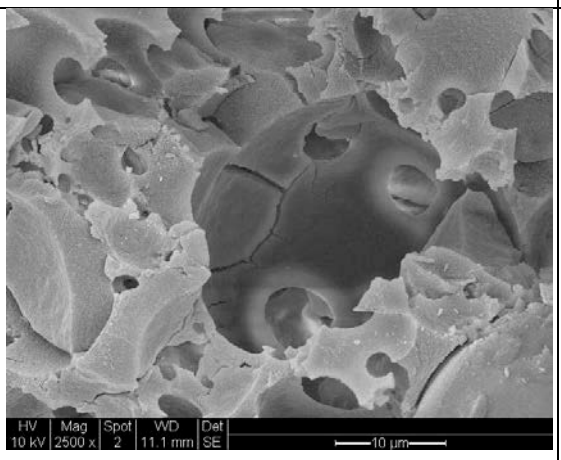

(c) B30AN, X2500

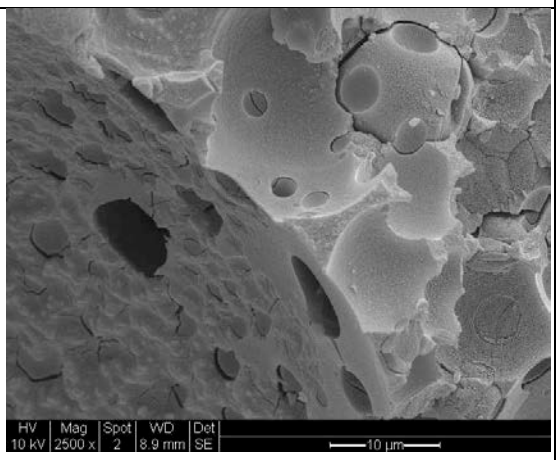

(d) B30BN, X2500

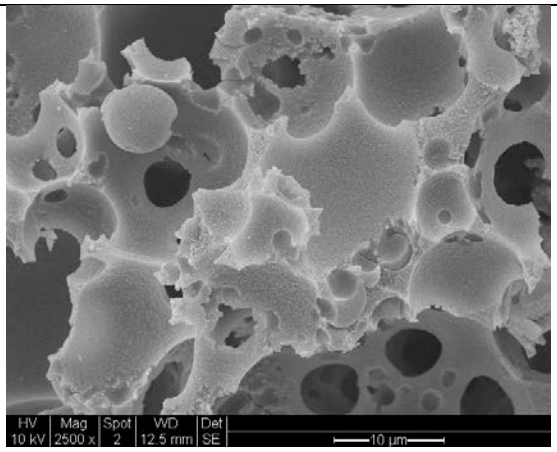

(e) B30CN, X2500

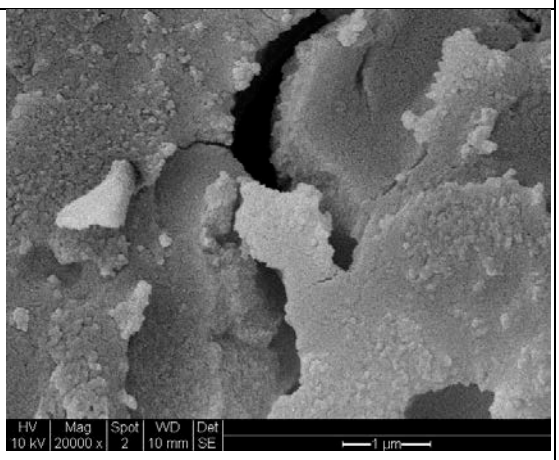

(f) B30CN, X20000

Figure 4.166: SEM images of sulphonated VTMS and Bindzil PHP

4.9.2 Isotherms

Comparison of isotherms of VTMS PHPs is presented in Figure 4.167. Volume adsorbed is less for sulphonated VTMS PHPs compared to VTMS PHP.

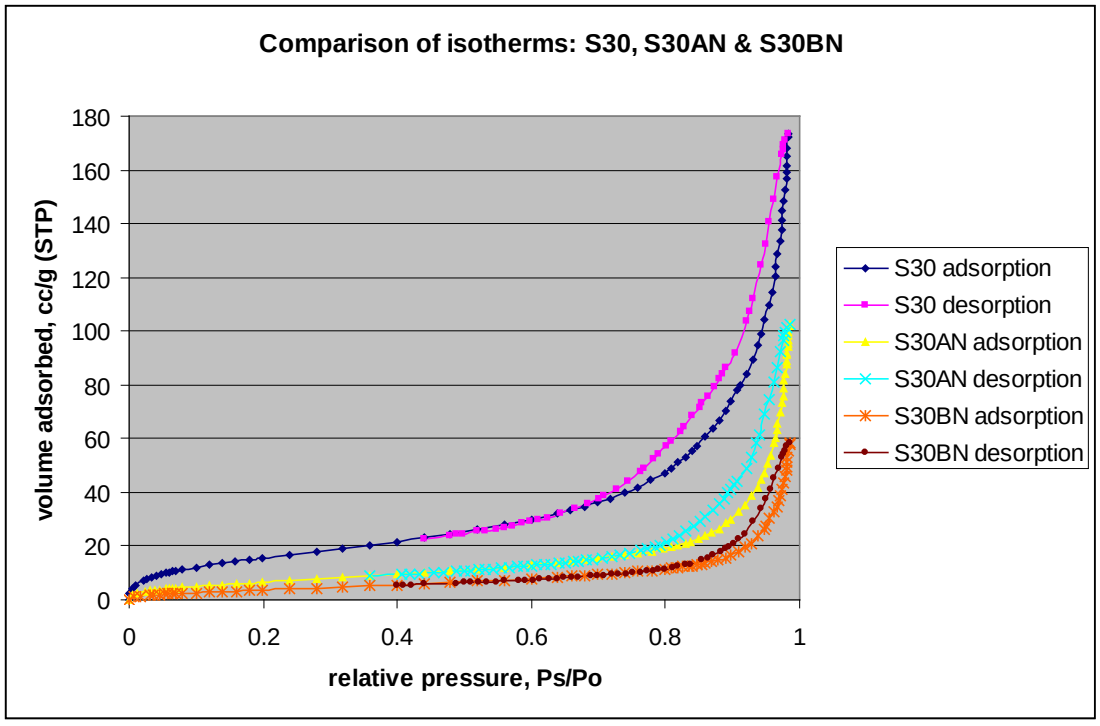

Figure 4.167: Isotherms of VTMS PHPs, unsulphonated vs. sulphonated.

Comparison of isotherms between sulphonated Bindzil PHPs and to Bindzil PHP is presented in Figure 4.168. B30CN exhibits the steepest slope and B30BN exhibits the least volume adsorbed of all the isotherms. This observation agreed with the surface area of B30BN, the smallest value as presented and discussed in the following section.

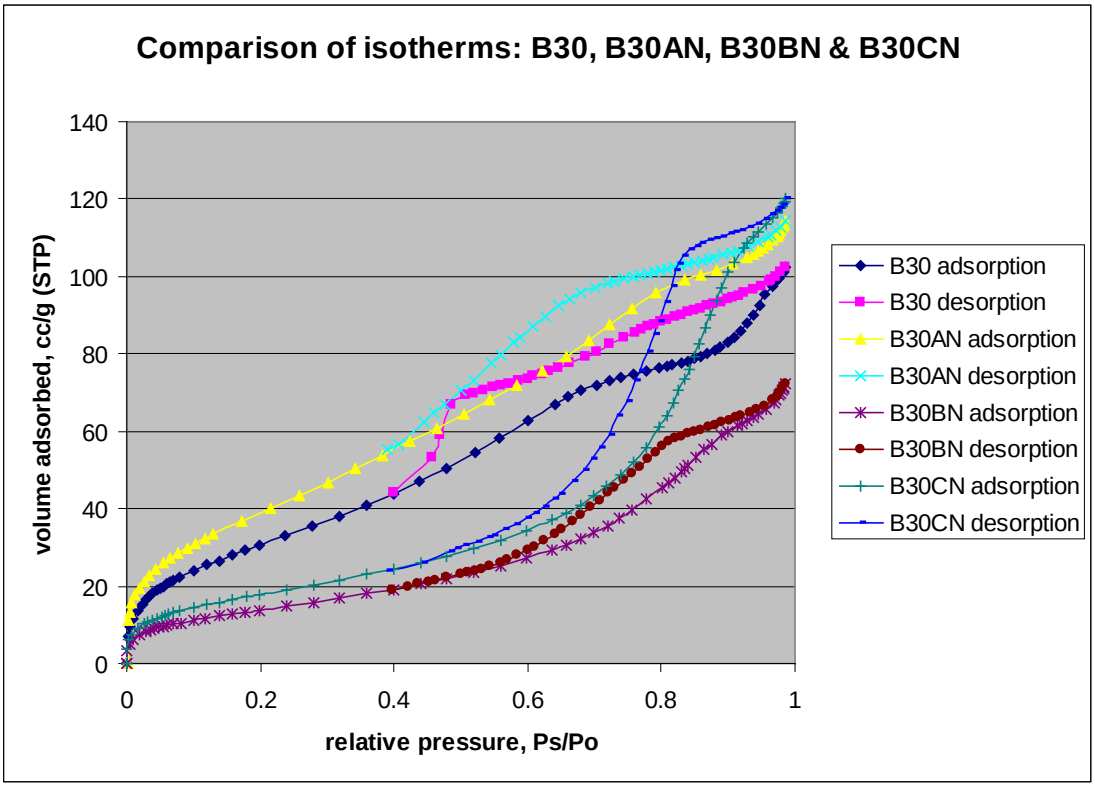

Figure 4.168: Isotherms of Bindzil PHPs, unsulphonated vs. sulphonated.

4.9.3 Surface area of sulphonated PHP

The results for surface area of sulphonated PHPs are presented in Table 4.31 and the comparison of surface area are presented in Figure 4.169. There was no overlapping of error bars; hence, all the surface areas of sulphonated PHPs are significantly different from those of the unsulphonated PHPs.

Table 4.31: Surface area of sulphonated PHPs

sample name	average m^2/g	std error
B30	113.4	3.1
B30AN	100.1	7.3
B30BN	37.7	2.5
B30CN	71.5	7.1
S30	54.2	2.3
S30AN	17.2	1.0
S30BN	9.0	0.7

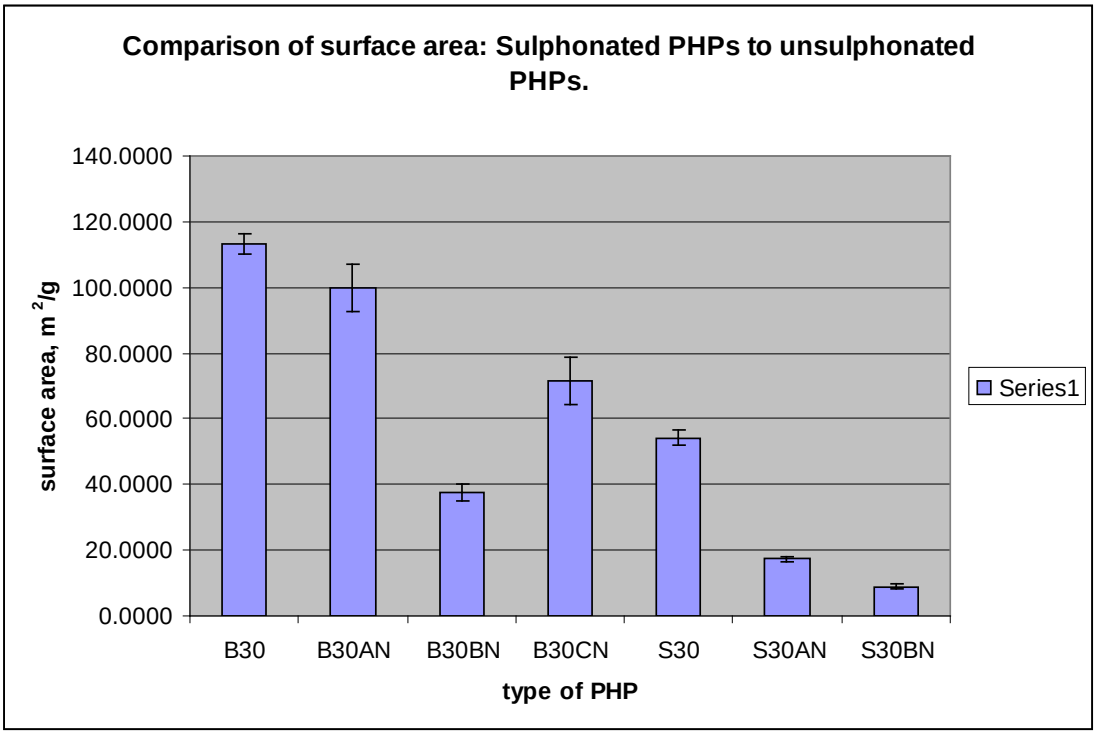

Figure 4.169: Surface area comparison of sulphonated PHPs to unsulphonated PHPs.

Analysis of Variance (ANOVA) was further performed to see how significant the differences are. At 5% significance level, it can be concluded that there are significant differences in the surface areas of the sulphonated bindzil (silica) PHPs. These differences are further analysed by Bonferroni test at 95.0% confident intervals. The pairs that are difference are B30 & B30BN, B30 & B30CN, B30AN & B30BN, and B30BN & B30CN. Surface area of B30AN, sulphonated bindzil PHP produced through soaking in 98% H_2SO_4 for 2 hours and microwave irradiation does not changed significantly when compared to bindzil PHP, B30.

For VTMS (silane) PHPs, it can be concluded that there are significant differences in the surface area of the polymers at 5% significance level. These differences are further analysed by Bonferroni test at 95.0% confident intervals. Significant differences exist between the surface areas of all the three types of VTMS PHPs. The surface area of VTMS PHP decreases significantly upon sulphonation. Sulphonated VTMS with 98% acid, S30BN has lower surface area compared to sulphonated VTMS with 10% acid, S30AN. This result agrees with the isotherms presented in Figure 4.167.

4.9.4 Pore size

The pore size distribution of sulphonated VTMS PHPs are presented in Figure 4.170 and Figure 4.171. In general, similar to VTMS PHP, the pore size distributions for desorption curves of both sulphonated VTMS PHPs are centred in the mesopore region. There are peaks observed for adsorption curves of both samples in the mesopore region but at a lower differential pore volume. However, adsorption curves of both samples exhibit higher differential pore volumes in the region of fine mesopore, less than 10 nm.

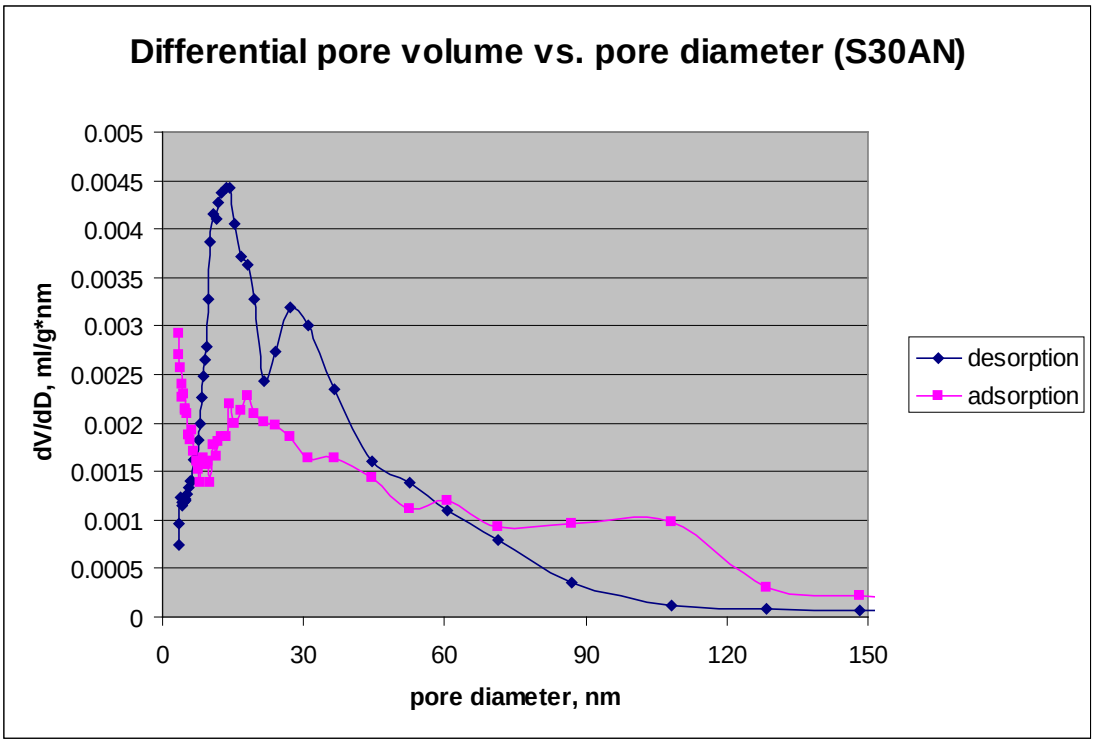

Figure 4.170: Pore size distribution of sulphonated VTMS PHP (S30AN), sulphonated in 10% sulphuric acid & thermally oven treated at 95 ° C

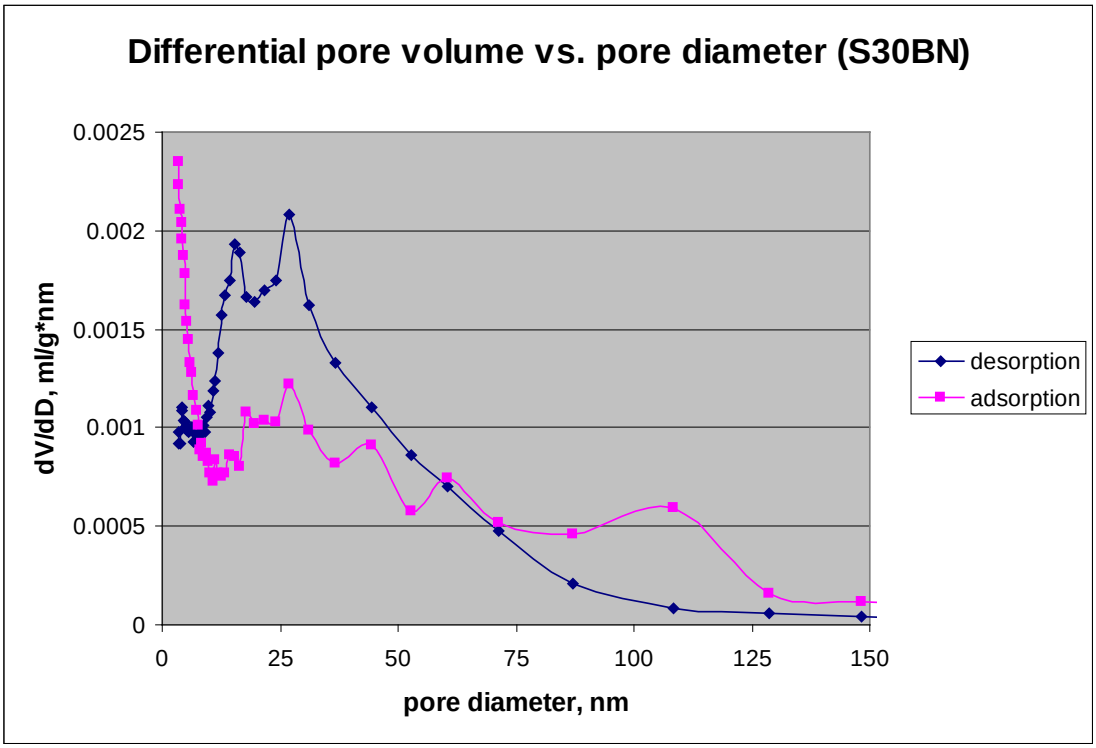

Figure 4.171: Pore size distribution of sulphonated VTMS PHP (S30BN), sulphonated in 98% sulphuric acid & thermally oven treated at 95 ° C.

Comparison of pore volumes of VTMS PHPs to sulphonated VTMS PHP is presented in Figure 4.172. Statistical analysis, ANOVA was performed and the results showed that there were significant differences in desorption mesopore volumes, total desorption pore volumes, adsorption mesopore volumes and total adsorption pore volumes of the VTMS PHPs and sulphonated VTMS PHPs. These differences were further analysed by Bonferroni test at 95.0% confident intervals and the results are presented in Table 4.32. Desorption mesopore volumes and total desorption pore volumes of VTMS decreased significantly upon sulphonation.

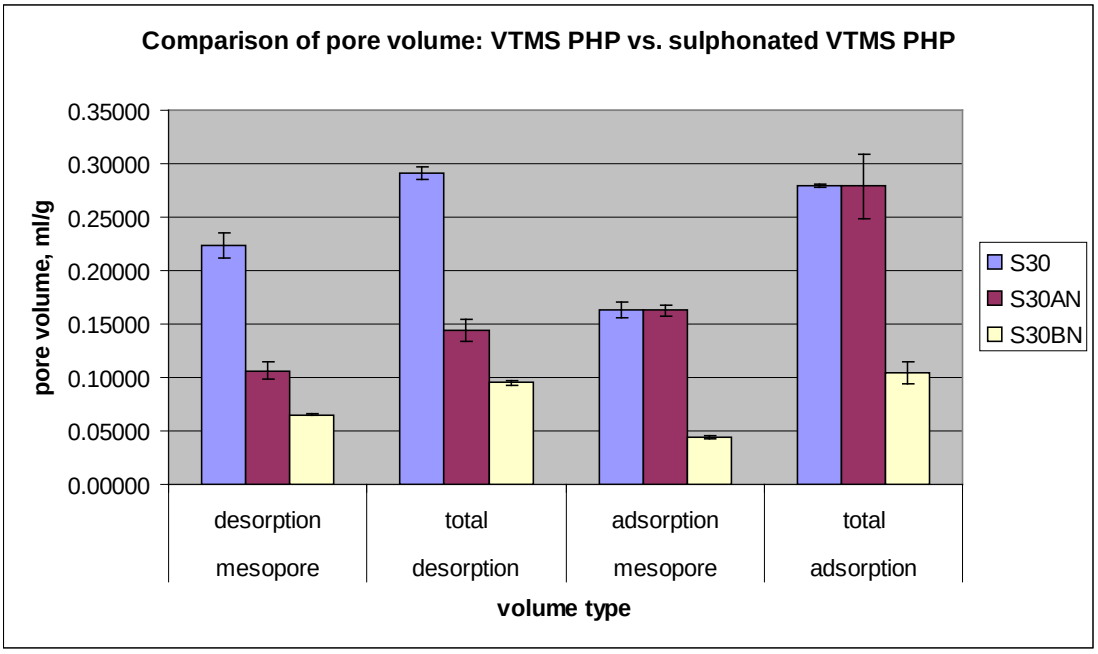

Figure 4.172: Comparison of pore volumes, sulphonated vs. unsulphonated VTMS PHPs.

Table 4.32: Results of Bonferroni test of VTMS and sulphonated VTMS PHPs, pairwise comparison.

Types of volumes	Pairs that are difference at 95% confident intervals
Desorption mesopore volumes	S30 & S30AN, S30 & S30BN
Total desorption pore volumes	S30 & S30AN, S30 & S30BN, S30AN & S30BN
Adsorption mesopore volumes	S30 & S30AN, S30 & S30BN
Total adsorption pore volumes	S30 & S30BN

The pore size distribution for sulphonated Bindzil PHPs are presented in Figure 4.173 through Figure 4.175. There is no significant peak observed for adsorption and desorption curves of B30AN in the mesopore region. However, both curves of B30AN exhibit higher differential pore volumes in the region of fine mesopore, less than 10 nm. In general, the pore size distributions for desorption curve and adsorption curve of B30BN and B30CN are centred in the mesopore region. Both samples exhibit monomodal distribution in the region of fine mesopore, less than 10nm. For B30BN, there is a peak centred at 7.93 nm for adsorption curve and a peak

centred at 5.61 nm for desorption curve. B30CN has a peak centred at 9.77 nm for adsorption curve and a peak centred at 7.64 nm for desorption curve.

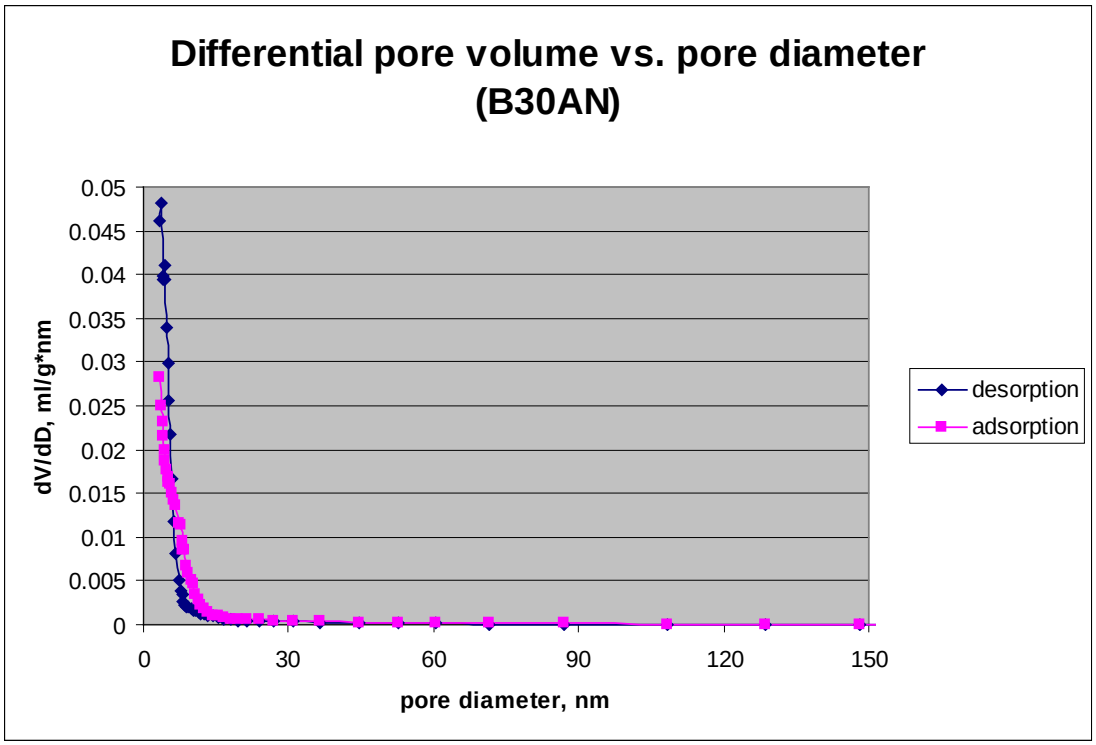

Figure 4.173: Pore size distribution of sulphonated bindzil PHP (B30AN), soaked 2 hours in 98% sulphuric acid & microwave irradiated.

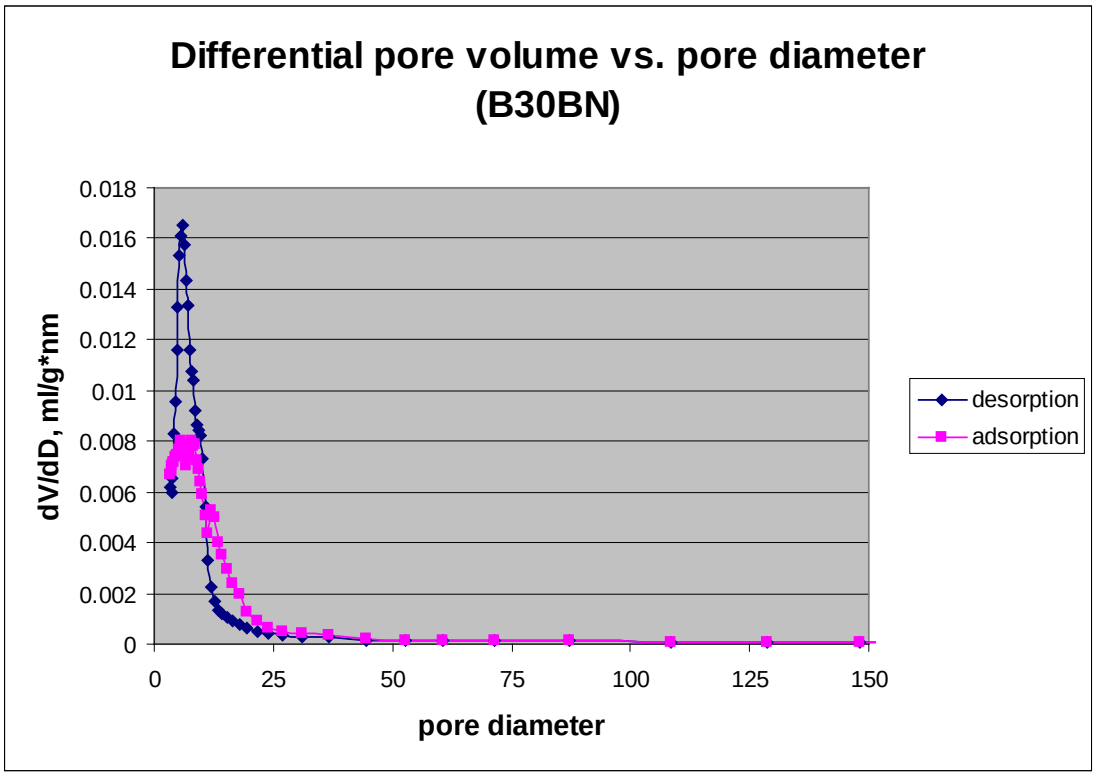

Figure 4.174: Pore size distribution of sulphonated Binzil PHPs (B30BN), soaked 24 hours in 98% sulphuric acid & microwave irradiated.

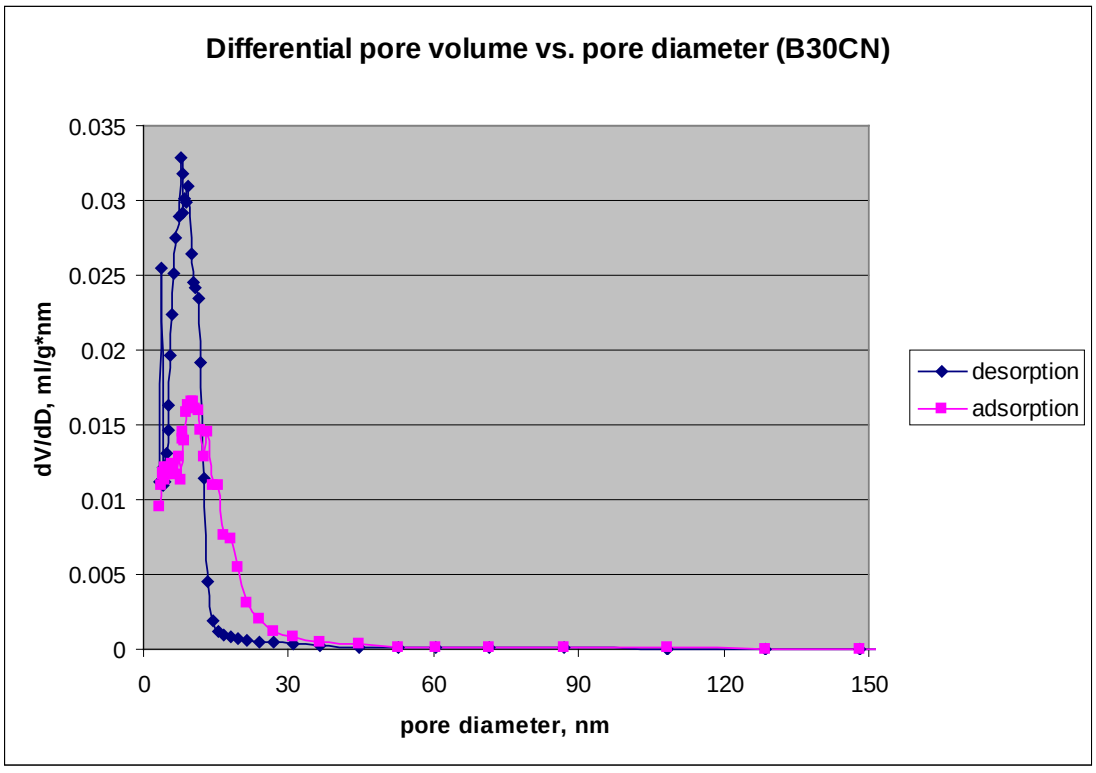

Figure 4.175: Pore size distribution of sulphonated Binzil PHPs (B30CN), soaked 24 hours in 98% sulphuric acid, thermally oven treated at 95 °C.

Comparison of pore volumes of B30 PHP to sulphonated B30 PHP is presented in Figure 4.176. Statistical analysis, ANOVA at 5% significance level was further performed to see how significant the differences were; the results showed there was no significant difference between all types of pore volumes of B30 and sulphonated B30 polymers.

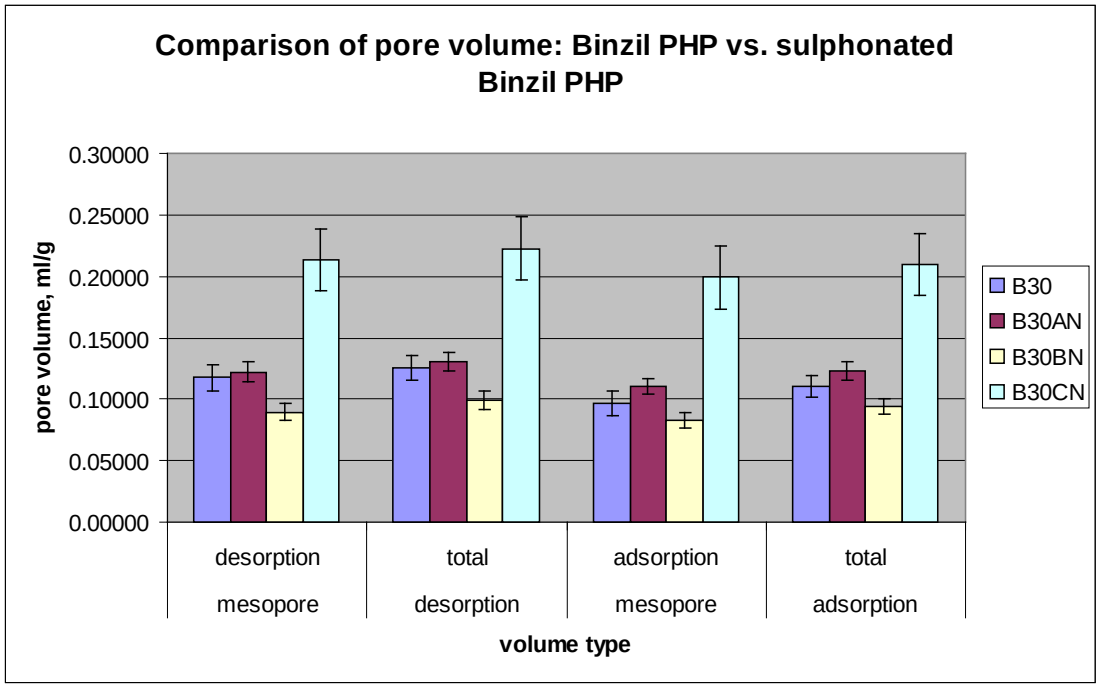

Figure 4.176: Comparison of pore volumes, sulphonated vs. unsulphonated Bindzil PHPs.

4.9.5 FTIR of sulphonated PHP

The spectra for sulphonated VTMS PHPs are presented in Figure 4.177 and Figure 4.178. Both spectra of S30AN and S30BN look similar but differ from the spectrum of S30, presented in Figure 4.63. Generally, it is observed that the peaks intensity shifted towards lower value of percent transmittance. There is a peak at 1638 cm^{-1} over a broad band of 1500 to 1900 cm^{-1} replacing two smaller peaks of 1602 and 1704 cm^{-1} (corresponds to bands of C=C in aromatic ring from styrene unit (Vinodh et al., 2010)). There is an apparent peak at 3400 cm^{-1} in a very broad absorption band of

3080 to 3680 cm^{-1} for both samples. These peaks are attributed to the vibration of the –OH group (Mustafa et al., 2010; Rubino et al., 2010; Sergienko, 2002; Ichikawa et al., 2001). This is due to neutralization process using sodium hydroxide. The two peaks between the absorption band of 960 to 1280 cm^{-1} still exist, these peaks are attributed to asymmetric vibration of –Si–O–CH_3 (Barzin et al., 2006; Rodriguez-Fernandez and Gilbert, 1997).

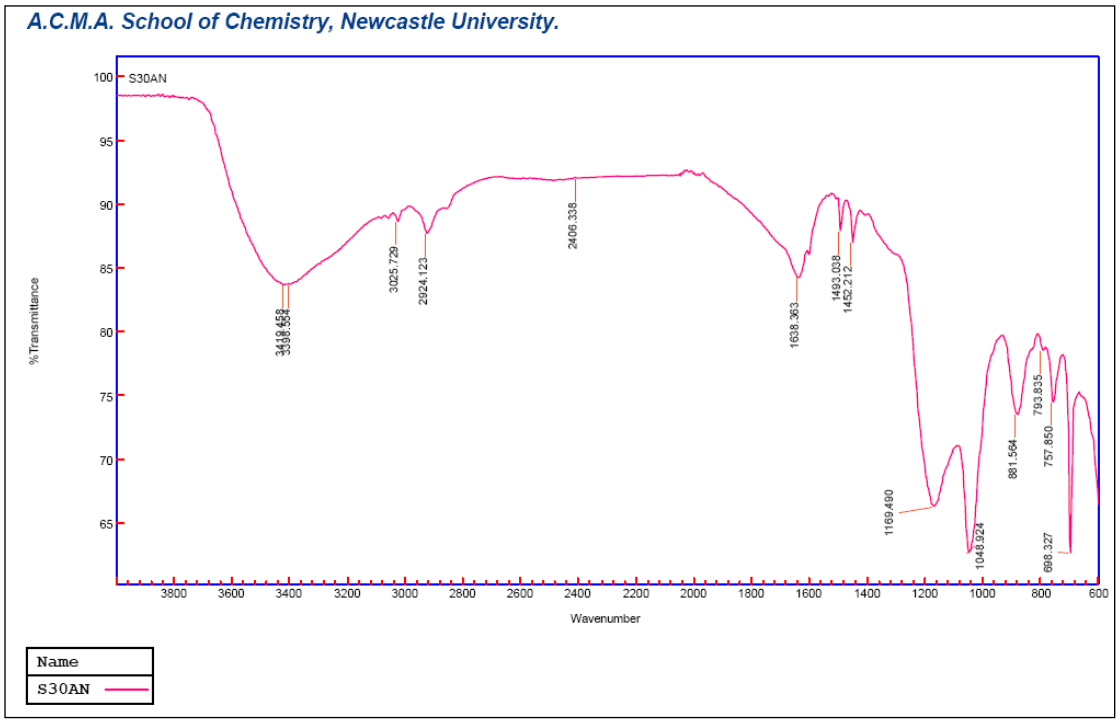

Figure 4.177: FTIR spectrum of sulphonated VTMS PHP, S30AN.

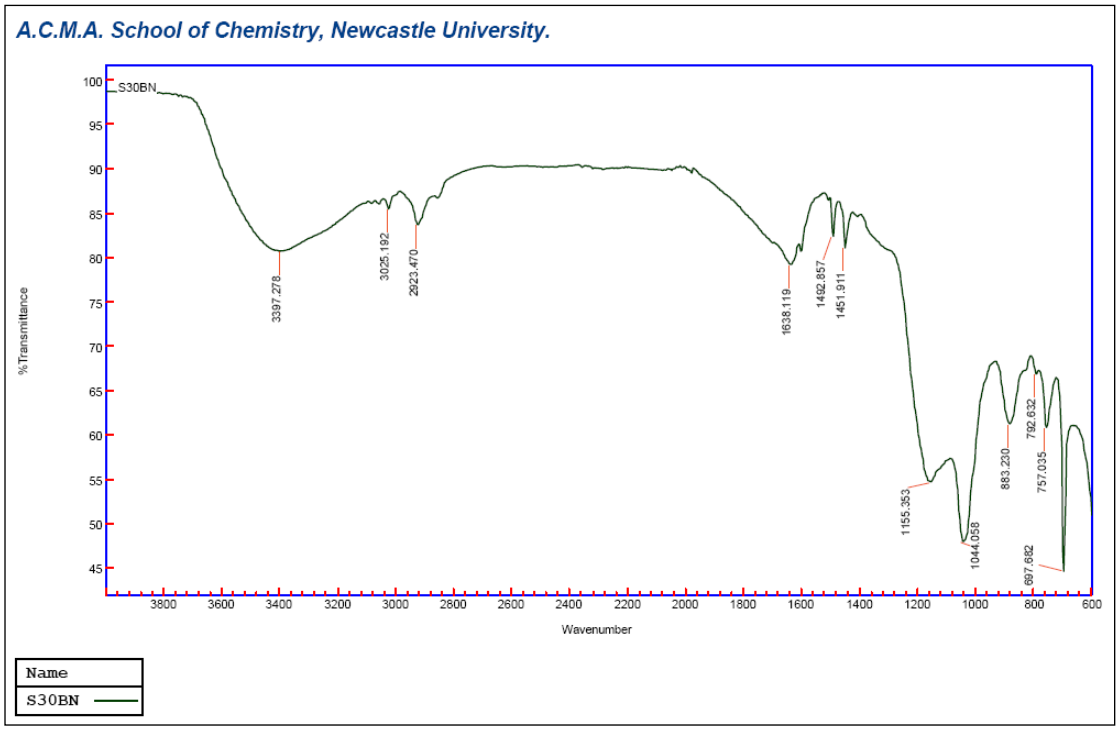

Figure 4.178: FTIR spectrum of sulphonated VTMS PHP, S30BN.

The spectra for sulphonated Binzil PHP are presented in Figure 4.179 to Figure 4.181. Generally, comparing the results to the spectrum of B30 in Figure 4.111, the spectra look similar except for disappearance of some weak peaks. There is still a strong absorption intensity of siloxane, –Si–O–Si stretching vibration at 1094.427, 1089.045 and 1055.551 cm^{-1} (Gamys et al., 2010; Hilonga et al., 2010; Mustafa et al., 2010; Prud'homme et al., 2010; Alemdar et al., 2009; Shi et al., 2009; Yang et al., 2009; Kim and Jang, 2000) for B30AN, B30BN and B30CN respectively, in a broad band of 980 to 1200 cm^{-1}. All spectra also have additional small peak at approximately 970 cm-1. These peaks are attributed to siloxane linkages (Kim and Jang, 2000). For B30CN, there is a peak of 3413.940 cm^{-1}, attributed to the vibration of the –OH group (Mustafa et al., 2010; Rubino et al., 2010; Sergienko, 2002; Ichikawa et al., 2001), over a wide absorption band between 3000 and 3640 cm^{-1}. This peak appears due to neutralization process using sodium hydroxide.

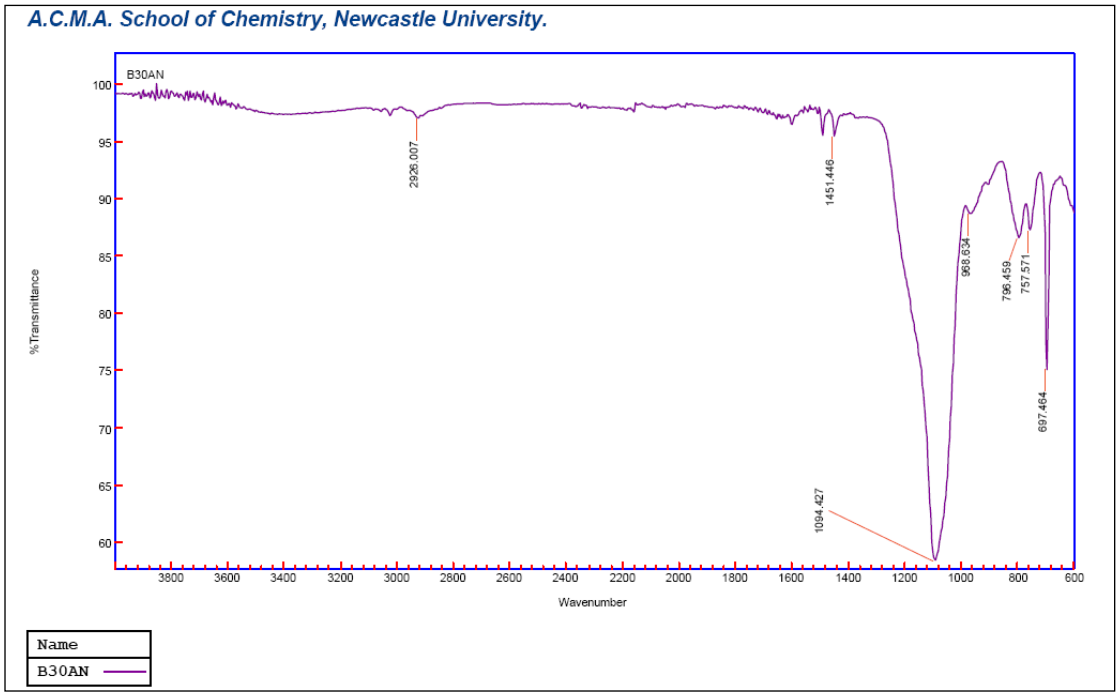

Figure 4.179: FTIR spectrum of sulphonated Bindzil PHP, B30AN.

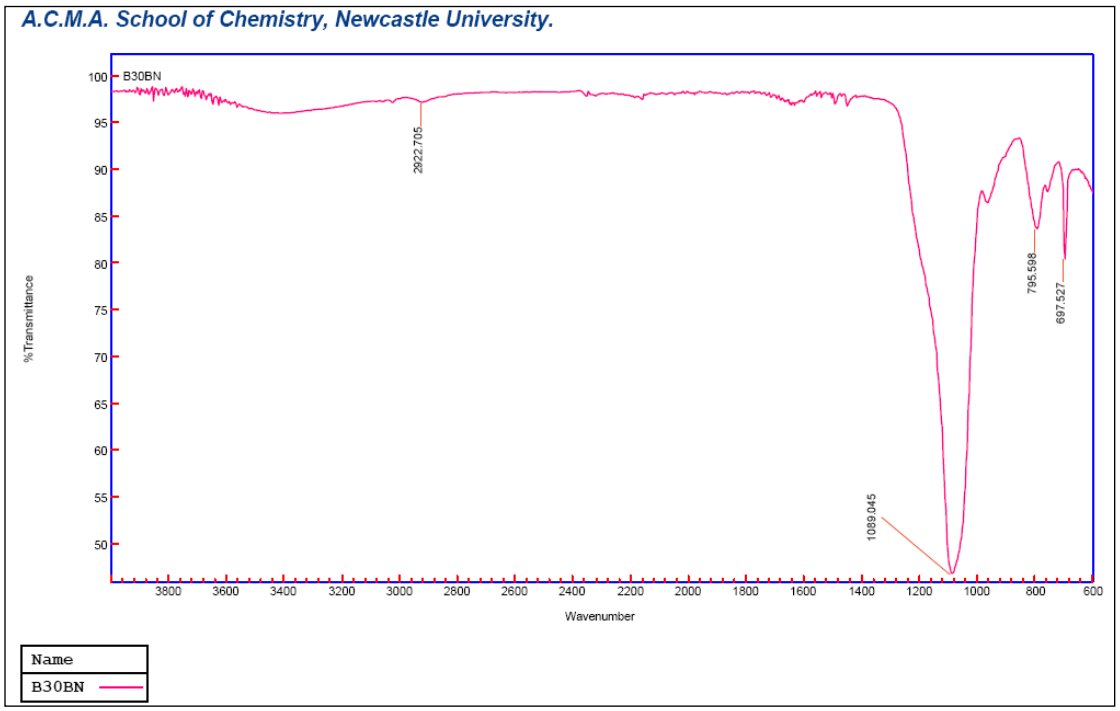

Figure 4.180: FTIR spectrum of sulphonated Bindzil PHP, B30BN.

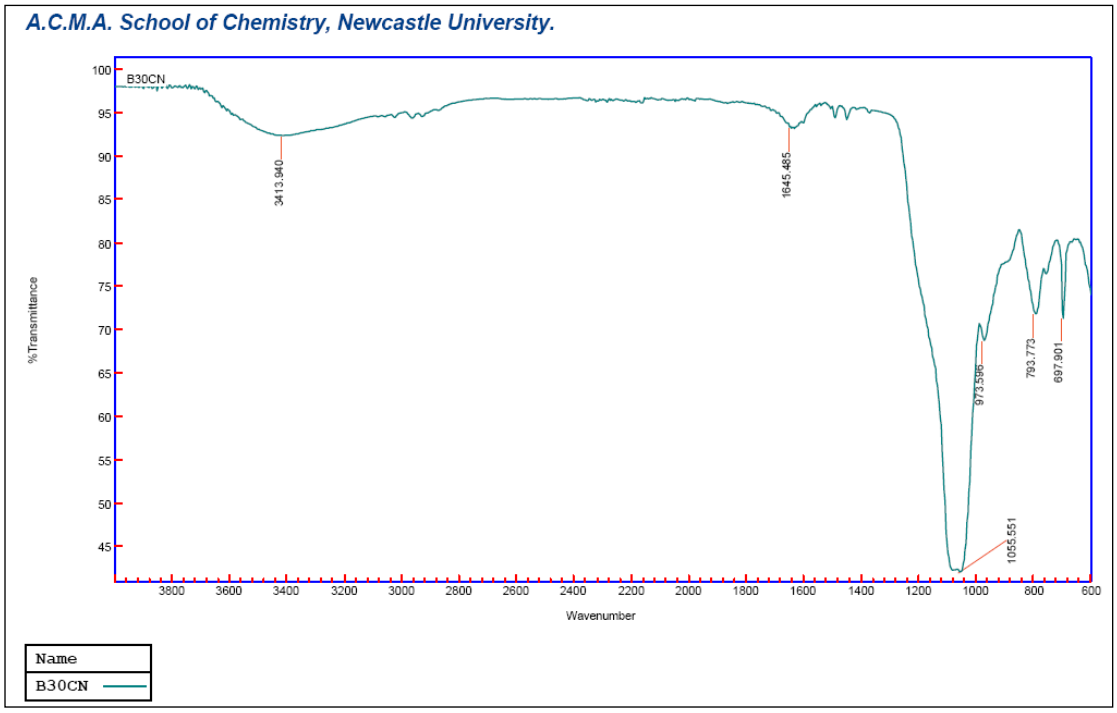

Figure 4.181: FTIR Spectrum of sulphonated Bindzil PHP, B30CN.

4.10 ***Water uptake***

Water uptake of the produced PHPs was tested and the results are presented in Table 4.33 and Figure 4.182. The results show that sulphonation process decreases the water uptake capability of VTMS PHP. The results for Binzil PHPs show a decrease and increase in water uptake capability upon sulphonation. The water uptake was as high as 4.7 fold for sulphonated Bindzil PHP.

Table 4.33: Water uptake of several PHPs.

Sample name	% water uptake	% water uptake, average	water uptake, fold
B30	100 - 155	141.2	1.2 - 1.6
S30	80 - 290	170.6	0.8 - 2.9
B30AN	140 - 470	284.8	1.4 - 4.7
B30BN	50 - 350	158.0	0.6 - 3.6
B30CN	180 - 320	264.0	1.9 - 3.2
S30AN	47 - 83	71.4	0.5 - 0.8
S30BN	27 - 69	45.0	0.3 - 0.7

Sulphonated Bindzil PHPs, B30AN and B30CN differ significantly from unsulphonated B30 in term of water uptake due to nonoverlapping error bars; the water uptake increased due to sulphonation process. B30BN does not differ from B30 due to overlapping error bars. The S30, S30AN and S30BN PHPs are significantly different from one another in term of water uptake due to non-overlapping error bars.

Statistical analysis, ANOVA was further performed to see how significance the difference is. The test for B30 and sulphonated B30 PHPs showed that there was no significant difference in the water uptake of the Bindzil polymers at significance level of 0.05. The test showed that there was significant difference in water uptake of the S30 PHPs at significance level of 0.05; however, Bonferroni test showed that none of them was different. Further analysis of ANOVA was performed at significance level of 0.025; the results showed that there was no significant difference in water uptake of the S30 polyHIPE polymers.

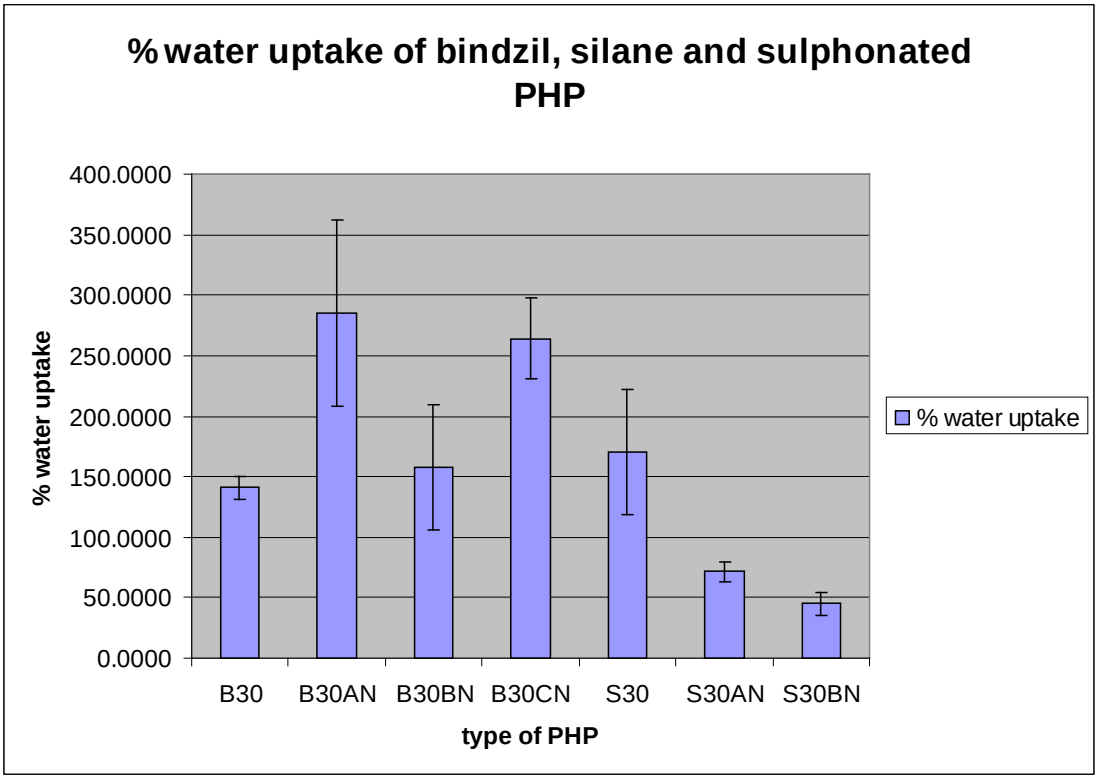

Figure 4.182: Comparison of water uptake capabilities of different PHPs, VTMS PHPs and Bindzil PHPs.

5 Tar removal: Results and Discussions.

Tar removal experiments were conducted using several techniques, which are PHP as the adsorption materials, high voltage, plasma, and combination of PHP and plasma technique. The results are summarised in the following paragraphs.

5.1 *PolyHIPE Polymer*

Several runs were done to investigate the adsorption of tar by PHP as polymer efficiency of several experiments on water and tar adsorption was good and proven successful by Calkan et al. (2006) and Calkan (2007). In this experiment, a stream of CO_2 gas was passed through a heated crude oil reactor and then through a glass reactor filled with crushed PHPs as discussed in Chapter 3. The sampling and analysis were done in sequence, before treatment and after treatment, 30 minutes apart due to availability of one GC machine only. The results for VTMS PHPs, Bindzil PHPs and VTMS-Bindzil PHPs are presented in Table 5.1, Table 5.2, and Table 5.3 respectively. The polymer efficiency was determined gravimetrically.

Table 5.1: GC results and PHP efficiency of tar removal using VTMS PHP.

Polymer type	Before treatment, area (µV.min)	After treatment, area (µV.min)	% reduction	Polymer efficiency, %
S10	11413.9	12150.8	-	14.84
	5987.4	7191.3	-	
	11315.0	20794.5	-	
S10	14416.3	14186.7	1.6	11.94
	13009.0	12600.7	3.1	
	11863.2	8537.9	28.0	
S30	4006.8	8775.3	-	14.05
	4020.9	8358.3	-	
	7400.9	12250.0	-	
S30	2076.9	14669.9	-	19.30
	5127.4	6289.4	-	
	2228.2	2050.4	8.0	
S30	16271.3	15815.9	2.8	47.27
	10934.7	11979.0	-	
	8587.5	10903.9	-	
S30	17590.2	15761.8	10.4	18.68
	13448.6	22133.0	-	
	10731.9	12276.0	-	

Table 5.2: GC results and PHP efficiency of tar removal using Bindzil PHP

Polymer type	Before treatment, area (µV.min)	After treatment, area (µV.min)	% reduction	Polymer efficiency, %
B30	5997.4	5018.8	16.3	6.51
	4815.0	6036.7	-	
	5841.3	4171.9	28.6	
B30	2676.6	3829.1	-	11.56
	2799.8	3319.4	-	
	7694.3	-	-	

Table 5.3: GC results and PHP efficiency of tar removal using VTMS-Bindzil PHP.

Polymer Type	Before treatment, area (µV.min)	After treatment, area (µV.min)	% reduction	Polymer efficiency, %
S30B10	58663.5	10690.3	81.8	1.80
	4975.5	5698.5	-	
	3814.5	9116.7	-	
S30B10	3842.9	40453.4	-	2.19
	60205.2	5005.7	91.7	
	4135.0	2928.0	29.2	
S30B10	2780.7	3082.7	-	1.93
	2642.2	3488.9	-	
	2937.5	2561.1	12.8	

The fluctuation in the composition of released gas made the comparison and analysis unreliable and did not reflect the actual result at any particular time. Sampling for analysis before treatment and after treatment was done subsequently; but it was done and injected into GC machine 30 minutes apart.

5.2 *High Voltage*

In this experiment, the same set-up used in section 5.1 are used, with a substitution of a reactor having high voltage applied to it instead of a glass reactor

filled with PHPs. Schematics and details are presented in Chapter 3. The results of tar removal/conversion using high voltage treatment are presented in Table 5.4. The results are arranged sequentially in the order the sampling was done and analysed, by line and from left to right. As explained previously, there are uncertainties in the results due to fluctuating values of released hydrocarbon from crude oil. The results are too complex to be analysed even on the basis of conversion from heavy hydrocarbon to light hydrocarbon. Hence, no further analysis on the result was carried on.

Table 5.4: GC results for tar removal/conversion using high voltage.

High Voltage	Before treatment, area (µV.min)	After treatment, area (µV.min)	% reduction
15 kV	12800.9	-	-
	171.6	309.7	-
	-	528.7	-
	1533.1	-	-
20 kV		1267.9	-
		693.9	-
	3771.8	2418.8	35.9
10 kV, top water.	-	5939.2	-
	286.6	4268.1	-
	476.0	-	-
15 kV, top water	13388.9	3466.1	74.1
	11763.8	12433.3	-
20 kV, top water	3210.1	2110.0	34.3
	2073.7	15696.0	-
	9766.4	9648.6	1.2
20 kV, bottom water	20265.3	18148.7	10.5
	483.6	14511.7	-
	9538.2	12788.8	-

5.3 *Plasma (Dielectric Barrier Discharge)*

Plasma experiment was conducted by passing CO_2 gas through a heated crude oil reactor and then passed through a glass reactor filled with glass beads. The plasma was applied across this glass reactor. For the experiment with both plasma and PHPs, the glass reactor was filled with glass beads and PHPs. Details of the experiment are discussed in Chapter 3. The results for tar removal/conversion using non-thermal plasma technique are presented in Table 5.5. The results are arranged sequentially in the order the sampling was done and analysed as explained in the previous section. This explains some of the empty boxes in Table 5.5. There were still uncertainties in the result; due to fluctuating values of released hydrocarbon from crude oil. The results are complex to be analysed even on the basis of conversion from heavy hydrocarbon to light hydrocarbon. However, there were some conversions going on as confirmed by the result of Run 26, first run of plasma treatment at 50W, discussed in the next paragraph.

Table 5.5: GC results for tar removal/conversion using non-thermal plasma.

Plasma	Before treatment, area (μV.min)	After treatment, area (μV.min)	% reduction
50W, 1st run	11129.3	7669.0	31.1
	-	11495.8	-
	-	7098.0	-
	10511.8	-	-
	14306.9	-	-
50W, 2nd run	3605.2	3714.7	-
	3644.8	3223.6	11.6
		2058.5	-
30W, 1st run (Fresh Crude)	12100.9	14830.7	-
		13020.0	-
	10088.4	13052.9	-
	9481.3	10015.2	-
30W, 2nd run	7290.7	8334.6	-
	6978.1	7866.4	-
	6507.2	6691.2	-
Combination of B30 PHP & 30W Plasma	5719.8	6653.1	-
	3737.5	3007.4	19.5
	3624.6	3321.2	8.4
	3068.8	2148.8	30.0

The GC chromatograms of Run 26 for before treatment and after treatment are presented in Figure 5.1 and Figure 5.2, respectively. Detail result of the chromatograms is presented in Appendix 2. Comparing chromatogram 26-1(before treatment) to chromatogram 26-2 (after treatment), it was observed that some conversions have taken place. There were changes in the peaks and the heights of the peaks. Looking at 26-3 (after treatment) that was sampled and analysed 30 minutes after 26-2, the chromatogram resembles the chromatogram of 26-1. However looking at the chromatograms of 26-4 (after treatment), the results resemble the one of 26-2. Comparing 26-5 and 26-6, the chromatograms look similar to the chromatogram of 26-1, except for the peak intensity. In conclusion, the results are too complex to be

interpreted. There is evidence of tar conversion/decomposition taking place, i.e., from long chain hydrocarbon to short chain hydrocarbon, due to reduction of peak intensity of some of the spectra.

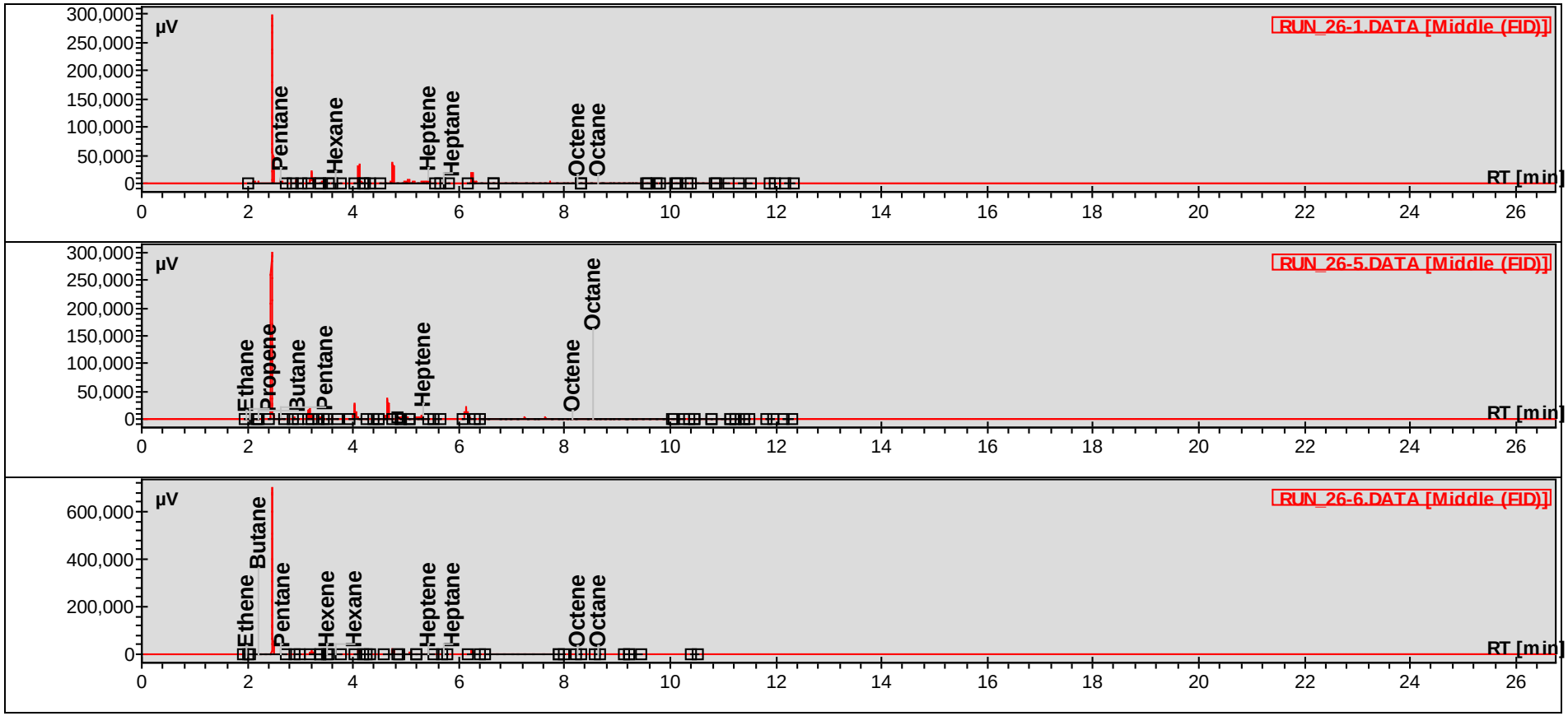

Figure 5.1: GC Chromatograms of before treatment sample for Run 26.

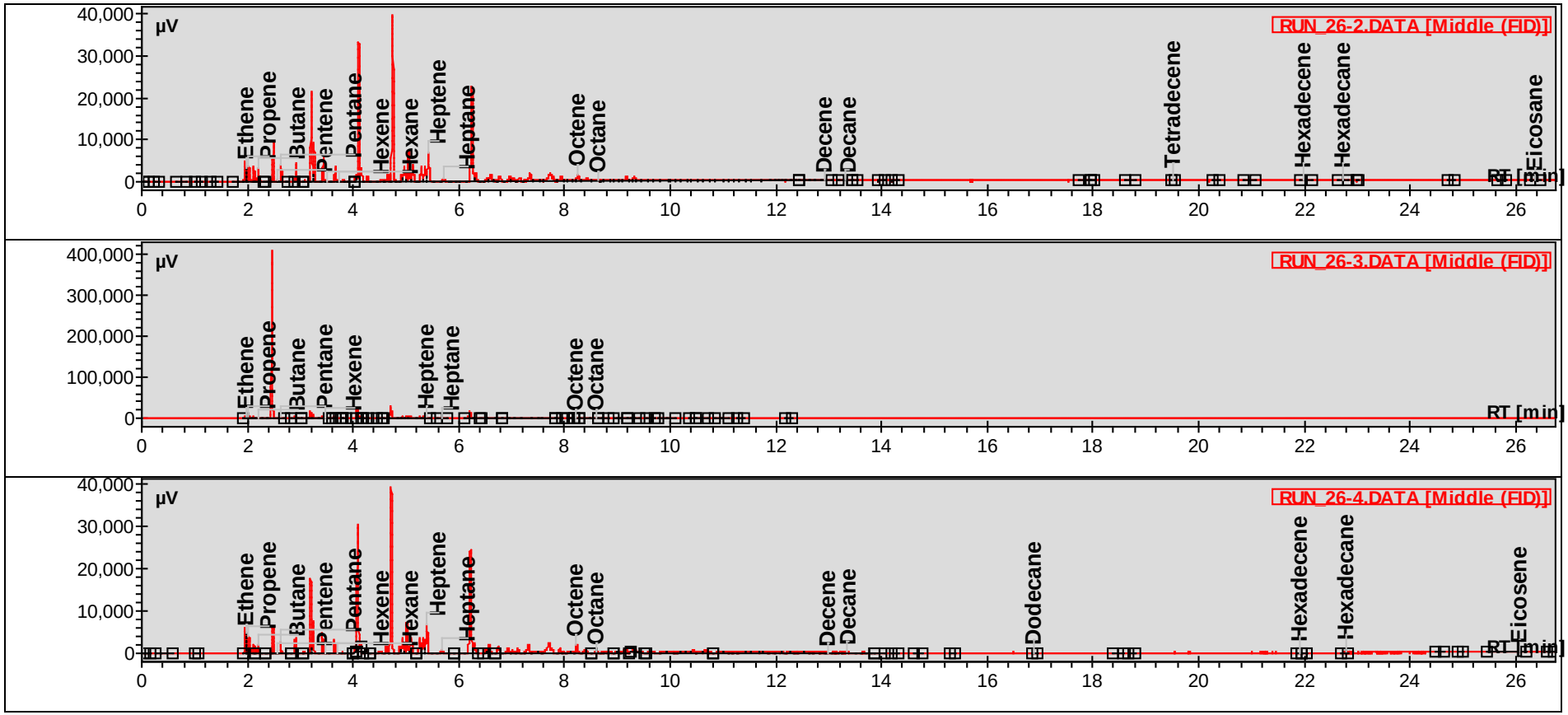

Figure 5.2: GC Chromatogram of after treatment sample for Run 26.

Gas sample was drawn from the sampling point using 5 ml plastic syringe and injected into Gas Chromatograph (GC). The sampling, before and after treatment was done randomly and not in sequence. In order to minimise the uncertainties in the data collected and to get the best representative data, the sampling was done systematically, one after the other. Since there was only one GC machine available, the sampling was done 30 minutes apart. This sampling and injection techniques may lead to unreliability and inaccuracy in the result obtained. The sampling results before and after treatments represent the result at 2 different times, which is 30 minute difference. For the experiment of 30W Plasma combined with B30PHP, the analysis was done by withdrawing the sample one after another and wrapping the syringe with clear wrap, but injecting the “after treatment” sample 30 minutes apart due to availability of one GC machine only. The results show the decrease in the amount of hydrocarbon detected for three sampling times, the leaking of the sample through the syringe over the waiting period might contribute to this.

What was happening? The crude oil as a model for tar is not suitable due to its complex chemical composition. The crude oil was used as many as four times for four runs, but the volume used was kept the same by topping up fresh crude oil after each run. For every run with fresh crude as the sample, the amount of liquid trapped in the u-tube was always high. There are some effects from the treatment, but the results are inconclusive due to the complexity of crude oil composition.

The fluctuating values of tar/hydrocarbon released from crude oil was further checked by running two blank experiments, one is by passing the syngas through glass reactor with glass beads inside and another one is through empty glass reactor. There was no treatment applied to the system and the results are presented in Table 5.6. The results confirmed the fluctuating values; hence, crude oil was a bad choice of tar model.

Table 5.6: Result of blank experiments, no treatment.

Experiment	Glass reactor inlet, Area (µV.min)	Glass reactor outlet, Area (µV.min)
Glass reactor with glass beads inside	15375.1	14715.2
	10023.4	11309.6
	6802.9	8416.3
Empty glass reactor	5618.8	7767.4
	6263.2	5313.3
	5736.4	3408.9

5.4 *Analysis of simulated syngas.*

Experiments were done to analyse simulated syngas composition by passing CO_2 gas at a flow rate of 1.0 l/min through heated crude oil for several hours at a reactor temperature of 80 °C without any treatment. This was done to get background data of the simulated syngas used in the tar removal/conversion experiments. The liquid product was collected in three u-tubes soaked in an ice bath. The first, second and third u-tubes were packed with glass beads, silica gel and glass wool, respectively. Analysis of the gas stream and the liquid collected was done after 3, 6, 9 and 12 hours.

The weight of liquid collected was recorded and presented in Figure 5.3. The pattern showed that the amount of liquid collected decreased with time. The data reflects the results obtained in the experiment of tar removal/conversion, the weight of liquid trapped decreased as the operating hours increased.

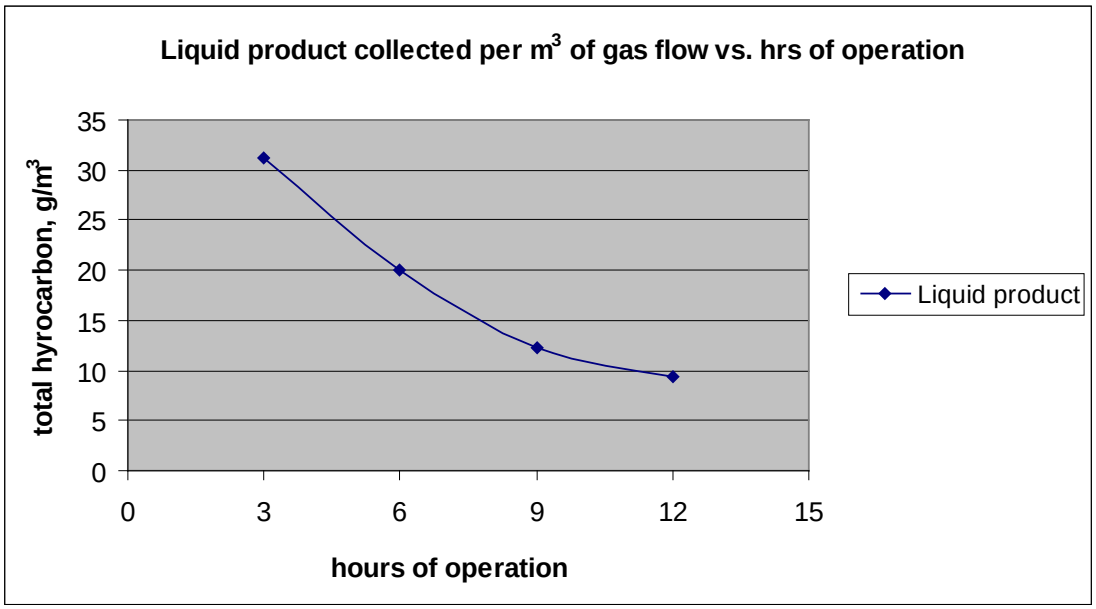

Figure 5.3: Analysis of crude oil via liquid product collected

The result of GC analysis on the gas stream is presented in Figure 5.4. Generally, it is observed that total hydrocarbon in the gas stream decreases with time. The amount released at 6 and 9 hours does not differ significantly due to the overlapping error bars. However, these two values differ significantly with the values released at 3 and 12 hours. The amount released at 3 hours and 12 hours differs significantly due to non-overlapping error bars. Big error bars are observed for the values at 3 hours and 6 hours.

Analysis of Variance (ANOVA), using fixed effect model was then performed to address the significant difference of the results. It can be concluded that at 5% significance level, there are significant differences in the amount of hydrocarbon released in the gas stream at four different operation times. These differences are further confirmed by Bonferroni test at 95.0% confident intervals. The amount of hydrocarbon released in the gas stream at 3 hours differs significantly with the amount released at 6, 9 and 12 hours. The rest of the comparison pairs do not differ significantly.

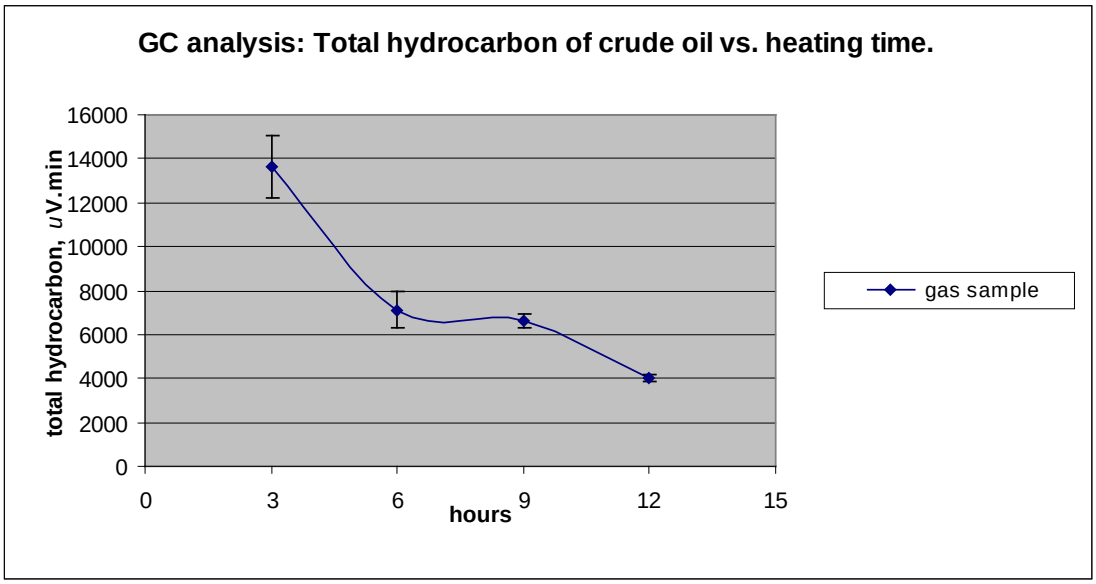

Figure 5.4: Total hydrocarbon released by crude oil vs. heating time.

Analysis of total hydrocarbon in the liquid product collected at four different times is presented in Figure 5.5. Based on non-overlapping error bars, the value at 6 hours differs significantly with the values at 3, 9 and 12 hours. The standard errors for the values of total hydrocarbon at 3, 9 and 12 hours overlapped; hence they do not differ significantly between one another. Statistical analysis, ANOVA at 5% significance level was performed in order to confirm the significant difference. Fixed effect model was used and the result concluded that there is no significant difference in the amount of hydrocarbon in the liquid product trapped at four different operation times.

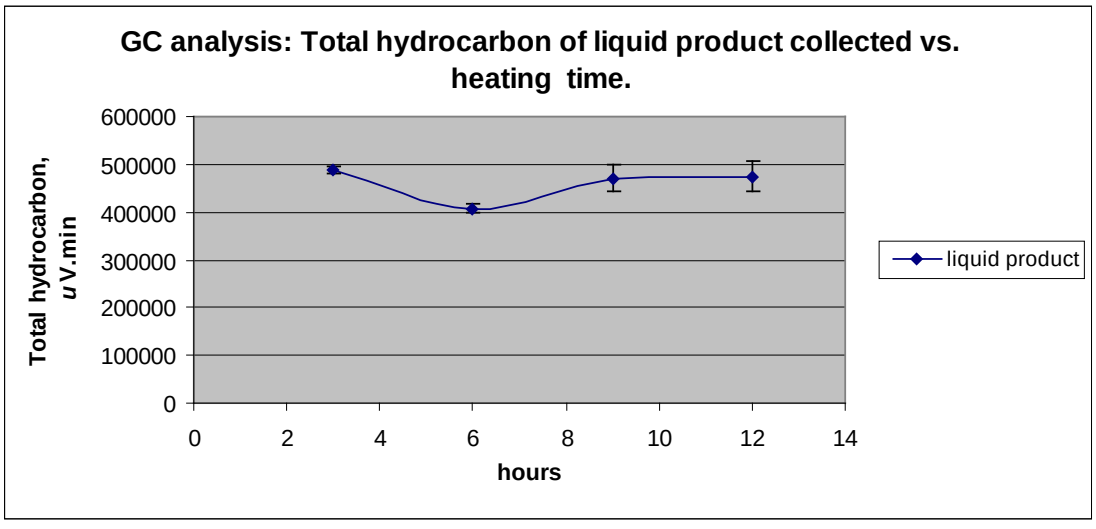

Figure 5.5: Analysis of total hydrocarbon in liquid product collected.

6 Conclusion.

In conclusion, several monoliths of PolyHIPE polymer with improved morphology and properties were successfully developed. The PHPs produced are Bindzil PHP, VTMS PHP and VTMS-Bindzil PHP.

In summary, functional filler was successfully incorporated into the HIPE through both aqueous phase and oil phase. It was possible to produce bindzil and alumina PolyHIPE Polymer (PHP) by addition of colloidal silica and alumina in the aqueous phase, respectively. On the other hand, VTMS PHP was successfully produced through addition of VTMS solution in the oil phase. Eventhough there was limitation in incorporating the filler through the oil phase due to small volume, VTMS PHP was successfully produced through this technique. The percentage of VTMS incorporated in the oil phase was achieved as high as 40%.

Selection between aqueous phase and oil phase initiator also play a significant role in production of PHP. Silane/VTMS PHP was successfully produced using either the aqueous phase initiator or oil phase initiator. However, the study showed that the VTMS PHP with aqueous phase initiator produced PHP with novel morphology whereas the one with oil phase initiator retained the typical morphology of polyHIPE when analysed under SEM. VTMS PHP produced through oil phase initiator was successful at 5% VTMS in the oil phase whereas higher percentage of VTMS attempts failed. Production of VTMS PHP was also possible through addition of aqueous phase and oil phase initiators simultaneously; this was proven through production of S10m, produced via incorporation of 10% VTMS in the oil phase. The alumina PHP and silica/bindzil PHP were successfully produced through oil phase initiator whereas VTMS-Bindzil PHP was successfully produced through aqueous phase initiator.

Bindzil (silica) was successfully reinforced into the HIPE producing silica reinforced PHP with a significant increase of surface area. As concluded earlier, selection between oil phase initiator and aqueous phase initiator also play a significant role in producing bindzil PHP. Production of bindzil PHP through oil phase initiator was a success whereas through aqueous phase initiator was a failure.

PHPs with novel morphology were successfully produced. The PHP with novel structure was produced by incorporating VTMS through the oil phase and by using aqueous phase initiator. The novelty in the structure is the coral-like shape of pore with banana-strand in the pore. VTMS-Bindzil PHP was successfully produced through incorporation of VTMS in the oil phase and Bindzil in the aqueous phase. VTMS-Bindzil PHP with knobbly-like morphology and closed cell pore was produced.

There was no progress in the morphology and properties of alumina PHP compared to the typical PHP. Hence, further modification in composition of incorporated filler in the aqueous phase and method in incorporating the alumina into HIPE are needed for alumina PHP.

Comparison of all the polymers concludes that the VTMS-Bindzil PHPs exhibit the highest surface area and pore volume. In summary, the high surface area always corresponds to high pore volume. All samples have mesopore as confirmed by the differential pore volume distribution plot. None of the samples have the micropore, as confirmed by t-Plot analysis.

Bindzil PHPs successfully underwent a sulphonation process through thermal treatment and microwave irradiation whereas VTMS PHPs were successfully sulphonated process through thermal treatment only. The sulphonated VTMS and Bindzil PHPs still retain the same pore structure of VTMS and Bindzil PHPs; however, cracks could be observed on the surface. For sulphonated VTMS PHP, sulphonation using more concentrated sulphuric acid results in more cracks. For sulphonated Bindzil PHP, the one produced through microwave irradiation results in more cracks compared to the one produced through thermal method. Moreover, the more is the soaking time, the more cracks observed in morphology of sulphonated Bindzil PHP. Sulphonation process decreased the surface area of Bindzil and VTMS PHP significantly. However, sulphonation through two-hour soaking in concentrated acid and microwave irradiation did not significantly change the surface area of Bindzil PHP. Desorption mesopore volumes and total desorption pore volumes of VTMS PHP decreased significantly upon sulphonation. Sulphonation process did not significantly change the pore volume of Bindzil PHP.

There was no significant difference in the water uptake capabilities of Binzil PHPs and VTMS PHPs upon sulphonation. However for Bindzil PHP, the water uptake capability increased to as high as 4.7 fold from 1.5 fold upon sulphonation.

Hence, the use of PHP in gas cleaning technologies is possible and should be explored further.

Study on tar adsorption capability of PolyHIPE polymers produced in the lab on the simulated syngas showed some promising results. However, the use of crude oil as a model for tar was a bad choice. The complexity of crude oil composition and fluctuating composition of gas coming out of crude oil made the results difficult to analyse. Moreover, the employed sampling technique due to availability of one GC machine also contributed to uncertainties in the results. Experiments with some controlled conditions and parameters are needed if crude oil were to be used again as model of tar.

The tar removal using high voltage and non-thermal plasma, specifically dielectric barrier discharge showed promising result, but further study is needed using the right model of tar. No conclusive result was obtained due to inadequate analysis apparatus such as GC, two GC machines are needed in order to sample and analyse the gas sample before and after treatment without having to wait for 30 minutes and ensuring the sample analysed is the one right after the treatment.

7 Recommendation and Future Work.

Future works should focus on producing various types of ceramic and metallic PHPs. Various types of functional fillers (chemical/material/particulate) should be incorporated into the aqueous phase or oil phase in order to improve and enhance properties and morphology of PHP. Among the PHPs that could be given consideration are magnesium silica ceramic and alumina/magnesium PHPs. Future works should also involve developing some more bindzil (colloidal silica), VTMS and alumina PHPs by manipulating some parameters, such as dosing and mixing time, emulsification temperature and composition of the HIPE. Properties of the produced PHPs, such as pore size distribution and surface area should be further studied. The effect of these parameters on tar removal efficiency should be investigated.

Further study on the effects of selection of initiator used should be carried further. For example, failure in preparing bindzil or silica PHP through aqueous phase initiator needs to be studied further. Knobbly structure of VTMS-Bindzil PHP with high surface area and volume should be tried in other gaseous application.

Since crude oil is a bad model for tar as discussed previously, careful consideration should be taken in choosing the right model of tar. As reported in many cases in the literature, only one component, for example, naphthalene was used in the study.

There should be two separate gas chromatography machines to monitor the properties of syngas before treatment and after treatment subsequently to reduce the inaccuracy and uncertainty in the reading.

References

Abatzoglou, N., Barker, N., Hasler, P. and Knoef, H. (2000) 'The development of a draft protocol for the sampling and analysis of particulate and organic contaminants in the gas from small biomass gasifiers', *Biomass and Bioenergy,* 18, (1), pp. 5-17.

Abatzoglou, N., Legast, P., Delvaux, P. and Bangala, D. (1997) *Biomass conference of the Americas: Making a business from biomass in energy, environment, chemicals, fibers, and materials.* Montreal; Canada, Aug.Oxford.

Akay, G. (1995) 'Flow induced phase inversion in powder structuring by polymers, Chapter 20', in Narkis, M. and Rozenzweig, N.(eds) *Polymer Powder Technology.*New York: Wiley, pp. 542-587.

Akay, G. (2004) *Method and apparatus for processing flowable materials.* International Patent Application. PCT Publication WO 2004/004880.

Akay, G. (2006a) 'Bioprocess and chemical process intensification.', in Lee, S.(ed), *Encyclopedia of Chemical Processing.*New York: Marcel Dekker, Inc.

Akay, G. (2006b) 'Process Intensification and Miniaturisation: Principals and Applications in Biological, Chemical and Environmental Technologies.', *Journal of Chemical Technology and Biotechnology*.

Akay, G., Bhumgara, Z. G. and Wakeman, R. J. (1995) 'Self-supported porous channel filtration modules - Preparation, Properties and Performance', *Chem Eng Res Des,* 73, (A7), pp. 782-797.

Akay, G., Birch, M. A. and Bokhari, M. A. (2004) 'Microcellular polyHIPE polymer supports osteoblast growth and bone formation in vitro', *Biomaterials,* 25, (18), pp. 3991-4000.

Akay, G., Bokhari, M. A., Byron, V. J. and Dogru, M. (2005a) 'Development of nano-structured micro-porous materials and their applications in bioprocess-chemical process intensification and tissue engineering, Chapter 7', in Galan, M. A. and del Valle, E. M.(eds) *Chemical Engineering: Trends and Development.*London: Wiley, pp. 171-197.

Akay, G., Bokhari, M.A., Byron, V.J., Dogru, M. (2005) 'Development of nano-structured micro-porous materials and their applications in bioprocess-chemical process intensification and tissue engineering, Chapter 7', in Galan, M. A. and del Valle, E. M.(eds) *Chemical Engineering: Trends and Development.*London: Wiley, pp. 171-197.

Akay, G., Dogru, M., Calkan, B. and Calkan, O. F. (2005b) 'Flow-induced phase inversion phenomenon in process intensification and microreactor technology - Preparation and applications of nanostructured microporous polymers and

metals, Chapter 18', in Wang, Y. and Holladay, J. D.(eds) *ACS Symposium Series 914: Microreactor Technology and Process Intensification.* pp. 286-308.

Akay, G., Downes, S. and Price, V. J. ITI Ltd. (2002) *Microcellular polymers as cell growth media and novel polymers*. European Patent 1,183,328.

Akay, G., Erhan, E. and Keskinler, B. (2005c) 'Bioprocess intensification in flow-through monolithic microbioreactors with immobilized bacteria', *Biotechnol Bioeng,* 90, (2), pp. 180-190.

Akay, G., Noor, Z. Z. and Dogru, M. (2005d) 'Process intensification in water-in-crude oil emulsion separation by simultaneous application of electric field and novel demulsifier adsorbers based on polyhipe polymers, Chapter 23', in Wang, Y. and Holladay, J. D.(eds) *ACS Symposium Series 914: Microreactor Technology and Process Intensification.* pp. 378-392.

Akay, G. and Vickers, J. ITI Ltd. (2003) *Method for separating oil in water emulsions*. European Patent 1,307,402.

Alemdar, N., Karagoz, B., Erciyes, A. T. and Bicak, N. (2009) 'Surface modification of silica, titania, and zinc oxide micro particles with epoxidized soybean oil for preparation of polystyrene composite films', *Journal of Applied Polymer Science,* 116, (1), pp. 165-171.

Antal, M. J. and Varhegyi, G. (1995) 'Cellulose Pyrolysis Kinetics: The Current State of Knowledge', *Industrial and Engineering Chemistry Research,* 34, (3), pp. 703-717.

Aznar, M. P., Corella,J., Gil, J., Martin, A., Caballero, M.A., Olivares, A., Peréz, P. (1997) *Developments in thermochemical Biomass Conversion.*Blackie Academic and Professional, London.

Baker, E. G., Brown, M. D., Moore, R. H., Mudge L. K. and Elliot, D. C. (1986) *Engineering analysis of biomass gasifier product gas cleaning technology.* Pacific Northwest National Laboratory, Richland, Washington. (PNL-5534).

Baker, E. G., Mudge, L. K. and Brown, M. D. (1987) 'Steam gasification of biomass with nickel secondary catalysts', *Industrial & Engineering Chemistry Research,* 26, (7), pp. 1335-1339.

Barbetta, A. and Cameron, N. R. (2004a) 'Morphology and surface area of emulsion-derived (PolyHIPE) solid foams prepared with oil-phase soluble porogenic solvents: Span 80 as surfactant', *Macromolecules,* 37, (9), pp. 3188-3201.

Barbetta, A. and Cameron, N. R. (2004b) 'Morphology and surface area of emulsion-derived (PolyHIPE) solid foams prepared with oil-phase soluble porogenic solvents: Three-component surfactant system', *Macromolecules,* 37, (9), pp. 3202-3213.

Barby, D. and Haq, Z. (1982) *Low-density porous cross-linked polymeric materials and their preparation and use as carriers for included liquids*. European Patent 0,060,138.

Barzin, J., Azizi, H. and Morshedian, J. (2006) 'Preparation of silane-grafted and moisture cross-linked low density polyethylene: Part I: Factors affecting performance of grafting and cross-linking', *Polymer - Plastics Technology and Engineering,* 45, (8), pp. 979-983.

Beenackers, A. A. C. M., Maniatis, K. (1994) *Conclusions of the Workshop, Advances in thermochemical biomass conversion.*Blackie Academic Press, London,.

Bhagiyalakshmi, M., Anuradha, R., Park, S. D. and Jang, H. T. (2010) 'Octa(aminophenyl)silsesquioxane fabrication on chlorofunctionalized mesoporous SBA-15 for CO2 adsorption', *Microporous and Mesoporous Materials,* 131, (1-3), pp. 265-273.

Bhumgara, Z. (1995a) 'PHP foam materials as filtration media', *Filtration & Separation,* 32, pp. 245-251.

Bhumgara, Z. (1995b) *A study of development of PHP foam materials use in separation processes.* PhD thesis. University of Exeter.

Bokhari, M. (2003) *Bone Tissue Engineering using Novel Microcellular Polymers.* PHD thesis. University of Newcastle upon Tyne.

Bokhari, M., Birch, M. and Akay, G. (2003) 'Polyhipe polymer: A novel scaffold for in vitro bone tissue engineering', *Tissue Engineering, Stem Cells and Gene Therapies,* 534, pp. 247-254.

Bridgwater, A. V. (1994) 'Catalysis in thermal biomass conversion - a Review', *Applied Catalysis A,* 116, (1/2), pp. 5-47.

Brown, I. J., Clift, D. and Sotiropoulos, S. (1999) 'Preparation of microporous nickel electrodeposits using a polymer matrix', *Materials Research Bulletin,* 34, (7), pp. 1055-1064.

Brunauer, S., Deming, L. S., Deming, W. E. and Teller, E. (1940) 'On a Theory of the van der Waals Adsorption of Gases', *Journal of the American Chemical Society,* 62, (7), pp. 1723-1732.

Burke, D. R., Akay, G. and Bilsborrow, P. (2006) *CHISA 2006 - 17th International Congress of Chemical and Process Engineering.*

Byron, V. J. (2000) *The development of microcellular polymers as support for tissue engineering.* PhD thesis. University of Newcastle upon Tyne.

Caballero, M. A., Aznar, M. P., Corella, J., Gil, J. and Martin, J. A. (1999) *Biomass conference of the Americas.* Oakland, CA, Aug.Pergamon, Oxford.

Caballero, M. A., Corella, J., Aznar, M. P. and Gil, J. (2000) 'Biomass gasification with air in fluidized bed. Hot gas cleanup with selected commercial and full-size nickel-based catalysts', *Industrial & Engineering Chemistry Research,* 39, (5), pp. 1143-1154.

Calkan, O. F. (2007) *Intensified Integrated Gasification System Development.* Ph. D. thesis. University of Newcastle Upon Tyne.

Calkan, O. F., Dogru, M. and Akay, G. (2005) 'Nano-structured electrically conductive polymers: fabrication and applications.', *7th. World Congress of Chemical Engineering.* Glasgow, Scotland, IchemE, pp.

Calkan, O. F., Dogru, M. and Akay, G. (2006) *CHISA 2006 - 17th International Congress of Chemical and Process Engineering.*

Cameron, N. R. (2005) 'High internal phase emulsion templating as a route to well-defined porous polymers', *Polymer,* 46, (5), pp. 1439-1449.

Cameron, N. R. and Sherrington, D. C. (1996) 'High internal phase emulsions (HIPEs) - Structure, properties and use in polymer preparation', *Biopolymers Liquid Crystalline Polymers Phase Emulsion,* 126, pp. 163-214.

CEN Task Force, C.-C. d. N. (2004) *Biomass Gasification-Tar and Particles in Product Gases-Sampling and Analysis*. Available at: http://www.tarweb.net/results/pdf/CEN-Tar-Standard-draft-version-2_1-new-template-version-05-11-04.pdf (Accessed: 27 September 2007)

Choudhary, B., Chawla, S., Jayanthi, K., Sood, K. N. and Singh, S. (2000) 'Synthesis and surface modification of ZnO:Cu nanoparticles by silica and PMMA', *Current Applied Physics,* 10, (3), pp. 807-812.

Coll, R., Salvado, J., Farriol, X. and Montane, D. (2001) 'Steam reforming model compounds of biomass gasification tars: conversion at different operating conditions and tendency towards coke formation', *Fuel Processing Technology,* 74, (1), pp. 19-31.

Corella, J., Caballero, M. A., Aznar, M. P. and Gil, J. (1999a) *Biomass conference of the Americas.* Oakland, CA, Aug.Pergamon, Oxford.

Corella, J., Narvaez, I., Orio, A. (1996) 'Effectiveness factors for a commercial steam reforming (Ni) catalyst and for a calcined dolomite used downstream biomass gasifiers', *VTT Symposium 163,* pp. 185-190.

Corella, J., Orio, A. and Aznar, P. (1998) 'Biomass gasification with air in fluidized bed: Reforming of the gas composition with commercial steam reforming catalysts', *Industrial & Engineering Chemistry Research,* 37, (12), pp. 4617-4624.

Corella, J., Orio, A. and Toledo, J. M. (1999b) 'Biomass gasification with air in a fluidized bed: Exhaustive tar elimination with commercial steam reforming catalysts', *Energy & Fuels,* 13, (3), pp. 702-709.

Courson, C., Makaga, E., Petit, C. and Kiennemann, A. (2000) 'Development of Ni catalysts for gas production from biomass gasification. Reactivity in steam- and dry-reforming', *Catalysis Today,* 63, (2-4), pp. 427-437.

Dayton, D. (2002) *A review of the literature on catalytic biomass tar destruction.* National Renewable Energy Laboratory (NREL/TP -510-32815).

Delgado, J., Aznar, M. P. and Corella, J. (1996) 'Calcined dolomite, magnesite, and calcite for cleaning hot gas from a fluidized bed biomass gasifier with steam: Life and usefulness', *Industrial & Engineering Chemistry Research,* 35, (10), pp. 3637-3643.

Delgado, J., Aznar, M. P. and Corella, J. (1997) 'Biomass gasification with steam in fluidized bed: Effectiveness of CaO, MgO, and CaO-MgO for hot raw gas cleaning', *Industrial & Engineering Chemistry Research,* 36, (5), pp. 1535-1543.

Devi, L., Ptasinski, K. J. and Janssen, F. J. (2003) 'A review of the primary measures for tar elimination in biomass gasification processes', *Biomass and Bioenergy,* 24, (2), pp. 125-140.

Devi, L., Ptasinski, K. J. and Janssen, F. J. (2005) 'Pretreated olivine as tar removal catalyst for biomass gasifiers: investigation using naphthalene as model biomass tar', *Fuel Processing Technology,* 86, (6), pp. 707-730.

Dogru, M. and Akay, G. ITI Ltd. (2004) *Gasification, International Patent Application*. PCT/GB2004/004651.

Ekstrom, C., Lindman, N., Petterson, R. (1982) *Proceedings of the Fundamentals of Thermochemical Conversion of Biomass Conference.* R.P. Overend:Elsevier Applied Press, London.

Fridman, A., Kennedy, L.A. (2004) *Plasma Physics and Engineering.* New York & London: Taylor & Francis.

Gamys, C. G., Beyou, E. and Bourgeat-Lami, E. (2010) 'Micellar behavior of well-defined polystyrene-based block copolymers with triethoxysilyl reactive groups and their hydrolysis-condensation', *Journal of Polymer Science, Part A: Polymer Chemistry,* 48, (4), pp. 784-793.

Garcia, L., French, R., Czernik, S. and Chornet, E. (2000) 'Catalytic steam reforming of bio-oils for the production of hydrogen: effects of catalyst composition', *Applied Catalysis A,* 201, (2), pp. 225-239.

Gebhard, S. C., Wang, D., Overend, R. P. and Paisley, M. A. (1994) 'Catalytic conditioning of synthesis gas produced by biomass gasification.', *Biomass & Bioenergy*, 7, (1-6), pp. 307-313.

Good, J., Ventress, L., Knoef, H., Zielke, U., Hansen, P. L., van de Kamp, W., de Wild, P., Coda, B., van Passen, S., Kiel, J., Sjostrom, K., Liliedahl, T., Unger, C., Neeft, J., Suomalainen, M. and Simell, P. (2005) *Sampling and analysis of tar and particles in biomass producer gases.* Available at: http://www.tarweb.net/results/pdf/Technical-Report-version-3_8-final.pdf (Accessed: 4 July 2007).

Graham, B. (2001) 'Technological Plasmas', *Physics World*, 14, (3), pp. 31-36.

Graham, R. G., Bain, R. (1993) *Biomass Gasification: Hot Gas Clean-up. Report Submitted to IEA Biomass Gasification Working Group.* NREL

Gregg, S. J. and Sing, K. S. W. (1982) *Adsorption, Surface Area and Porosity.* London: Academic Press Inc. (London) Ltd.

Haibach, K., Menner, A., Powell, R. and Bismarck, A. (2006) 'Tailoring mechanical properties of highly porous polymer foams: Silica particle reinforced polymer foams via emulsion templating', *Polymer*, 47, (13), pp. 4513-4519.

Hainey, P., Huxham, I. M., Rowatt, B., Sherrington, D. C. and Tetley, L. (1991) 'Synthesis and Ultrastructural Studies of Styrene Divinylbenzene Polyhipe Polymers', *Macromolecules*, 24, (1), pp. 117-121.

Hepola, J. and Simell, P. (1997a) 'Sulphur poisoning of nickel-based hot gas cleaning catalysts in synthetic gasification gas - I. Effect of different process parameters', *Applied Catalysis B-Environmental*, 14, (3-4), pp. 287-303.

Hepola, J. and Simell, P. (1997b) 'Sulphur poisoning of nickel-based hot gas cleaning catalysts in synthetic gasification gas - II. Chemisorption of hydrogen sulphide', *Applied Catalysis B-Environmental*, 14, (3-4), pp. 305-321.

Herrera, N. N., Letoffe, J. M., Reymond, J. P. and Bourgeat-Lami, E. (2005) 'Silylation of laponite clay particles with monofunctional and trifunctional vinyl alkoxysilanes', *Journal of Materials Chemistry*, 15, (8), pp. 863-871.

Hilonga, A., Kim, J.-K., Sarawade, P. B. and Kim, H. T. (2010) 'Rapid synthesis of homogeneous titania-silica composite with high-BET surface area', *Powder Technology*, 199, (3), pp. 284-288.

Hubbard, K. L., Finch, J. A. and Darling, G. D. (1998) 'The preparation and characteristics of poly(divinylbenzene-co-ethylvinylbenzene), including Amberlite XAD-4. Styrenic resins with pendant vinylbenzene groups', *Reactive and Functional Polymers*, 36, (1), pp. 17-30.

Ichikawa, K., Mori, T., Kitano, H., Fukuda, M., Mochizuki, A. and Tanaka, M. (2001) 'Fourier transform infrared study on the sorption of water to various kinds of

polymer thin films', *Journal of Polymer Science, Part B: Polymer Physics,* 39, (18), pp. 2175-2182.

Jess, A. (1996) 'Catalytic upgrading of tarry fuel gases: A kinetic study with model components', *Chemical Engineering and Processing,* 35, (6), pp. 487-494.

Jiang, G. and Zeng, J. (2009) 'Preparation of nano-TiO2/polystyrene hybride microspheres and their antibacterial properties', *Journal of Applied Polymer Science,* 116, (2), pp. 779-784.

Juutilainen, S. J., Simell, P. A. and Krause, A. O. (2006) 'Zirconia: Selective oxidation catalyst for removal of tar and ammonia from biomass gasification gas', *Applied Catalysis B,* 62, (1-2), pp. 86-92.

Katsoyiannis, I. A., Zauboulis, A.I. (2002) 'Removal of arsenic from contaminated watre sources by sorption onto iron-oxide-coated polymeric materials', *Water Research,* 36, pp. 5141-5155.

Kim, H. and Jang, J. (2000) 'Corrosion protection and adhesion promotion for polyimide/copper system using silane-modified polymeric materials', *Polymer,* 41, (17), pp. 6553-6561.

Kinoshita, C. M., Wang, Y. and Zhou, J. C. (1995) 'Effect of Reformer Conditions on Catalytic Reforming of Biomass-Gasification Tars', *Industrial & Engineering Chemistry Research,* 34, (9), pp. 2949-2954.

Knoef, H. A. M. (2000) 'The UNDP/World Bank Monitoring Program on Small-Scale Biomass Gasifiers', *Biomass and Bioenergy,* 18, pp. 39-55.

Knoeff, H. A. M., Koele, H.J. (2000) 'Survey of tar measurement protocols', *Biomass and Bioenergy,* 18, pp. 55-60.

Krajnc, P., Stefanec, D., Brown, J. F. and Cameron, N. R. (2005) 'Aryl acrylate based high-internal-phase emulsions as precursors for reactive monolithic polymer supports', *Journal of Polymer Science Part a-Polymer Chemistry,* 43, (2), pp. 296-303.

Leber, N., Fay, J. D. B., Cameron, N. R. and Krajnc, P. (2007) '2,4,6-Trichlorophenyl acrylate emulsion-templated porous polymers (PolyHIPEs). Morphology and reactivity studies', *Journal of Polymer Science, Part A: Polymer Chemistry,* 45, (17), pp. 4043-4053.

Lissant, K. J. (1974) 'Emulsions and Emulsion Technology, Part 1, Chapter 1', in Lissant, K. J.(ed), *Surfactant Science Series.* Vol. 6 New York: Marcel Dekker.

Maniatis, K. and Beenackers, A. A. C. M. (2000) 'Tar Protocols. IEA Bioenergy Gasification Task', *Biomass and Bioenergy,* 18, (1), pp. 1-4.

Menner, A., Haibach, K., Powell, R. and Bismarck, A. (2006) 'Tough reinforced open porous polymer foams via concentrated emulsion templating', *Polymer,* 47, (22), pp. 7628-7635.

Mercier, A., Deleuze, H. and Mondain-Monval, O. (2000) 'Preparation and functionalization of (vinyl)polystyrene polyHIPE. Short routes to binding functional groups through a dimethylene spacer', *Reactive and Functional Polymers,* 46, (1), pp. 67-79.

Mercier, A., Deleuze, H. and Mondain-Monval, O. (2001) 'Thiol addition to the pendant vinylbenzene groups of (vinyl)polystyrene polyHIPE via a batch and a cross-flow method', *Macromolecular Chemistry and Physics,* 202, (13), pp. 2672-2680.

Milne, T. A., Abatzoglou, N., Evans, R.J. (1998) *Biomass Gasifier Tars: Their nature, formation and conversion.* National Renewable Energy Laboratory (NREL/TP-570-25357).

Moine, L., Deleuze, H. and Maillard, B. (2003) 'Preparation of high loading PolyHIPE monoliths as scavengers for organic chemistry', *Tetrahedron Letters,* 44, (42), pp. 7813-7816.

Mudge, L., Baker, E.G., Mitchell, D.G. (1981) *Investigation on catalyzed steam gasification of biomass.* Pacific Northwest National Laboratory, Richland, WA (PNL-3695).

Mustafa, S., Waseem, M., Naeem, A., Shah, K. H. and Ahmad, T. (2010) 'Cd2+ ions removal by silica, iron hydroxide and their equimolar mixed oxide from aqueous solution', *Desalination,* 255, (1-3), pp. 148-153.

Nair, S. A., Pemen, A. J., Yan, K., van Gompel, F. M., van Leuken, H. E., van Heesch, E. J., Ptasinski, K. J. and Drinkenburg, A. A. (2003) 'Tar removal from biomass-derived fuel gas by pulsed corona discharges', *Fuel Processing Technology,* 84, (1/3), pp. 161-173.

Nair, S. A., Yan, K., Pemen, A. J., Winands, G. J., van Gompel, F. M., van Leuken, H. E., van Heesch, E. J., Ptasinski, K. J. and Drinkenburg, A. A. (2004) 'A high-temperature pulsed corona plasma system for fuel gas cleaning', *Journal of Electrostatics,* 61, (2), pp. 117-127.

Nair, S. A., Yan, K., Safitri, A., Pemen, A. J., van Heesch, E. J., Ptasinski, K. J. and Drinkenburg, A. A. (2005) 'Streamer corona plasma for fuel gas cleaning: comparison of energization techniques', *Journal of Electrostatics,* 63, (12), pp. 1105-1114.

Narvaez, I., Corella, J. and Orio, A. (1997) 'Fresh tar (from a biomass gasifier) elimination over a commercial steam-reformimg catalyst. Kinetics and effect of different variables of operation', *Industrial & Engineering Chemistry Research,* 36, (2), pp. 317-327.

Neeft, J. P. A., Knoef, H. A. M. and Onaji, P. (1999a) *Behaviour of tars in biomass gasification systems.* MHP Management Services, P.O. box 127, 3950 AC Maarn, Netherlands (9919).

Neeft, J. P. A., Knoef, H. A. M., Zielke, U., Sjöström, K., Hasler, P., Simell, P. A., Dorrington, M. A., Abatzoglou, N., Deutch, S., Greil, C., Buffinga, G. J., Brage, C. and Suomalainen, M. (1999b) *Guideline for sampling and analysis of tar and particles in biomass producer gases - Version 3.1.* Prepared for the European Commission (DGXII), the Netherlands Agency for Energy and the Environment (NOVEM), the Swiss Federal Office of Education and Science, the Danish Energy Agency (Energistyrelsen), the US Department of Energy (DoE), and the National Resources Canada

Neeft, J. P. A., Knoef, H.A.M., Zielke, U., Sjostrom, K., Hasler, P., Simell, P.A., Dorrington, M.A., Thomas, L., Abatzoglou, N., Deutch, S., Greil, C., Buffinga, G.J., Brage, C., Suomalainen, M. *Guideline for Sampling and Analysis of Tar and Particles in Biomass Producer Gases, Version 3.3*. Available at: http://www.tarweb.net/results/pdf/guideline-3.3-v2.pdf (Accessed: 27 September 2007).

Noor, Z. Z. (2006) *Intensification of Separation Processes using Functionalised PolyHIPE Polymers.* PhD thesis. University of Newcastle upon Tyne.

Noor, Z. Z., Akay, G., Dogru, M. and Larter, S. R. (2005) 'Process intensification in water-crude oil separation by simultaneous application of electric field and novel micro-porous polymeric demulsifiers.', *7th. World Congress of Chemical Engineering.* Glasgow, Scotland, IChemE, pp.

Northcott, K., Oshima, S., Perera, J., Komatsu, Y. and Stevens, G. (2007) 'Synthesis, characterization and evaluation of mesoporous silicates for adsorption of metal ions', *Advanced Powder Technology,* 18, (6), pp. 751-762.

Nozaki, T., Muto, N., Kadio, S. and Okazaki, K. (2004b) 'Dissociation of vibrationally excited methane on Ni catalyst - Part 2. Process diagnostics by emission spectroscopy', *Catalysis Today,* 89, (1-2), pp. 67-74.

Nozaki, T., Muto, N., Kado, S. and Okazaki, K. (2004a) 'Dissociation of vibrationally excited methane on Ni catalyst - Part 1. Application to methane steam reforming', *Catalysis Today,* 89, (1-2), pp. 57-65.

Olivares, A., Aznar, M. P., Caballero, M. A., Gil, J., Frances, E. and Corella, J. (1997) 'Biomass gasification: Produced gas upgrading by in-bed use of dolomite', *Industrial & Engineering Chemistry Research,* 36, (12), pp. 5220-5226.

Pacheco, M., Pacheco, J., Moreno, H. and Santana, A. (2008) *Physica Scripta T.*

Pemen, G. A. J. M., Devi, L., Yan, K., Van Heesch, B. E. J. M., Kerst, R., Ptasinski, K. J. and Nair, S. A. (2007) 'Plasma-catalytical removal of tars from fuel gas obtained by biomass gasification', *Journal of Advanced Oxidation Technologies,* 10, (1), pp. 116-120.

Perez, P., Aznar, P. M., Caballero, M. A., Gil, J., Martin, J. A. and Corella, J. (1997) 'Hot gas cleaning and upgrading with a calcined dolomite located downstream a biomass fluidized bed gasifier operating with steam-oxygen mixtures', *Energy & Fuels,* 11, (6), pp. 1194-1203.

Prud'homme, E., Michaud, P., Joussein, E., Peyratout, C., Smith, A., Arrii-Clacens, S., Clacens, J. M. and Rossignol, S. (2010) 'Silica fume as porogent agent in geo-materials at low temperature', *Journal of the European Ceramic Society,* 30, (7), pp. 1641-1648.

Rapagna, S., Jand, N., Kiennemann, A. and Foscolo, P. U. (2000) 'Steam-gasification of biomass in a fluidised-bed of olivine particles', *Biomass and Bioenergy,* 19, (3), pp. 187-197.

Raveendran, K., Ganesh, A. and Khilar, K. C. (1995) 'Influence of mineral matter on biomass pyrolysis characteristics', *Fuel,* 74, (5), pp. 631-653.

Raveendran, K., Ganesh, A. and Khilar, K. C. (1996) 'Pyrolysis characteristics of biomass and biomass components', *Fuel,* 75, (8), pp. 987-998.

Richards, G. N., Zheng, G. (1991) 'Influence of metal ions and salts on products from pyrolysis of wood: applications to thermochemical processing of newsprint and biomass', *J. Anal. Appl. Pyrolysis,* 21, pp. 133-146.

Rodriguez-Fernandez, O. S. and Gilbert, M. (1997) 'Aminosilane grafting of plasticized poly(vinyl chloride) II. Grafting and crosslinking reactions', *Journal of Applied Polymer Science,* 66, (11), pp. 2121-2128.

Rubino, M., Netramai, S., Auras, R. and Annous, B. A. (2010) 'Effect of chlorine dioxide gas on physical, thermal, mechanical, and barrier properties of polymeric packaging materials', *Journal of Applied Polymer Science,* 115, (3), pp. 1742-1750.

Sergienko, A. Y., Tai, H., Narkis, M., Silverstein, M.S. . (2002) 'Polymerized high internal-phase emulsions: Properties and interaction with water', *Journal of Applied Polymer Science,* 84, (11), pp. 2018-2027.

Shi, B., Wang, Y., Guo, Y., Wang, Y., Wang, Y., Guo, Y., Zhang, Z., Liu, X. and Lu, G. (2009) 'Aminopropyl-functionalized silicas synthesized by W/O microemulsion for immobilization of penicillin G acylase', *Catalysis Today,* 148, (1-2), pp. 184-188.

Simell, P. and Kurkela, E. (1997a) *Biomass gasification and pyrolysis: state of the art and future prospects.* Stuttgart; Germany, Apr.CPL Press.

Simell, P. and Kurkela, E. (1997b) 'Tar removal from gasification gas, in Biomass Gasification and Pyrolysis', in Kaltschmitt, M., Bridgwater, A. V. eds.,(ed), CPL Press, Stuttgart, pp. 207-217.

Simell, P., Kurkela, E., Staahlberg, P. and Hepola, J. (1996a) 'Development of catalytic gas cleaning in biomass gasification', *Vtt Symposium,* 164, pp. 133-142.

Simell, P., Kurkela, E., Stahlberg, P. and Hepola, J. (1996b) 'Catalytic hot gas cleaning of gasification gas', *Catalysis Today,* 27, (1-2), pp. 55-62.

Simell, P., Stahlberg, P., Kurkela, E., Albrecht, J., Deutsch, S. and Sjostrom, K. (2000) 'Provisional protocol for the sampling and anlaysis of tar and particulates in the gas from large-scale biomass gasifiers. Version 1998', *Biomass & Bioenergy,* 18, (1), pp. 19-38.

Simell, P. A., Bredenberg, J. B. S. (1990) 'Catalytic purification of tarry fuel gas', *Fuel,* 69, (10), pp. 1219-1225.

Simell, P. A., Hepola, J. O. and Krause, A. O. I. (1997) 'Effects of gasification gas components on tar and ammonia decomposition over hot gas cleanup catalysts', *Fuel,* 76, (12), pp. 1117-1127.

Simell, P. A., Leppaelahti, J. K. and Kurkela, E. A. (1995) 'Tar-decomposing activity of carbonate rocks under high CO~2 partial pressure', *Fuel,* 74, (6), pp. 938.

Simell, P. A., Leppälahti, J. K., Bredenberg, J. B. S. (1992) 'Catalytic purification of tarry fuel gas with carbonate rocks and ferrous materials', *Fuel,* 71, (2), pp. 211-218.

Sing, K. S. W., Everett, D. H., Haul, R. A. W., Moscou, L., Pierotti, R. A., Rouquerol, J. and Siemieniewska, T. (1985) 'Reporting Physisorption Data for Gas/Solid Systems withSpecial Reference to the Determination of Surface Area and Porosity', *Pure & Apllied Chemistry,* 57, (4), pp. 603 - 619.

Sotiropoulos, S., Brown, I. J., Akay, G. and Lester, E. (1998) 'Nickel incorporation into a hollow fibre microporous polymer: a preparation route for novel high surface area nickel structures', *Materials Letters,* 35, (5-6), pp. 383-391.

Stevens, D. J. (2001) *Hot Gas Conditioning: Recent progress with larger scale biomass gasification systems, Update and summary of recent progress.* National Renewable Energy Laboratory (NREL/SR-510-29952).

Tai, H., Sergienko, A. and Silverstein, M. S. (2001) 'Organic-inorganic networks in foams from high internal phase emulsion polymerizations', *Polymer,* 42, (10), pp. 4473-4482.

Taralas, G. (1996) 'Catalytic steam cracking of n-heptane with special reference to the effect of calcined dolomite', *Industrial & Engineering Chemistry Research,* 35, (7), pp. 2121-2126.

Taralas, G., Vassilatos, V., Sjostrom, K. and Delgado, J. (1991) 'THERMAL AND CATALYTIC CRACKING OF N-HEPTANE IN PRESENCE OF CAO,

MGO AND CALCINED DOLOMITES', *Canadian Journal of Chemical Engineering*, 69, (6), pp. 1413-1419.

Umez-Eronini, N., Neal, D., Collins, A.,. (2003) 'In vitro xenograft model using polyHIPE as a three-dimensional scaffold in the tissue engineering of urological tissue', *European Urology Supplements*, 2, pp. 121.

Ungureanu, S., Birot, M., Laurent, G., Deleuze, H., Babot, O., Julia?n-Lo?pez, B., Achard, M. F., Popa, M. I., Sanchez, C. and Backov, R. (2007) 'One-pot syntheses of the first series of emulsion based hierarchical hybrid organic-inorganic open-cell monoliths possessing tunable functionality (organo-Si(HIPE) series)', *Chemistry of Materials*, 19, (23), pp. 5786-5796.

Van Veldhuizen, E. M. (2000) *Electrical Discharges for Environmental Purposes: Fundamentals and Applications.*: NOVA Science Publishers Inc.

Vassilatos, V., Taralas, G., Sjostrom, K. and Bjornbom, E. (1992) 'CATALYTIC CRACKING OF TAR IN BIOMASS PYROLYSIS-GAS IN THE PRESENCE OF CALCINED DOLOMITE', *Canadian Journal of Chemical Engineering*, 70, (5), pp. 1008-1013.

Vickers, J. (2001) *Organic effluent treatment in nuclear fuel reprocessing: Interfacial crud.* PhD thesis. University of Newcastle upon Tyne.

Vinodh, R., Ilakkiya, A., Elamathi, S. and Sangeetha, D. (2010) 'A novel anion exchange membrane from polystyrene (ethylene butylene) polystyrene: Synthesis and characterization', *Materials Science and Engineering B: Solid-State Materials for Advanced Technology*, 167, (1), pp. 43-50.

Wakeman, R. J., Bhumgara, Z. G. and Akay, G. (1998) 'Ion exchange modules formed from polyhipe foam precursors', *Chemical Engineering Journal*, 70, (2), pp. 133-141.

Walsh, D. C., Stenhouse, J.I.T, Kingsbury, L.P., Webster, E.J. (1996) 'PolyHIPE Foams: Production, Characterisation and Performance as Aerosol Filtration Materials', *Journal of Aerosol Science*, 27, pp. S629-S630.

Wang, J. G., Liu, C. J. and Eliassion, B. (2004) 'Density functional theory study of synthesis of oxygenates and higher hydrocarbons from methane and carbon dioxide using cold plasmas', *Energy & Fuels*, 18, (1), pp. 148-153.

Whitehead, J. C. (2007) *What is Plasma*. Available at: http://people.man.ac.uk/~mbdsszjw/Pages/WhatisaPlasma.php (Accessed: 31 Jan 2007).

Williams, J. M., Gray, A. J. and Wilkerson, M. H. (1990) 'Emulsion Stability and Rigid Foams from Styrene or Divinylbenzene Water-in-Oil Emulsions', *Langmuir*, 6, (2), pp. 437-444.

Williams, J. M. and Wrobleski, D. A. (1988) 'Spatial-Distribution of the Phases in Water-in-Oil Emulsions - Open and Closed Microcellular Foams from Cross-Linked Polystyrene', *Langmuir*, 4, (3), pp. 656-662.

Yang, X. K., Chen, L. F., Wang, J. A., NoreÃ±a, L. E. and Novaro, O. (2009) 'Study of the Keggin structure and catalytic properties of Pt-promoted heteropoly compound/Al-MCM-41 hybrid catalysts', *Catalysis Today*, 148, (1-2), pp. 160-168.

Appendix 1 Statistical Analysis

VTMS PHP: Effect of silane percentage:

The model, hypothesis, significance level used and the results of ANOVA are as follows.

Model : Fixed effect.

Let x_{ij} be the observed response of the jth unit on percentage of silane i,

for $i = 1,\ldots,8$,

$j = 1,\ldots,3$

$x_{ij} = \mu + \alpha_i + e_{ij}$ where $\sum \alpha_i = 0$

where e_{ij} are independent and identically distributed $N(0,\sigma^2)$

μ = parameter common to all treatments i.e. the overall mean

α_i = ith percentage of silane

e_{ij} = random error component

Hypothesis:

$H\phi$: $\alpha_1 = \alpha_2 = \alpha_3 = \alpha_4 = \alpha_5 = \alpha_6 = \alpha_7 = \alpha_8 = 0$

$H1$: $\alpha_i \neq 0$ for at least one i .

Significance Level:

SL = 0.05

One-way ANOVA: C1 versus C2

```
Source  DF       SS      MS      F      P
C2       8  5033.46  629.18  82.57  0.000
Error   18   137.15    7.62
Total   26  5170.61

S = 2.760   R-Sq = 97.35%   R-Sq(adj) = 96.17%
```

$F_{cal} = 82.57$ (From ANOVA table)

$F_{critical} = F_{8,\ 18;\ 0.05} = 2.510$ (from F-distribution table)

RR = $\{F : F > F_{8,18;0.05}\}$

= 2.510.

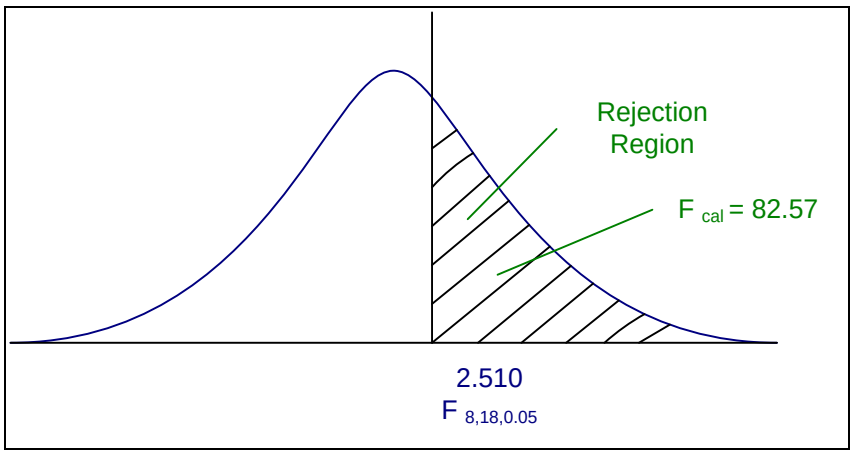

Therefore reject *Hϕ*.

Since F $_{cal}$ = 82.57 falls in the rejection region, *Hϕ* can be rejected in favour of *H1*. Hence, it can be concluded that there are significant differences in the surface area of the polymer based on the percentage of silane used. These differences are further analysed by Bonferroni test at 95.0% confident intervals. The pairs that are different are 0 & 30, 0 & 35, 5 & 25, 5 &30, 5 & 35, 5 & 40, 10 & 30, 10 & 35, 10 & 40, 15 & 30, 15 & 35, 15 & 40, 20 & 30, 20 & 35, 25 & 30, 25 & 35, 30 & 35, 30 & 40.

From the diagrams of normal probability plot and residual vs. fitted value, it can be concluded that the model assumptions of constant variance and normally distributed data are satisfied.

```
Bonferroni 95.0% Simultaneous Confidence Intervals
Response Variable C1
All Pairwise Comparisons among Levels of C2

C2 =  0  subtracted from:

C2   Lower  Center   Upper  ----+---------+---------+---------+--
 5  -14.83  -6.323   2.183           (--*--)
10  -13.42  -4.916   3.591            (-*--)
15  -12.39  -3.880   4.626            (--*--)
20   -7.43   1.073   9.579              (-*--)
25   -5.39   3.114  11.620              (--*--)
```

```
30   32.07  40.581  49.088                          (--*-)
35    4.11  12.613  21.120                (--*--)
40   -0.83   7.677  16.183                (--*-)
                           ----+---------+---------+---------+--
                             -30         0        30        60



C2 =  5  subtracted from:

C2   Lower  Center   Upper  ----+---------+---------+---------+--
10  -7.099   1.408   9.914             (-*--)
15  -6.063   2.443  10.950             (--*--)
20  -1.110   7.396  15.903               (-*--)
25   0.931   9.437  17.944               (--*--)
30  38.398  46.905  55.411                           (--*-)
35  10.430  18.937  27.443                  (--*--)
40   5.494  14.000  22.506                (--*--)
                           ----+---------+---------+---------+--
                             -30         0        30        60



C2 = 10  subtracted from:

C2   Lower  Center   Upper  ----+---------+---------+---------+--
15  -7.471   1.036   9.542             (-*--)
20  -2.518   5.989  14.495              (--*--)
25  -0.477   8.030  16.536               (--*--)
30  36.991  45.497  54.003                         (--*--)
35   9.023  17.529  26.035                  (--*--)
40   4.086  12.592  21.099                (--*--)
                           ----+---------+---------+---------+--
                             -30         0        30        60



C2 = 15  subtracted from:

C2   Lower  Center  Upper  ----+---------+---------+---------+--
20  -3.553   4.953  13.46              (--*-)
25  -1.512   6.994  15.50              (--*--)
30  35.955  44.461  52.97                          (--*--)
35   7.987  16.493  25.00                 (-*--)
40   3.050  11.557  20.06               (--*--)
                          ----+---------+---------+---------+--
                            -30         0        30        60
```

```
C2 = 20  subtracted from:

C2   Lower  Center  Upper  ----+---------+---------+---------+--
25  -6.465   2.041  10.55             (--*--)
30  31.002  39.508  48.01                         (--*--)
35   3.034  11.540  20.05               (--*--)
40  -1.903   6.604  15.11              (--*--)
                           ----+---------+---------+---------+--
                             -30         0        30        60


C2 = 25  subtracted from:

C2   Lower  Center  Upper  ----+---------+---------+---------+--
30  28.961  37.467  45.97                          (-*--)
35   0.993   9.499  18.01               (--*--)
40  -3.944   4.563  13.07              (--*-)
                           ----+---------+---------+---------+--
                             -30         0        30        60


C2 = 30  subtracted from:

C2   Lower  Center   Upper  ----+---------+---------+---------+--
35  -36.47  -27.97  -19.46    (--*--)
40  -41.41  -32.90  -24.40  (--*--)
                            ----+---------+---------+---------+--
                              -30         0        30        60


C2 = 35  subtracted from:

C2   Lower  Center  Upper  ----+---------+---------+---------+--
40  -13.44  -4.937  3.570           (-*--)
                           ----+---------+---------+---------+--
                             -30         0        30        60
```

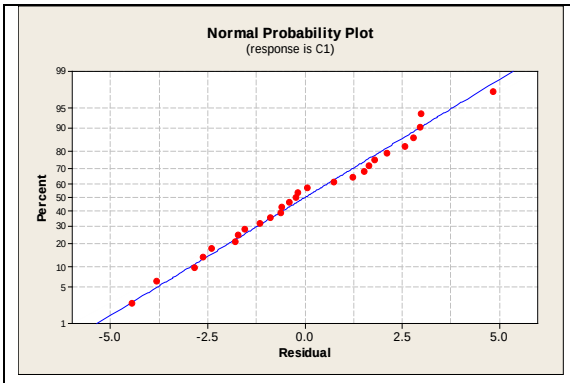

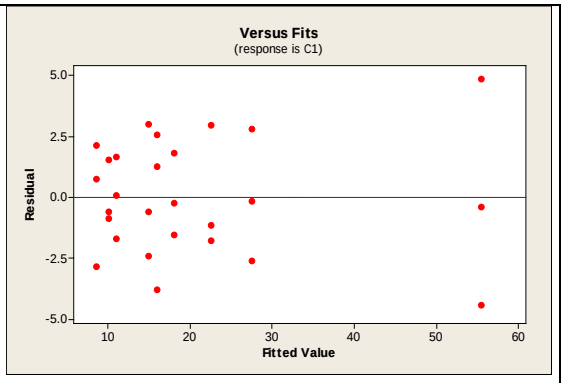

VTMS PHP: Oil phase initiator vs. aqueous phase initiator:

Two-Sample T-Test and CI: C1, C2

```
Two-sample T for C1 vs C2

    N    Mean  StDev  SE Mean
C1  2  10.004  0.972     0.69
C2  2  11.345  0.807     0.57


Difference = mu (C1) - mu (C2)
Estimate for difference:  -1.341
95% CI for difference:  (-12.692, 10.010)
T-Test of difference = 0 (vs not =): T-Value = -1.50  P-Value = 0.374 DF = 1
```

Hypothesis

$H\phi : \mu_1 = \mu_2.$

$H1 : \mu_1 . \neq \mu_2$

Significance Level: 0.05

Test Statistic: $T = \dfrac{\overline{X}_1 - \overline{X}_2}{\sqrt{\left[s_p^2 \left(\dfrac{1}{n_1} + \dfrac{1}{n_2} \right) \right]}} =$ -1.50

Evaluation of Test Statistic

$\overline{X}_1 = 10.004 \quad s_1^2 = 0.972 \quad \overline{X}_2 = 11.345 \quad s_2^2 = 0.807$

$$s_p^2 = \frac{(n_1 - 1)s_1^2 + (n_2 - 1)s_2^2}{n_1 + n_2 - 2}$$

Distribution of test statistic under $H\phi$

$$T \sim t_{n_1+n_2-2}$$

Critical Region

$$\{T : |T| > t_{2;0.025} = 4.303\}$$

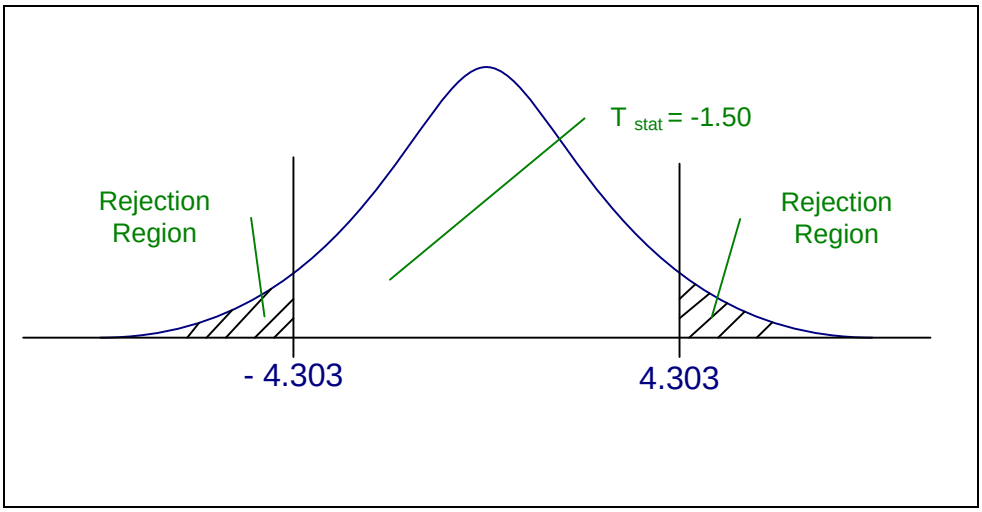

Conclusion

Cannot reject $H\phi$ in favour of *H1*, hence conclude the means are equal i.e. there is no effect of initiator used on surface area of VTMS PHP produced at 5% silane.

Basic PHP: Effect of styrene percentage on pore volumes

Two-Sample T-Test and CI: desorption mesopore, % styrene

```
Two-sample T for desorption mesopore

% styrene  N     Mean    StDev  SE Mean
68         3  0.08341  0.00248   0.0014
78         3  0.02814  0.00368   0.0021


Difference = mu (68) - mu (78)
```

```
Estimate for difference:  0.05527
95% CI for difference:  (0.04712, 0.06341)
T-Test of difference = 0 (vs not =): T-Value = 21.60 P-Value = 0.000 DF = 3
```

Hypothesis:

$H\phi : \mu_1 = \mu_2.$

$H1 : \mu_1 . \neq \mu_2$

Significance Level: 0.05

Test Statistic: $T = \dfrac{\overline{X}_1 - \overline{X}_2}{\sqrt{\left[s_p^2 \left(\dfrac{1}{n_1} + \dfrac{1}{n_2} \right) \right]}} = 21.60$

Evaluation of Test Statistic

$\overline{X}_1 = 0.08341 \quad s_1^2 = 0.00248 \quad \overline{X}_2 = 0.02814 \quad s_2^2 = 0.00368$

$$s_p^2 = \frac{(n_1 - 1)s_1^2 + (n_2 - 1)s_2^2}{n_1 + n_2 - 2}$$

Distribution of test statistic under $H\phi$

$$T \sim t_{n_1 + n_2 - 2}$$

Critical Region

$$\left\{ T : |T| > t_{4;0.025} = 2.776 \right\}$$

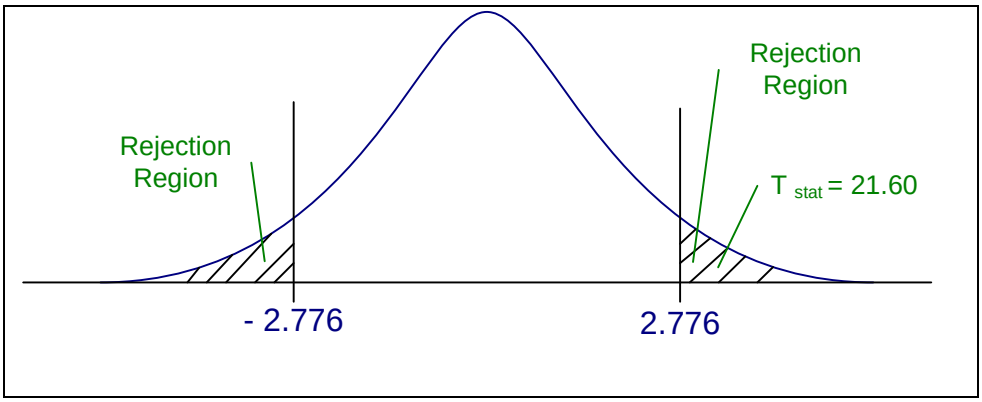

Conclusion

Can reject $H\phi$ in favour of *H1*, hence conclude the means are not equal i.e. there is effect of styrene percentage on desorption mesopore volume of basic PHP.

Two-Sample T-Test and CI: total desorption, % styrene

```
Two-sample T for total desorption

% styrene  N     Mean    StDev  SE Mean
68         3  0.08764  0.00241   0.0014
78         3  0.03260  0.00390   0.0023


Difference = mu (68) - mu (78)
Estimate for difference:  0.05504
95% CI for difference:  (0.04662, 0.06346)
T-Test of difference = 0 (vs not =): T-Value = 20.80 P-Value = 0.000 DF = 3
```

Hypothesis:

$H\phi : \mu_1 = \mu_2$.

$H1 : \mu_1 . \neq \mu_2$

Significance Level: 0.05

Test Statistic: $T = \dfrac{\overline{X}_1 - \overline{X}_2}{\sqrt{\left[s_p^2 \left(\dfrac{1}{n_1} + \dfrac{1}{n_2} \right) \right]}} = 20.80$

Evaluation of Test Statistic

$\overline{X}_1 = 0.08764 \quad s_1^2 = 0.00241 \quad \overline{X}_2 = 0.03260 \quad s_2^2 = 0.00390$

$$s_p^2 = \frac{(n_1 - 1)s_1^2 + (n_2 - 1)s_2^2}{n_1 + n_2 - 2}$$

Distribution of test statistic under $H\phi$

$$T \sim t_{n_1+n_2-2}$$

Critical Region

$$\{T : |T| > t_{4;0.025} = 2.776\}$$

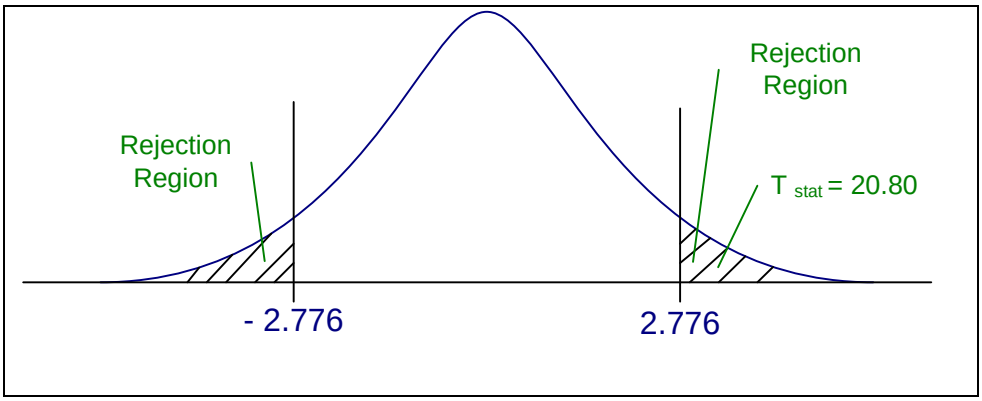

Conclusion

Can reject $H\phi$ in favour of *H1*, hence conclude the means are not equal i.e. there is effect of styrene percentage on total desorption pore volume of basic PHP.

Two-Sample T-Test and CI: adsorption mesopore, % styrene

```
Two-sample T for adsorption mesopore

% styrene  N     Mean    StDev  SE Mean
68         3  0.06819  0.00237   0.0014
78         3  0.02080  0.00361   0.0021


Difference = mu (68) - mu (78)
```

```
Estimate for difference:  0.04739
95% CI for difference:  (0.03945, 0.05533)
T-Test of difference = 0 (vs not =): T-Value = 18.99 P-Value = 0.000 DF = 3
```

Hypothesis:

$H\phi : \mu_1 = \mu_2.$

$H1 : \mu_1. \neq \mu_2$

Significance Level: 0.05

Test Statistic: $T = \dfrac{\overline{X}_1 - \overline{X}_2}{\sqrt{\left[s_p^2 \left(\dfrac{1}{n_1} + \dfrac{1}{n_2} \right) \right]}} = 18.99$

Evaluation of Test Statistic

$\overline{X}_1 = 0.06819 \quad s_1^2 = 0.00237 \quad \overline{X}_2 = 0.02080 \quad s_2^2 = 0.00361$

$$s_p^2 = \frac{(n_1 - 1)s_1^2 + (n_2 - 1)s_2^2}{n_1 + n_2 - 2}$$

Distribution of test statistic under $H\phi$

$$T \sim t_{n_1 + n_2 - 2}$$

Critical Region

$$\left\{ T : |T| > t_{4;0.025} = 2.776 \right\}$$

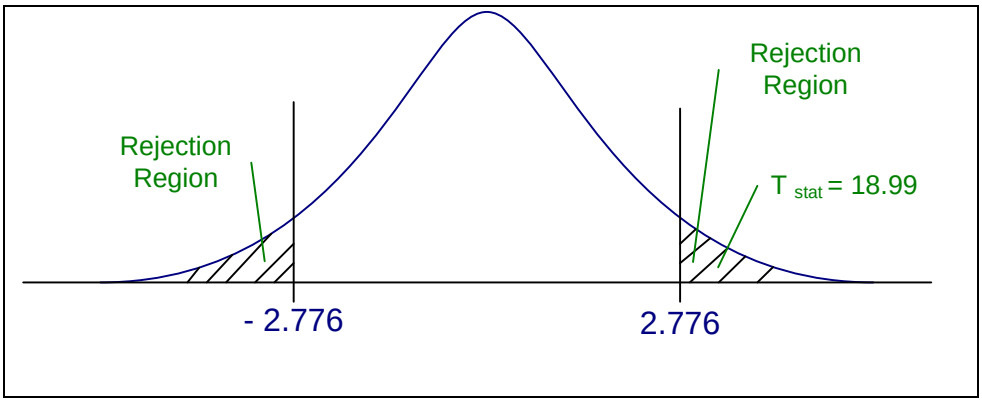

Conclusion

Can reject $H\phi$ in favour of *H1*, hence conclude the means are not equal i.e. there is effect of styrene percentage on adsorption mesopore volume of basic PHP.

Two-Sample T-Test and CI: total adsorption, % styrene

```
Two-sample T for total adsorption

% styrene  N     Mean    StDev  SE Mean
68         3  0.07987  0.00147  0.00085
78         3  0.03252  0.00394   0.0023


Difference = mu (68) - mu (78)
Estimate for difference:  0.04734
95% CI for difference:  (0.03690, 0.05779)
T-Test of difference = 0 (vs not =): T-Value = 19.50 P-Value = 0.003 DF = 2
```

Hypothesis:

$H\phi : \mu_1 = \mu_2$.

$H1 : \mu_1 . \neq \mu_2$

Significance Level: 0.05

Test Statistic: $T = \dfrac{\overline{X}_1 - \overline{X}_2}{\sqrt{\left[s_p^2 \left(\dfrac{1}{n_1} + \dfrac{1}{n_2} \right) \right]}} = 19.50$

Evaluation of Test Statistic

$\overline{X}_1 = 0.07987 \quad s_1^2 = 0.00147 \quad \overline{X}_2 = 0.03252 \quad s_2^2 = 0.00394$

$$s_p^2 = \frac{(n_1 - 1)s_1^2 + (n_2 - 1)s_2^2}{n_1 + n_2 - 2}$$

Distribution of test statistic under $H\phi$

$$T \sim t_{n_1 + n_2 - 2}$$

Critical Region

$$\{T : |T| > t_{4;0.025} = 2.776\}$$

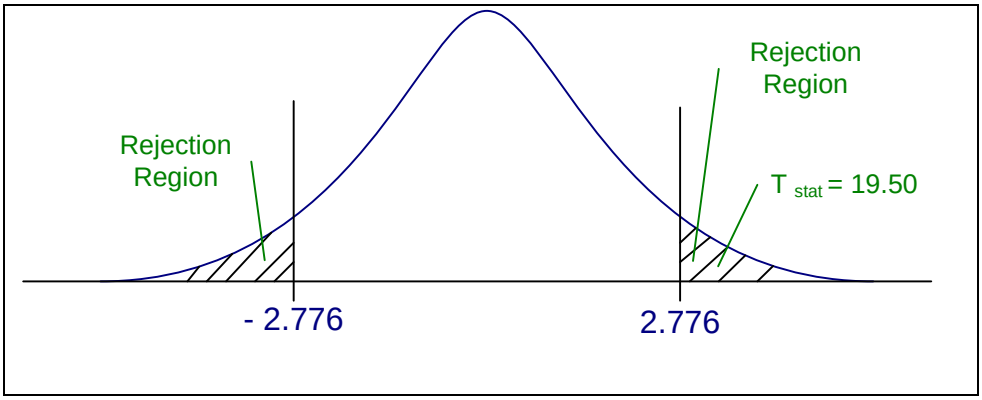

Conclusion

Can reject $H\phi$ in favour of *H1*, hence conclude the means are not equal i.e. there is effect of styrene percentage on total adsorption pore volume of basic PHP.

Appendix 2 GC Analysis

Example of GC result, Run 26, treatment using Plasma, 60 Volt, 50 Watt.

Detail result GC chromatogram for Run 26-1, before treatment:

Name	Time [Min]	Quantity [wt %]	Height [µV]	Area [µV.Min]	Area % [%]
Ethene	1.96	N.D.	N.D.	N.D.	N.D.
Ethane	1.97	N.D.	N.D.	N.D.	N.D.
Propene	2.02	N.D.	N.D.	N.D.	N.D.
Propane	2.03	N.D.	N.D.	N.D.	N.D.
Butene	2.18	N.D.	N.D.	N.D.	N.D.
Butane	2.2	N.D.	N.D.	N.D.	N.D.
Pentene	2.56	N.D.	N.D.	N.D.	N.D.
Pentane	2.64	0.01	4845	84.3	0.758
Hexene	3.52	N.D.	N.D.	N.D.	N.D.
Hexane	3.67	0.01	3476.3	84.4	0.758
Heptene	5.43	0.02	6192.6	219.3	1.971
Heptane	5.72	0	546.9	19	0.171
Octene	8.26	0	1238.9	47.3	0.425
Octane	8.63	0	326.6	18.2	0.163
Decene	12.98	N.D.	N.D.	N.D.	N.D.
Decane	13.29	N.D.	N.D.	N.D.	N.D.
Dodecene	16.55	N.D.	N.D.	N.D.	N.D.
Dodecane	16.84	N.D.	N.D.	N.D.	N.D.
Tetradecene	19.43	N.D.	N.D.	N.D.	N.D.
Tetradecane	19.71	N.D.	N.D.	N.D.	N.D.
Hexadecene	21.92	N.D.	N.D.	N.D.	N.D.
Hexadecane	22.2	N.D.	N.D.	N.D.	N.D.
Octadecene	24.14	N.D.	N.D.	N.D.	N.D.
Octadecane	24.24	N.D.	N.D.	N.D.	N.D.

Eicosene	26.15	N.D.	N.D.	N.D.	N.D.
Eicosane	26.24	N.D.	N.D.	N.D.	N.D.

Detail result of GC chromatogram for Run 26-2, after treatment:

Name	Time [Min]	Quantity [wt %]	Height [µV]	Area [µV.Min]	Area % [%]
Ethene	1.96	0.57	3051	20.7	0.27
Ethane	1.97	N.D.	N.D.	N.D.	N.D.
Propene	2.02	0.29	3553.1	71.8	0.936
Propane	2.03	N.D.	N.D.	N.D.	N.D.
Butene	2.18	N.D.	N.D.	N.D.	N.D.
Butane	2.2	0.22	3050.5	58.8	0.767
Pentene	2.57	0	178.7	3.1	0.041
Pentane	2.64	0.01	4197.6	77.5	1.011
Hexene	3.5	0	95.9	3.3	0.043
Hexane	3.73	0	53.9	1.6	0.021
Heptene	5.42	0.02	6653.1	238.4	3.109
Heptane	5.71	0.01	719.6	35.3	0.46
Octene	8.25	0	1494.2	63.9	0.833
Octane	8.63	0	424.9	28.3	0.369
Decene	12.94	0	44.4	2.4	0.031
Decane	13.3	0	7.4	0.7	0.008
Dodecene	16.55	N.D.	N.D.	N.D.	N.D.
Dodecane	16.84	N.D.	N.D.	N.D.	N.D.
Tetradecene	19.52	0	20.8	0.5	0.007
Tetradecane	19.71	N.D.	N.D.	N.D.	N.D.
Hexadecene	21.98	0	35.7	1.1	0.015
Hexadecane	22.71	0	16.5	0.6	0.008
Octadecene	24.14	N.D.	N.D.	N.D.	N.D.
Octadecane	24.24	N.D.	N.D.	N.D.	N.D.

Eicosene	26.15	N.D.	N.D.	N.D.	N.D.
Eicosane	26.37	0	25	2	0.026

Detail result of GC chromatogram for Run 26-3, after treatment:

Name	Time [Min]	Quantity [wt %]	Height [µV]	Area [µV.Min]	Area % [%]
Ethene	1.96	0.57	3952.3	29.9	0.261
Ethane	1.97	N.D.	N.D.	N.D.	N.D.
Propene	2.03	0.28	3279.8	64	0.556
Propane	2.03	N.D.	N.D.	N.D.	N.D.
Butene	2.18	N.D.	N.D.	N.D.	N.D.
Butane	2.2	0.22	2204.9	70.8	0.616
Pentene	2.56	N.D.	N.D.	N.D.	N.D.
Pentane	2.63	0.01	3024.2	57.9	0.504
Hexene	3.47	0	84.5	2.8	0.024
Hexane	3.7	N.D.	N.D.	N.D.	N.D.
Heptene	5.38	0.01	4912.8	172.3	1.499
Heptane	5.67	0	463.9	17.6	0.153
Octene	8.22	0	1001.9	37.3	0.324
Octane	8.59	0	251.2	11.2	0.097
Decene	12.98	N.D.	N.D.	N.D.	N.D.
Decane	13.29	N.D.	N.D.	N.D.	N.D.
Dodecene	16.55	N.D.	N.D.	N.D.	N.D.
Dodecane	16.84	N.D.	N.D.	N.D.	N.D.
Tetradecene	19.43	N.D.	N.D.	N.D.	N.D.
Tetradecane	19.71	N.D.	N.D.	N.D.	N.D.
Hexadecene	21.92	N.D.	N.D.	N.D.	N.D.
Hexadecane	22.2	N.D.	N.D.	N.D.	N.D.
Octadecene	24.14	N.D.	N.D.	N.D.	N.D.
Octadecane	24.24	N.D.	N.D.	N.D.	N.D.

Eicosene	26.15	N.D.	N.D.	N.D.	N.D.
Eicosane	26.24	N.D.	N.D.	N.D.	N.D.

Detail result of GC chromatogram for Run 26-4, after treatment:

Name	Time [Min]	Quantity [wt %]	Height [µV]	Area [µV.Min]	Area % [%]
Ethene	1.96	0.57	4646.7	33.5	0.473
Ethane	1.97	N.D.	N.D.	N.D.	N.D.
Propene	2.02	0.29	3974	78.8	1.111
Propane	2.03	N.D.	N.D.	N.D.	N.D.
Butene	2.18	N.D.	N.D.	N.D.	N.D.
Butane	2.2	0.22	1834.6	57.6	0.811
Pentene	2.56	0	220.9	4	0.056
Pentane	2.63	0.01	2900.6	56.1	0.79
Hexene	3.48	0	125.1	4.7	0.067
Hexane	3.7	0	35.5	1.7	0.024
Heptene	5.39	0.02	6662.5	236.2	3.327
Heptane	5.69	0	693.1	27.8	0.392
Octene	8.23	0	1718.1	66	0.93
Octane	8.6	0	432.1	18.6	0.262
Decene	12.99	0	27.5	2.2	0.031
Decane	13.34	0	56	6.9	0.097
Dodecene	16.55	N.D.	N.D.	N.D.	N.D.
Dodecane	16.89	0	15.6	0.6	0.008
Tetradecene	19.43	N.D.	N.D.	N.D.	N.D.
Tetradecane	19.71	N.D.	N.D.	N.D.	N.D.
Hexadecene	21.92	0	15.6	0.3	0.004
Hexadecane	22.78	0	8.1	0.7	0.01
Octadecene	24.14	N.D.	N.D.	N.D.	N.D.
Octadecane	24.24	N.D.	N.D.	N.D.	N.D.

Eicosene	26.06	0	46.8	7.8	0.11
Eicosane	26.24	N.D.	N.D.	N.D.	N.D.

Detail result of GC Chromatogram for Run 26-5, before treatment:

Name	Time [Min]	Quantity [wt %]	Height [µV]	Area [µV.Min]	Area % [%]
Ethene	1.96	N.D.	N.D.	N.D.	N.D.
Ethane	1.97	0.36	40.7	1.4	0.013
Propane	2.03	N.D.	N.D.	N.D.	N.D.
Propene	2.03	0.27	258.8	5.5	0.052
Butene	2.18	N.D.	N.D.	N.D.	N.D.
Butane	2.2	0.21	1060.9	14.9	0.141
Pentene	2.56	N.D.	N.D.	N.D.	N.D.
Pentane	2.62	0.01	2524.2	43.8	0.417
Hexene	3.52	N.D.	N.D.	N.D.	N.D.
Hexane	3.7	N.D.	N.D.	N.D.	N.D.
Heptene	5.31	0.02	6173.1	218.6	2.079
Heptane	5.7	N.D.	N.D.	N.D.	N.D.
Octene	8.16	0	1406.7	55	0.524
Octane	8.54	0	379.1	17.7	0.168
Decene	12.98	N.D.	N.D.	N.D.	N.D.
Decane	13.29	N.D.	N.D.	N.D.	N.D.
Dodecene	16.55	N.D.	N.D.	N.D.	N.D.
Dodecane	16.84	N.D.	N.D.	N.D.	N.D.
Tetradecene	19.43	N.D.	N.D.	N.D.	N.D.
Tetradecane	19.71	N.D.	N.D.	N.D.	N.D.
Hexadecene	21.92	N.D.	N.D.	N.D.	N.D.
Hexadecane	22.2	N.D.	N.D.	N.D.	N.D.
Octadecene	24.14	N.D.	N.D.	N.D.	N.D.
Octadecane	24.24	N.D.	N.D.	N.D.	N.D.

Eicosene	26.15	N.D.	N.D.	N.D.	N.D.
Eicosane	26.24	N.D.	N.D.	N.D.	N.D.

Detail results for Run 26-6, before treatment:

Name	Time [Min]	Quantity [wt %]	Height [µV]	Area [µV.Min]	Area % [%]
Ethene	1.97	0.56	20.6	0.6	0.004
Ethane	1.97	N.D.	N.D.	N.D.	N.D.
Propene	2.02	N.D.	N.D.	N.D.	N.D.
Propane	2.03	N.D.	N.D.	N.D.	N.D.
Butene	2.18	N.D.	N.D.	N.D.	N.D.
Butane	2.2	0.21	1010	18.4	0.129
Pentene	2.56	N.D.	N.D.	N.D.	N.D.
Pentane	2.64	0.01	1935.8	34.9	0.244
Hexene	3.49	0	15	0.4	0.002
Hexane	3.66	0.01	1791.3	44.3	0.31
Heptene	5.42	0.01	3572.3	126	0.881
Heptane	5.72	0	303.3	11.1	0.077
Octene	8.26	0	692.5	25.2	0.176
Octane	8.63	0	178.1	7.5	0.052
Decene	12.98	N.D.	N.D.	N.D.	N.D.
Decane	13.29	N.D.	N.D.	N.D.	N.D.
Dodecene	16.55	N.D.	N.D.	N.D.	N.D.
Dodecane	16.84	N.D.	N.D.	N.D.	N.D.
Tetradecene	19.43	N.D.	N.D.	N.D.	N.D.
Tetradecane	19.71	N.D.	N.D.	N.D.	N.D.
Hexadecene	21.92	N.D.	N.D.	N.D.	N.D.
Hexadecane	22.2	N.D.	N.D.	N.D.	N.D.
Octadecene	24.14	N.D.	N.D.	N.D.	N.D.
Octadecane	24.24	N.D.	N.D.	N.D.	N.D.

Eicosene	26.15	N.D.	N.D.	N.D.	N.D.
Eicosane	26.24	N.D.	N.D.	N.D.	N.D.